

Measurements in Swirl-stabilised Spray Flames at Blow-off



Ruoyang Yuan
Robinson College
University of Cambridge

A thesis submitted for the degree of

Doctor of Philosophy

March 2015

To my parents and friends

Acknowledgements

I am extremely grateful to many people for their support and their help. First and foremost, I would like to express my sincerest gratitude to my supervisor, Prof. E. Mastorakos, for his enormous support and aspiring guidance. His immense knowledge, patience, encouragement, and broad vision were the key motivation throughout my PhD. I want to thank my advisor Prof. J. Dawson for his valuable suggestions and help. I want to thank Prof. B. Rogg for his thoughtful discussion and great support on laminar flame simulations via COSILAB software. I want to express my gratitude to Prof. G. Continillo, Mr. S. Lombardi for the valuable collaboration on the POD analysis, and to Prof. S. Couris, Dr. M. Kotzagianni for the precious collaboration on LIBS measurements. I want to thank Dr. J. Kariuki, Dr. D. Cavaliere, and Dr. N. Karimi for their assistance on many laser diagnostic set-ups and valuable discussions on the flame behaviour. I would like to express my sincere thanks to Mick Underwood, Ken Griggs, Robert Leroy and John Harvey, Roy Slater for their great support during the fabrication and installation of the test rig. Without them this thesis could not exist. I also wish to thank Mr. Peter Benie for his help with the computing facilities and Mrs. Kate Graham and Ms. Katia Babayan for their assistances and useful suggestions. I want to thank my colleagues D. Farrow, E. Demosthenous, E. Machover, J. Sidey, J. Hobbs, H. Zhang, A. Giusti for their supports.

I would like to thank Mr. C. Y. Lee, for his support and insightful discussions along the way. I value his modest attitude and infinite passion of the truth, work and combustion physics.

I want to express my sincere gratitude to my parents, Ms. L. H. Li and Prof. X. J. Yuan, for their endless love, understanding and supports.

I want to acknowledge EPSRC Dorothy Hodgkin Studentship for the financial support for my study and this work.

Publications

Journal publications

Yuan, R., Kariuki, J., Dowlut, A., Balachandran, R., & Mastorakos, E. (2014). Reaction zone visualisation in swirling spray n-heptane flames. *Proceedings of the Combustion Institute* 35 (2015) 1649–1656.

Kariuki, J., Dowlut, A., Yuan, R., Balachandran, R., & Mastorakos, E. (2014). Heat release imaging in turbulent premixed methane–air flames close to blow-off. *Proceedings of the Combustion Institute* 35 (2015) 1443–1450.

Conference publications

Yuan, R., Kotzagianni, M., Couris, S., & Mastorakos, E. (2014). Laser-induced breakdown spectroscopy measurements in spray flames. In 17th International Symposium on Applications of Laser Techniques to Fluid Mechanics Lisbon, Portugal, 07-10 July.

Yuan, R., Giusti, A., Kotzagianni, M., & Mastorakos, E. (2015). Experimental and numerical investigation of a swirling ethanol spray flame with local extinction. In Ninth Mediterranean Combustion Symposium, Rhodes, Greece. To Appear.

Kotzagianni, M., Yuan, R., Mastorakos, E., & Couris, S. (2014). Laser-induced breakdown spectroscopy measurements in turbulent methane flames. 52nd AIAA Aerospace Sciences Meeting - AIAA Science and Technology Forum and Exposition, SciTech 2014.

Declaration

This dissertation is submitted to the University of Cambridge in fulfilment for the degree of Doctor of Philosophy. It is an account of the research I have undertaken in the Department of Engineering at the University of Cambridge, under the supervision of Prof. E. Mastorakos. The work described is original and a result of my own work and includes nothing which is the outcome of work done in collaboration except where specifically indicated in the text. This dissertation contains approximately 40,426 words, 79 figures and 6 tables, and no part of it has already been, or is currently being, submitted for any other degree, diploma, or other qualification, at any other University.

Hopkinson Laboratory, University of Cambridge

13th March 2015

Ruoyang Yuan

Abstract

This thesis describes an experimental investigation of swirl-stabilised spray flames of various fuels at conditions close to lean stability limits, to compare flames of fuels with different volatility in the same burner, and to develop further understanding on local flame extinctions, and how these result in global extinction.

The first part of the thesis describes a set of 1D laminar flame simulations of premixed and non-premixed flames of the single-component gaseous fuel: ethanol, heptane, decane, and dodecane and of a kerosene surrogate: the “Aachen” fuel surrogate. The purposes of these simulations are to obtain detailed flame structures under various flow conditions for different fuels, to examine the correlation between the heat release rate (HRR) and hydroxyl (OH) radical and formaldehyde (CH_2O) radical for these flames, and to provide a reference for experimental observations. Detailed chemical mechanisms and transport properties are applied in the simulations. The results suggest that the product $\text{CH}_2\text{O} \times \text{OH}$ marks relatively well the spatial location of the heat release in both premixed and non-premixed flames for these fuels. Furthermore, in non-premixed flames, the outline of CH_2O profile aligns close to the stoichiometric mixture fraction line at all the strain rates investigated.

The second part describes an experimental investigation of swirl-stabilised spray flames of high volatility (ethanol, n-heptane) fuels and low volatility (n-decane, n-dodecane) fuels at conditions approaching blow-off, and at the blow-off event. The measurements included OH^* chemiluminescence, Planar Laser Induced Fluorescence (PLIF) of OH and CH_2O , Mie scattering, and Phase Doppler Anemometry (PDA). The results show that the spray flames take a predominantly non-premixed character. Two main heat release (HR) zones shown from OH^* signal lie around the spray jet at the inner recirculation zone (IRZ) and along the outer shear layer. The HR region is shortened and moves towards the atomiser as the flame is approaching blow-off. Similar spatial distributions of the Sauter Mean Diameter (SMD) are observed for the four fuels for identical flow conditions, with the exception of significant presence of droplets for the ethanol spray in the nominally hollow cone. The OH-PLIF movies of the stable flames at conditions away from blow-off show asymmetric lift-off and

extinction along the outer shear layer, with less extinction occurrence at the inner flame branch along the spray. However, at the blow-off conditions, a more variable behaviour is shown in the OH-PLIF images, where local extinctions frequently appear at both inner and outer flame branches. These findings are independent of the fuel used, although the flame shapes show some minor differences.

Next, the blow-off correlation, the transient process of the blow-off event, and the large-scale motion present in the spray flames at blow-off conditions are examined. The blow-off correlation, by Radhakrishnan et al., is found to collapse reasonably well the blow-off data from the present experiments with different liquid fuels. The transient blow-off process shows a gradual reduction of the size of the HR region. The average blow-off duration, τ_{ext} , calculated from the OH* evolution is a few tens of milliseconds for all fuels and a range of fuel loadings. The normalised duration by the flow characteristic time, $\tau_{\text{ext}}/(D/U_B)$, is around 11, but with large scatter. The percentage of quenched stoichiometric mixture fraction iso-surface is quantified and is found to be 21% and 34% at condition far from and close to blow-off respectively. Proper Orthogonal Decomposition (POD) is used to analyse OH* and OH-PLIF images. The OH* POD modes indicate a strong transverse motion more prominent at the blow-off condition than at the condition far from blow-off. The OH-PLIF POD modes show an intermittent lift-off. The measurements provide useful information for validation of combustion models focusing on local and global extinction.

The final part of the thesis describes an attempt at local equivalence ratio measurements by Laser Induced Breakdown Spectroscopy (LIBS) in swirl-spray flames of heptane. A series of turbulent gaseous-fuelled flames (premixed, non-premixed) were examined with LIBS methods prior to the spray flames. A new calibration scheme by using spectrum intensity ratio H_α/O and C_2/CN in the lean and rich mixture conditions respectively was proposed to apply LIBS in a wide range of fuel mixtures, especially in non-premixed systems. The LIBS by the averaging method shows reasonable results in all flames studied. However, the single-shot LIBS measurements show a variance of 15-20% in uniform mixtures and require further studies. For turbulent spray flames, LIBS also provides reasonable measurements of local equivalence ratio, and the values are consistent with expectations.

Contents

Contents

List of Figures

List of Tables

Chapter 1 Introduction	1
1.1 Motivation	1
1.2 Literature Background	3
1.2.1 Swirl stabilisation	4
1.2.2 Local extinction and flame lift-off	4
1.2.3 Spray combustion	6
1.2.4 Blow-off of turbulent gas flames: premixed and non-premixed	11
1.2.5 Blow-off of spray flames	15
1.2.6 Heat release visualisation by joint PLIF measurement	17
1.2.7 Proper orthogonal decomposition analysis on flow structure	18
1.2.8 Laser induced breakdown spectroscopy of turbulent flames	19
1.3 Scope of the thesis	20
1.4 Structure of the thesis	21
Chapter 2 Experimental methods	23
2.1 Burner configuration	23
2.2 Flow measurement methodology	24
2.2.1 Flow-rate measurements	24
2.2.2 Determination of the blow-off point	24

2.3 Diagnostic methods	25
2.3.1 Laser Doppler Velocimetry/Phase Doppler Anemometry	25
2.3.2 Chemiluminescence measurements	26
2.3.3 Planar Laser Induced Fluorescence measurements	26
2.3.5 Mie scattering measurements	27
2.3.6 LIBS configuration	27
2.4 Data analysis	28
2.4.1 Data processing	28
2.4.2 Duration of the blow-off event	32
2.4.3 Lift-off height analysis	32
2.4.4 Statistics of local quenching size	32
2.4.5 Proper orthogonal decompositions (POD) analysis	32
2.5 Figures for Chapter 2	35
Chapter 3 Laminar flame calculations	39
3.1 Freely propagating premixed gas flames	40
3.1.1 Background and equations	40
3.1.2 Laminar flame speed	41
3.1.3 Laminar flame structure	42
3.2 Counterflow non-premixed gas flames	43
3.2.1 Background and equations	43
3.2.2 Lamina flame structure	44
3.2.3 Strain rate at blow-off	47
3.3 Conclusions	48
3.4 Figures for Chapter 3	49
Chapter 4 Spray flame blow-off: Flame Structure	57
4.1 Experiment methods and data analysis	57
4.2 Results and Discussion	60
4.2.1 Stability limits	60
4.2.2 Flame appearance	61
4.2.3 Droplet size and velocity distributions	61
4.2.4 Heat release	65

4.2.5	Flame sheet characteristics by OH – PLIF measurements	68
4.2.6	Mie scattering images	69
4.2.7	Reaction zone visualisation by Joint CH ₂ O-OH PLIF	70
4.3	Conclusions	72
4.4	Tables for Chapter 4	74
4.4	Figures for Chapter 4	77
	Chapter 5 Spray flame behaviour at the blow-off event	92
5.1	Results and Discussion	93
5.1.1	Blow-off correlation	93
5.1.2	Blow-off transient and its duration	93
5.1.3	Lift-off height statistics	94
5.1.4	Local quenching analysis	95
5.1.5	OH morphology analysis	96
5.1.6	POD analysis	96
5.2	Conclusion	102
5.3	Tables for Chapter 5	104
5.4	Figures for Chapter 5	105
	Chapter 6 Laser-induced breakdown spectroscopy measurements on turbulent flames	116
6.1	LIBS measurements in turbulent gaseous flames	117
6.1.1	Burner configurations and flow conditions	117
6.1.2	Uniform-flowing methane-air mixtures -- Calibration scheme	118
6.1.3	Turbulent premixed flames	124
6.1.4	Turbulent reacting and non-reacting jets	125
6.2	LIBS measurements in swirling spray flames	127
6.2.1	Burner configurations and flow conditions	127
6.2.2	Uniform dispersed C ₇ H ₁₆ -air mixture	128
6.2.3	Measurements in turbulent spray flames	130
6.3	Conclusions	133
6.4	Figures for Chapter 6	134
	Chapter 7 Conclusions and suggestions for further research	146

7.1 Conclusions from this work	146
7.1.1 Laminar flame calculations	147
7.1.2 Spray flame structure	149
7.1.3 Spray flames dynamic behaviour	151
7.2 Suggestions for further research	152
Appendix	
LDA/PDA measurements results on spray profiles of bluff-body swirl spray flames	154
A.1 Flow conditions	154
A.2 Results	155
A.2.1 Heptane flames (H1S1 vs. H1S2)	155
A.2.2 Heptane flames (H0S1 vs. H0S2)	156
A.2.3 Decane flames (D1S1 vs. D1S2)	157
A.2.4 Dodecane flames (DD1S1 vs. DD1S2)	159
References	161

Nomenclature

Roman letters

$A_{m,n}$	constant
a	strain rate
B	fuel mass transfer number
B_g	blockage ratio
c_p	specific heat capacity at constant pressure
D	diameter of bluff body
Da	Damköhler number
Da_t	turbulent Damköhler number
D_l	nozzle diameter at exit
D_d	droplet diameter
d	liquid jet diameter
f_f	fraction of fuel evaporated
h_i	total enthalpy of species i
I	local OH* chemiluminescence emission
Ka	Karlovitz number
k	thermal diffusivity
L	length of the recirculation zone
Le	Lewis number
L_{lf}	lift-off height
l	integral length scale
\dot{m}_f	fuel mass flow rate
\dot{m}_a	air mass flow rate
P	the projection of the line-of-sight OH* signal
p	pressure
R	gas constant
Re	Reynolds number
r	the radial distance in the cylindrical coordinate system

r_b	radial position at breakup
S_L	laminar flame speed
S_N	swirl number
Sc	Schmidt number
St	Stokes number
T	temperature
Ta	Taylor parameter
T_{ad}	adiabatic flame temperature
U	droplet mean axial velocity
U'	root mean square of droplet axial velocity
U_b	air bulk velocity
U_B	air bulk velocity at blow-off conditions
U_l	liquid jet velocity at nozzle exit
U_g	gas axial velocity
u'	turbulent velocity fluctuations
V	droplet mean radial velocity
V'	root mean square of droplet radial velocity
V_c	combustion volume
W	droplet mean tangential velocity
W'	root mean square of droplet tangential velocity
W_i	molecular weight of species i
We	Weber number
w_i	production rate of species i
Oh	Ohnesorge number
X	molar fraction
x	Cartesian coordinate
Y	mass fraction
y	Cartesian coordinate
Z	axial coordinate

Greek letters

δ_L	laminar flame thickness
λ	thermal conductivity
λ_T	Taylor microscale
μ	dynamic viscosity, [kg/m/s]
ξ	mixture fraction
ξ_{st}	stoichiometric mixture fraction
ρ	density
σ	surface tension coefficient
τ	characteristic time
τ_c	characteristic chemical time scale
τ_e	eddy time
τ_{ext}	average blow-off duration
τ_f	characteristic flow time scale

ϕ	equivalence ratio
ϕ_{BO}	overall equivalence ratio at blow-off
χ	scalar dissipation rate, [1/s]
ψ	vaporisation Damköhler number

Subscripts

BO	blow-off
b	bulk property
d	droplet
ext	extinction
f	fuel
g	gas
i	species, index
j, k	pixel indexes
l	liquid
st	stoichiometry

Abbreviations

CMC	Conditional Moment Closure
CSP	Cumulative Spectral Power
FAR	Fuel Air Ratio
LBO	Lean Blow-off
LDA	Laser Doppler Velocimetry
LES	Large Eddy Simulations
LHV	Lower Heating Value of the fuel
LIBS	Laser Induced Breakdown Spectroscopy
PDA	Phase Doppler Anemometry
PLIF	Planar Laser Induced Fluorescence
POD	Proper Orthogonal Decomposition
PSD	Power Spectral Density
SMD	Sauter Mean Diameter
WSR	Well-Stirred Reactor

List of Figures

Figure 1. Schematic of bluff-body swirl spray burner (left), and experimental set ups for swirling spray flames (right).

Figure 2. (I) Photograph of the pressure atomiser (A), the ensemble of the atomiser (B and C) showing the spiral grooves to ensure swirling of the liquid (B), the schematic diagram of the internal flow and the hollow-cone spray profile (D [221]), and the bluff-body atomiser holder (E). The red arrow (in A) points the exit of the liquid fuel. (II) Photograph of the swirler and the dimensions.

Figure 3. Schematic of the laser layout and acquisition system set ups of (a) OH-PLIF, (b) joint CH₂O-OH PLIF, and (c) LIBS arrangement.

Figure 4. (a) The data processing flowchart of the product of CH₂O-OH PLIF, and (b) an example of the sensitivity of the binarisation threshold for OH image and CH₂O image: 1st row - the OH image with various threshold values (defined in the text); 1st column – the CH₂O image with various threshold values; and the remaining images of the matrix – the corresponding product image of CH₂O and OH after applying the thresholds of the same row and column. The red box indicates the final image reported in the results.

Figure 5: (a) An example image from fast OH-PLIF of decane (D1S1, fuel flow rate is 0.27 g/s and air bulk velocity is 17.1 m/s). The lift-off height (h_{lf}) is marked in the image. (b) Example images from the joint CH₂O-OH PLIF image of stable heptane flame (H1S1, fuel flow rate is 0.27 g/s and air bulk velocity is 17.1 m/s). The image includes the binarised OH signal (red), CH₂O signal (colour, from blue-pink), and the CH₂O signal's boundary (white line), which can be used as a rough estimate of the stoichiometric contour (discussed later in Ch.3). L is measured as the length of the CH₂O boundary that has zero overlap with the OH signal. The total length of the CH₂O boundary (the white line) is calculated as Σ . The quenching percentage, b , of the stoichiometric iso-line is then obtained as L/Σ .

Figure 6. Laminar flame speeds (a) and adiabatic flame temperatures (b) at various equivalence ratios obtained from the laminar premixed flame simulations of the various fuels: ethanol (E, Ranzi et al. mechanism [190]); heptane (H, Held et al. mechanism [191]); decane (D, Honnet et al. mechanism [192]); dodecane (DD, Ranzi et al. mechanism [190]); and Aachen fuel surrogate (Aa, Honnet et al. mechanism [192]).

Figure 7. Laminar premixed flame calculations of ethanol flames: temperature, heat release rate (HRR), and molar fraction of O₂, C₂H₅OH, OH and CH₂O at (a) stoichiometric, (b) lean ($\phi=0.7$), and (c) rich ($\phi=1.4$) conditions; and (d) the correlation between the HRR and the product CH₂O x OH for a range of equivalence ratios ($\phi = 0.6 \sim 1.4$).

Figure 8. Laminar premixed flame calculations of (a-b) heptane, (c-d) decane, (e-f) dodecane and (g-h) ‘‘Aachen’’ fuel surrogate: the temperature, HRR, and molar fraction of O₂, C₇H₁₆,

OH and CH₂O profile at (left) stoichiometric and (right) lean ($\phi=0.7$) conditions.

Figure 9. Laminar premixed flame calculations of (a) heptane, (b) decane, (c) dodecane and (d) “Aachen” fuel surrogate: the correlation between the normalised HRR and normalised product CH₂O x OH for a range of equivalence ratios ($\phi = 0.7 \sim 1.4$).

Figure 10. Comparison of the temperature (a); molar fraction of CH₂O (b) and OH (c); and HRR (d) obtained from the laminar premixed flame calculations of ethanol (E), heptane (H), decane (D), dodecane (DD), and “Aachen” fuel surrogate (Aa) at the stoichiometric condition.

Figure 11. Percentage of the normalised area of HRR represented by the normalised area of product CH₂O x OH for a range of equivalence ratios of the laminar premixed flames of the four fuels.

Figure 12. Laminar counterflow non-premixed flames simulations of heptane: i. temperature and various species molar fractions *vs.* mixture fraction for strain rate (a) 100 s⁻¹ and (b) 500 s⁻¹; ii. normalised mole fractions of OH and CH₂O, normalised HRR, and normalised $X_{\text{CH}_2\text{O}} \times X_{\text{OH}}$ at strain rate (c) 100 s⁻¹ and (d) 500 s⁻¹; and iii. HRR *vs.* $X_{\text{CH}_2\text{O}} \times X_{\text{OH}}$ (e), and HRR *vs.* $(X_{\text{CH}_2\text{O}} + X_{\text{C}_7\text{H}_{16}}) \times X_{\text{OH}}$ (f) for the indicated strain rate.

Figure 13. Laminar counterflow non-premixed gas flames simulations of ethanol: i. temperature and various species molar fractions *vs.* mixture fraction for strain rate (a) 100 s⁻¹ and (b) 500 s⁻¹; ii. normalised mole fractions of OH and CH₂O, normalised HRR, and normalised $X_{\text{CH}_2\text{O}} \times X_{\text{OH}}$ at strain rate (c) 100 s⁻¹ and (d) 500 s⁻¹; and iii. HRR *vs.* $X_{\text{CH}_2\text{O}} \times X_{\text{OH}}$ (e) for the indicated strain rate.

Figure 14. Laminar counterflow non-premixed gas flames simulations of n-decane: i. temperature and various species molar fractions *vs.* mixture fraction for strain rate (a) 200 s⁻¹ and (b) 800 s⁻¹; ii. normalised mole fractions of OH and CH₂O, normalised HRR, and normalised $X_{\text{CH}_2\text{O}} \times X_{\text{OH}}$ at strain rate (c) 200 s⁻¹ and (d) 800 s⁻¹; and iii. HRR *vs.* $X_{\text{CH}_2\text{O}} \times X_{\text{OH}}$ (e) for the indicated strain rate.

Figure 15. Comparison of the temperature (a); molar fraction of CH₂O (b) and OH (c); and HRR (d) obtained from the laminar counterflow non-premixed flame calculations of ethanol (E), heptane (H), and decane (D) at low (solid lines; $a=100\text{S}^{-1}$) and high (dash lines; $a=500\text{S}^{-1}$) strain rate conditions; (e) percentage of the normalised area of HRR represented by the normalised area of product CH₂O x OH for a range of strain rates these fuels; and (f) peak temperatures *vs.* strain rates of laminar counterflow non-premixed flames of ethanol (E, Marinov et al. mechanism [194]), heptane (H, Held et al. mechanism [191]), and n-decane (D, Honnet et al. mechanism [192]).

Figure 16. Blow-off velocities (closed symbols) as a function of fuel flow rate for (a) ethanol, (b) heptane, (c) decane, and (d) dodecane. Open symbols mark various test conditions of stable flames discussed in the text. The labels at the top and right lines mark the fuel flow rate and air velocity respectively of the indicated flame code.

Figure 17. Photographs of stable spray flames of (from left to right) ethanol at E1S1, heptane at H1S1, n-decane at D1S1, and n-dodecane at DD1S1 (for all, $\dot{m}_f = 0.27\text{g/s}$ and $U_b=17.1\text{ m/s}$, $Re_g = 13466$).

Figure 18. Distributions of (a) Sauter mean diameter, and normalised droplet mean (b) axial and (c) radial velocity, normalised rms fluctuations of (d) axial and (e) radial velocity, and (f) the ratio of the two velocity component fluctuations. Ethanol stable flames: E1S1 (open symbols) and E1S2 (closed symbols) at various downstream locations. E1S1 and E1S2 have the same fuel loading ($\dot{m}_f = 0.27\text{g/s}$) and air velocity of 17.1 m/s and 20.0 m/s respectively.

Figure 19. Mean (a, c, e, g) and rms (b, d, f, h) axial droplet velocity conditional on the droplet size ranges (square: 10-40 μm ; circle: 40-80 μm ; triangle: 80-100 μm) and the mean and rms axial velocity using all droplets (star) vs. radius, measured at various downstream locations (a,b: 10; c,d: 20; e,f: 30; g,h: 40, mm). Ethanol stable flame: E1S1($\dot{m}_f = 0.27\text{g/s}$, $U_b=17.1\text{ m/s}$).

Figure 20. Distributions of (a) Sauter mean diameter, and normalised droplet mean (b) axial and (c) radial velocity, normalised rms fluctuations of (d) axial and (e) radial velocity, and (f) the ratio of the two velocity component fluctuations. Heptane stable flames: HS0 (open symbols) and HOS0 (closed symbols) at various downstream locations. HS0 and HOS0 have the same air velocity of 14.3 m/s ($Re_g=11222$) and different fuel loading of 0.15g/s and 0.20g/s (corresponding to We_l of 339 and 602) respectively.

Figure 21. Comparison of the SMD (a-d) and normalised mean axial velocity (e-h) of the ethanol (E1S1, square), heptane (H1S1, circle), decane (D1S1, up triangle), and dodecane (DD1S1, down triangle) flames at (a,e) $z=10\text{ mm}$, (b,f) $z=20\text{ mm}$, (c,g) $z=30\text{ mm}$ and (d,h) $z=40\text{ mm}$. The fuel and air flow are identical for all flames ($\dot{m}_f = 0.27\text{g/s}$, $U_b=17.1\text{ m/s}$). The liquid Weber number is in the range of 774 to 1098 as indicated above.

Figure 22. Comparison of the normalised mean radial velocity of the ethanol (E1S1, square), decane (D1S1, up triangle), and dodecane (DD1S1, star) flames at (a) $z=10\text{ mm}$ (open) and 20 mm (closed), and (b) $z=30\text{ mm}$ (open) and $z=40\text{ mm}$ (closed). The fuel and air flow are identical for all flames ($\dot{m}_f = 0.27\text{g/s}$, $U_b=17.1\text{ m/s}$).

Figure 23. Inverse Abel transformed mean OH^* of stable flames at far from (column 1: S1) and close to blow-off (column 2: S2), and unstable flames at blow-off condition (column 3: B) from the four fuels: row 1: ethanol (E1), row 2: heptane (H1), row 3: decane (D1) and row 4: dodecane (DD1). The fuel flow rate of these flames is 0.27 g/s. The corresponding air flow rate is indicated in Table 1.

Figure 24. The mean and instantaneous images of OH^* chemiluminescence (row 1, 4), OH-PLIF (row 2, 5), and Mie scattering (row 3, 6) from different stable flames (a-d) of ethanol (E1S1), heptane (H1S1), decane (D1S1) and dodecane (DD1S2), and unstable flames (e-h) of ethanol flame E1B, heptane flame H1B, decane flame D1B and dodecane flame DD1B at the blow-off condition, but using data before the blow-off event. The mean OH^* image is shown

after inverse Abel transform. All the flames above have the same fuel flow rate at 0.27 g/s, and the stable cases have the same air velocity of 17.1 m/s, while the unstable flame cases at blow-off conditions have bulk velocities as shown in Table 1. Same colormap per row.

Figure 25. Inverse Abel transformed mean OH* chemiluminescence images for (a-d) stable flames of ethanol, and (e-s) flames at blow-off conditions (e-j. ethanol, k-p. heptane and q-s. dodecane). The corresponding fuel mass flow rate and air bulk velocities are shown next to the flame names.

Figure 26: Instantaneous OH* images of swirl-stabilised spray flames of (a) ethanol (E1B), (b) heptane (H1B), (c) decane (D1B) and (d) dodecane (DD1B) at the blow-off transient event (same colormap for each flame). The fuel flow rates of the four flames are the same, at 0.27 g/s. The relative time referenced to the time of complete disappearance of OH* is indicated on top of each image.

Figure 27. Instantaneous OH-PLIF images of (a,b) ethanol stable flames and (c) the ethanol unstable flame at the blow-off condition before the blow-off event. The fuel flow rate is 0.27 g/s. Images not in sequence (same colormap for each flame). Dot-circle: breaks in inner or outer branch, dot-square: lift-off at bluff-body edge, dash-square: attachment at bluff-body edge, red-arrow: divergence of outer OH branch, yellow-arrow: lift of inner OH branch, yellow-dash-arrow: absence of inner OH branch, yellow-dash-rectangular: movement of inner OH branch, and yellow-dash-circle: spread of flame kernel.

Figure 28. Instantaneous OH-PLIF images of (a) the stable heptane spray flame and (b) the unstable heptane spray flame at blow-off condition before the blow-off event. The fuel flow rate is 0.27 g/s. Images not in sequence (same colormap for each flame). Dot-circle: breaks in inner or outer branch, dot-square: lift-off at bluff-body edge, dash-square: attachment at bluff-body edge, yellow-dash-arrow: absence of inner OH branch, yellow-dash-rectangular: movement of inner OH branch, and yellow-dash-circle: spread of flame kernel.

Figure 29. Instantaneous OH-PLIF images of (a,b) the stable decane spray flame and (c) the unstable decane spray flame at blow-off condition before the blow-off event. The fuel flow rate is 0.27 g/s. Images not in sequence (same colormap for each flame). Dot-circle: breaks in inner or outer branch, dot-square: lift-off at bluff-body edge, dash-square: attachment at bluff-body edge, and yellow-dash-arrow: absence of inner OH branch.

Figure 30. Instantaneous OH-PLIF images of (a) the stable dodecane spray flame and (b) the unstable dodecane spray flame at blow-off condition before the blow-off event. The fuel flow rate is 0.27 g/s. Images not in sequence (same colormap for each flame). Dot-circle: breaks in inner or outer branch, dot-square: lift-off at bluff-body edge, dash-square: attachment at bluff-body edge, and yellow-dash-arrow: absence of inner OH branch.

Figure 31. Instantaneous OH-PLIF images from flames of ethanol (a), heptane (b), decane (c) and dodecane (d) during the blow-off event (same colormap for each flame). The fuel flow rate was 0.27 g/s and the velocity for each blow-off event is indicated. The relative time referenced to the time of complete disappearance of OH is indicated on top of each image.

Figure 32. (a) Un-ignited spray, CH₂O image; (b) example CH₂O image of H1S1 flame. The colour map is logarithmic.

Figure 33. Instantaneous CH₂O, OH, and images for H1S1 and H1S2. I-IV are discussed in the text. The CH₂O image colour map is logarithmic.

Figure 34. Mean OH, CH₂O, and CH₂O×OH for H1S1 and H1S2.

Figure 35. The blow-off limits correlation for the four fuels studied in this work (E-ethanol; H-heptane; D-decane and DD-dodecane), calculated with the method proposed by Radhakrishnan et al. [43].

Figure 36. (Left) Integrated OH* during the blow-off event (the color line stands for instantaneous time series, black line indicates the average value) and (right) the normalised transient duration at various fuel loadings of flames of (a,b) ethanol (flame E1B), (c,d) heptane (flame H1B), (e,f) decane (flame D1B) and (g,h) dodecane (flame DD1B). The fuel flow rate of (a),(c),(e), and (g) is 0.27g/s.

Figure 37. PDF of lift-off height of flames of (a) ethanol, (b) heptane, (c) decane, and (d) dodecane at different distances from the blow-off condition. The fuel flow rate for all the flames is 0.27 g/s. The flow parameters are listed in Table 1.

Figure 38. The average lift-off height normalised by the bluff body diameter for various flames. The fuel flow rate is 0.27 g/s and the air velocity for each flame is marked on Fig. 16.

Figure 39. PDF of the percentage of quenched stoichiometric mixture fraction iso-line of heptane spray flames at far from (H1S1) and close to (H1S2) blow-off condition. The fuel flow rate for both flames is 0.27 g/s. The flow parameters are listed in Table 1.

Figure 40. An example OH-PLIF image of stable decane flame (D1S1, fuel flow rate is 0.27g/s and air bulk velocity is 17.1m/s). The image includes four separated ‘‘islands’’. The total area of the binarised OH signal normalised by D^2 (D is the bluff-body diameter) is 0.60. The circularity (F) of these subregions is 0.08, 0.25, 0.57, 0.32 for regions 1-4 respectively.

Figure 41. Morphology of the OH-PLIF images from the different flames: the average value of (a) normalised integral binary area, (b) the average circularity, F . Open symbols: unstable flames; Closed symbols: stable flames.

Figure 42. Mean image and the first 5 POD modes from OH* of the four fuels flames at stable condition and blow-off, (a) flame E1S1 and E1B, (b) flame H1S1 and flame H1B, (c) flame D1S1 and flame D1B, and (d) flame DD1S2 and flame DD1B.

Figure 43. Relative energy of the OH* POD modes of the spray flames at stable condition (left) and blow-off (right). Rows 1 to 4 are flames of ethanol, heptane, decane and dodecane respectively.

Figure 44. Cumulative energy of the POD modes of OH* chemiluminescence for flames of the four fuels at stable condition and blow-off.

Figure 45. (a) flame D1S1 and (b) flame D1B: (Upper) Snapshots from raw OH* movie; Snapshots at the same times from reconstructed OH* movie using (middle) the mean and mode 1 only; and (lower) the mean and modes 1 to 5.

Figure 46. PSD of POD coefficients from modes 1 to 10 of OH* (a,c,e,g) and OH-PLIF (b,d,f,h) for the four fuels spray flames at stable condition (left) and at blow-off (right): (a-b) ethanol flames, (c-d) heptane flames, (e-f) decane flames, and (g-h) dodecane flames.

Figure 47. Mean OH-PLIF and modes 1 - 5 of spray flames at stable condition (upper row) and at blow-off (lower row), (a) flame E1S1 and E1B, (b) flame H1S1 and flame H1B, (c) flame D1S1 and flame D1B, and (d) flame DD1S2 and flame DD1B.

Figure 48. Relative energy of the OH-PLIF POD modes of the spray flames at stable condition (left) and blow-off (right). Rows 1 to 4 are flames of ethanol, heptane, decane and dodecane respectively.

Figure 49. Cumulative energy of the POD modes of OH-PLIF for flames of the four fuels at stable condition and blow-off.

Figure 50. (a) flame D1S1 and (b) flame D1B: (row 1) Snapshots from raw OH-PLIF movie; Snapshots at the same times from reconstructed OH-PLIF movie using (row 2) the mean and mode 1 only; (row 3) the mean and modes 1 to 5; and (row 4) the mean and modes 1 to 25.

Figure 51. Schematic of the experimental arrangements used for calibration (a), turbulent premixed flames (b), turbulent jet non-premixed flames (c), and schematics of the uniform dispersion apparatus [217] (d).

Figure 52. Emission spectra of laser induced plasma in methane-air mixtures with $X_{\text{CH}_4} = 0, 0.1, 0.7, \text{ and } 1$.

Figure 53. Total intensity of H_α (656.3 nm) and O (777.3 nm) atomic lines calculated by the averaging method as a function of the mole fraction of methane, or the equivalence ratio (ϕ), calculated from the emission spectra of the plasma resulting from three different laser energies and induced in the centre of the 23 mm ID burner.

Figure 54. Total intensity of CN (388 nm) and C_2 (516.5 nm) molecular bands calculated by the averaging method as a function of the mole fraction of methane, or the equivalence ratio (ϕ), calculated from the emission spectra of the plasma resulting from three different laser energies and induced in the centre of the calibration burner.

Figure 55. Calibration curve for the ratio $\text{H}_\alpha(656.3 \text{ nm}) / \text{O}(777.3 \text{ nm})$ as a function of X_{CH_4} calculated by the averaging method, measured from emission spectra of plasma resulting from three different laser energies.

Figure 56. Calibration curve for the ratio C_2 (516.5 nm) / CN (388.3nm) as a function of X_{CH_4} calculated by the averaging method, measured from emission spectra of plasma resulting from three different laser energies.

Figure 57. Ratio H_α (656.3) / O (777.3) obtained in air and in different mixtures of methane and air obtained from the 100 single-shot spectra. The dashed lines represent the average values of the ratios in the cases of $X_{CH_4} = 0.10, 0.20,$ and 0.30 .

Figure 58. Ratio C_2 (516.5) / CN (388.3) obtained in different mixtures of methane and air obtained from the 100 single-shot spectra. The dashed lines represent the average values of the ratios in the cases of $X_{CH_4} = 0.10, 0.20,$ and 0.30 .

Figure 59. Calibration curve for the H_α (656.3) / O (777.3) ratio obtained by the averaging method and the instantaneous method respectively. Each data point of the instantaneous method corresponds to the average of 100 single-shot measurements taken under the same experimental conditions.

Figure 60. Calibration curve for the C_2 (516.5) / CN (388.3) ratio obtained by the averaging method and the instantaneous method respectively. Each data point of the instantaneous method corresponds to the average of 100 single-shot measurements taken under the same experimental conditions.

Figure 61. Left: Photograph of the swirling premixed flame. Equivalence ratio: 0.81, velocity at annulus 10.2 m/s. Right: Photograph of the lifted methane air flame with a spark visible. Jet velocity 17 m/s, jet fluid composition 70% CH_4 , 30% air by volume. The horizontal lines on each photo reflect the locations where radial profiles of equivalence ratio were taken. Not to scale.

Figure 62. Radial distribution of mean equivalence ratio in the premixed recirculating flame at different heights from the bluff body as a function of radius. The filled squares correspond to measurements at $h=10$ mm from the burner employing both suggested analytical methods, namely averaging and instantaneous. The inlet equivalence ratio of 0.81 is shown by the horizontal line.

Figure 63. Left: Radial distribution of mean mixture fraction in the turbulent jet flame at two different axial stations as a function of the radial position r/d . Included is the empirical fit from Lawn [90]. Right: the same data, but normalized by the centreline value plotted versus radial distance normalised by the radius at FWHM mixture fraction.

Figure 64. Inert flow. Left: Radial distribution of mean mixture fraction in the non-reacting jet at two different axial stations as a function of the radial position r/d . Included is the empirical fit from Lawn [90]. Right: the same data, but normalized by the centreline value plotted versus radial distance normalised by the radius at FWHM mixture fraction.

Figure 65. Radial distribution of normalised r.m.s. by the centreline value the mean mixture fraction at two different axial stations in the non-reacting jet (left), and in the lifted jet flame

(right).

Figure 66. (a) Photograph of the swirl heptane spray flame. Region A marks the air annular jet and the outer recirculation zone; region B marks the flame brush around the hollow-cone spray; region C indicates the inner recirculation zone. (b) Photograph of the spray flame showing the measurement stations (horizontal lines) where radial profiles of equivalence ratio were taken. Not to scale.

Figure 67. Photographs of a typical spark generated in homogeneous C_7H_{16} -air dispersion in the uniform-dispersion spray burner by three different focusing lenses: top $f = 150$ mm, centre $f = 75$ mm, and bottom $f = 50$ mm. (Red arrows point at the focusing direction of the laser beam.)

Figure 68a. Emission spectra from plasma created in uniform heptane-air dispersions for various equivalence ratios from lean (top) to rich (bottom).

Figure 68b. Top: Laser induced plasma emission spectra obtained from the swirl heptane spray flame corresponding to various locations in region B (upper) and regions A and C (lower).

Figure 69: (a) Dependence of the ratio H_α (656.3 nm) / O (777.3 nm) vs. ϕ in uniform C_7H_{16} -air dispersion. (b) Total intensity of the H_α and O atomic emission lines obtained from 200 instantaneous spectra measurements in uniform C_7H_{16} -air dispersions ($\phi = 0.62$).

Figure 70. Dependence of the ratio C_2 (516.5 nm) / CN (388.3 nm) vs. ϕ in uniform C_7H_{16} -air dispersion. The ratio is calculated by the averaging method.

Figure 71. Time-averaged images of (a) spray Mie scattering and (b) OH-PLIF images superimposed on the Mie scattering image of the swirl spray flame. From Cavaliere et al. [6].

Figure 72. Radial distribution of the species emission (H_α (656.3 nm), O (777.3 nm), C_2 (516.5nm) and CN (388.3nm)) obtained at the indicated axial station in the swirl spray flame by the averaging method. Each data point corresponds to the average of 200 single-shot measurements.

Figure 73. Radial distribution of mean equivalence ratio in the swirl spray flame at different heights from the bluff body as a function of radius. $h_1=5$ mm, $h_2=15$ mm, $h_3=40$ mm, $h_4=100$ mm.

Figure A.1. (a) Distributions of Sauter mean diameter (left), normalised droplet mean axial velocity (middle), and normalised rms fluctuations of axial velocity (right); (b) mean and rms axial droplet velocity conditional on the droplet size ranges (square: 0-10 μ m; circle: 10-40 μ m; up-triangle: 40-80 μ m; down-triangle: 80-100 μ m) and the mean and rms axial velocity using all droplets (star) vs. radius, measured at various downstream locations (10, 20, 30 and 40 mm). Heptane stable flames: H1S1 ($\dot{m}_f = 0.27$ g/s, $U_b=17.1$ m/s) and H1S2 ($\dot{m}_f = 0.27$ g/s, $U_b=20.0$ m/s).

Figure A.2. Distributions of (a) Sauter mean diameter, normalised droplet mean (b) axial and (c) radial velocity, normalised rms fluctuations of (d) axial and (e) radial velocity, and (f) the ratio of the two velocity component fluctuations. Heptane stable flames: H0S1 ($\dot{m}_f = 0.20\text{g/s}$, $U_b=17.1\text{ m/s}$) and H0S2 ($\dot{m}_f = 0.20\text{g/s}$, $U_b=20.0\text{ m/s}$).

Figure A.3. Distributions of (a) Sauter mean diameter, normalised droplet mean (b) axial and (c) radial velocity, normalised rms fluctuations of (d) axial and (e) radial velocity, and (f) the ratio of the two velocity component fluctuations. Decane stable flames: D1S1 ($\dot{m}_f = 0.27\text{g/s}$, $U_b=17.1\text{ m/s}$) and D1S2 ($\dot{m}_f = 0.27\text{g/s}$, $U_b=20.0\text{ m/s}$).

Figure A.4. Mean (a-d) and rms (e-h) axial droplet velocity conditional on the droplet size ranges (square: 0-10 μm ; circle: 10-40 μm ; up-triangle: 40-80 μm ; down-triangle: 80-100 μm) and the mean and rms axial velocity using all droplets (star) vs. radius, measured at various downstream locations (10, 20, 30 and 40 mm). Decane stable flames: D1S1 ($\dot{m}_f = 0.27\text{g/s}$, $U_b=17.1\text{ m/s}$) and D1S2 ($\dot{m}_f = 0.27\text{g/s}$, $U_b=20.0\text{ m/s}$).

Figure A.5. Distributions of (a) Sauter mean diameter, normalised droplet mean (b) axial and (c) radial velocity, normalised rms fluctuations of (d) axial and (e) radial velocity, and (f) the ratio of the two velocity component fluctuations. Dodecane stable flames: DD1S1 ($\dot{m}_f = 0.27\text{g/s}$, $U_b=14.3\text{ m/s}$) and DD1S2 ($\dot{m}_f = 0.27\text{g/s}$, $U_b=17.1\text{ m/s}$).

Figure A.6. Mean (a-d) and rms (e-h) axial droplet velocity conditional on the droplet size ranges (square: 0-10 μm ; circle: 10-40 μm ; up-triangle: 40-80 μm ; down-triangle: 80-100 μm) and the mean and rms axial velocity using all droplets (star) vs. radius, measured at various downstream locations (10, 20, 30 and 40 mm). Dodecane stable flames: DD1S1 ($\dot{m}_f = 0.27\text{g/s}$, $U_b=14.3\text{ m/s}$) and DD1S2 ($\dot{m}_f = 0.27\text{g/s}$, $U_b=17.1\text{ m/s}$).

List of Tables

Table 1. Conditions used for most of the experiments, corresponding to various stable and blow-off conditions. For all, the fuel mass flow rate was 0.27 g/s. U_b corresponds to the bulk air velocity at the annular opening around the bluff-body.

Table 2. Conditions at various fuel flow rates used for the experiments, corresponding to various stable and blow-off conditions. The optical diagnostics applied are indicated by the filled cells.

Table 3. Fuel properties and flow parameters at the main test conditions.

Table 4. Flow parameters of the stable ethanol flames used in OH* measurements to explore fuel flow rate effects.

Table 5. Average lift-off heights of stable and unstable spray flames. The fuel flow rate (\dot{m}_f) for each condition was 0.27 g/s.

Table A. Test cases evaluated by PDA for various departures from blow-off of the spray flames of heptane, decane and dodecane.

Chapter 1

Introduction

1.1 Motivation

Lean combustion has the promise of significantly reducing NO_x emissions, but the accompanying increased danger of global extinction, referred to here as blow-off, needs to be addressed. In aero engine applications, lean blow-off (LBO) limit plays an important role in the combustor operating envelope, especially when the aircraft is descending through inclement weather with the engine idling. It is also desirable to extend the flame LBO limit to provide a safety margin to sudden changes in throttle setting, fuel controls, and harsh weather encountered, such as ingestion of tropical rain or ice [1]. With the increasing emphasis on alternative aviation fuels, it is also important to explore the effect of fuel properties on the LBO limits. From an engineering perspective, experimental investigations have been carried out focused on establishing a model to correlate LBO limits of spray flames for various burner geometries and operating conditions [1–6]. Whereas the effect of volatility of multi-component fuels on flame blow-off has been investigated [2], the effect of volatility of single-component fuels for identical flow and burner conditions has received little

attention. Additionally, little information is available on the structure of spray flames at conditions near blow-off, which can be of help not only to designing combustors with better stability limits, but also to promoting our fundamental understanding of a challenging phenomenon affected by a range of factors including turbulence, kinetics, and phase change. Although the structure of spray flames has been studied from the perspective of droplet velocities and global stability [7,8], further work is needed to extend such data to conditions very close to blow-off.

Local flame extinction is a phenomenon observed at conditions close to LBO [1], but the mechanism linking local and global extinction is not always clear. In non-premixed gaseous-fuel flames, local extinction has been studied extensively and a solid body of knowledge exists concerning the degree and causes of local extinction, from both experimental [9–25] and numerical [26–38] viewpoints. However, only a few studies have investigated local extinctions in turbulent swirling spray flames [6]. Local breakups along the flame sheet are observed in swirling spray flames of heptane [6] using 5 kHz OH-PLIF, which, however, cannot reveal with certainty whether a flame is extinguished or not. Besides, OH alone cannot reveal whether the spray flames take a premixed or a non-premixed character. As a second scalar for flame structure studies, formaldehyde (CH_2O) has been used extensively. CH_2O is produced in the low temperature oxidation process and consumed in the subsequent high temperature oxidation. Simultaneous CH_2O and OH imaging and then taking the product $X_{\text{CH}_2\text{O}} \times X_{\text{OH}}$ (X being the mole fraction, taken as proportional to the PLIF signal intensity) has been used successfully as a marker of heat release rate in non-premixed and premixed flames [39–42]. The performance of this technique to simulate heat release in swirling spray flames has not been addressed before. The simultaneous CH_2O and OH imaging in the stabilisation region of spray flames in a swirl-induced recirculation zone, and in particular for flames close to the stability (i.e. extinction) limits, is beneficial to visualise reaction zones in swirl spray flames, and to examine how these zones are altered close to blow-off.

The global extinction behaviours and mechanisms have been widely investigated in turbulent gaseous flames (premixed [43–52], and non-premixed [53–56]); in laminar spray flame simulations [57–60] and in counterflow configurations

experimentally [61]. Only a few studies have looked into the behaviour of swirling spray flames during the blow-off event [6,62]. One of the studies compares heptane spray flames with methane premixed and methane non-premixed flames in the same swirl burner at conditions both close to and during the blow-off event [6]. Significant changes in spray flame shape are observed. It is also worth noting that recent efforts for the premixed, non-premixed and spray flames with fast OH* have quantified the duration of the blow-off event as quite substantial compared to a characteristic residence time in the combustor [6,49,51].

In the present work, the study of Ref. [6] is continued and new experiments in the same swirl burner are performed including more volatile (ethanol) and less volatile (n-decane, n-dodecane) fuels to examine the fuel volatility effect on blow-off limits and on flame structure from the perspective of local extinctions. The main objectives of this work are to investigate the effect of fuel properties on the behaviour of swirling spray flames at both stable and blow-off conditions, and to develop further understanding of the role of local flame extinctions in the global extinction of recirculating spray flames. The following section presents the background information for the present study. The specific objectives of the work are discussed in section 1.3, and the structure of the thesis is described in section 1.4.

1.2 Literature Background

The lean blow-off behaviour of various flame regimes has received a vast amount of research attention since around 1940s. Knowledge of the structure of the flame close to blow-off is important not only from a practical perspective, but also from the viewpoint of validating advanced turbulent combustion models. In this section, some of the investigation on local extinctions and flame lift-off are discussed; the laminar flame simulations and some experimental investigations on spray flames are summarised; and a review on the blow-off behaviours in different flame regimes is presented.

1.2.1 Swirl stabilisation

Swirl is often applied in industrial burners and gas turbine combustors for flame stabilisation [1,63]. A toroidal flow reversal is established through the swirl which entrains and recirculates a portion of the hot combustion gases to provide continuous ignition to the incoming air and fuel. Combustion length is reduced by producing higher rates of entrainment of the incoming fluid and fast mixing close to the burner exit and on the boundary of recirculation zone [63,64]. Reviews of swirling flows and combustions in swirling flames are given in [63,65,66]. Recently, space- and time-resolved experimental studies of flow, temperature, composition of swirling non-premixed flames are enabled with advanced laser diagnostics in confined [6,16,67–69] and unconfined [10,11,70–72] configurations. It is concluded that with a sufficient high swirl number, the flame stability is improved. It also shows that high swirl promotes the rapid mixing rate in the recirculation zone, which increases turbulence level.

1.2.2 Local extinction and flame lift-off

1.2.2.1 Local extinction

Local extinction of the flame is a phenomenon often accompanied with lean combustion [1]. Theoretically, the flame is extinguished when the local net heat release cannot initiate further reactions [73]. When the local heat release rate from the chemical reactions cannot balance with the heat loss transport away from the flame surface, local extinction of the flame surface may occur [15]. Local extinction is found correlated with high scalar dissipation rates [27–29] and high strain rates [74,75].

A flame hole may recover due to edge-flame propagation [13,15,76–79] or turbulent transport [15,37,80,81]. At the site where the flame is extinguished, local premixing of the fuel and oxidizer may occur. The extinction front at the hole edge may transit to an ignition front and propagate inwards along the stoichiometric mixture fraction (ξ_{st}) iso-surface [76,77]. Turbulent transport of temperature and reactive species could also cause flame-hole re-ignitions [15,80].

Experimentally, local extinction and re-ignition has been studied extensively [9,11–13,16–23,82–84] with advanced laser diagnostics methods providing the

availability of the space- and time-resolved visualisation of reactive species, temperature, and flow fields. In agreement with theoretical studies, high scalar dissipation rates and high strain rates are found correlated with local extinctions by experimental studies. In jet flames, it has been recognised from combined LIF and Rayleigh scattering measurements that the coincidence of high scalar dissipation rate layers with the stoichiometric contour is an important cause of local extinction [18–20]. In swirl non-premixed flames, some complex characteristics are observed [6,10,11]. The intense recirculation zone and higher turbulence levels give rise to a broad range of flow time scales which strongly interact with the chemistry leading to wide variations in flame shapes. Local extinction is found to occur at earlier jet velocities with respect to the extended blow-off velocities. Besides, a strong correlation is found with the occurrence of local extinctions and high shear stress regions [10].

1.2.2.2 Lift-off

In turbulent jet flames and bluff-body stabilised flames, lift-off is a phenomenon in which flame is detached and stabilised downstream from the burner rim [85–87]. As the velocity further increases after lift-off, the flame will blow-off and flame cannot be stabilised in the mixing region [85,86]. The critical exit velocity at which lift-off appears is called lift-off velocity. For jet flames, the lift-off height is the centreline distance from the duct exit to the plane of flame stabilisation [86]. For bluff-body flames, the lift-off height is recognised as the axial distance of the first emergence plane of the outer flame branch for the bluff body corner [6]. Lift-off characteristics are of practical importance in connection with flame stabilisation [86]. The review by Pitts [88] summarises many of the standard theories concerning jet flame stability, discussing the roles of premixedness, scalar dissipation and large scale structures in controlling of lifted jet flame stabilisation, extinguishing and blow-off. Lyons [89] includes recent progress in experimental studies in turbulent lifted hydrocarbon jet flames and the stabilisation conditions. Lawn [90] addresses the influence of the co-flowing air and discusses the results from acoustically excited lifted jet flames and some computational simulations.

In bluff-body non-premixed flames, Chen et al. [87] suggested that at low fuel velocities, local flame extinction dominates lifting of the flames, due to a strong interaction between the recirculating air flows and the jet flame front. At high fuel velocities, the annular air flows have little effect on the lift-off heights and premixed flame propagation dominates. The different lift-off behaviour between air dominant and fuel dominant conditions on bluff-body non-premixed flames is also picked up by Nishimura et al. [91].

There are fewer experimental studies [6,70,72] on lift-off behaviours in non-premixed swirl flames than in the simpler geometries. The observation of the non-premixed swirl flame by Cavaliere et al. [6] shows intermittent lift-off. It quantifies the lift-off heights at conditions far from and close to blow-off statistically, and finds that the average lift-off height decreases as air velocity increases. It also finds that the lift-off height increases with fuel jet velocities in the fuel velocity range studied (20-40 m/s) [6]. Tummers et al. [70] have studied lifted swirl flames with high fuel and air flow rates and have pointed that the scalar dissipation in the near burner field increases with both the fuel and air flow rates, and presumably the high scalar dissipation rate results in quenching and lift-off [70].

1.2.3 Spray combustion

In gas-turbine applications, the combustion efficiency is often related to fuel evaporation rate, mixing rate and chemical reaction rate. The maximum heat release rate under any given operating conditions may be governed by either one of these three factors [1]. To increase the rates of heat and mass transfer, liquid fuels are disintegrated or atomised into a spray of vast number of small droplets to increase the surface area. The discrete liquid droplets may have a range of sizes and different velocities to that of the main stream of gas, thus the burning spray is not uniform in composition and differs from a premixed combustible gaseous system [92]. The fundamental of liquid atomisation, evaporation and droplets combustion are discussed in Refs. [1,92–94] and many text books [85,95,96]. In this section, laminar flame calculations of spray flames focusing on the effects of fuel volatility and flow strain rate on flame propagation and flame structures is firstly discussed. What follows is the

discussion on experimental observations on spray flame structures at various flow conditions.

1.2.3.1 Laminar flame calculations of spray flames

Laminar flame calculations of spray flames are often carried out with monodisperse droplets where spray combustion may be regarded as an ensemble of individual burning or evaporating particles. A statistical description of the droplets that make up the spray with regard to droplet size and distribution in space (polydisperse spray) is also necessary and applicable to advanced simulations [92]. The spray flame structure has been investigated with uniform or non-uniform spray model in one-dimensional laminar flame simulations [57–60,97–109]. The following discussion focuses on the volatility effect on spray flame propagation, counterflow spray flame structures and extinction behaviour.

The evaporation of droplets is found to promote laminar flame speed [106,107]. In a numerical study of flame stretch in premixed spray flames, it is found that the presence of the spray causes acceleration of the flame due to droplet evaporations [107]. This acceleration effect may be competitive with or be combined with the mixture Lewis number effect [110]. They suggest that for low volatile fuels the spray evaporation effect is dominant, whereas for high volatile fuels the Lewis number effect is dominant. The acceleration effect on flame propagation has also been investigated with detailed chemistry [106] of n-heptane and n-decane flames. Effects of droplet size, equivalence ratio, and droplet residence time before flame zone on the flame propagation speed in atmospheric and relight conditions are examined. It is found that the maximum flame speed is achieved with small diameters and with long residence time under lean conditions. Under rich conditions, flame speed is greater for relatively large droplet size which causes the effective equivalence ratio to be near unity. The conclusion is in agreement with previous studies [111,112]. Further, they suggest that the reactive species generated (mainly H_2 , C_2H_2 , C_2H_4) by fuel pyrolysis behind the reaction zone diffuse back towards the oxidation zone and enhance the reaction rate. This leads to the enhanced flame speed above the gaseous flame speed even for rich mixtures. For both low and high volatile fuels, the inverse dependence of the flame speed on the initial diameter is observed. The reduction of flame speed at

large droplet size is stronger in the low volatile fuel case due to its low evaporation rate.

Spray flame structures and extinction behaviour have been studied in the counterflow configuration numerically focusing on the effect of strain rates, initial droplet sizes and stream temperatures. One of the pioneering works is carried by Continillo and Sirignano [57]. They use a hybrid Eulerian-Lagrangian formulation for monodisperse spray of n-octane. The transient droplet heat-up and vaporisation are modelled [113]. The following effects are taken account of in the modelling: non-unitary Lewis number in the gas film, the Stefan flow on heat and mass transfer, the internal circulation and transient liquid heating. They find that larger and faster droplets presented cross the stagnation plane and possibly pass the flame zone. Two distinct flame zones are encountered in some configurations, where the flame shows both premixed-like and diffusion-like characters. They also find that the initial droplet size and the flow strain rate are important factors to the two flame zone separation. Increasing initial droplet diameter or reducing strain rate tends to cause a separation of the flame into a premixed flame zone and a diffusion flame zone.

An extension of this study considering extinction behaviour of counterflow spray flames of methanol is carried out by Gutheil and Sirignano [58] with detailed chemistry and transport. It shows that detailed chemistry and transport are necessary to predict correctly the structure and extinction of laminar spray flame. As strain rate increases, the methanol droplets may reverse towards their injection plane and they may oscillate around the stagnation plane as flame extinction is approached. It also demonstrates that the structure of spray flames, flame temperature and extinction, not only depend on the strain rate but also on both initial droplet velocity and initial droplet size.

The extinction behaviour is different with mono- or bidisperse sprays [59]. The flame thickness, the vaporisation zone width and location, and the reaction zone location are found different with the two models [98]. The Sauter Mean Diameter (SMD) is found to be a good approximation for the bidisperse spray at low strain rates conditions [98]. However, the SMD is not suggested to be suitable to represent a bidisperse spray at extinction conditions [59].

Steady-state combustion and flame extinction are investigated with polydisperse spray, detail transport, and finite evaporation rate by Dvorjetski and Greenberg [60,100,102], following the approach proposed by Greenberg et al. [97,103]. Effects of fuel volatility, droplet size, and liquid fuel loading are examined. It is found that the heat loss in the vaporisation front profoundly affects the flame temperature, location, and extinction properties [60]. The analysis is also carried in large Stokes number (St) conditions and successfully predicts the occurrence of droplet reversal [100].

1.2.3.2 Experimental studies of spray flame structure at various strain rates

Spray flame structure and flame global extinction have been investigated experimentally in laminar counterflow configurations [61,101,114–124], in turbulent pilot flames [125–128], and some has been done in turbulent swirling flames [6]. The structure of laminar counterflow diffusion flames of quasi-monodisperse sprays of n-heptane has been studied experimentally [114]. Droplet size, velocity and gas-phase temperature are measured at two flames with low and high strain rate but identical overall equivalence ratio. They observe that the low strain rate flame behaved like purely gaseous diffusion flame since the droplets never directly interact with the flame. The flame appears as a thin blue sheet at low strain rate conditions. However, in the high strain rate flame droplets penetrate the blue flame. The flame appears to be an additional thick orange region on the oxidiser side. The higher strain rate flame also presents a broader temperature profile and a slightly higher peak temperature. This is in contrast to the expected trend in gaseous diffusion flames in which theoretically the width of the temperature profile is inversely proportional to the square root of the strain rate [129]. The mean velocity profile shows that the droplets first decelerate and subsequently accelerate as they enter the highest temperature region. They have also observed a good correlation between droplet size and velocity.

The post-flame motion of large droplets at high strain rate conditions has also been reported by Li et al. [115–117], who have studied counterflow diffusion spray flames for the geometries that Continillo and Sirignano [57] investigated numerically. They have observed that at high strain rate larger droplets are able to cross the stagnation plane and pass through the flames. These droplets are then found to undergo underdamped oscillation in the counterflowing streams or collide with the target wall

1. Introduction

in an impinging stream. When the strain rate is low and droplets are relatively small, all droplets vanish at a vaporisation plane before the stagnation plane. The distance between the vaporisation plane and flame sheet decreases as the strain rate increases. They also present thermocouple and gas-chromatographic measurements of temperature and concentrations of main species profiles in two laminar counterflow n-heptane flames at a low strain rate and the simulation results from the detailed chemistry are found in good agreement with the measurements.

The extinction behaviour of laminar counterflow spray flames for different droplet size distributions are discussed by Mikami et al. [61] based on the Stokes number St , and the vaporisation Damköhler number ψ (the ratio of evaporation time to characteristic flow time). They suggest that the extinction strain rate limit is widened as St increases, and the extinction limit is narrowed as ψ increases.

Niioka [130,131] has studied the influence of droplet spacing on flame propagation in dispersed spray of n-decane under microgravity. A maximum flame spread speed is found to attain at around the droplet spacing equals half of the flame diameter, for which the heat transfer to the neighbouring unburned droplet is considered to be roughly the largest [131]. When the spacing of droplets array is large, heat transfer to the neighbouring unburned droplet is weakened, thus flame spread rate decreases as the spacing increases. However, when the droplet spacing is small, the heat capacity increases, and a large amount of heat is taken by fuel evaporation. Therefore, the reaction rate and the flame spread speed decreases.

The flame structures are found to be different and depend on the fuel volatilities in turbulent pilot-stabilised jet flames of dilute sprays of acetone or ethanol at approaching global extinction [125]. The temperature, reactive scalar and flow field of droplets are studied. The flow fields of droplets are found similar for both ethanol and acetone flames, and do not change much with jet velocity. However, the temperature and reactive fields vary and undergo departure indicative of non-premixed to premixed flame behaviour depending on the vapour pressure of the fuel and proximity to blow-off. Broad regions of OH as well as breaks in the OH profile marking possible local extinction are observed in the ethanol flame only.

The spray flame behaviours at conditions approaching blow-off of a bluff-body

swirl burner fuelled with n-heptane are studied by Cavaliere et al. [6]. They observed local extinctions by visualising the OH radicals along flame sheet at close to blow-off conditions. The occurrence of extinction hole of OH sheet increases approaching blow-off. However, due to the lack of detailed information on the out-of-plane motion, whether the flame is extinguished or not may not be revealed by OH alone. The quantification on the dynamics (i.e. the “growth” and “closure”) of local extinction holes similar to the one studied in turbulent non-premixed flames [13,19] were not discussed in their study. The flame extinction behaviour of swirl spray flames still requires more research.

1.2.4 Blow-off of turbulent gas flames: premixed and non-premixed

Studies on flame blow-off mechanisms have two focal points. One is on the measurement and correlation of blow-off limits under various combustor operating conditions and system configurations, which forms the majority of the literature in earlier decades. They all reach to a similar criterion describing on a competition between two time scales: flow characteristic time scale and chemical characteristic time scale. The other focal point is on the observation and characterisation of the dynamic and the critical structures of the flame approaching blow-off and at the blow-off event; the amount of work on this is very limited.

Premixed flames (1) Blow-off correlations

Several methods to understand blow-off mechanisms and predict blow-off limits for a typical or general configuration have been proposed. Longwell et al. [132] view the bluff-body recirculation zone as a homogeneous chemical reaction volume, where the unburnt mass is fed at constant rate and is instantaneously mixed with the fluid within the zone. The concept is identical to a well-stirred reactor. The blow-off occurs when the entrainment rate of reactants cannot balance the burning rate of these gases [132]. Thus, lean blow-off could be viewed as the competition between a fluid mechanical time and a chemical time. Plee and Mellor [3] suggest the two time scales to be evaluated in the shear-layer region between the hot recirculation zone and the free stream. Another view has suggested that the flame blow-off occurs when the

1. Introduction

residence time of the recirculation zone is too short for ignition to be accomplished (Zukoski and Marble [43]). Glassman [85] concludes that these studies all describe a similar blow-off criterion in terms of a Damköhler number, Da , i.e. the ratio of a characteristic flow time scale τ_f and a characteristic chemical time scale τ_c (Eq. 1).

$$Da = \tau_f / \tau_c \quad \text{Eq. 1}$$

Radhakrishnan et al. [45] propose a correlation for the blow-off velocity of premixed turbulent bluff-body stabilised flames. The correlation is based on a conceptual picture of combustion in small-scale (Kolmogorov) turbulent structures proposed by Tabaczynski [133]. It is suggested that for successful flame propagation, the time for laminar flame propagation across the spacing of the vortex tubes (Taylor microscale λ) should be less than a characteristic fluid mechanic time, which is better represented by shear layer mixing time. Thus, the chemical time is defined to be the time characteristic of burning across the microscale λ_T , and is given by $\tau_c = \lambda_T / S_L$. For isotropic turbulence, λ_T can be written as $\lambda_T = (15/A_n)^{1/2} l (u' l / \nu)^{-1/2}$, where A_n is constant of order unity, l is the integral length scale, u' is local turbulent velocity fluctuations, ν is the kinematic viscosity. For characteristic turbulent flow time, the eddy time (τ_e) is used, $\tau_e = l / u'$. The blow-off is deemed to occur when the ratio of the two time scales, $1/Da_1$, exceeds a critical value (R_τ). By making further assumption that $u' \propto U_B$, and $l \propto L$, L is the length of the recirculation zone, the following correction (Eq. 2) could be derived at blow-off condition:

$$\frac{1}{Da_1} = \frac{\tau_c}{\tau_e} = \left(\frac{U_B \nu}{L}\right)^{1/2} / S_L > R_\tau \quad \text{Eq. 2}$$

where ν is the kinematic viscosity, evaluated at the unburnt reactants conditions for premixed systems. S_L is the laminar flame speed, evaluated at the premixed mixture equivalence ratio for premixed flames. L is the length of the recirculation zone taken as proportional to the characteristic size of the flame holder.

This blow-off criterion (Eq. 2, [45]) is applied in enclosed swirl-stabilised premixed methane flames (Kariuki et al. [134]) and was found to collapse the blow-

1. Introduction

off velocity data. The values of Da_1 based on Eq. 2 lay in the range 1.19 to 1.34 for the premixed flames with the square enclosure, 1.15 to 1.23 with the circular enclosure. The blow-off criterion (Eq. 2, [45]) for swirl-stabilised non-premixed flames and spray flames of n-heptane as well [6] are found to collapse the blow-off data and lay in the range of 0.9 to 1.23 for the non-premixed case, and 0.87 to 0.99 for the spray flames. It demonstrates that all three flame regimes at the same burner extinguish at approximately the same critical value of Da_1 . It is noted that the spray flame is to be evaluated at stoichiometry when employing such blow-off correlation and not at the global equivalence ratio. And the kinematic viscosity (ν) is to be evaluated at a temperature halfway between the reactants and the adiabatic flame temperature, as tested by Cavaliere et al. [6] following the suggestion by Mellor [135].

Premixed flames (2) Typical flame structures close to blow-off

In premixed flames, the dynamic and the critical structure observed prior or during the blow-off event has been studied intensively [44,46–51,136,137]. Large scale fluctuations are observed at conditions approaching flame blow-off [136]. Increasing occurrence of local extinction events along the flame sheet is observed prior to the global blow-off event surrounding the RZ and the flame downstream in rod-stabilised premixed flames [44], and in bluff-body stabilised flames [47–51,137]. It is observed that the blow-off occurs ‘‘instantly’’ due to the abrupt inflow of cool unburned mixture from the open end of the recirculation zone [44]. Note that the duration of the blow-off event is found not instant but quite substantial compared to a characteristic residence time in the combustor [6,49,51]. During the blow-off event, many flame fragments are observed inside the recirculation zone for a significant time relative to the residence time of the recirculation zone. ‘They grow, diminish, and rotate, but they progressively become less in number, and smaller in size, until complete extinction occurs’ [49]. These flame fragments seem unable to grow enough to re-ignite the whole. This observation supports the blow-off model based on concepts of well-stirred reactor (WSR) rather than shear layer ignition [49].

Additionally, for both confined and unconfined bluff-body flames, it is observed [49] that the conical flame brush of a stable flame at far from blow-off becomes shorter and remains anchored as it is approaching blow-off. Close to blow-off, the

downstream flame brush merges to form a closed ‘M’ shape. The change of flame shapes is suggested to be related by the change in the location where the turbulent flame speed balances the flow velocity.

Further on, local turbulence-chemistry interactions are studied [51] in the same flames as in Ref. [49]. Local characteristic turbulent velocity fluctuations (u') and local integral turbulent length scale (l) are obtained via PIV measurements. The two mixing variables together with laminar flame speed (S_L) and laminar flame thickness (δ_L) enable the calculation of two non-dimensional parameters: the turbulent Damköhler number (Da_t) and the Karlovitz number (Ka). $Da_t = (l/\delta_L)/(u'/S_L)$ as defined by Peters [28], and $Ka = 0.25(u'/S_L)^2 Re_t^{-1/2}$ as defined by Bradley et al. [138], where $Re_t = u' l/\nu$, (ν the kinematic viscosity). As approaching blow-off, a significant increase in the maximum values of Ka is observed along the flame. Besides, a decrease in the minimum values of Da_t is obtained. Additionally, flame is extinguished first at positions with the maximum Ka value, which occurs at a downstream distance of about 1.2 times bluff-body diameter where the flame begins to bend to close at the axis [51].

Non-premixed flames

In non-premixed flames, blow-off mechanisms have been studied in turbulent jet flames [53–56,139,140] and in non-premixed swirling flames [6,141]. For jet flames, blow-off is connected with the intense local quenching of the flame due to high scalar dissipation rates [139]. Mixing is also a controlling parameter in the blow-off mechanisms of turbulent non-premixed jet flames [54,55]. Broadwell et al. [54] have proposed that the blow-off occurs when the mixing between re-entrained hot reaction products and the unburned jet fluid allows insufficient time for ignition. They propose that the blow-off criterion is that the ratio of local mixing time, $\tau_m = D/U_b$, to a characteristic chemical reaction time, $\tau_c = k/S_L^2$, k is thermal diffusivity, is less than some critical value.

Moore et al. [142] have looked into the transient process of methane-air jet flame blow-off and reported that the prior disappearance of the axially oriented trailing diffusion flame branch acts as a predictor of blow-off. They believe that the blow-off

occurs when the leading edge progressing downstream reaches the vicinity of the lean-limit contour.

The research by Feikema et al [141] is among the earliest studies on the blow-off of non-premixed swirl flames. The addition of swirl is found to improve the blow-off limits by as much as a factor of 6. The use of the swirl is suggested to have reduced local strain rates near the forward stagnation point of the recirculating vortex where the flame is stabilised. Cavaliere et al. [6] investigate the blow-off behaviour of confined swirl-stabilised non-premixed flames via fast imaging techniques. They have visualised the transient process of the blow-off event and observed the shortening and fragmentation of the flame brush above the bluff-body.

Recent studies [6,49,51] have visualised the blow-off transient process of both premixed and non-premixed flames via fast (5 kHz) OH* imaging. They found that during the blow-off event, the flame fragments survive in the recirculation zone for a time of the order of tens of milliseconds, and they progressively become smaller in size and less in number. They quantified the duration of the blow-off event, τ_{ext} , as the time needed for the emission to decrease from 90-10% [49]. The extinction times for all regimes are found within the range 10-50 ms, which is one order of magnitude larger than the residence time of the recirculation zone.

1.2.5 Blow-off of spray flames

For spray flames, Ballal and Lefebvre [2] propose that the flame blow-off occurs when the rate of heat released in the combustion zone becomes insufficient to heat the incoming fresh mixture up to the required reaction temperature with account of the additional heat required for fuel evaporation. For fuel sprays of low volatility and large mean droplet size, the evaporation process is relatively long and often limits the overall rate of heat release [4]. Following Longwell et al. [132] that the reaction zone of a bluff-body flameholder is viewed as a homogeneous chemical reactor, Ballal and Lefebvre [2] propose that the correlation at blow-off be expressed in terms of the combustion volume, pressure, initial temperature and mass flow rate, as in Eq. 3.

$$FAR_{LBO}(\text{heterogeneous}) \propto \left[\frac{\dot{m}_a}{V_c P_3^n \exp\left(\frac{T_3}{b}\right)} \right]^x / f_f \quad \text{Eq. 3}$$

where FAR_{LBO} is the lean blow-off fuel/air ratio of heterogeneous mixtures, n is the reaction order, x and b are constants determined experimentally. The vaporisation effect is introduced to the up equation through the factor f_f , describing the fraction factor of fuel which is vaporised within the primary zone.

The fraction of fuel evaporated f_f could be expressed as [2]:

$$f_f = 8 \frac{\rho_g}{\rho_f} \left(\frac{k}{c_p} \right)_g \ln(1 + B) (1 + 0.22 Re_{D_{32}}^{0.5}) \frac{V_c}{\dot{m}_a D_{32}^2} \quad \text{Eq. 4}$$

where subscript f and g denote the property of fuel droplet and the surrounding gas separately, D_{32} is the mean droplet diameter in the primary zone represented by Sauter Mean Diameter (SMD), B is mass transfer number, k is the thermal conductivity, c_p is the specific heat capacity at constant pressure, and $Re_{D_{32}}$ is the droplet Reynolds number, evaluated with the initial droplets SMD.

Incorporating the heating value of the fuel (LHV) into the expression of LBO limit (Eq. 3) in which fuels with a high heat content should be capable of burning down to weaker mixture strengths than fuels having a lower heat content [4]. The Eq. 3 is modified to the following,

$$FAR_{LBO}(\text{heterogeneous}) = A_m \left[\frac{\dot{m}_a}{V_c P_3^n \exp\left(\frac{T_3}{b}\right)} \right]^x \frac{1}{(f_f LHV)} \quad \text{Eq. 5}$$

where A_m is mixing related parameter. At lower temperatures, the role of fuel evaporation outweighs any other parameter. Once temperatures reach sufficient levels, the role of the mixing parameter becomes important. At elevated inlet air temperatures (477 K), the LBO performance becomes governed more by mixing as opposed to fuel evaporation [4].

There is very little information [5,6] from literature regarding the detailed flame structure and flow fields information on spray flames at close to lean blow-off limits.

Marinov et al. [5] have compared kerosene-fuelled spray flame on an optically accessible swirl burner at conditions far from and close to blow-off. An airblast atomiser is applied in this study. Some information has been obtained, i.e. the gaseous phase velocity field via LDA, in-flame measurements of gas concentration (O_2 , CO_2 , CO , UHC) via sampling probe, and temperature field measured by thermocouples. They have observed quite different features of flow fields and reacting fields (AFR and temperature) of the spray flames at condition far from blow-off and close to blow-off.

Recently, Cavaliere et al. [6] have compared the stable flames and the blow-off behaviour of methane premixed, methane non-premixed, and n-heptane spray flames on a swirl burner with additional information of heat release rate (via 5 kHz OH^* chemiluminescence) and reactive scalar field (via 5 kHz OH-PLIF). For all types of flame, the blow-off event (i.e. the slow reduction of flame area to zero) lasts a significant time (i.e. tens of ms) compared with the residence time in the burner, and before this process begins the flame seems stable. However, significant changes in flame shape are evident when one compares flames at operating conditions far from extinction and at the blow-off condition before the blow-off event. The information on swirl spray flame structures close to blow-off is still limited and requires more investigation.

1.2.6 Heat release visualisation by joint PLIF measurement

Hydroxyl radical (OH) has been used in numerous combustion studies to represent reaction zone locations [6,15,39,143]. Cavaliere et al. [6] have visualised n-heptane spray flames via fast OH-PLIF imaging and seen local breakups present along the OH images and randomly-occurring lift-off at bluff-body edges. However, the OH signal alone may not reveal whether a flame is extinguished or not. In particular, OH is also present in the post-flame gases in premixed flames. But in non-premixed flames, OH is found roughly along the stoichiometric contour only.

As a second scalar for flame structure studies, formaldehyde (CH_2O) has been used extensively. CH_2O is produced in the low temperature oxidation process and consumed in the subsequent high temperature oxidation. Formaldehyde LIF has been used for autoignition of methane jets [40], methanol, ethanol and acetone spray jet

1. Introduction

flames [126,127], and diesel fuel [144–146] and n-heptane [146,147] in HCCI engines. Najm et al. [148] have conducted detailed chemical kinetic computations of methane premixed flame and found that the concentration of formyl radical (HCO) is very well correlated with flame heat release rate. They have also found that the production of HCO is directly dependent on the availability of its precursor CH₂O ($\text{CH}_2\text{O} \xrightarrow{\text{OH,H,O,M}} \text{HCO}$). However, as the PLIF of HCO is difficult for single shot imaging diagnostics when applied to fully turbulent flows due to its short fluorescence lifetime and low concentrations [148], the product of simultaneous OH and CH₂O PLIF is considered as an alternative. Simultaneous CH₂O and OH imaging and then taking the product $X_{\text{CH}_2\text{O}} \times X_{\text{OH}}$ (X being the mole fraction, taken as proportional to the PLIF signal intensity) has been used successfully as a marker of heat release in non-premixed and premixed flames [39–42]. Even when quantitative imaging has not been possible, the qualitative comparison of CH₂O and OH regions has been very fruitful. Medwell and Dally [149] have discussed formaldehyde in MILD combustion conditions, while Masri and co-workers have looked at simultaneous CH₂O and OH in jet flames of ethanol and methanol [126,127] and very interesting comments on the nature of the reaction zones in these spray flames could be made. They observed that for ethanol flames, the heat release zone (represented by the product CH₂O × OH) lies on the inner edge of the relatively broad region of OH, and the HR in turn surround the inner droplets. When increasing the droplet loading for the same carrier velocity, it appeared pockets of OH indicating premixing on the centreline of the jet separated from the outer OH which becomes thinner and diffusion like [126]. The existence of double reaction zones in these flames was later observed in methanol flames [127]. They also quantified the reaction zone thickness by the width of HR zone at various axial locations as an assistance indicator of the degree of partial premixing, and concluded that the reaction zone width, thus the degree of partial premixing increases with axial distance.

1.2.7 Proper orthogonal decomposition analysis on flow structure

The Proper Orthogonal Decomposition (POD) is increasingly being used with the recent advent of fast (i.e. kilo-Hertz) combustion diagnostics and the growing use of

Large Eddy Simulations, to extract dominant structures from an ensemble of data [150] from simulations or experiments. Applications of POD span a broad range of physical systems, including fluid mechanics [151] and combustion [152]. The POD bases act as the morphologic features of the studied flames and its coefficients are viewed as measure of their corresponding variability [153]. The POD has been used to reconstruct the images of the flames to reveal typical flame shapes and their connection with the acoustics [154] and the flow [155]. In the study of the blow-off dynamics, POD has also been applied to chemiluminescence images of stratified premixed flames [156] and vortex shedding [157]. In simulations, POD has been used to represent DNS data [158,159] and for analysis of LES [160,161]. The above references contain literature reviews on POD applications in flames and fluid mechanics and could be referred for further background information.

Assuming that POD can be used to reveal structural changes in the flames as operating conditions are altered, it is interesting to explore flame shapes at different degrees of extinction. POD of OH^* of a premixed flame at extinction without swirl has been productively used [156] and this partly motivates the present analysis of swirling spray flame extinction data with POD.

1.2.8 Laser induced breakdown spectroscopy of turbulent flames

Laser Induced Breakdown Spectroscopy (LIBS) is a laser based spectroscopic technique, which employs the radiation of a focused laser beam to excite, atomise, and dissociate the species present at the focal volume and has been used widely in various fields, including the determination of the fuel to air ratio (FAR) in combustion [162]. In LIBS measurements, the high intensity of a strongly focused beam provokes the dielectric breakdown of the medium and the plasma formation. The emitted light of the decaying plasma is then collected and spectroscopically analysed. During the initial stages of the decay of the plasma, the emitted radiation is mostly due to Bremsstrahlung radiation, which means that the spectra are dominated by a continuum background. As time evolves, the intensity of the background weakens and spectral features of atomic and molecular origin finally dominate the spectra [163,164]. By this means, temporally resolved measurements allow initially the identification of the species of the target, while the determination of the concentration of the constituents is

feasible through the intensity of their characteristic spectral lines, since they are directly associated to the population of the excited species [165,166]. Such an investigation can be performed in all kinds of samples, with only optical access to the target required. Moreover, LIBS can perform measurements on-line, in-situ and remotely. In view of these characteristics, the LIBS techniques has proven to be a very useful diagnostic tool for reacting flows, such as hydrocarbon-air flames.

In more detail, during most LIBS experiments available in the literature, laser beams of different pulse durations are focused in a region where the mixture is considered to be uniform, such as at the exit of a Bunsen burner. From the acquired emission spectra corresponding to mixtures with different compositions, the intensity or the ratio of the intensities of some spectral lines are also proven to correlate in a linear way to the amount of fuel in the flame [167]. In most cases, it is atomic lines or molecular band that were used while their ratios (e.g. H_{α}/O (at 777nm), H_{α}/N (at 567nm or 744nm), or CN (integrated from 705 to 733 nm)/ O (at 776.6 nm)) were proposed for quantitative equivalence ratio measurements in gaseous fuels [168–177] and in IC engines [178,179]. However, the study of liquid fuels in the form of droplets is rather limited [180–183]. In all the aforementioned works, the presented calibration curves were covering only a limited range of equivalence ratios (mainly lean) and so the proposed relationships could hardly be applied to a diffusion flame where the local mixture fraction ranges from 0 (pure air; equivalence ratio 0) to 1 (pure fuel; equivalence ratio infinity). A robust calibration scheme covering a wide range of mixture fractions is thus requested to be developed in order to apply LIBS in non-premixed systems as well as in spray flames. Besides, the precision of LIBS for turbulent systems should also be investigated.

1.3 Scope of the thesis

The scope of this work is to use laser diagnostic methods to make progress in understanding of the blow-off phenomena of turbulent swirl-stabilised spray flames. The main objectives of this work are to investigate the effect of fuel properties on the behaviour of swirling spray flames at both stable and blow-off conditions, and develop further understanding of the role of local flame extinctions in the global

extinction of recirculating spray flames.

The objectives of this work are:

- to obtain the detailed laminar premixed and non-premixed flame structure of the four fuels studied: ethanol, heptane, decane and dodecane, under a wide range of equivalence ratios or strain rates;
- to examine the correlation between real heat release rate and the species of OH, CH₂O and the product OH × CH₂O for these flames;
- to visualise the flame structure of the recirculating spray flame and its alteration at different departures from the blow-off condition;
- to visualise the spray flame blow-off transient process by high-speed diagnostics and quantify the duration of the blow-off event of various fuels and fuel flow conditions;
- to quantify lift-off heights from OH-PLIF images and characterise the topology of the OH islands at far from blow-off and at the blow-off condition;
- to analyse the local extinction in terms of the quenching percentage of stoichiometric mixture fraction iso-line at far from and close to blow-off conditions from joint CH₂O-OH PLIF images;
- to characterise the dominant flame structure and its motion by POD analysis of OH* and OH-PLIF images;
- to obtain local fuel content in turbulent gas flames and turbulent spray flames via LIBS technique.

1.4 Structure of the thesis

Chapter 2 describes the experimental set-ups and laser diagnostic methods applied in this study to visualise the structures of swirl-stabilised spray flames. In Chapter 3, laminar flame calculations results from gaseous mixtures (ethanol/air, heptane/air, decane/air and dodecane/air) on free propagation premixed flames and counterflow non-premixed flames with detailed chemistry and transport properties are presented, and some basic information on flame structures at various equivalence ratios or strain rates are provided as a reference for the following experimental observations. Chapter

4 presents the experimental observations on swirling spray flames structures at various departures from blow-off and at the blow-off event. The influence of fuel volatility on the spray flame behaviour is discussed. In Chapter 5, the four fuels blow-off limits are presented, the transient time of blow-off event, the lift-off heights statistics, and the local extinction percentages statistics are described, and the dominant structures and their motions subtracted by the POD analysis are discussed. The POD analysis, although has been widely applied for flow dynamics and bluff-body gas flames, is attempted in swirling spray flames and at different departures to blow-off for the first time, to author's knowledge. Chapter 6 describes Laser Induced Breakdown Spectroscopy (LIBS) measurements on local equivalence ratio/mixture fraction in turbulent premixed, turbulent non-premixed, and spray flames. The technique provides useful information on flame structures. The technique application in spray flames is new and is suggestive for further exploration. In Chapter 7, the findings of the investigation are summarised and guidelines for future research are suggested.

There is an appendix attached to this thesis. The appendix presents the droplet size and velocity distribution results from heptane, decane and dodecane flames, as supplemental material for Chapter 4.

Chapter 2

Experimental methods

2.1 Burner configuration

A bluff-body swirl spray burner was used to study gas turbine like spray flames at different departures from blow-off. The same burner was studied before by Cavaliere et al. [6] and Letty et al. [184] for blow-off study of non-premixed and heptane spray flames, and for ignition study of heptane spray flames, except for a new atomiser being adopted in this work to perform different fuel atomisation under a wider flow rate range. An ensemble of four pieces of fused Quartz plates (Cambridge glassblowing Ltd. UV-IR transmittance: $\geq 80\%$ at 200 nm \sim 3.6 μm ; $\geq 90\%$ at 275 nm \sim 3.3 μm ; dimensions: 50 mm \times 103 mm \times 3 mm thick \times 2 pieces and 150 mm \times 97 mm \times 3 mm thick \times 2 pieces) enclosure was used to have a confined area, an inner recirculation zone, and a clear transmittance for UV-IR range laser diagnostics. The schematic of the bluff-body swirl spray burner is shown in Figure 1. For the spray atomisation, a pressurised axial-flow hollow-cone atomiser (Lechler, Part#.212.054.17.AC) (Figure 2(I) left) was used and fitted into a conical bluff-body holder (Fig. 2(I) right). The bore diameter of the atomiser nozzle was 0.2 mm, while

the narrowest exit jet free cross section was 0.15 mm. The supplier certifies a spray cone of around 60° . The atomiser was fitted into a bluff-body holder, with the exit plane level with burner base plate. The outer diameter of the bluff-body was 25 mm, while the inner diameter of the burner plate was 37 mm, the area in between provided an annular air pathway. The air stream passed through an annular swirler (Fig. 2(II)) before going into the combustion chamber. The swirler had a constant vane angle of 60° , and a swirl number (S_N) of 1.23 calculated by the expression in Ref. [64].

2.2 Flow measurement methodology

2.2.1 Flow-rate measurements

The experimental set-up is shown in Figure 1. Liquid fuel was pressurised by nitrogen (BOC, 99.9995% vol/vol purity) supplied from a compressed cylinder regulated at 0-6.0 bar. The liquid flow rate was altered by adjusting the setting pressure from the fuel feeding tank, and was monitored by a liquid mass flow controller (MFC) (Bronkhorst, LIQUI-flow, L30, 0-2 g/s, uncertainty of ± 0.02 g/s). A digital readout (Bronkhorst, E-7000) was connected with L30, through which the operation liquid and the target flow rate could be adjusted accordingly. The operating fluids in this work were respectively ethanol, n-heptane, n-decane, and n-dodecane. The flow rate range was in the range 0.15-0.45 g/s. The calibration of the MFC was performed by measuring the weight (± 0.1 g) of the liquid output and hand-held stopwatch (± 0.01 s) as a function of the reading on the MFC for each operating cycle (fuel and date).

Air stream was supplied by the laboratory compressor, pre-filtered for water, particulates, and oil content. A regulator was used along with a pressure gauge to adjust and maintain the back pressure at 6.0 bar. Air flow rate was controlled by an Air-MFC (Alicat, MFC 1000 SLPM, uncertainty of $\pm (0.8\%$ of reading + 0.2% of full scale (FS)); repeatability of $\pm 0.2\%$ of FS). The operating flow range was 500-990 SLPM, which corresponds to a bulk velocity (U_b) between 14.3 m/s to 28.2 m/s.

2.2.2 Determination of the blow-off point

For reaching the lean blow-off limit of the spray flame, the fuel flow rate was kept fixed, while the air flow rate increased gradually in steps of approximately 2% (0.258

2. Experimental methods

m/s) every 40-60 seconds until blow-off occurred recording the blow-off velocity, U_B . At each fuel flow rate, an average blow-off velocity of at least 10 individual U_B measurements is calculated and reported in the table shown in Ch. 4.

2.3 Diagnostic methods

Several diagnostic methods were applied in the work to visualise the flame structures of bluff-body swirl spray flames. The techniques include direct photography of the stable spray flames, 5 kHz 2D OH* chemiluminescence measurements of heat release rate, 5 kHz Planar Laser Induced Fluorescence (PLIF) measurements of hydroxyl radical (OH), simultaneous planar measurements of formaldehyde (CH₂O) PLIF and OH-PLIF (10 Hz), Mie scattering from droplets and Laser Doppler Velocimetry / Phase Doppler Anemometry (LDA/PDA) for droplet velocity and size measurements. In the end, point measurement of Laser Induced Breakdown Spectroscopy (LIBS) is described, and preliminary results of local equivalence ratio of n-heptane spray flame are described. The schematics of the related laser diagnostics methods are shown in Figure 3.

2.3.1 Laser Doppler Velocimetry/Phase Doppler Anemometry

Droplets size and velocity (axial and radial component) were measured using a standard two channel Laser Doppler/Phase Doppler Anemometry (LDA/PDA, DANTEC). The transmitting probe had a focusing length of 500 mm with the green beams (514.5 nm) crossing in the vertical direction to measure the axial velocity component and droplet size. The blue beams (488 nm) crossed horizontally and measured the radial velocity component. The receiving optics had a focusing length of 310 mm and a receiving angle of 30°. The measuring volume was 3.4 mm in the length, 0.15 mm in height and width (perpendicular direction of the beam transmitting plane, and the direction of droplet profiles measurement taken). Either 20,000 samples or 30 seconds acquisition time were collected at each measurement location. The validation rate for the Doppler burst was close to 100% and the spherical validation was over 80% during the acquisition for all locations. The present instrument and its controlling software operated only within a user-supplied diameter range and this was

2. Experimental methods

set at 0-100 μm , which may underestimate the SMD values than the real value when the measured droplets size ranges are towards a large value, i.e. 80 μm .

2.3.2 Chemiluminescence measurements

OH* chemiluminescence was measured as an indicator of heat release of the spray flame both at stable case and blow-off event. An IRO intensifier (LaVision, spectral range of 190-800 nm) was fitted with a UV filter (270-370 nm) for OH*. The intensifier was coupled with a Photron SA1.1 monochrome high speed CMOS camera with 1024 \times 1024 pixel resolution up to 5.4 kHz. OH* chemiluminescence was captured at 5 kHz. 1000-5000 images (0.2-1.0 s) were recorded per run.

2.3.3 Planar Laser Induced Fluorescence measurements

2.3.3.1 Fast OH – PLIF measurements

OH-PLIF was measured to visualise flame sheet structure. Identical diagnostic system was used in premixed flames by Kariuki et al. [51] and non-premixed flames and heptane spray flames by Cavaliere et al. [6] at flames close to blow-off. The OH-PLIF system consisted of a high-repetition rate diode solid state laser (532 nm, model JDSU Q201-HD), with a power of 14 W at 5 kHz and a pulse length of around 18 ns, and a SIRAH Credo high speed dye laser (model 2400), with the output beam at 566 nm doubled by a BBO crystal. The output beam was tuned near 283 nm to excite the Q₁ (6) line in the $A^1\Sigma - X_2II$ (1,0) band. The output power was 300 mW at 5 kHz (60 $\mu\text{J/pulse}$). The laser beam was expanded into a sheet of around 0.23 mm thick and 35 mm height using sheet optics. An IRO intensifier (LaVision, spectral range of 190-800 nm) was fitted with a narrower filter (300-325 nm) for OH-PLIF. The intensifier was coupled with a Photron SA1.1 monochrome high speed CMOS camera with 1024 \times 1024 pixel resolution up to 5.4 kHz. The resolution of OH-PLIF images was around 0.1 mm per pixel. OH-PLIF movies were captured at 5 kHz. 1000-5000 images (0.2 - 1.0 s) were recorded per run.

2.3.3.2 Joint CH₂O - OH PLIF measurements

Two 10 Hz Nd:YAG lasers and one dye laser were used for the joint CH₂O and OH

2. Experimental methods

PLIF system [185]. The system was in UCL (University College London). The OH-PLIF was excited at 283 nm, while the CH₂O - PLIF was excited at 355 nm. The fluorescence of OH was captured in the range of 309 - 375 nm with WG305 and UG11 Schott glass filters applied. The fluorescence of CH₂O was captured in the range of 375 - 610 nm using an intensified CCD camera through a filter set (laser line notch filter: OD > 4, 17.8 nm FWHM, GG395 and BG 40) to eliminate scattering, flame luminosity, and soot emission interference. A 355 nm laser line notch filter was added to the CH₂O camera to further cut-off any scattering of laser light by droplets. Because heptane (liquid and / or vapor) and PAH may also fluoresce in the range 350 - 600 nm [186,187], possible interference from fluorescence of the fuel and PAH cannot be subtracted from the CH₂O signals. Some comments on the importance of this interference are made later based on laminar flame simulations and on some preliminary experiments. The nominal resolution of the imaging system was 0.05 mm/pixel. The gain of the image intensifier was 30,000 FL/FC and 80,000 FL/FC for CH₂O and OH respectively. The laser powers were 12 mJ/pulse for OH PLIF and 300 mJ/pulse for CH₂O PLIF. The intensifiers were triggered off the Q switch of each laser with a gate of 220 ns. The CH₂O PLIF laser was triggered at 300 ns delay from the triggering of the OH laser. The laser pulse width was 10-12 ns.

2.3.5 Mie scattering measurements

2D Mie scattering from the spray droplets were measured with 532 nm incident laser wavelength and a narrow band laser line filter. The laser sheet thickness was around 1 mm. The pulse laser and camera systems are the same with the ones used in OH-PLIF kHz systems. A neutral density filter was fitted before the camera to prevent damage. The scattering signal from soot particles of the spray flames was relatively minor compared with the scattering signal of droplets. A sequence of 1000 images of stable flames and 800 images of unstable flames before blow-off transient was averaged for getting the mean Mie scattering profiles.

2.3.6 LIBS configuration

For the plasma creation, the focused laser beam of a Q-switched Nd:YAG laser (Continuum Surelite) operated at 1064 nm at a repetition rate of 10 Hz repetition rate,

2. Experimental methods

delivering 6 ns pulses. The focus length of the incident laser beam was carefully chosen to obtain a compact excitation volume. A 150 mm focal length plano-convex lens was used for the measurements in gaseous flames, and a focusing lens of $f = 75$ mm was used for the measurements in spray flames. For gaseous flames, the energy of the laser beam was set to be 250 mJ, in order to induce successful sparks in every position of the flame, except for some measurements that investigated the effect of laser energy where this was varied. Note that this energy is generally considered high, but this is necessary to ensure consistent plasma creation in the hot flame products. For spray flames, a range of laser energies were applied both in the uniform dispersions and the chosen spray flame, and a minimum laser energy was chosen so as to provide minimum disturbance to the flow but to be enough to ensure breakdown everywhere in the flame zone. 140 mJ laser energy was sufficient for the current study.

The plasma emission was collected via a 100 mm focal length lens and collimated to an optical fiber (200-1100 nm) attached to a portable spectrometer (Ocean Optics USB 2000, UV-VIS: 178-877 nm, 0.34 nm resolution). A fast photodiode (amplified, IR range) was used to detect the incidence laser pulse and to trigger a pulse generator (TGP110), from which a delayed pulse was sent to trigger the spectrometer. The total delay time between the laser pulse and the start of the acquisition of the spectra was 8 μ s, while an integration time of 3 ms was used to improve the signal to noise ratio by maximising the emission and minimising the continuum background (i.e., Bremsstrahlung radiation, soot emission, and flame luminosity). The laser system schematic is shown in Fig. 3c.

Two calibration rigs were used in LIBS measurements, providing uniform-flowing mixtures of gaseous fuel – air and liquid fuel – air respectively. The rigs configurations as well as flow conditions are described in Ch. 6.1.1.

2.4 Data analysis

2.4.1 Data processing

2.4.1.1 Inverse Abel transform

To reconstruct the image of the local heat release from the line-of-sight OH*

2. Experimental methods

chemiluminescence measurements, the Inverse Abel Transform (IAT) was applied with the assumption of axisymmetry of the OH* signals. Only the mean image of each flame was processed with the IAT, as the axisymmetric assumption is hardly valid on an instantaneous basis. In addition, when there is asymmetry in the average 2D projected image due to experimental non-uniformity issues, a reconstructed axisymmetric image from the selected half of the mean image is used for the IAT. For a particular horizontal plane, the measured OH* signal, $P(x)$, is given in terms of local OH* emission, $I(r)$, through the Abel transform

$$P(x) = 2 \int_0^{\infty} I(r) dy = 2 \int_x^{\infty} I(r) \frac{r}{\sqrt{r^2 - x^2}} dr \quad \text{Eq. 6}$$

where x, y are the Cartesian coordinate in the horizontal plane centring on the burner axis; r is the radius of the local emission; I is the local OH* emission, which is a function of the radius; P is the one dimensional projected OH* emission, which is an integral of I along the projecting direction. In the IAT, I could be obtained from the derivative of the projection P . The discrete IAT is given by

$$I(r_j) = -\frac{1}{\pi} \sum_{k=j}^{\infty} \int_{ll}^{\Delta x/2} \frac{P'(r_k + \delta)}{\sqrt{(r_k + \delta)^2 - r_j^2}} d\delta \quad \text{Eq. 7}$$

in Eq. 7, ll is the lower limit of the integral, $ll = 0$ for $k = j$, and $ll = -\frac{\Delta x}{2}$ for $k > j$. j, k are the pixel indexes in the x direction; Δx is the grid size; and the derivative P' is calculated using the centred difference approximation. The IAT method employed is fast and produces satisfactory results, but it has a drawback in producing artificial structures on the central axis ($r = 0$).

2.4.1.2 PLIF images

The OH-PLIF images were filtered using a 2-D median non-linear filter for noise reduction (3×3 filter size) and corrected for inhomogeneities in the laser sheet profile for further processing to get various quantities such as morphological features of isolated OH regions and the lift-off height of the flame from the bluff body.

For joint PLIF data processing, both OH and CH₂O PLIF images were transformed to be spatially aligned with each other on a pixel-by-pixel basis. The alignment needs

2. Experimental methods

to be precise and follows several stages. Firstly, a target image (a grid pattern with several reference points) was taken using both cameras. Secondly, the CH₂O image was mirrored and the corresponding coordinates of the same reference point were identified. Thirdly, a transformation matrix relating the two sets of coordinates was computed and then used to map the OH images onto the coordinates system of the CH₂O images. The images were further processed via Matlab with background subtraction, laser profile correction, 3×3 median filtering, and a threshold below in which the signal was put to zero. The product CH₂O×OH was then calculated and plotted as indicator of local reaction zone. 400 images were recorded for each flow condition. The processing flowchart is drawn in Fig. 4a.

For both fast OH-PLIF and joint CH₂O-OH PLIF data processing, the binarisation threshold of the image is carefully chosen using the following process: first, the PDF of the PLIF image intensity for each instantaneous image was used to evaluate the most probable intensity values of the background (I_b) and the PLIF signal (I_s), indicated by the distinct peaks in the bimodal PDF plots. A threshold was set as an extra 40% of the difference of the I_s and I_b above the value of I_b . The sensitivity of the binarisation threshold was examined. An example of set of sample images are plotted in Fig. 4b showing the binarised PLIF images of OH and CH₂O respectively from several threshold values of 15%, 40% and 70% of the ($I_s - I_b$) above the I_b , as well as the product of the two PLIF images filtered by the product of the two binarised images, from OH and CH₂O, with the corresponding thresholds. The plots show that a threshold of (40% ($I_s - I_b$) + I_b) is optimum as it filtered most of the noise and avoided cutting out too much signal. Thus, 40% was further applied in the data processing.

2.4.1.2 PDA data

The PDA system was carefully set-up in order to minimise the measurement uncertainties: (1) the collecting angle (30°) was chosen in the refraction dominant region to avoid various modes of scattering dominating the scattered light at the collecting angle; the reason for which is that the PDA estimates the droplet size from the phase differences of the Doppler bursts received by the different Photo-Multipliers (PM) in the receiving optics, and different modes of scattering give rise to different

2. Experimental methods

phase factors; (2) a sufficiently long measurement time (30 s) or a large number of samples (20000) were collected in each position in case of the high turbulence; (3) the high voltage to the PM, the gain of the PM signal amplifier, and the record length settings were adjusted to optimise data rate and burst validation; (4) the laser-line interference filters were installed in the detector unit to block out the light carrying the other velocity components; (5) 40MHz frequency shift was applied to resolve the directional ambiguity; and (6) a maximum allowable deviation from sphericity was specified to reduce the uncertainty associated with phase measurements. For processing the PDA data, statistics were calculated for each collecting volume. Locations with data less than 50 counts (an average sampling rate $< 1.7 \text{ s}^{-1}$) were excluded. For some measurements, the PDA data at each location were classified by the size in the ranges $[0, 10) \mu\text{m}$, $[10, 40) \mu\text{m}$, $[40, 80) \mu\text{m}$, and $[80, 100) \mu\text{m}$ and the average velocities conditioned on the size category are reported. Data with few counts (< 10) for each category were omitted.

2.4.1.3 LIBS measurements

The measurements of the emission spectra of the plasma were carried out in two different ways. In the first case, called “averaging method”, each spectrum was the average of 100 (200 for the measurements in spray flames) spectra accumulated through the spectrometer’s software. In the alternative way, here called “instantaneous method”, 100 different single shot spectra, acquired under the same experimental conditions, were analysed to give 100 instantaneous measurements of the emission spectra. The use of the instantaneous method on the uniform mixtures used for calibration also results in an assessment of the precision of the technique.

For calculating the intensity ratio between different emission species, no obvious difference in the results could be seen either by taking the peak intensity or the total intensity (i.e., the total area below the spectral feature) of species spectral lines into account. The total intensity was then used for the H_α (646.3 nm), O (777.3 nm), C_2 (516.5 nm), and CN (388.3 nm) species.

2.4.2 Duration of the blow-off event

OH* chemiluminescence were captured at 5 kHz were recorded at the blow-off. The acquisition was triggered continuously and the last 5000 (1 s) frames were recorded before the visible flame completely extinguishes. The obtained image series were averaged without the transient process. The transient time was calculated by the duration of averaged integral OH* intensity drop from 90% to 10% of its mean value.

2.4.3 Lift-off height analysis

Lift-off height was obtained from OH-PLIF images and was calculated as the vertical distance between the edges from the closest OH fragment to the bluff-body edges. An example image was shown in Fig. 5a. 2000-5000 frames were accounted per flame with two lift-off height values at each side of bluff-body per frame. The distribution of the lift-off height was obtained for stable flames far from blow-off and close to blow-off, and for unstable flames without the transient process.

2.4.4 Statistics of local quenching size

The size of the local quenching region was obtained from the joint CH₂O-OH PLIF measurements. The CH₂O images were applied by 3 × 3 median filtering and then the boundary of CH₂O images was subtracted using Matlab. The outline of CH₂O images acts an approximation of the stoichiometric iso-line. OH signal was then searched the presentence along this line. The integral length along this boundary with absence of OH signal was calculated and marked as the local quenching size along the stoichiometric iso-line (example images are shown in Fig. 5b).

2.4.5 Proper orthogonal decomposition (POD) analysis

Given a data set $u_k(x)$, where x is the spatial variable and k is the snapshot (or temporal) index, the POD provides an optimal orthonormal basis function set, called the “POD modes”, $\phi = \{\phi_1, \dots, \phi_N\}$, so that the ensemble of the data can be written as a linear combination of these POD modes. The data can be organised in the matrix of snapshots U :

2. Experimental methods

$$U = \begin{pmatrix} u(x_1, t_1) & \cdots & u(x_1, t_N) \\ \vdots & \ddots & \vdots \\ u(x_M, t_1) & \cdots & u(x_M, t_N) \end{pmatrix} \quad \text{Eq. 8}$$

where M is the dimension of the discretised spatial domain, and N is the number of snapshots. When the number of the snapshots is much smaller than the dimension of the spatial discretisation, $M \ll N$, it is useful to adopt the ‘‘method of snapshots’’ proposed by Sirovich [188] which permits to express the POD basis functions (POD modes) as linear combination of the snapshots $\varphi_1(x) = \sum_{k=1}^N \psi_{1k} u_k(x)$, where $\Psi = \{\psi_1, \psi_2, \dots, \psi_N\}$ is obtained by solving the eigenvalue problem $C\Psi = \lambda\Psi$ where $C = (U^T \cdot U)/(N - 1)$ is the space correlation matrix. Then, $u(x, t)$ can be approximated by a linear combination of the first K modes $u(x, t) \approx c_0\varphi_0(x) + \sum_{i=1}^K c_i(t)\varphi_i(x)$, where $c_i(t)$ are the POD coefficients that can be calculated by projection of the data set onto the modes. Mode 0, $\varphi_0(x)$, multiplied by its coefficient c_0 , is the mean field of the snapshots. The i -th eigenvalue, λ_i , represents the energy captured by the i -th POD mode about the data set. Usually, the POD modes are ordered according to decreasing magnitude of their corresponding eigenvalues (real, positive). The cumulative energy portion of the first K modes is calculated by $E_K = \sum_{i=1}^K \lambda_i / \sum_{i=1}^N \lambda_i$. The resulting eigenvalue problem is solved by using the Matlab routine ‘‘eigs’’. Since the temporal variable appears only in the POD coefficients, and the spatial variable appears only in the POD modes, it can be said that the modes carry information on the spatial features, whereas the coefficients describe the temporal features.

In this work, the POD has been used to extract and analyse the dominant structures from the ensemble of collected images, both OH* chemiluminescence and OH-PLIF, during the experiments described previously. The acquired frames were 1024 x 1024 pixels but to reduce the computational cost they were cropped to the region of interest (831 x 365). The time series of the POD coefficients were normalised to have unit energy (or standard deviation one), that is: $\zeta_i(t) = c_i(t)/\sqrt{\lambda_i}$. Following this, the Power Spectral Density (PSD) and Cumulative Spectral Power (CSP) of the normalised POD coefficients were estimated. Welch’s method with a Bartlett-Hanning

2. Experimental methods

window was used to estimate the PSD. Since the POD coefficients were normalised to have unit energy and the data set was centred to have mean zero, $\int_0^{+\infty} PSD_i(f)df = 1$ $\Rightarrow \lim_{f \rightarrow \infty} CSP_i(f) = 1$ for all normalized POD coefficients, where f is the frequency. Analysis of the PSD of the POD coefficients can reveal any periodic features and the frequency content of the associated POD mode.

2.5 Figures for Chapter 2

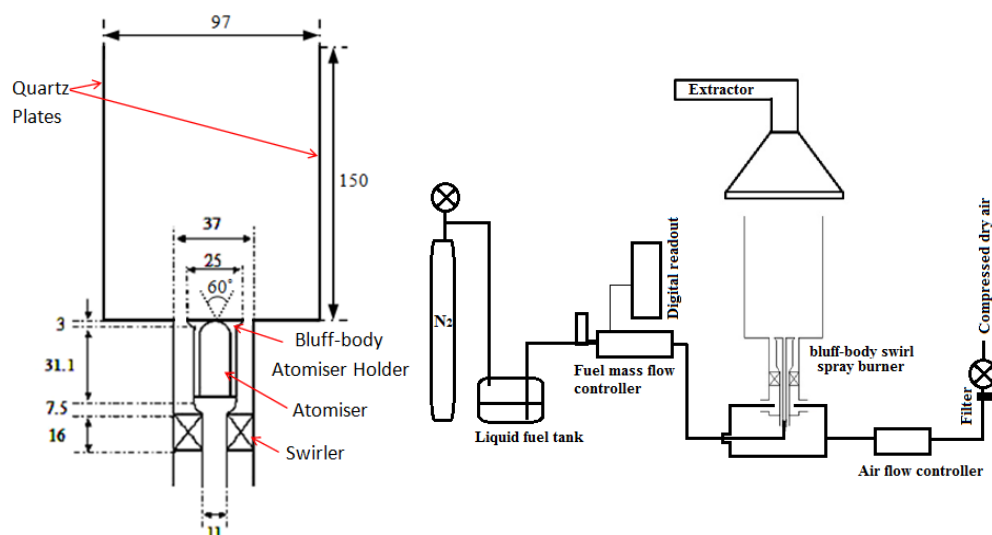


Figure 1. Schematic of bluff-body swirl spray burner (left), and experimental set ups for swirling spray flames (right).

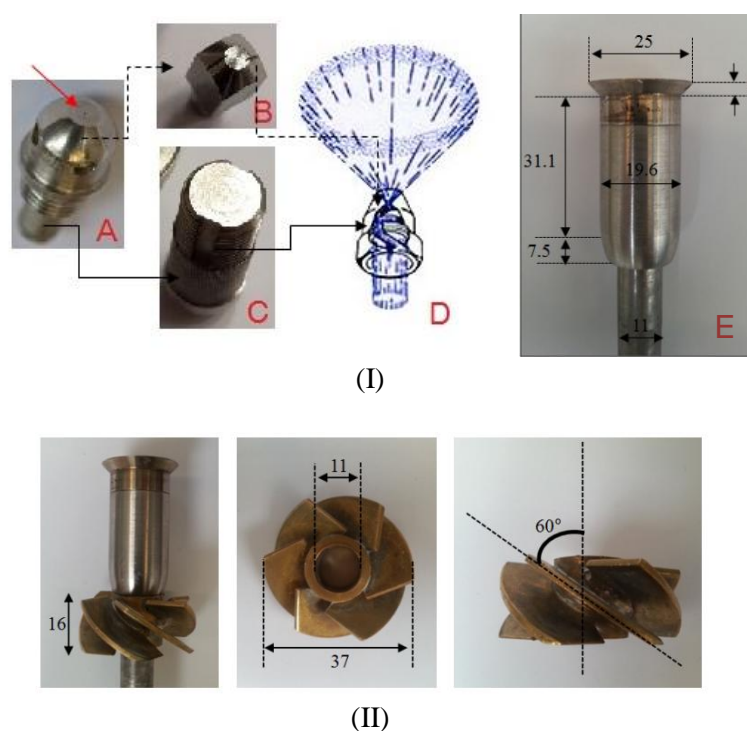


Figure 2. (I) Photograph of the pressure atomiser (A), the ensemble of the atomiser (B and C) showing the spiral grooves to ensure swirling of the liquid (B), the schematic diagram of the internal flow and the hollow-cone spray profile (D [221]), and the bluff-body atomiser holder (E). The red arrow (in A) points the exit of the liquid fuel. (II) Photograph of the swirler and the dimensions.

2. Experimental methods

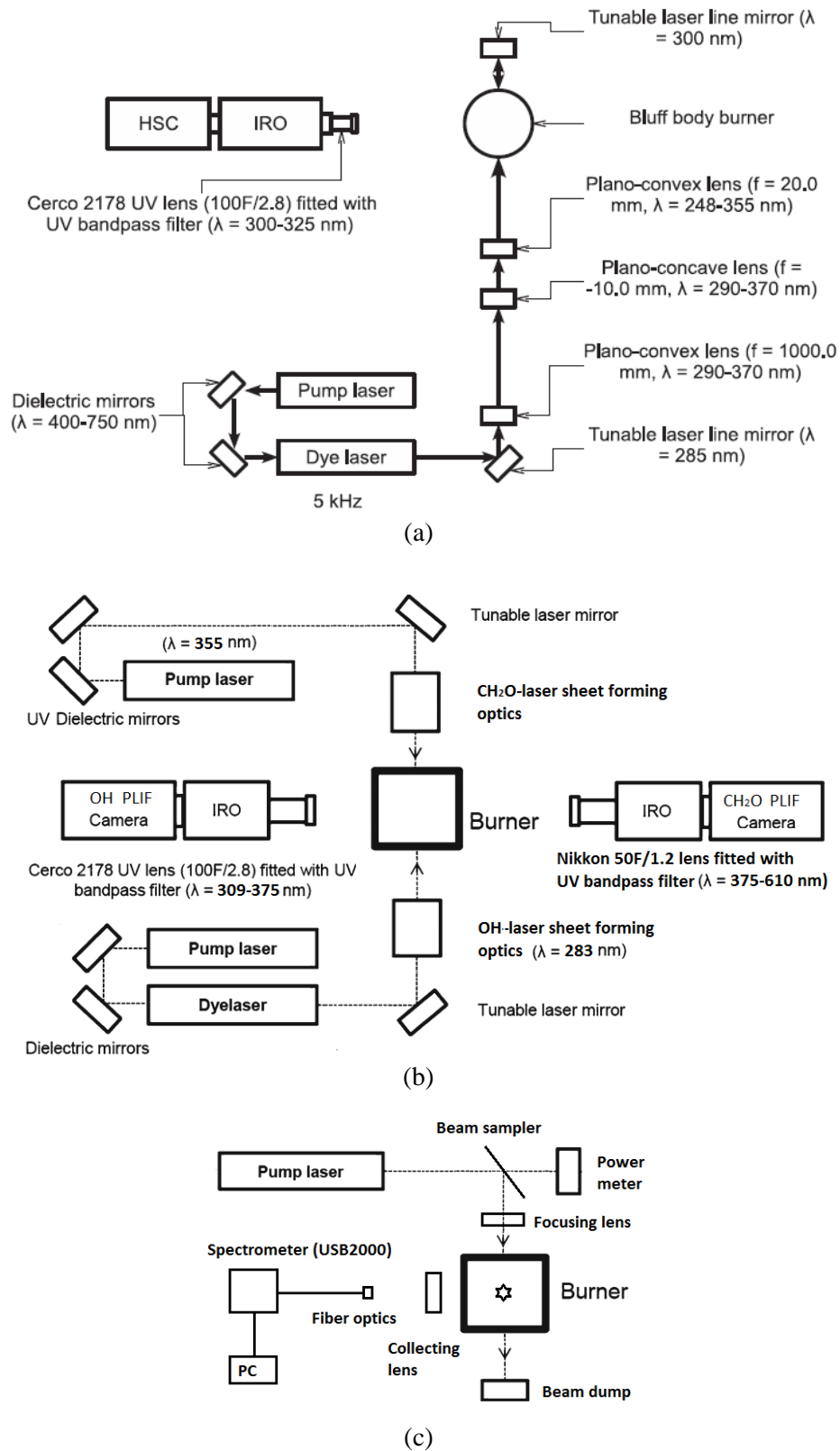
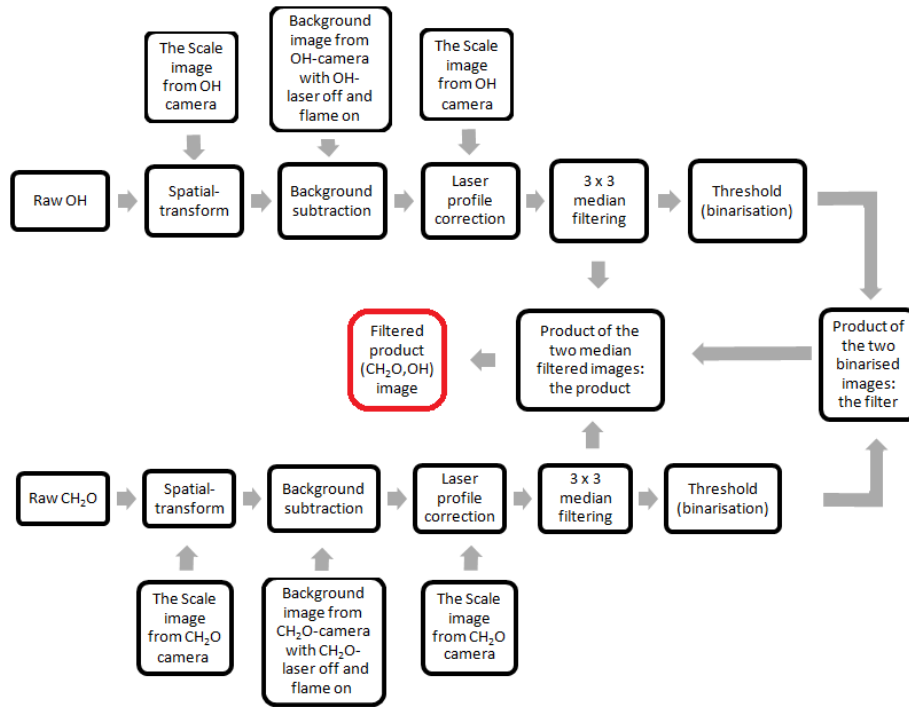
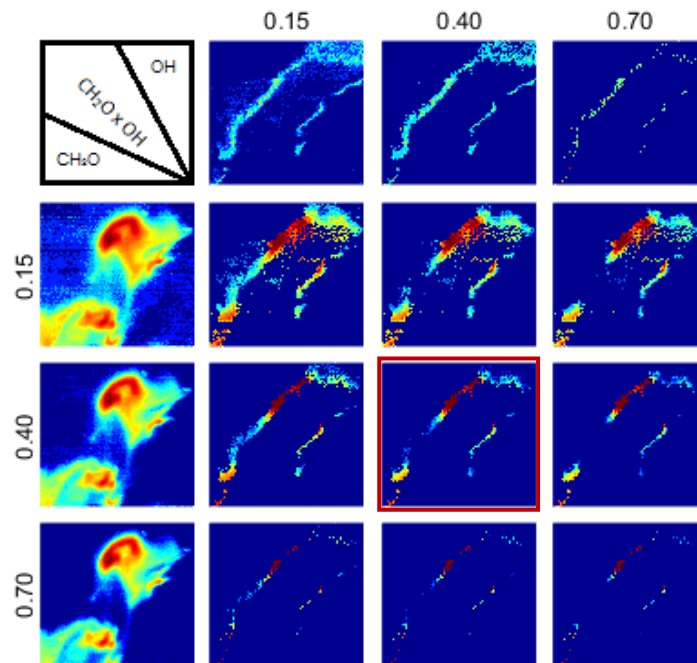


Figure 3. Schematic of the laser layout and acquisition system set ups of (a) OH-PLIF, (b) joint CH₂O-OH PLIF, and (c) LIBS arrangement.

2. Experimental methods



(a)



(b)

Figure 4. (a) The data processing flowchart of the product of CH_2O -OH PLIF, and (b) an example of the sensitivity of the binarisation threshold for OH image and CH_2O image: 1st row - the OH image with various threshold values (defined in the text); 1st column - the CH_2O image with various threshold values; and the remaining images of the matrix - the corresponding product image of CH_2O and OH after applying the thresholds of the same row and column. The red box indicates the final image reported in the results.

2. Experimental methods

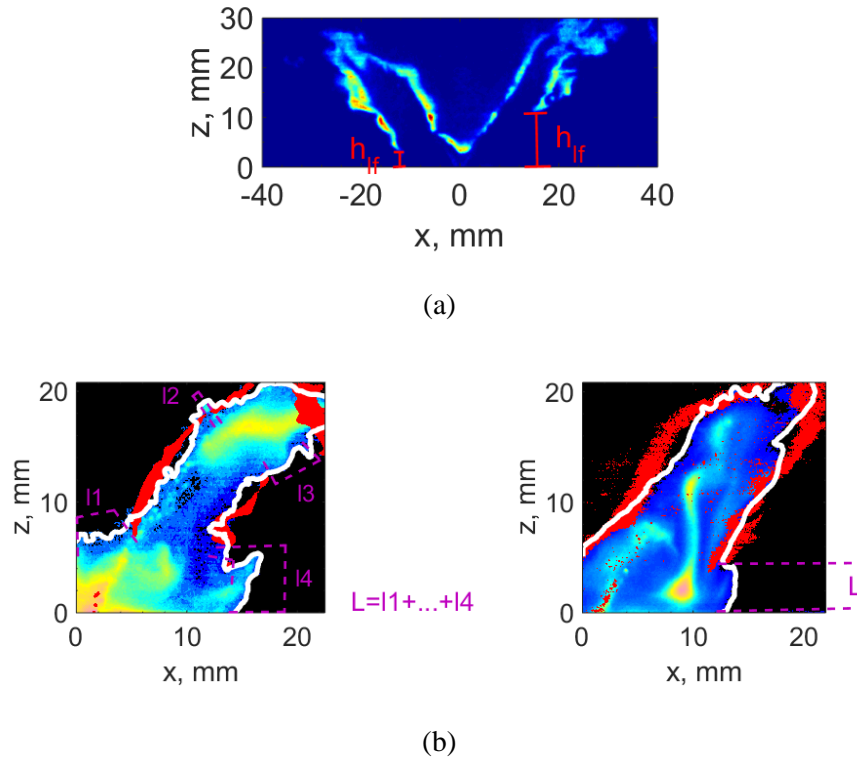


Figure 5: (a) An example image from fast OH-PLIF of decane (D1S1, fuel flow rate is 0.27 g/s and air bulk velocity is 17.1 m/s). The lift-off height (h_{lf}) is marked in the image. (b) Example images from the joint CH₂O-OH PLIF image of stable heptane flame (H1S1, fuel flow rate is 0.27 g/s and air bulk velocity is 17.1 m/s). The image includes the binarised OH signal (red), CH₂O signal (colour, from blue-pink), and the CH₂O signal's boundary (white line), which can be used as a rough estimate of the stoichiometric contour (discussed later in Ch.3). L is measured as the length of the CH₂O boundary that has zero overlap with the OH signal. The total length of the CH₂O boundary (the white line) is calculated as Σ . The quenching percentage, b , of the stoichiometric iso-line is then obtained as L/Σ .

Chapter 3

Laminar flame calculations

This chapter describes laminar flame calculations of premixed and non-premixed gaseous flames of the various fuels applied in the current study: ethanol, heptane, n-decane, n-dodecane, and a kerosene surrogate: the ‘‘Aachen’’ fuel surrogate. Detailed chemistries and transport properties were applied in the simulations. The purposes of these calculations are to obtain the detailed flame structure, and to examine the correlation between the heat release rate (HRR) and hydroxyl (OH) radical and formaldehyde (CH_2O) radical in various flow conditions, in order to assist the image interpretation in the following chapters.

For the laminar premixed flame calculations, the species and the HRR across a flame at a range of equivalence ratios were obtained for each fuel. For counterflow non-premixed flames calculations, the species and the HRR in mixture fraction space were resolved at various strain rates from very low to near extinction. The correlation between HRR and the product $\text{CH}_2\text{O} \times \text{OH}$ was examined for all conditions.

3.1 Freely propagating premixed gas flames

3.1.1 Background and equations

One-dimensional, premixed, and freely propagating laminar flames calculations were performed using the COSILAB software [189] at atmospheric pressure with detailed chemistry and transport properties to obtain the laminar flame speed, S_L , and to compute the laminar flame structure in terms of profiles of temperature T , species mole fraction X_i , especially the mole fraction of OH and CH₂O (the PLIF of the two radicals is measured in the following experiments), and the heat release rate HRR. The governing equations are:

(1) the continuity equation

$$\frac{\partial \rho}{\partial t} + \frac{\partial(\rho v)}{\partial x} = 0 \quad \text{Eq. 9}$$

(2) the species-mass conservation equations

$$\rho \left(\frac{\partial Y_i}{\partial t} + v \frac{\partial Y_i}{\partial x} \right) = - \frac{\partial(\rho Y_i V_i)}{\partial x} + w_i, \quad i = 1, \dots, I \quad \text{Eq. 10}$$

(3) the energy equation

$$\begin{aligned} \rho c_p \left(\frac{\partial T}{\partial t} + v \frac{\partial T}{\partial x} \right) \\ = \frac{\partial \left(\lambda \frac{\partial T}{\partial x} \right)}{\partial x} - \frac{dT}{dx} \sum \rho Y_i V_i c_{pi} - \sum_{i=1}^I h_i w_i + \frac{dp}{dt} \end{aligned} \quad \text{Eq. 11}$$

(4) the ideal-gas equation of state

$$p = \rho \bar{R} T \sum_{i=1}^I \frac{Y_i}{W_i}, \quad i = 1, \dots, I \quad \text{Eq. 12}$$

and (5) the momentum equation

$$\rho \left(\frac{\partial v}{\partial t} + v \frac{\partial v}{\partial x} \right) = - \frac{\partial p}{\partial x} + \frac{\partial(\mu \frac{\partial v}{\partial x})}{\partial x} \quad \text{Eq. 13}$$

In Eqs.9-13, x is the spatial coordinate, ρ is the gas density, v is the one-

3. Laminar flame calculations

dimensional velocity, T is the temperature, p is the pressure, c_p is the specific heat capacity of the mixture at constant pressure, λ is the thermal conductivity, and μ is the dynamic viscosity of the mixture. Properties of the species are denoted with subscript i . Y_i is the mass fraction, V_i denotes the diffusion velocity of species i [222], and $\rho Y_i V_i$ is the diffusion flux. c_{pi} and h_i is the constant pressure specific heat and enthalpy, respectively, w_i is the mass rate of production. The radiation term is neglected in the energy equation. The system is closed with $(I + 4)$ equations for $(I + 4)$ unknowns of ρ , v , T , p , and Y_1, \dots, Y_I .

The boundary conditions are as follows: far upstream of the flame is the cold boundary set with inlet temperature of 300 K for each case, and the reactant with equivalence ratio ϕ . Far downstream of the flame is the hot boundary. The laminar flame speed S_L is an eigenvalue determined as part of the solution. The system is adiabatic, hence the adiabatic flame temperature is obtained far downstream. For each fuel a range of equivalence ratios were set to obtain the flame structure and the corresponding laminar flame speed.

The detailed mechanisms applied in the laminar premixed flames calculations are: (1) the high and low temperature kinetic scheme (482 species, 19072 reactions) from Ranzi et al. [190] for ethanol and n-dodecane flames, from which S_L validated with the experimental data for ethanol-air flames at 347 K and for n-dodecane-air flames at 400 K and 470 K; (2) the Held et al. mechanism [191] (41 species, 266 reactions) for heptane flames, with S_L validated with experimental data at 298 K; and (3) n-decane / trimethylbenzene mechanism by Honnet et al. [192] (122 species, 900 reactions) for n-decane and Aachen fuel surrogate (a mixture of n-Decane 80% and 1,2,4-trimethylbenzene 20% by volume) flames, and the validation was given for n-decane at 900K and 473K and for 1,2,4-trimethylbenzene at 900 K.

3.1.2 Laminar flame speed

The laminar flame speed S_L obtained from these simulations is plotted in Figure 6a against various equivalence ratios for each fuel. It shows that S_L peaks at around $\phi = 1.1$ as supported in Refs. [1,85,96], and decreases as the mixture is leaner or richer. The maximum S_L for all these fuels is around 0.30-0.45 m/s. S_L is in a

3. Laminar flame calculations

reasonable range and its trend against ϕ is captured well for each fuel.

The adiabatic flame temperature (T_{ad}) at various equivalence ratios is plotted in Fig. 6b for each fuel. The corresponding curve of these fuels aligns close to each other. A slight increase in the peak value of T_{ad} can be seen with a lower volatility fuel. The peak temperatures for ethanol and heptane flames are around 2000 K, and for decane, dodecane and Aachen surrogate flames are around 2100 K.

3.1.3 Laminar flame structure

The plots of species mole fraction (X), the temperature (T) and the heat release rate (HRR) across a flame at lean, stoichiometric and rich mixture condition of the various fuels are shown in Figures 7-11. The normalised HRR is also plotted against the normalised product of X_{CH_2O} and X_{OH} to show the correlation.

We begin with ethanol flames. At the stoichiometric condition (Fig. 7a), as expected, CH_2O (blue dot line) is produced in the preheat zone, peaks in the mid-temperature region of the flame, and is consumed at the high temperature zone. On the other hand, OH (pink dot line) is produced at high temperature regions where CH_2O decreases. X_{OH} peaks in the high temperature post-flame region where CH_2O is absent. The amount of OH is still high at post-flame region. The HRR (red dot line) starts at around the peak of X_{CH_2O} , peaks close to the centre of the overlap region of OH and CH_2O , and goes down after CH_2O but before OH decreases. The trend is in agreement with the results from premixed methane flames [52,193]. Similar trends of T , HRR, and species profiles are obtained at the lean ($\phi = 0.7$, Fig. 7b) and rich ($\phi = 1.4$, Fig. 7c) conditions. The peak HRR is larger at stoichiometric condition than at $\phi = 0.7$ and at $\phi = 1.4$. The width of HRR is narrower at stoichiometric condition. Next, the HRR overall coincides with the overlapped of CH_2O and OH at all conditions. This supports the use of the pixel-by-pixel product of X_{CH_2O} and X_{OH} as a reliable indicator of the HRR in premixed ethanol flames. The normalised HRR is plotted against the normalised product $X_{CH_2O} \times X_{OH}$ in Fig. 7d (anti-clockwise direction indicates the reactants to products direction) for a range of ϕ . It is evident that the HRR is correlated well with the product $X_{CH_2O} \times X_{OH}$ for a range of equivalence ratio conditions of laminar ethanol premixed flames.

Similar profiles of the flame structure (OH , CH_2O , HRR, T , etc.) are found in the

3. Laminar flame calculations

other laminar premixed flames (n-heptane, n-decane, n-dodecane and “Aachen” surrogate) shown in Figs. 8a-h. Additionally, the peak of HRR in general aligns close to the peak of the product $X_{\text{CH}_2\text{O}} \times X_{\text{OH}}$ at the various equivalence ratio conditions of the laminar premixed flames studied. Although the HRR overall correlates with the product $X_{\text{CH}_2\text{O}} \times X_{\text{OH}}$ for the single component fuel’s flames (Figs. 9a-c), it is not well represented by the product $X_{\text{CH}_2\text{O}} \times X_{\text{OH}}$ for “Aachen” fuel surrogate’s flames, especially at lean conditions where the product $X_{\text{CH}_2\text{O}} \times X_{\text{OH}}$ underestimates HRR (Fig. 9d). Figure 10 compares the species, T and HRR with the various fuels’ flames at the stoichiometric condition. Note that the relative profiles characteristics (magnitude, width, etc.) may be related to the corresponding detailed mechanism applied, which for ethanol and dodecane flames was from Ranzi et al. [190]; for heptane flames was from Held et al. [191]; and for decane and “Aachen” surrogate was from Honnet et al. [192]. The profiles obtained from the same mechanism align close to each other. The temperature for the heptane flame shows a smaller slope than the others. OH curves show a similar gradient for all the flames. The lowest molar fraction of CH_2O was shown for the heptane flame, where the width of CH_2O is the largest. The ethanol flame has a higher $X_{\text{CH}_2\text{O}}$ than the dodecane flame. The decane flame has the largest $X_{\text{CH}_2\text{O}}$ among all these flames. The HRR in general shows a larger value for a higher carbon number fuels (e.g. in descending order: dodecane, decane, heptane and ethanol), except for the “Aachen” surrogate where HRR is the lowest. Finally, the area covered by the normalised product $X_{\text{CH}_2\text{O}} \times X_{\text{OH}}$ is compared with the area of normalised HRR at a range of equivalence ratios for all fuels (Fig. 11). It shows that the percentage of the normalised HRR covered by the normalised product $X_{\text{CH}_2\text{O}} \times X_{\text{OH}}$ lies in between 70-105%, and in some fuels (heptane, dodecane and “Aachen” sur.) the value increases with equivalence ratio.

3.2 Counterflow non-premixed gas flames

3.2.1 Background and equations

Counterflow non-premixed gas flames calculations of ethanol, heptane and n-decane were performed in mixture fraction space at a range of strain rates until extinction. Detailed mechanisms (Marinov et al. [194] for ethanol flames, Held et al. [191] for

3. Laminar flame calculations

heptane flames, and Honnet et al. [192] for n-decane flames) and transport properties were applied. The governing equations are:

(1) the energy equation

$$\frac{\partial T}{\partial t} = \frac{\chi_{st}}{2} \frac{\partial^2 T}{\partial \xi^2} - \sum_{i=1}^N \frac{h_i w_i}{c_p \rho} \quad \text{Eq. 14}$$

(2) the species equations

$$\frac{\partial Y_i}{\partial t} = \frac{\chi_{st}}{2} \frac{1}{Le_i} \frac{\partial^2 Y_i}{\partial \xi^2} - \frac{w_i}{\rho}, \quad i = 1, \dots, I \quad \text{Eq. 15}$$

where ξ is the mixture fraction, defined by Bilger, $\xi = \frac{Y_f - Y_{f,2}}{Y_{f,1} - Y_{f,2}}$, and subscript 1 and 2 stands for the fuel stream and air stream respectively. ξ expresses the fraction of mass in a sample that originated from the fuel nozzle. χ , the scalar dissipation rate, is defined as

$$\chi = 2D_\xi \nabla \xi \cdot \nabla \xi \quad \text{Eq. 16}$$

where D_ξ is the mixture diffusivity.

χ can be related the strain rate, a , by the following equation:

$$\chi = \frac{a}{\pi} \exp(-2[\text{erf}^{-1}(1 - 2\xi)]^2) \quad \text{Eq. 17}$$

where erf is the error function. The strain rate a is set as an input parameter instead of χ in the counterflow calculations performed using the COSILAB software [189].

3.2.2 Laminar flame structure

Beginning with heptane flames, results from the counterflow non-premixed flame calculations at two strain rates conditions in terms of mole fractions (X) vs. mixture fraction (ξ) are plotted in Figs. 12a-b. C_2H_2 is plotted here as an indicator of soot precursors. Formaldehyde is present in the fuel-rich region, with X_{CH_2O} increasing from $\xi = 1$ toward the stoichiometric ξ_{st} ($\xi_{st} = 0.062$ for heptane), decreases sharply close to ξ_{st} , and is not present at all in the lean side. In contrast, X_{OH} peaks near ξ_{st} just before the temperature and the formaldehyde peaks. At the higher strain rate shown,

3. Laminar flame calculations

$X_{\text{CH}_2\text{O}}$ reaches its maximum around $\xi = 0.4$, and the values are higher compared to the low strain rate. C_7H_{16} and C_2H_2 are present in the fuel rich region, but the overlap between these species and OH is minor. This suggests that any fuel or PAH fluorescence will not coincide with the OH-containing region.

Figures 12c-d shows the OH and CH_2O normalised by their peak values and includes the similarly normalised HRR and the normalised product of $X_{\text{CH}_2\text{O}} \times X_{\text{OH}}$. It can be seen that the HRR curve (circle) contains the curve showing the product $X_{\text{CH}_2\text{O}} \times X_{\text{OH}}$ (cross) (Figs. 12c-d). The reaction pathway analysis shows that high percentage of CH_2O originates from the decomposition of the methoxy radical ($\text{CH}_3\text{O} + \text{M} \Rightarrow \text{CH}_2\text{O} + \text{H} + \text{M}$) and from CH_3 ($\text{CH}_3 + \text{O} \Rightarrow \text{CH}_2\text{O} + \text{H}$). Also, formaldehyde is consumed by H-atom abstraction reaction mainly through the reaction $\text{CH}_2\text{O} + \text{H} \Rightarrow \text{HCO} + \text{H}_2$ and $\text{CH}_2\text{O} + \text{OH} \Rightarrow \text{HCO} + \text{H}_2\text{O}$. At low strain rate, the reaction $\text{CH}_3 + \text{O} \Rightarrow \text{CH}_2\text{O} + \text{H}$ and $\text{CH}_3\text{O} + \text{M} \Rightarrow \text{CH}_2\text{O} + \text{H} + \text{M}$ is seen approximately in the region $\xi = 0.066$ to $\xi = 0.097$, and the reaction $\text{CH}_2\text{O} + \text{OH} \Rightarrow \text{HCO} + \text{H}_2\text{O}$ is mostly observed in mixture fraction space from $\xi = 0.070$ to $\xi = 0.099$. This region correlates well with the product $X_{\text{CH}_2\text{O}} \times X_{\text{OH}}$ region. However, due to the consumption of CH_2O in the lower mixture fraction region, the discrepancy between HRR and the product $X_{\text{CH}_2\text{O}} \times X_{\text{OH}}$ is high and the heat release rate comes mainly from other reactions (such as $\text{CO} + \text{OH} \Rightarrow \text{CO}_2 + \text{H}$, $\text{HO}_2 + \text{OH} \Rightarrow \text{H}_2\text{O} + \text{O}_2$). Thus, at low strain rate, the HRR is not quantitatively represented by the product $\text{CH}_2\text{O} \times \text{OH}$: the latter could only contribute around 50% of the true HRR. In contrast, at high strain rate, the two quantities are quite close. A further observation is that the OH peaks at the lean side of the HRR peak, while for both low and high strain rates the peak $\text{CH}_2\text{O} \times \text{OH}$ coincides with the HRR peak. Unlike the strong variation of CH_2O with strain rate, the OH curve and levels do not vary too much, although a decrease in the peak OH is evident.

Figures 12e-f shows the normalised HRR plotted vs. the normalised $\text{CH}_2\text{O} \times \text{OH}$ and vs. the normalised $(\text{CH}_2\text{O} + \text{C}_7\text{H}_{16}) \times \text{OH}$ for a range of strain rates. It is evident that for high strain rate the correlation is high and that there is likely no effect from any fuel fluorescence. As the strain rate decreases, it is evident that the product underestimates the heat release, however it can still be used as a spatial marker of the

3. Laminar flame calculations

location of a large fraction of the heat release.

Figure 13 shows the results from ethanol counterflow non-premixed flames. Similar to the observation in heptane flames, OH (green curve) is almost unchanged for the various strain rates of ethanol flames (Figs. 13a-b) and peaks close to the stoichiometric mixture fraction line ($\xi_{st,E} = 0.1$). CH₂O, however, is quite different compared to the one shown in heptane flames. There are two peaks in CH₂O (blue) of ethanol flames (Figs. 13a-b). One lies in the main reaction zone as shown previously in heptane flames, the other peak lies in the fuel rich region at around $\xi = 0.5$. The latter is more dominant. The quantity of peak X_{CH_2O} shown in the reaction zone is minor compared with the one in the fuel rich zone. Thus the CH₂O measurement at the reaction zone could suffer the drawback of low signal to noise ratios. However, the peak in the fuel rich zone never coincides with OH; hence the product of CH₂O and OH peaks in the reaction zone and could be potentially applied to mark the main HRR in the reaction zone.

The normalised quantities of OH, CH₂O, the product CH₂O × OH and the HRR are plotted in Figs. 13c-d for various strain rates conditions. The peak of product CH₂O × OH (black) overlaps with the peak HRR (red) at both low and high strain rate conditions, similar to the results from heptane flames. Additionally, the outline of CH₂O (blue) lies close to the stoichiometric mixture fraction iso-line (pink) at all strain rates. Finally, the normalised HRR and the product CH₂O × OH are compared in Fig. 13e at various strain rates. It shows that the HRR is not quantitatively represented by the product CH₂O × OH, and that the correlation between normalised product CH₂O × OH and the normalised HRR is not strong especially at lean side of ξ_{st} for both low and high strain rate conditions.

The similar plots of n-decane counterflow non-premixed flames at low and high strain rates are shown in Figs. 14a-e. The conclusions are similar as the one from the previous flames of heptane: OH does not vary too much at low and high strain rates and peaks around the stoichiometric line; CH₂O is found on fuel rich region, and its outline coincides with stoichiometric line at both strain rates (Figs. 14a-d); and HRR is correlated with the product CH₂O × OH (Fig. 14e) at high strain rates, however, at low strain rates, the HRR is not represented by the product CH₂O × OH for both lean

3. Laminar flame calculations

and rich sides of the stoichiometric line, and the correlation between the two variables is worse.

Finally, the flame structure of the various fuels is compared at low and high strain rates in Figs. 15a-d in terms of T , $X_{\text{CH}_2\text{O}}$, X_{OH} and HRR. The profiles of T and OH are similar within these fuels. Ethanol flames show a higher peak value of X_{OH} and a wider profile of OH than the others; whereas heptane flames has the lowest peak value of X_{OH} and a narrower width than the other fuels' flames. Both the amount of CH_2O and the HRR increase evidently at the higher strain rate for all the fuels. In the main reaction zone ($\xi \in (0, 0.2)$, where the main HRR lies in), $X_{\text{CH}_2\text{O}}$ shows the highest and lowest peak value for decane and ethanol flames respectively; however, in the fuel rich region, ethanol flames have the largest molar fraction of CH_2O . The overlap between CH_2O and OH in the fuel rich region is minor for all three fuels. When compared the area of overlap region of CH_2O and OH (normalised by the peak product $\text{CH}_2\text{O} \times \text{OH}$) with the area of HRR region (normalised by the peak HRR) from low to high strain rates conditions for all the fuels non-premixed flames, it is evident (Fig. 15e) that percentage of HRR represented by the product $\text{CH}_2\text{O} \times \text{OH}$ increases with the strain rate for each fuel (e.g. for ethanol flames, the ratio $\approx 65\%$ and 85% at strain rate of 50 s^{-1} and 800 s^{-1} separately). It suggests the product $\text{CH}_2\text{O} \times \text{OH}$ represents the HRR better at conditions close to extinction.

3.2.3 Strain rate at blow-off

Figure 15f compares the peak temperatures at a range of strain rates of ethanol, heptane and n-decane flames from the counterflow non-premixed flame calculations. It shows that the peak temperature decreases as the strain rate increases, until at the extinction strain rate that the temperature drops sharply to the inlet temperature, indicating flame extinction at this strain rate. A relatively higher temperature is shown with a higher carbon number fuel under the same strain rate condition. Additionally, it shows that the extinction strain rate of decane flames is higher than ethanol flames and heptane flames. The result suggests that with a higher peak temperature, the higher carbon number fuel is more resistant to flame extinction.

3.3 Conclusions

This chapter described laminar gaseous flame calculations of two configurations: freely propagating premixed flames and counterflow non-premixed flames in mixture fraction space. Detailed mechanism and transport properties were applied for ethanol, heptane, n-decane and n-dodecane flames. Laminar flame structure at various equivalence ratios (for premixed flames) and various strain rates (for non-premixed flames) are obtained. The simulations indicate that for premixed flames, OH forms at high temperature region and also presents in post-reaction zone. For non-premixed flames, OH profile is thin and peaks close to the stoichiometric line. Its width is not sensitive to the change of strain rates. CH₂O forms at low temperature zone and is consumed at high temperature zone in premixed flames. For non-premixed flames, CH₂O presents at fuel rich region. The outline of CH₂O aligns close to the stoichiometric mixture fraction line at all the strain rates investigated. The simulations suggest that the product $X_{\text{CH}_2\text{O}} \times X_{\text{OH}}$ marks relatively well the spatial location of the heat release in both premixed and non-premixed flames of each fuel applied in the current study, although, the latter is not quantitatively represented by the former especially for the lean and the low strain rate conditions. The counterflow non-premixed calculations also suggest the flame of higher carbon number fuel has a higher extinction strain rate than the lower carbon number fuels.

3.4 Figures for Chapter 3

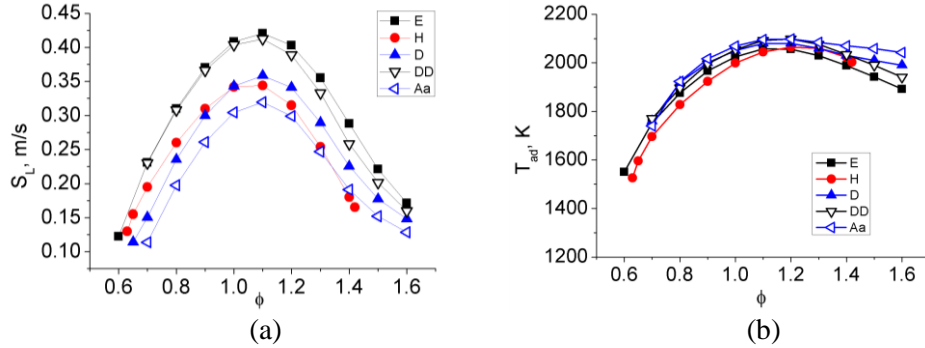


Figure 6. Laminar flame speeds (a) and adiabatic flame temperatures (b) at various equivalence ratios obtained from the laminar premixed flame simulations of the various fuels: ethanol (E, Ranzi et al. mechanism [190]); heptane (H, Held et al. mechanism [191]); decane (D, Honnet et al. mechanism [192]); dodecane (DD, Ranzi et al. mechanism [190]); and Aachen fuel surrogate (Aa, Honnet et al. mechanism [192]).

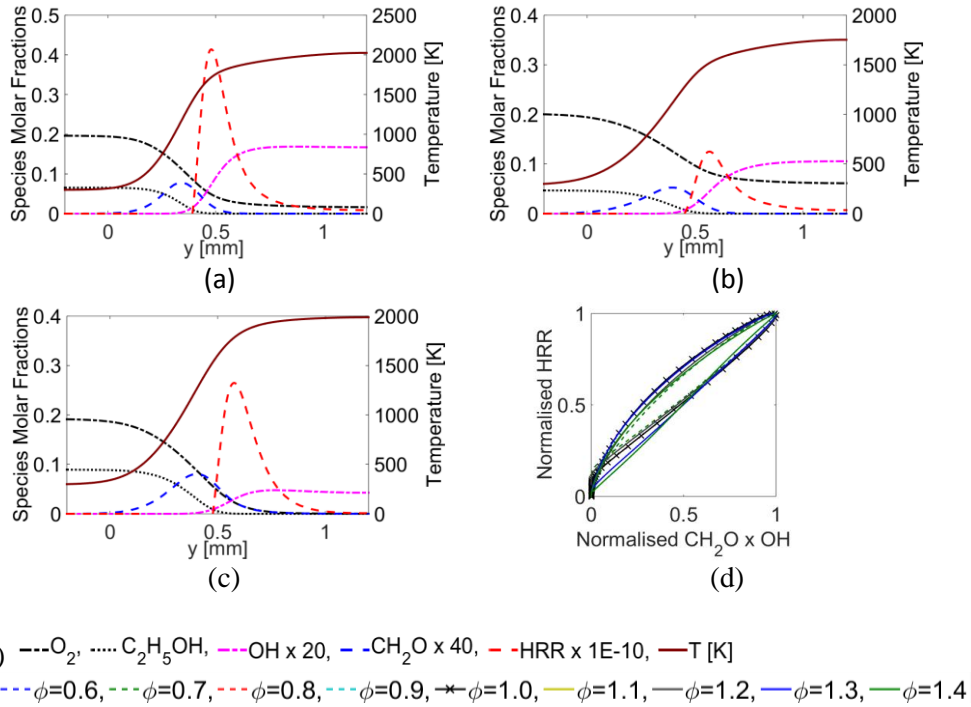


Figure 7. Laminar premixed flame calculations of ethanol flames: temperature, heat release rate (HRR), and molar fraction of O_2 , $\text{C}_2\text{H}_5\text{OH}$, OH and CH_2O at (a) stoichiometric, (b) lean ($\phi=0.7$), and (c) rich ($\phi=1.4$) conditions; and (d) the correlation between the HRR and the product $\text{CH}_2\text{O} \times \text{OH}$ for a range of equivalence ratios ($\phi = 0.6 \sim 1.4$).

3. Laminar flame calculations

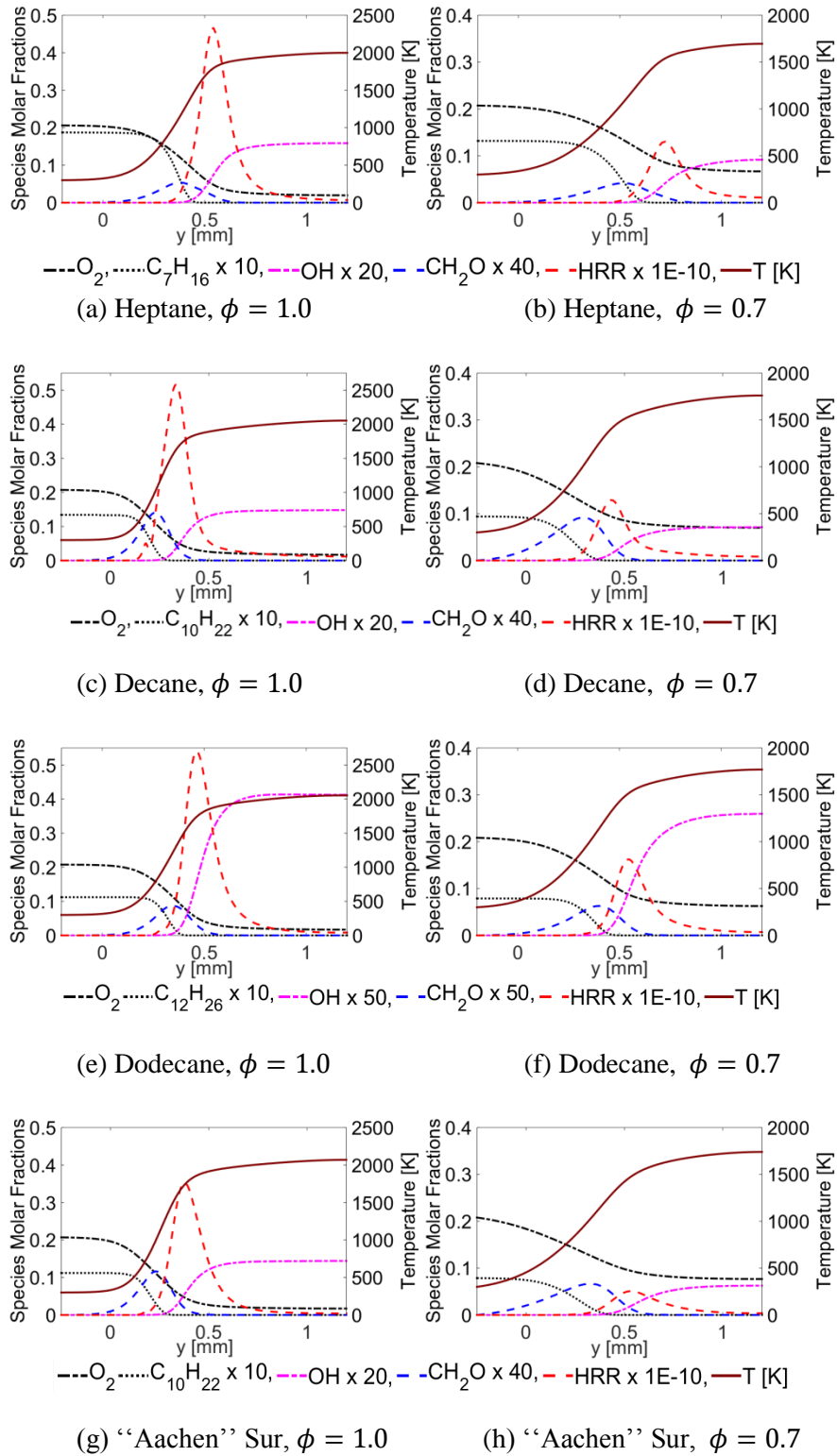


Figure 8. Laminar premixed flame calculations of (a-b) heptane, (c-d) decane, (e-f) dodecane and (g-h) "Aachen" fuel surrogate: the temperature, HRR, and molar fraction of O_2 , C_7H_{16} , OH and CH_2O profile at (left) stoichiometric and (right) lean ($\phi=0.7$) conditions.

3. Laminar flame calculations

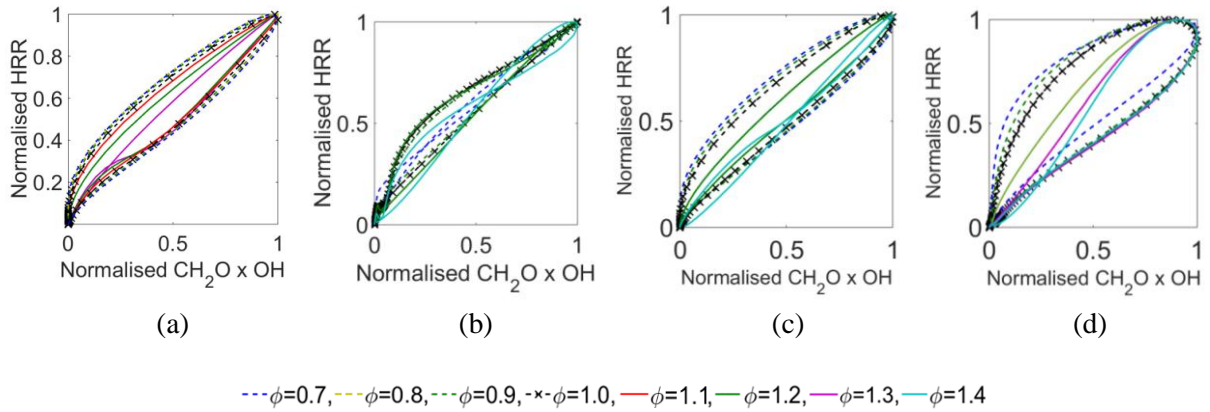


Figure 9. Laminar premixed flame calculations of (a) heptane, (b) decane, (c) dodecane and (d) “Aachen” fuel surrogate: the correlation between the normalised HRR and normalised product $\text{CH}_2\text{O} \times \text{OH}$ for a range of equivalence ratios ($\phi = 0.7 \sim 1.4$).

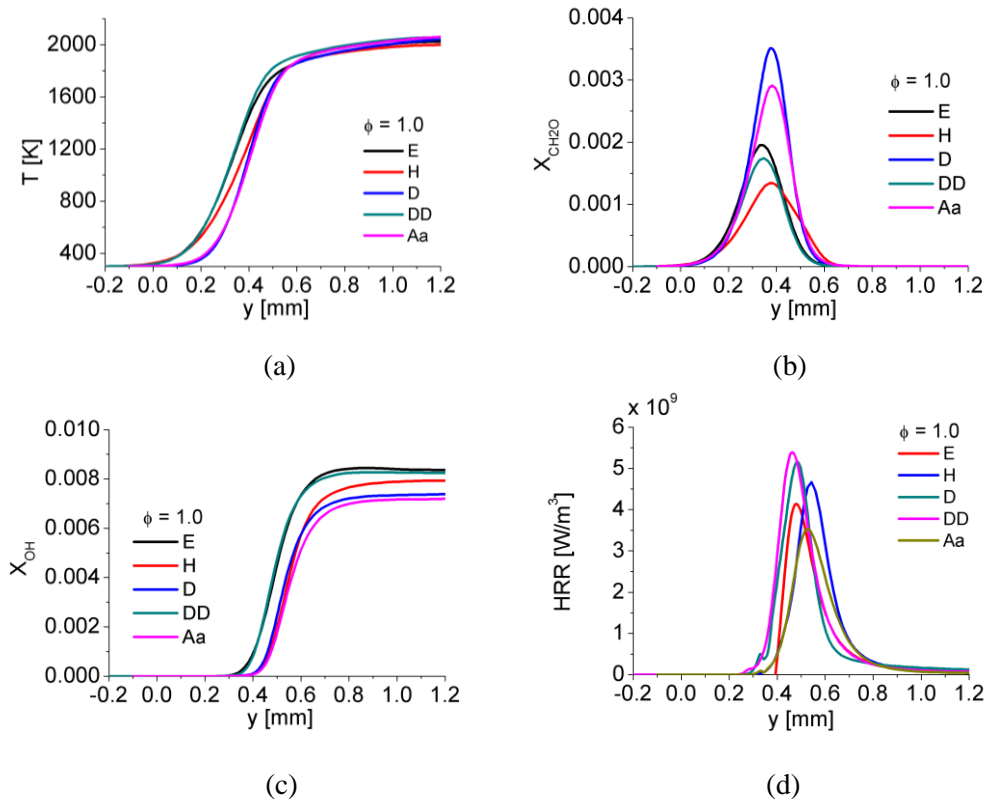


Figure 10. Comparison of the temperature (a); molar fraction of CH_2O (b) and OH (c); and HRR (d) obtained from the laminar premixed flame calculations of ethanol (E), heptane (H), decane (D), dodecane (DD), and “Aachen” fuel surrogate (Aa) at the stoichiometric condition.

3. Laminar flame calculations

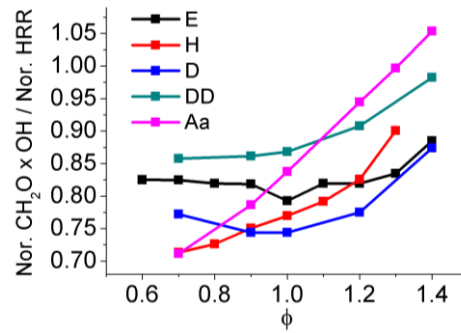
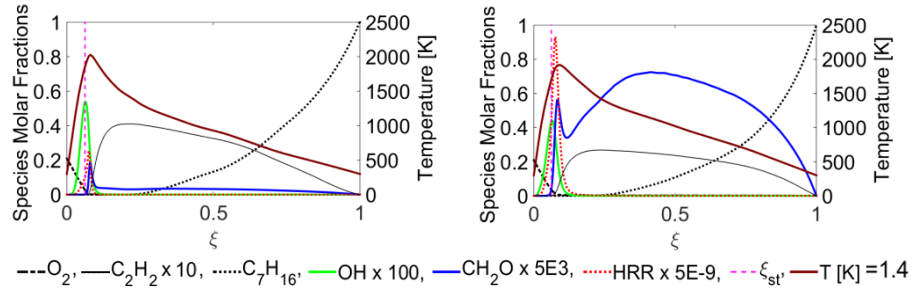


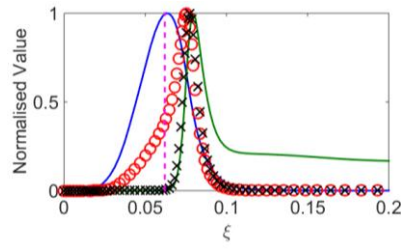
Figure 11. Percentage of the normalised area of HRR represented by the normalised area of product $\text{CH}_2\text{O} \times \text{OH}$ for a range of equivalence ratios of the laminar premixed flames of the four fuels.

3. Laminar flame calculations

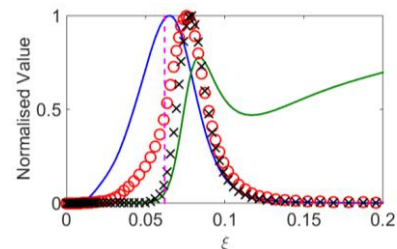


(a) $a = 100 \text{ s}^{-1}$

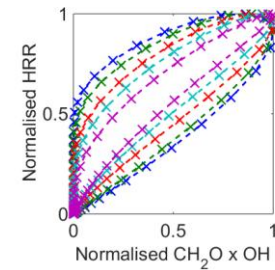
(b) $a = 500 \text{ s}^{-1}$



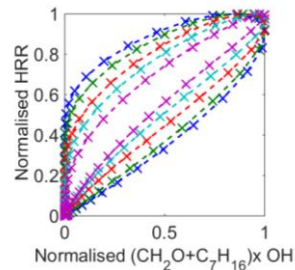
(c) $a = 100 \text{ s}^{-1}$



(d) $a = 500 \text{ s}^{-1}$



(e) $a = [50 \sim 700] \text{ s}^{-1}$



(f) $a = [50 \sim 700] \text{ s}^{-1}$

Figure 12. Laminar counterflow non-premixed flames simulations of heptane: i. temperature and various species molar fractions vs. mixture fraction for strain rate (a) 100 s^{-1} and (b) 500 s^{-1} ; ii. normalised mole fractions of OH and CH_2O , normalised HRR, and normalised $X_{\text{CH}_2\text{O}} \times X_{\text{OH}}$ at strain rate (c) 100 s^{-1} and (d) 500 s^{-1} ; and iii. HRR vs. $X_{\text{CH}_2\text{O}} \times X_{\text{OH}}$ (e), and HRR vs. $(X_{\text{CH}_2\text{O}} + X_{\text{C}_7\text{H}_{16}}) \times X_{\text{OH}}$ (f) for the indicated strain rate.

3. Laminar flame calculations

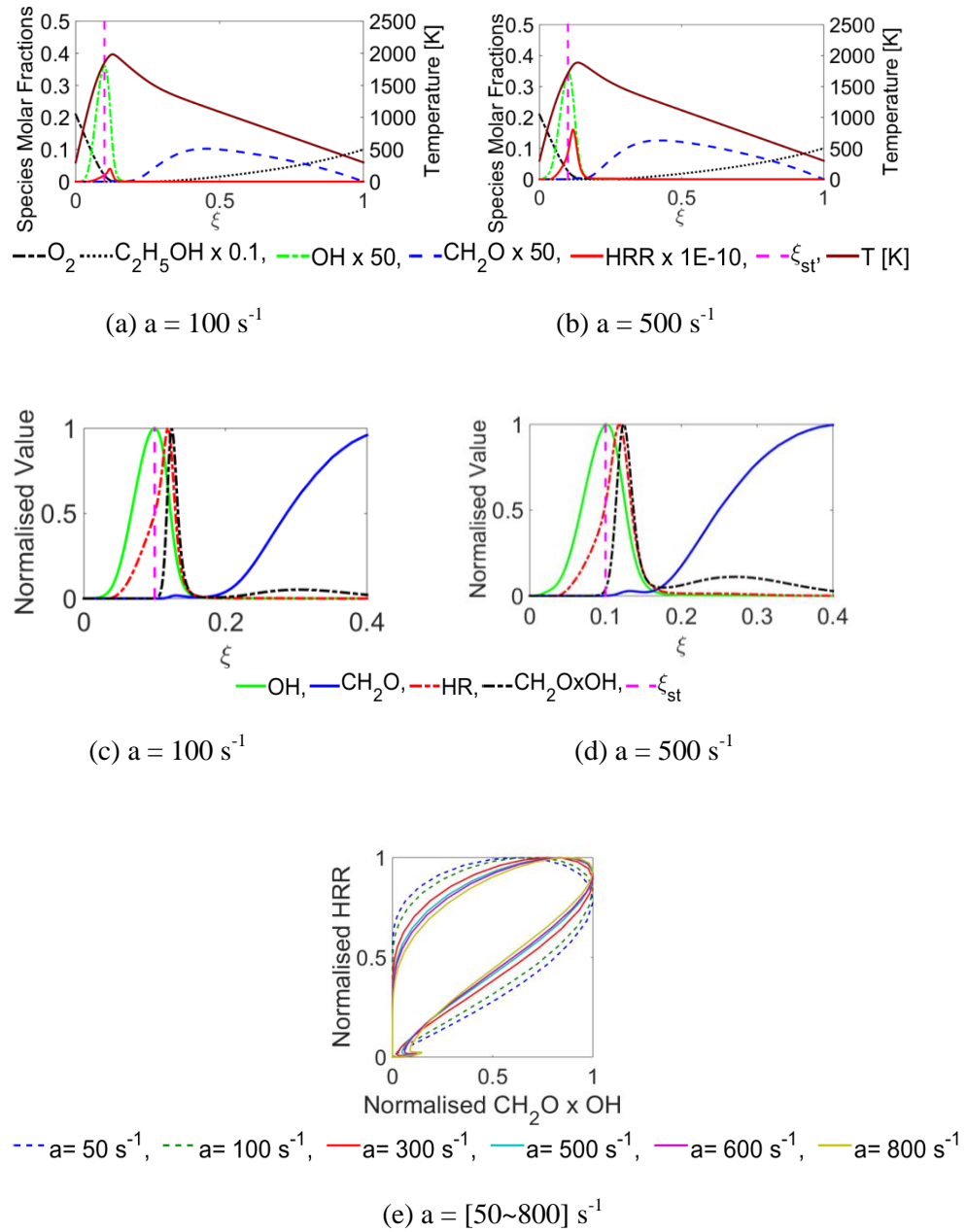


Figure 13. Laminar counterflow non-premixed gas flames simulations of ethanol: i. temperature and various species molar fractions vs. mixture fraction for strain rate (a) 100 s^{-1} and (b) 500 s^{-1} ; ii. normalised mole fractions of OH and CH_2O , normalised HRR, and normalised $X_{\text{CH}_2\text{O}} \times X_{\text{OH}}$ at strain rate (c) 100 s^{-1} and (d) 500 s^{-1} ; and iii. HRR vs. $X_{\text{CH}_2\text{O}} \times X_{\text{OH}}$ (e) for the indicated strain rate.

3. Laminar flame calculations

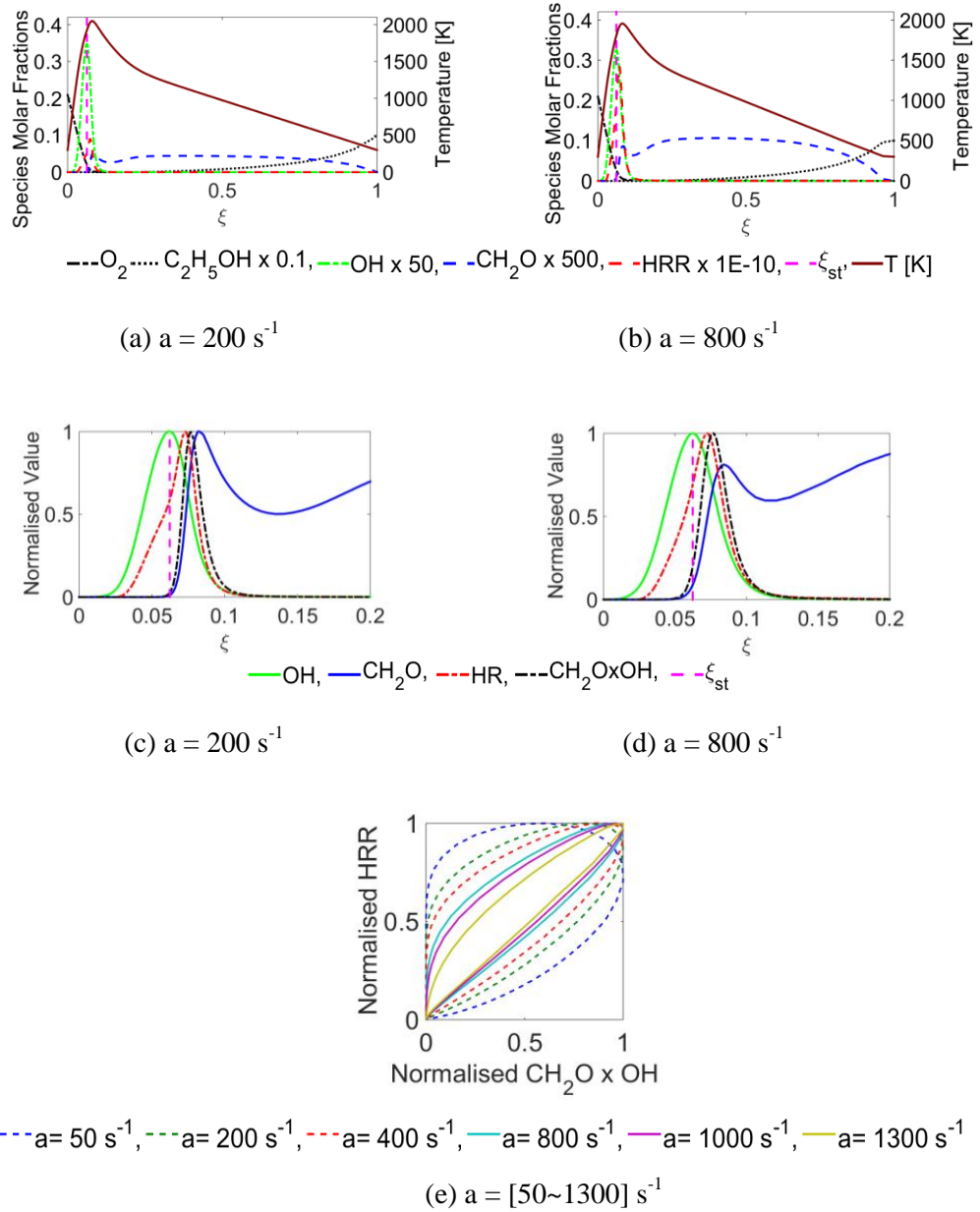


Figure 14. Laminar counterflow non-premixed gas flames simulations of n-decane: i. temperature and various species molar fractions vs. mixture fraction for strain rate (a) 200 s^{-1} and (b) 800 s^{-1} ; ii. normalised mole fractions of OH and CH_2O , normalised HRR, and normalised $X_{\text{CH}_2\text{O}} \times X_{\text{OH}}$ at strain rate (c) 200 s^{-1} and (d) 800 s^{-1} ; and iii. HRR vs. $X_{\text{CH}_2\text{O}} \times X_{\text{OH}}$ (e) for the indicated strain rate.

3. Laminar flame calculations

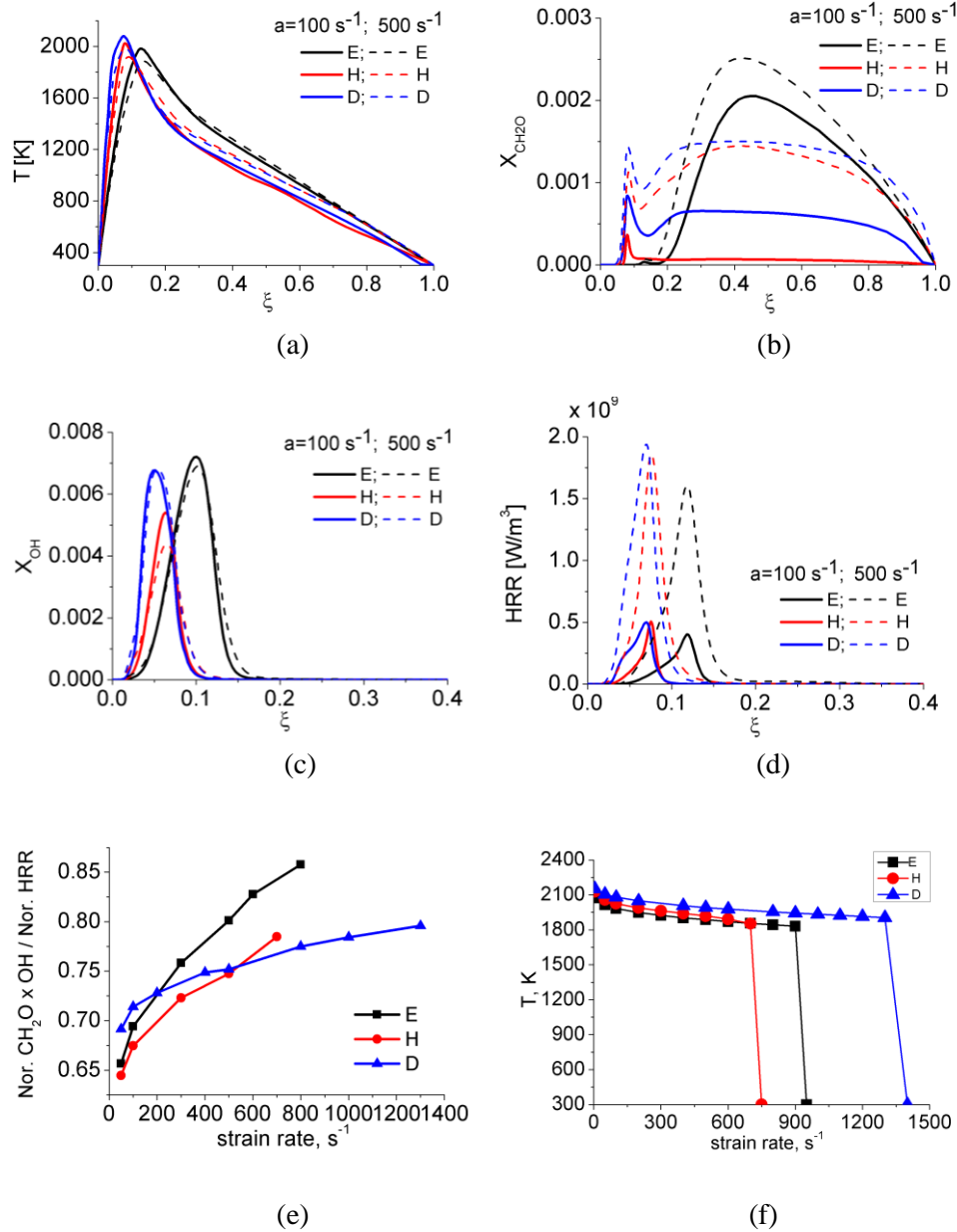


Figure 15. Comparison of the temperature (a); molar fraction of CH_2O (b) and OH (c); and HRR (d) obtained from the laminar counterflow non-premixed flame calculations of ethanol (E), heptane (H), and decane (D) at low (solid lines; $a=100\text{ s}^{-1}$) and high (dash lines; $a=500\text{ s}^{-1}$) strain rate conditions; (e) percentage of the normalised area of HRR represented by the normalised area of product $\text{CH}_2\text{O} \times \text{OH}$ for a range of strain rates these fuels; and (f) peak temperatures vs. strain rates of laminar counterflow non-premixed flames of ethanol (E, Marinov et al. mechanism [194]), heptane (H, Held et al. mechanism [191]), and n-decane (D, Honnet et al. mechanism [192]).

Chapter 4

Spray flame blow-off:

Flame Structure

This chapter discusses experimental observations on the blow-off limit and the flame structure of swirling spray flames of various volatility fuels (ethanol, heptane, decane and dodecane) at conditions far from and close to blow-off, and at the blow-off event. The “Aachen” fuel surrogate suffers difficulty in the ignition process in the current spray burner. For this reason, this fuel is not further used in experimental measurements in this work. The mechanism of swirling spray flame blow-off has not been discussed much in the literature. The main objectives of this chapter are to provide more information on the behaviour and flame structure of swirling spray flames before and at blow-off, and to reveal the differences and similarities in the spray flame behaviour among the various volatility fuels used.

4.1 Experimental methods and data analysis

The apparatus and the diagnostic techniques are described in Ch.2. The flow

4. Spray Flame Blow-off: Flame Structure

conditions investigated for most of the experiments are summarised in Table 1. Codes “S” imply stable flames, while codes “B” imply flames at the blow-off velocity. For most flames, the fuel mass flow rate was 0.27 g/s, but some experiments were also done at different fuel flow rates. Table 2 includes these test conditions and the respective diagnostic methods applied. To account for the difference in atomisation process with altering the fuel and fuel flow rate, Table 3 includes several parameters for characterising the atomisation process: the non-dimensional numbers of liquid Weber number We_l (describing the ratio between deforming inertial forces and stabilising cohesive forces), Ohnesorge number Oh (comparing viscous forces with inertial and surface tension forces), gaseous Weber number We_g (We_g are involved in the second wind-induced and atomisation regimes where aerodynamic forces reinforces), and the Taylor parameter Ta . The various non-dimensional parameters are calculated as follows:

$$\begin{cases} We_l = \frac{\rho_l U_l^2 D_l}{\sigma}, Oh = \frac{\mu_l}{\sqrt{\rho_l D_l \sigma}}, Re_l = \frac{\rho_l U_l D_l}{\mu_l} \\ Ta = \frac{\rho_l}{\rho_g} \left(\frac{Re_l}{We_l} \right)^2, We_g = \frac{\rho_g U_l^2 D_l}{\sigma} \end{cases} \quad \text{Eq. 18}$$

where U_l is the liquid jet velocity at the nozzle exit, U_b the air bulk velocity at the annulus, D_l the nozzle diameter at its exit, D the bluff body diameter, ν_l and ν_g are the kinematic viscosity of liquid and gas, respectively, σ_l is the liquid surface tension coefficient, and ρ_l and ρ_g are liquid and gas density, respectively. To evaluate the droplet breakup mechanisms, the local Weber number based on local quantities should be appropriate. However, local We_l varies from location to location. Thus, the We_l reported in this work was evaluated at the exit of the fuel injector. Given that the gas velocity at the fuel jet exit is negligible compared to the liquid velocity, the relative velocity employed in the We_l equation was taken as U_l . The physical properties of the fuels and air are evaluated at 20°C. Shown in Table 3, that for most of the cases in the current work, We_l lies in the range 800 ~ 1100, and We_g lies in the range 1.2 ~ 2.0. According to Lin and Reitz [195], the primary breakup of the spray studied could fall

4. Spray Flame Blow-off: Flame Structure

into the first wind-induced breakup regime. The Ohnesorge number of the spray in the current study is low and lies in the range $0.016 \sim 0.024$. For low $Oh < 0.1$, multiple satellite droplet formation is usually observed instead of a single droplet [196]. Further, Oh and Re_l are also used together to determine the governing breakup regimes [197–199], from which it is suggested that at intermediate Re_l number of the current study, the breakup of the jet is assisted by the aerodynamic forces, and lies in the first wind-induced breakup regime [198,199]. Additionally, Oh , We_g , and Ta are used in the secondary break-up models [200–202] to determine parameters of the unstable disturbance.

The droplet size and velocity profiles in the flow field were measured by a LDA/PDA system. The relative information about the collection is given in Ch.2. For each location, droplet SMD, and the mean and the variance of axial and radial velocities are evaluated.

OH^* was measured at 5 kHz to locate the HR zone of stable flames and unstable flames during the blow-off transient process. To compare the HR image for the various fuels, the OH^* were captured at the same flow conditions of air (600 SLPM) and fuel mass flow rate (0.27 g/s) for each of the fuels. The corresponding flames are named as E1S1, H1S1, D1S1 and DD1S2, respectively. Secondly, spray flames with identical fuel loading were examined at several air bulk velocities at far from (S1) and close to (S2) blow-off, and at the blow-off condition (B). Finally, to evaluate fuel loading effect on heat release for both stable and unstable (blow-off) flames, OH^* were taken at several fuel flow rates with air bulk velocity fixed or at the corresponding U_B . To obtain the 2D heat release image from the line-of-sight OH^* images, inverse Abel transform was applied to the mean images of OH^* , with the assumption of the axisymmetric behaviour of the original projected mean images.

To visualise the dynamics of the spray flame front, OH-PLIF was performed at 5 kHz. OH-PLIF was taken at each fuel at a constant fuel loading (0.27 g/s) from stable flames (S1, S2) to blow-off (B). The transient event at blow-off was also visualised with OH-PLIF. During data processing, each individual image was filtered with a 2-D median non-linear filter for noise reduction (3×3 filter size) and then applied with inhomogeneity of laser sheet profile correction. The lift-off heights of OH images are

4. Spray Flame Blow-off: Flame Structure

discussed in Ch.5.

Mie imaging was taken at 5 kHz at stable and unstable flames of each fuel to locate spray location. The binary image of the instantaneous Mie image was calculated and then averaged to obtain the mean Mie scattering image.

Another active scalar visualised in the current study is CH_2O with the potential to outline the stoichiometric mixture fraction iso-line of the flames, while the simultaneously measured PLIF of OH and CH_2O have also shown advantages in marking the main heat release zone. The imaging technique and data processing was discussed in Ch. 2.4.1.

4.2 Results and Discussion

This section presents results on the structure and stability of spray flames at conditions far from, close to and at the blow-off event. Firstly, the blow-off limits are shown. Next, PDA results are discussed for the four fuels. Following that, images from OH*, joint CH_2O -OH PLIF, OH-PLIF and Mie scattering are shown and discussed. The dynamic behaviour in terms of the blow-off transient duration, the lift-off height statistics, the topology of the OH islands and the POD analysis and the corresponding motion are to be discussed in Ch. 5 as additional measures that can help with the validation of combustion models focusing on capturing extinction.

4.2.1 Stability limits

Figure 16 shows the lean blow-off limits obtained for the current set-up. “E1” etc (horizontal direction) stands for different fuel flow rates, while ‘S’ and ‘B’ indicates stable condition and blow-off condition, respectively. “S1”, “S2” (vertical direction) stands for different air flow rates (and hence distances from the blow-off condition). The stable flames are shown with open symbols. Because of the stochastic nature of blow-off, the bulk velocity value at blow-off (U_B) in the figure is an average value of ten blow-off events. The standard deviation of blow-off bulk velocities normalised by the mean value is around 0.02.

The trend of the blow-off limit for each fuel is consistent. In general, as the fuel flow rate (\dot{m}_f) increases, the blow-off air velocity increases, especially for the flames

4. Spray Flame Blow-off: Flame Structure

of the low-volatile fuels (n-decane and n-dodecane), for which the positive correlation observed between U_B and \dot{m}_f is stronger. A slightly different behaviour is shown in the blow-off curves of the more volatile fuels (ethanol and n-heptane), where U_B seems to present a levelling-off in the intermediate fuel mass flow rate (0.35-0.45 g/s for ethanol flames, 0.2-0.35 g/s for heptane flames). This trend for heptane was also observed by Cavaliere et al. [6].

4.2.2 Flame appearance

Figure 17 shows photographs of stable flames for the four fuels. A typical feature of all flames is a double structure, with an inner region aligned with the spray cone and forming an apex at the injector, and an outer flame attached to the corner of the bluff-body. The ethanol flame is purple-blue, while the others appear overall blue and with soot, which increases as the molecular mass of the fuel increases. The soot-containing region seems to lie between the inner and the outer flame branches, and from above the bluff-body surface to the flame tip downstream. There is also a slight asymmetry, which could be related to the non-axisymmetry in the spray indicated by instantaneous Mie images (discussed later). The inner flame zone appears a little lifted from the injector exit, especially for the ethanol flames. For decane and dodecane, the first mm of the conical spray is also evident (illuminated by the flame itself).

The outer flame zone starts from the bluff-body edge and shows intermittent lift-off, which will be quantified through analysis of the OH-PLIF images later. The stable flame height of decane and dodecane is higher than that of the other fuels, probably because the spray traverses a longer length due to a larger mean droplet size (given by PDA measurements discussed later) and the lower volatility.

4.2.3 Droplet size and velocity distributions

Figures 18-22 show the results from PDA measurements for stable flames far from and close to blow-off for the four fuels. Some additional data can be found in the appendix of the thesis. Figure 18(a) shows the radial distribution of SMD (also noted as D_{32}) measured at four different axial distances (Z) corresponding to (0.4, 0.8, 1.2, 1.6) Z/D , (D is the bluff-body diameter), in two stable ethanol flames at conditions far from (E1S1) and close to (E1S2) blow-off, respectively. The two cases have the

4. Spray Flame Blow-off: Flame Structure

same fuel flow rate but different air bulk velocities. For all Z/D , only few droplets exist at radial locations larger than $1.2D$. At small Z/D , the location of the peak SMD is aligned with the hollow-cone spray path, where the maximum data rate is also observed. At longer distances downstream, the SMD is more uniform, with a smaller value obtained at locations close to the flame zone. The SMD measured for the two conditions (E1S1 and E1S2) are similar with the peak value close to spray jet around $70 - 80 \mu\text{m}$, although a smaller SMD is obtained at outer flame zone (i.e. $x/D \approx 0.56$, $Z/D = 0.4$) at the lower velocity case (E1S1). This may be due to the more complete combustion that provides faster evaporation. In addition, a larger SMD value is found at downstream locations. This is reasonable as the droplets with a larger diameter have a larger inertia and travel further, while the droplets with a smaller diameter are mostly consumed by combustion or captured by the recirculating gases, both of which shift the SMD to higher values as we go downstream. Finally, we mention that a unimodal distribution of droplet sizes was found at all the locations measured (not shown here). However, at high Z/D the size distribution for the larger SMD cases was slightly clipped at the cut-off ($\geq 100\mu\text{m}$) from the PDA collection settings, which will result in the shown SMD underestimating the real mean value.

Figure 18b shows that the droplet mean axial velocity (\bar{U}), for all Z/D , peaks at a location off-axis, and experience shows that this location overlaps with the maximum data rate location. At $Z/D=0.4$ (black line), \bar{U} is still positive at the centreline ($x/D=0$). At higher Z/D , \bar{U} along the centreline becomes close to zero, and the velocity probability density function becomes bimodal (not shown here). At $Z/D=1.6$, very few droplets were collected at the axis and the region nearby. As we go outwards towards the annular air stream, \bar{U} decreases and becomes negative at the flame zone, but further into the outer annular air \bar{U} becomes positive. Along the vertical direction, \bar{U} is maximised near the nozzle exit and decreases downstream. At the condition close to blow-off (filled symbols), \bar{U} is smaller in the region inside of the annular jet compared to the condition far from blow-off (empty symbols) due to the fact that the spray is injected with the same velocity (since the fuel flow rate is the same), but the air velocity is higher and so is, presumably, the velocity of the recirculating gases that decelerate the droplets. Where the droplets are captured by the fast annular air stream,

4. Spray Flame Blow-off: Flame Structure

the droplet velocities are a similar fraction of the bulk air velocity for both cases. At these locations, all droplets are likely to follow the fast air flow (as also discussed later through conditional statistics).

Figures 18d-e show the normalised rms fluctuations of the axial and radial velocities, respectively. The axial velocity fluctuations are higher at the axis and close to the annular air jet, while they are smaller close to the spray cone (Fig. 18d). The radial velocity fluctuations are smaller at the axis and larger at both spray cone and annular air jet locations (Fig. 18e). Fig. 18f plots the anisotropy ratio (axial/radial rms fluctuations) and it is clear that there is significant anisotropy, with the axial fluctuations being several times higher than the radial ones. This has been observed before in particle-laden inert jets [203,204], attributed to the finite inertia of the carried phase, and in droplet-laden jets [128], attributed additionally to ligament formation. In the present system, we may have a combination of these effects.

Figure 19 shows the profiles of mean velocity, conditioned on the droplet sizes at three size ranges: $[10, 40) \mu m$, taken as the range most representative of the air flow since the small droplets are expected to follow the air, $[40, 80) \mu m$, and $[80, 100) \mu m$. The unconditional \bar{U} is also plotted as reference. Only few droplets were found in the range $[0, 10) \mu m$, thus the corresponding curve is not presented as it suffers from large statistical error. At the annular air stream the smaller droplets carried by the air stream tend to show a higher mean velocity than the larger droplets, however the differences between the different droplet categories are much smaller than close to the axis (small x/D). Close to the axis, the small droplets have lower velocities than the larger ones, consistent with the view that they are decelerated more by the opposing (recirculating) flow. At $Z/D=0.8$, the small droplets have negative velocity, while the larger droplets have substantially positive velocity, which also explains the very large (unconditional) fluctuations of droplet axial velocity shown in Fig. 18. At $Z/D=1.2$, all droplet classes have similar velocities, possibly due to the fact that the initial high injection momentum has been eventually reduced due to drag and to the increase in the air velocity eddy scales that suggests that even larger droplets begin to follow the air flow.

Similar data for heptane are shown in Figure 20, but now the air velocity is the

4. Spray Flame Blow-off: Flame Structure

same and the fuel flow rate is changing. Figure 20a shows that the change in fuel loading has a minor effect on the droplet SMD, although a very small decrease can be seen in the higher fuel mass flow rate (H0S0). The difference in mean axial velocity (Fig. 20b) is more obvious, with \bar{U} increasing with fuel flow rate, suggesting that the spray penetrates more for the large fuel flow rate case. It is also suggested from the literature [205] that SMD decreases as We_l increases (H0S0), consistent with the present measurements. In addition, as the initial droplet velocity increases with fuel loading, the droplet residence time is shorter in case H0S0 and hence a higher \bar{U} is probably expected at downstream locations. The radial velocity component is also smaller at the flame with the lower fuel flow rate (Fig. 20c). The fluctuations of the two velocity components are also plotted in Figs. 20d-f. The results are consistent with the previous discussion around Figs. 18d-f.

A notable difference between the ethanol and the heptane flames is the absence of droplets close to the centreline for the heptane flame. The measurements suggest that the atomiser behaves truly as a hollow-cone atomiser for heptane but not so for ethanol, which gives droplets with significant positive axial velocity along the centreline. The differences between the four fuels are further highlighted in Fig. 21. Close to the nozzle, there is evidence of droplets from the ethanol flame at the centreline and the ethanol and heptane SMD is somewhat smaller compared to the other fuels that tend to have similar SMD. At large Z/D , all fuels show very similar SMD, suggestive of large droplets that have penetrated the inner flame zone, but at $Z/D=1.2$ even the ethanol droplets have disappeared from the centreline. The SMD decreases in the radial direction as we approach the flame sheet.

Next, the mean axial velocity (\bar{U}) profiles are shown in Figs. 21e-h at four downstream stations. In general, the high volatility fuels (ethane and heptane: black and red symbols) have a higher peak velocity around the spray jet than the less volatile ones for all Z/D . However, the peak \bar{U} of the ethanol spray decreases with distance faster than the other fuels. The heptane spray has an overall highest peak \bar{U} , which is consistent with the estimated jet exit velocity U_l shown in Table 3. Finally, downstream ($Z/D=0.8, 1.2$), droplets survived from the outer flame zone are seen to have an increased \bar{U} as they are captured by the annular air stream.

4. Spray Flame Blow-off: Flame Structure

The mean radial velocity (\bar{V}) profiles are plotted in Figure 22 at four downstream locations. It shows that \bar{V} profiles of the various fuels (ethanol-black, decane-blue, and dodecane-red) at the same height overlap on each other in general, positive correlate with the radial distance, and the slope of the curves decreases as the downstream distance increases. Inside of the outer flame brush, the droplets of the various fuels have a similar mean radial velocity as it is indicated in Figs. 22a-b. The droplets decelerate close to the outer flame zone (i.e. at around $x/D = 0.4 \sim 0.6$ for the axis location of $Z/D = 0.4$) and the residual droplets accelerate again in the outer annular air stream.

4.2.4 Heat release

In this sub-section, the instantaneous and mean OH* images are discussed for each fuel at conditions far from blow-off, and for the blow-off condition. For the latter, data are used from parts of the recordings before the final extinction event, which is separately discussed in sub-section 4.2.4.2. The effect of fuel type and fuel loading is also discussed. The mean heat release (HR) is estimated from the inverse Abel transformed mean OH* chemiluminescence images. For non-premixed and spray systems the quantitative nature of chemiluminescence is questionable, hence here OH* is used only to infer the flame shape and location.

4.2.4.1 OH* of stable flame far from and approaching blow-off

Inverse Abel transformed mean OH* for stable (far from-S1 and close to-S2 blow-off) and unstable flames (at blow-off condition-B and before the blow-off transient event) of the four fuels are plotted in Figure 23 and in Fig. 24 together with OH-PLIF and Mie scattering and the instantaneous images from these measurements. The double structure of the HR zone is evident for all fuels and for all conditions: there is an inner flame and an outer flame, with the spray roughly between the two. The inner flame seems quite close to the spray, while the outer flame sheet is further outwards in the radial direction and is anchored to the corner of the bluff body in the mean. In an instantaneous basis, the inner sheet can be lifted from the apex of the spray and the outer sheet can be lifted from the corner of the bluff-body.

The mean HR zone is in general thin and becomes thicker at unstable (blow-off)

4. Spray Flame Blow-off: Flame Structure

conditions. The ethanol flame's (Fig. 23 row 1) OH* emission is lower than that from the other fuels (Fig. 23 rows 2-4), which is supported by the laminar flame simulation results shown in Fig. 15d that the HRR are lower for ethanol than that for the other fuels (heptane and decane) at both low and high strain rates. In addition, the OH* emission shows that the length of the HR zone from ethanol (Fig. 23 row 1) is shorter than that from the other fuels (Fig. 23 rows 2-4), which is also supported by the PDA results shown in Fig. 21 that \bar{U} is smaller for the ethanol flame, especially at farther downstream locations. The angle of the inner HR branch seems narrower for ethanol flames than for the others, in agreement with the previous PDA results that show a narrower ethanol spray profile.

The mean HR region of the unstable flames (Fig. 23, column 3) is smaller compared to the corresponding stable flame (Fig. 23 columns 1-2), with the outer HR zone appearing more attached to the bluff-body surface. The inner HR zone is smaller in size and has lower emission intensity, while the outer HR is widened. The area of the HR region, observed from the instantaneous images (Figs. 24a-h, rows 1 and 4, to the right), for the unstable flames (Figs. 24e-h) is smaller than the stable counterparts (Figs. 24a-d) and appears non-axisymmetric, especially for the low-volatility fuels, for which almost half of the flame is missing, consistent with a wedge-like flame slowly moving around. This suggests the quenching of the flame in the IRZ for the flames at blow-off. The OH-PLIF and Mie images are discussed later, where the breaks of the OH sheet in the inner branch shown at blow-off conditions is consistent with the loss of OH* at the IRZ in both the mean and instantaneous OH* images.

The effect of fuel loading is now examined. Figure 25 shows a clear difference of the mean HR location between different fuel loadings, suggesting the influence of spray atomisation and penetration on the main HR regions. This is in agreement with the conclusion from laminar flame calculations in Refs. [57,60] that the initial droplet velocity and size are critical to the spray flame structures in addition to the flow strain rate. The PDA results of the lowest fuel loading case (E0S0) also show a different pattern of size and velocity distributions, where the centreline has the maximum data rate and the peak \bar{U} , indicating a jet-like rather than a hollow-cone spray profile. Also, We_l is lower ($We_l = 456$) for E0S0 so that the atomisation regime could be apparently

4. Spray Flame Blow-off: Flame Structure

different from the rest of the cases. From these HR images (a-d), it can be concluded that as the injection velocity increases (E0-E5), the distance of the inner branch from the nozzle exit decreases. A larger spray angle seems to be obtained at higher Weber number conditions of E4S1 and E5S1 than the low We_l cases of E0S0 and E1S0. The HR zones in E5S1 and E4S1 are similar and slightly longer for the higher injection velocity case (E5S1).

Figures 25e-s compares the influence of fuel loading on the mean HR zone of unstable flames of ethanol (e-j), heptane (k-p) and dodecane (q-s). The fuel flow rates are indicated in Fig. 25. The bulk velocities at blow-off are different (see Fig. 16), but in general they increase with fuel flow rate. One of the common features of these unstable flames is a slightly larger area of the HR region with increasing fuel loading. In addition, the flames look more attached to the bluff-body surface with a smaller fuel loading, for all fuels.

4.2.4.2 OH* of unstable flame during the blow-off event

Figure 26 shows the sequence of OH* images of the blow-off event of the ethanol (E1B), heptane (H1B), decane (D1B) and dodecane (DD1B) flames. The time line is referred to the instant of the flame's complete disappearance and is marked above the images. A gradual decrease of the size of the HR zone is observed and the last flame fragment is usually seen around the spray injection point. The images from the low-volatility fuels (decane and dodecane) present a distinctive asymmetric pattern, consistent with half the flame surviving in a wedge-like shape and rotating around the burner. Such a feature is not very prominent in ethanol or heptane. The asymmetry of the HR image suggests the importance of fuel evaporation on the heat release region close to blow-off. The low volatility could result in the lack of fuel vapour in the gas mixture. The asymmetric wedge-like pattern is not seen clearly in stable flames of decane and dodecane, suggesting that the significant local quenching leads to the possibility of spray penetration there, diminishing further the generation of vapour at that part of the flame, breaking axi-symmetry and resulting in a large local extinction that can rotate with the swirl.

4. Spray Flame Blow-off: Flame Structure

4.2.5 Flame sheet characteristics by OH – PLIF measurements

Figure 24 (and later, Figs. 27-31) show the images from fast OH-PLIF measurements of the stable and blow-off flames of each fuel. The average OH-PLIF images are firstly described (Fig. 24, rows 2,5, to the left) and reveal the main reaction zone locations of these swirl spray flames. The mean OH zone in general overlaps with the mean HR region represented by the mean OH* images (Fig. 24, rows 1,4, to the left) and surrounds the spray visualised by the mean Mie images (Fig. 24, rows 3,6, to the left). The mean OH is very small (even below the detection threshold) at the anchoring point at the bluff body corner, suggesting intermittent flame lift-off there, which is clearly evident in the instantaneous OH-PLIF images. At blow-off conditions, the mean OH of the outer flame branch from all the fuels seems more attached at the bluff body edge and the OH-containing region is shorter. The inner flame branch seems shorter and unconnected with the outer branch for the low-volatility fuels. On an instantaneous basis, the stable flame is relatively continuous (albeit with breaks, especially along the outer branch), while the flame at blow-off is severely broken apart and fragmented, with the inner zone completely disappearing occasionally for the heavier fuels.

Figures 27-30 show several instantaneous images of the OH radical for stable and unstable flames for all fuels. Starting with ethanol and with the flame far from blow-off (Fig. 27a), it is evident that the OH region is overall thin and curved and continuous for its most part, although there are occasional breaks at either inner or outer branch. A highly variable behaviour is seen between snapshots. The time evolution is not shown here, but playback of the movies shows that the sheet holes can close (i.e. we have re-ignition) and new local extinctions can develop. Due to the highly three-dimensional nature of the flow, however, further analysis of the speed of local extinction hole closing or opening, as pursued by [13–15], is not permitted in the present flame. At 93% of the extinction bulk velocity (Fig. 27b), the degree of fragmentation is higher, more breaks are evident, and the length of the OH zone seems to have decreased compared to the flame farther from blow-off. Complete absence of a half branch can also be seen. The outer branch seems to be more often attached, however. At the blow-off condition, the OH is still thin and sheet-like, but the degree

4. Spray Flame Blow-off: Flame Structure

of extinction is much higher than in the stable flames. The various features discussed above are marked in Fig 27: the absence of inner flame zone (Fig. 27c arrow), the local extinctions (Fig 27a-b, red circle), a spreading of a pocket of OH radicals downstream (Fig. 27c yellow circle), attachment and lift-off at the bluff body edge (Fig 27a-c, rectangles).

Data for heptane are shown in Fig. 28. Similar to ethanol, the stable flame OH sheet (Fig. 28a) is thin, lifts-off at the bluff body edge, and has breaks and closures. However, the inner OH branch looks more stable than ethanol flame, presenting an overall ‘V’ shape. The unstable heptane spray flame (Fig. 28b) also shows similar features, but a more variable behaviour is shown with large breaks and even complete absence of inner or the outer reaction zone. The results are consistent with the one reported previously [6] with a different atomiser.

The decane and dodecane flames are quite similar (Figs. 29-30). Far from blow-off, the OH sheets are relatively continuous, thin, with occasional breaks (circles) and lift-off (rectangles), and the inner flame is securely anchored to the spray nozzle. The OH region is well aligned to the hollow-cone spray jet, probably due to the low volatility of the fuel that restricts the penetration of vapour into the recirculation zone. For the unstable cases (Fig. 29c and Fig. 30b), both inner and outer branch show intense break-ups and the OH appears more attached to the bluff-body surface; the inner reaction zone is apparently missing or shifts towards the outer shear layer.

The transient blow-off process from the OH-PLIF images of the spray flames of the four fuels are shown in Fig. 31. As the flame becomes fragmented, the out-of-plane motion makes interpretation of these images difficult. An absence of the inner branch is often observed at the blow-off transient process. The last fragment of OH radicals appears close to the bluff-body. No significant differences are seen between the fuels.

4.2.6 Mie scattering images

Figure 24 rows 3,6 shows the instantaneous and mean Mie scattering images for each fuel at conditions far from blow-off, and for the blow-off condition. The instantaneous Mie images of unstable flames also present a non-axisymmetric profile of the spray, supporting the observation of single wedge-like HR regions shown in the

4. Spray Flame Blow-off: Flame Structure

instantaneous OH* images.

The mean Mie images show a more dispersed spray in the ethanol flames compared to the others, and a slightly less dispersed spray in the unstable flames (Fig. 24e-h row 6) compared to the stable flames (Fig. 24a-d row 3). The lack of axisymmetry of the Mie images in the unstable flames is consistent with the OH* and the OH images. The spray angles for all the conditions are similar at around 60°, however, a slightly narrower spray angle is found in the ethanol flames.

4.2.7 Reaction zone visualisation by Joint CH₂O-OH PLIF

4.2.7.1 The instantaneous images

Figure 32 shows an image obtained in un-ignited flow with the fuel running and an example of reacting flow image, both captured by the CH₂O camera. The inert flow image suggests that the CH₂O images contain some information from the droplets. This is not likely to be Mie scattering, as the laser wavelength has been filtered out. The droplet-like shape of the high intensity regions suggests fluorescence of heptane from the liquid phase, but the intensity is not very high. Considering the density ratio between vapour and liquid suggests that the fuel vapour is not likely to be picked up by the system. The flame images are usually smooth, but occasionally contain similar bright circular spots: see, for instance, the circled spot in Fig. 32b. These are thought to originate from fuel droplets. The percentage of images showing droplet-like shapes in the dataset is small (around 10%) and such images are removed before the calculation of averages. In addition, such droplet-like regions virtually always do not overlap with the OH image.

Figure 33 presents a few typical OH, CH₂O, and CH₂O×OH (HR) images from the two flames. For both flow conditions, the OH signal shows discontinuities, similar to what has been observed previously with 5 kHz OH-PLIF imaging (Fig. 28, and [6]). The OH-containing regions are quite thin and the recirculation zone is void of OH, contrary to premixed flames that have [6,51] significant amounts of OH inside the recirculation zone. In both H1S1 and H1S2, the OH regions are overall thin, indicating that the present spray flames have non-premixed flame characteristics. The OH line follows a relatively straight path along the spray in the inner part of the flame, and a

4. Spray Flame Blow-off: Flame Structure

very convoluted part roughly aligned with the shear layer outer flame, which is occasionally anchored at the corner of the bluff body. The location of OH seems more variable in H1S2 than in H1S1, which indicates that at a condition far from blow-off (H1S1), the flame sheet is less often extinguished along the spray path.

The region A (inside the recirculation zone) and region C (in the annular air jet), Row I, Fig 33a, have very low CH₂O and OH. Occasionally, some formaldehyde appears in the outer recirculation zone (further outwards from the annular air stream), likely to be due to the capture of unburnt or partially-burnt fuel from the wall region where the spray impinges on the wall. Between the spray and the air flow in the annular jet (i.e. region B), intense CH₂O is visible. Inside the hollow cone spray (region A, i.e. close to the axis), where hot gases recirculate, the CH₂O signal is virtually zero. There is a transition region that overlaps with the OH signal and this marks the inner flame branch. This inner branch is likely to be a diffusion flame between evaporated fuel and the air that recirculates that is mixed with hot products from the flame itself. Such a flame is less prone to extinction [29] and this might explain why the outer branch along the shear layer detaches and seems extinguished more often than the inner part. This is also consistent with the temporal analysis of visualisation of blow-off events in this spray flame by 5 kHz OH* imaging (Fig. 26, and [6]) that showed that the inner part of the flame was the last to extinguish.

Individual images vary significantly. Some images show an attached flame (circled in Fig.33), some present a flame lifted from the bluff-body edge (square), and some show an absence of flame sheet either in the outer shear layer (IIIa, IIb) or the inner recirculation zone (IVb). In the region close to the bluff body and radially outwards from the spray, a significant amount of CH₂O is present and, when the OH shows a continuous sheet, the CH₂O region is bounded by the OH. In conjunction with the laminar flame simulation results, that show that the CH₂O-containing regions are fuel-rich ($\xi > \xi_{st}$), we may conclude that the region between the spray and the annular air is fuel-rich, while the region inside the spray cone is lean. Note also that the region between the spray and the annular air occasionally contain no CH₂O signal. This can be either unburnt fuel or air penetrated through the sheet, both possibilities alluding to an extinction event. Row IV, Fig. 33b, shows a region void of both OH and CH₂O;

4. Spray Flame Blow-off: Flame Structure

such regions tend to exist when the OH has breaks.

The image showing the product $\text{CH}_2\text{O} \times \text{OH}$ representing heat release is very strongly correlated to the corresponding OH image, contrary to premixed flames [6,41,51] that show OH even in regions very far from the region of coincidence with the CH_2O . This provides support to the use of OH-PLIF for marking reaction zones in such spray flames, which was discussed earlier in section 4.2.5 and in Fig. 28, that it visualises a thin, relative continuous, ‘V’ shaped inner reaction zone and an intermittent lift-off of the outer reaction zone of the stable flame (Fig. 28a) becoming fragmented and severely broken apart at the blow-off condition (Fig. 28b).

4.2.7.2 Average images

Figure 34 presents the average images of OH, CH_2O , and HR from the two cases. Again, the HR regions are similar to the OH regions. The region of the recirculation zone between the spray and the shear layer has significant CH_2O . Close to the blow off condition, the flame seems closer to the bluff body, as concluded from the mean OH and HR images. In addition, higher values of CH_2O are seen, consistent with the laminar flame simulations that show higher CH_2O mole fraction at rich mixture fractions as the strain rate increases (Fig. 12). In addition, the mean HR images (Fig. 34) show very similar results to the Abel-transformed mean OH^* chemiluminescence images taken at the same conditions (Fig. 24b row 1 and Fig. 24f row 4). A relatively high intensity region at the inner reaction zone, aligned with the spray, and an outer branch, along the shear layer, are evident by both techniques. The inner branch starts a few mm from the fuel nozzle and the outer branch seems lifted, but by a distance that is decreasing at the high velocity condition (H1S2). The inner branch seems to have a higher mean heat release rate than the outer branch. These details are seen in both OH^* and HR data. As the OH^* images do not have interference from Mie scattering or fuel fluorescence, the agreement supports the view that the flame shape and location of heat release zones obtained with $\text{CH}_2\text{O} \times \text{OH}$ images is trustworthy.

4.3 Conclusions

This chapter discussed experimental observations with swirling spray flames at conditions far from blow-off, close to blow-off, at the blow-off condition before the

4. Spray Flame Blow-off: Flame Structure

final blow-off event, and during the final blow-off transient. Four different fuels were studied, two considered of high volatility (ethanol, heptane) and two considered of low volatility fuels (decane and dodecane). It is shown that the flame location is affected by the fuel type. The low volatility fuels show a longer penetrating length of the droplets and a slightly larger mean droplet size with a smaller dispersion of the spray, ensuring a longer, straighter, more anchored flame sheet represented by the OH* and OH-PLIF images. The stable flames are intermittently lifting at the bluff-body edges, with the average lift-off height decreasing as the air velocity increases and as fuel volatility increases. Fewer breaks are shown in the inner recirculation zone flame than in the outer shear layer for stable flames, but the occurrence of inner branch quenching increases at blow-off. The intense local extinction eventually leads to the global blow-off of the spray flame. The asymmetry of the instantaneous OH* and OH-PLIF images of decane and dodecane flames is more prominent at blow-off than at stable conditions and for ethanol and heptane flames.

Joint CH₂O and OH PLIF was applied to swirl n-heptane spray flames close to extinction. The CH₂O-PLIF measurement has limitations due to the interference by fuel and PAH fluorescence. Nevertheless, because the laminar flame simulations show a sharp destruction of CH₂O, soot precursors, and fuel at stoichiometry, it can be assumed that CH₂O-PLIF marks fuel-rich regions, and that the outline of the CH₂O region can be thought of as close to the stoichiometric mixture fraction iso-line. The PLIF showed that the HR regions followed very well the OH regions, which were thin, characteristic of non-premixed combustion at high strain. With an increase in bulk air velocity, the flame was fragmented more and extinguished more often. The instantaneous images showed great variability and significant parts of the flame sheet could at times be extinguished. The good correlation of the HR image with the OH signal indicates that high-speed OH-PLIF measurements could be a reliable marker for HR regions in swirling spray flames. Compared with line-of-sight inverse Abel-transformed OH* chemiluminescence measurements, the CH₂O×OH heat release rate estimation reveals quite similar flame shape and locations.

4. Spray Flame Blow-off: Flame Structure

4.4 Tables for Chapter 4

Table 1. Conditions used for most of the experiments, corresponding to various stable and blow-off conditions. For all, the fuel mass flow rate was 0.27 g/s. U_b corresponds to the bulk air velocity at the annular opening around the bluff-body.

Fuel type	Name	Case	U_b [m/s]	$\phi_{overall}$
Ethanol	E1S1	Stable	17.1	0.19
	E1S2	Stable	20	0.16
	E1B	Blow-off	21.6	0.15
n-Heptane	H1S1	Stable	17.1	0.32
	H1S2	Stable	20	0.27
	H1B	Blow-off	22.8	0.24
n-Decane	D1S1	Stable	17.1	0.31
	D1S2	Stable	20	0.27
	D1B	Blow-off	20.3	0.27
n-Dodecane	DD1S1	Stable	14.3	0.38
	DD1S2	Stable	17.1	0.32
	DD1B	Blow-off	20.1	0.27

Table 2. Conditions at various fuel flow rates used for the experiments, corresponding to various stable and blow-off conditions. The optical diagnostics applied are indicated by the filled cells.

Fuel type	Name	Case	\dot{m}_f [g/s]	U_b [m/s]	$\phi_{overall}$	$\frac{U_b}{U_{BO}}$	OH*	OH-PLIF	Mie	PDA
Ethanol	E0S0	Stable	0.20	14.3	0.17	0.72				
	E0B	Blow-off	0.20	19.7	0.12	1				
	E1S0	Stable	0.27	14.3	0.23	0.66				
	E1S1	Stable	0.27	17.1	0.19	0.79				
	E1S2	Stable	0.27	20.0	0.16	0.93				
	E1B	Blow-off	0.27	21.6	0.15	1				
	E2B	Blow-off	0.30	22.1	0.16	1				
	E3B	Blow-off	0.35	23.3	0.18	1				
	E4S1	Stable	0.40	17.1	0.27	0.75				
	E4S2	Stable	0.40	20.0	0.27	0.75				
	E4B	Blow-off	0.40	23.7	0.27	0.75				
	E5S1	Stable	0.45	17.1	0.31	0.75				
	E5B	Blow-off	0.45	22.7	0.31	0.75				

4. Spray Flame Blow-off: Flame Structure

(Continued) **Table 2.** Conditions at various fuel flow rates used for the experiments, corresponding to various stable and blow-off conditions. The optical diagnostics applied are indicated by the filled cells.

Fuel type	Name	Case	\dot{m}_f [g/s]	U_b [m/s]	ϕ_{overall}	$\frac{U_b}{U_{BO}}$	OH*	OH-PLIF	Mie	PDA
n-Heptane	H1S1	Stable	0.27	17.1	0.32	0.75				
	H1S2	Stable	0.27	20.0	0.27	0.88				
	H1B	Blow-off	0.27	22.8	0.24	1				
	HS0	Stable	0.15	14.3	0.21	0.81				
	HB	Blow-off	0.15	17.7	0.17	1				
	HOS0	Stable	0.20	14.3	0.29	0.68				
	HOS1	Stable	0.20	17.1	0.25	0.81				
	HOS2	Stable	0.20	18.5	0.23	0.88				
	H0B	Blow-off	0.20	21.0	0.20	1				
	H2S2	Stable	0.35	20.0	0.35	0.88				
	H2B	Blow-off	0.35	22.8	0.31	1				
	H3B	Blow-off	0.40	23.5	0.34	1				
	H4B	Blow-off	0.45	23.8	0.38	1				
	n-Decane	D1S1	Stable	0.27	17.1	0.31	0.84			
D1S2		Stable	0.27	20.0	0.27	0.99				
D1B		Blow-off	0.27	20.3	0.27	1				
n-Dodecane	DD1S1	Stable	0.27	14.3	0.38	0.71				
	DD1S2	Stable	0.27	17.1	0.32	0.85				
	DD1B	Blow-off	0.27	20.1	0.27	1				
	DD3S1	Stable	0.40	17.1	0.46	0.78				
	DD3S2	Stable	0.40	20.0	0.40	0.91				
	DD3B	Blow-off	0.40	22.0	0.36	1				
	DD0B	Blow-off	0.20	18.8	0.20	1				
	DD2S	Stable	0.30	17.1	0.35	0.84				
	DD2B	Blow-off	0.30	20.4	0.29	1				

4. Spray Flame Blow-off: Flame Structure

Table 3. Fuel properties and flow parameters at the main test conditions.

Name	E1S1	E1S2	H1S1	H1S2	D1S1	D1S2	DD1S1	DD1S2
U_b [m/s]	17.11	19.97	17.11	19.97	17.11	19.97	14.26	17.11
U_l [m/s]	10.68	10.68	12.64	12.64	11.93	11.93	11.41	11.41
ρ_l [kg/m ³]	804.9		668.3		720.7		753.2	
σ [N/m]	2.21×10^{-2}		2.01×10^{-2}		2.38×10^{-2}		2.54×10^{-2}	
ν_l [m ² /s]	1.42×10^{-6}		0.61×10^{-6}		1.29×10^{-6}		1.98×10^{-6}	
P [kW]	8.0		12.0		11.94		11.92	
Re_l	1504		4192		1849		1153	
Re_g	13466	15711	13466	15711	13466	15711	11222	13466
We_l	830		1098		860		774	
We_g	1.23		1.95		1.42		1.22	
Ta	2220		8201		2800		1406	
Oh	0.019		0.008		0.016		0.024	

Table 4. Flow parameters of the stable ethanol flames used in OH* measurements to explore fuel flow rate effects.

Name	E0S0	E1S0	E4S1	E5S1
\dot{m}_f , g/s	0.20	0.27	0.40	0.45
U_b [m/s]	14.3	14.3	17.1	17.1
U_l [m/s]	7.9	10.7	15.8	17.8
ρ_l [kg/m ³]	804.9			
σ [N/m]	2.21×10^{-2}			
ν_l [m ² /s]	1.42×10^{-6}			
Re_l	1114	1504	2228	2506
Re_g	11222		13466	
We_l	456	830	1823	2307
We_g	0.7	1.2	2.7	3.4
Ta	4046	2220	1011	800
Oh	0.019			
P [kW]	6	8	12	13

4.5 Figures for Chapter 4

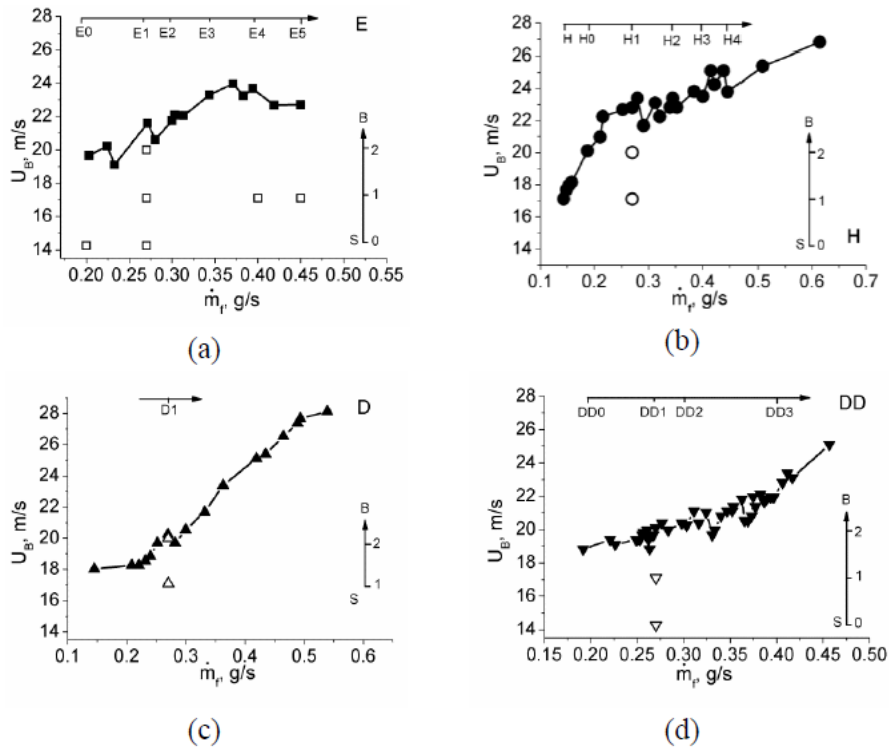


Figure 16. Blow-off velocities (closed symbols) as a function of fuel flow rate for (a) ethanol, (b) heptane, (c) decane, and (d) dodecane. Open symbols mark various test conditions of stable flames discussed in the text. The labels at the top and right lines mark the fuel flow rate and air velocity respectively of the indicated flame code.

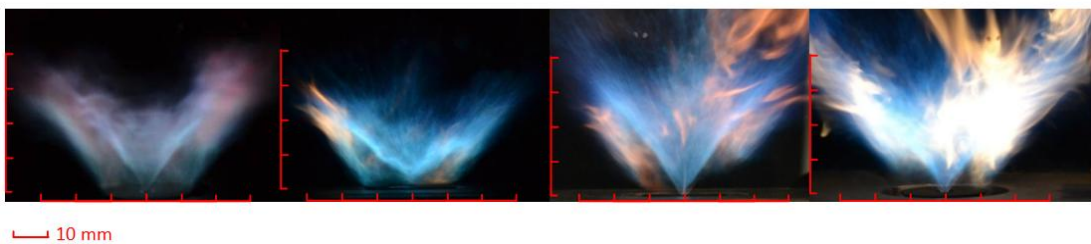


Figure 17. Photographs of stable spray flames of (from left to right) ethanol at E1S1, heptane at H1S1, n-decane at D1S1, and n-dodecane at DD1S1 (for all, $\dot{m}_f = 0.27$ g/s and $U_b = 17.1$ m/s, $Re_g = 13466$).

4. Spray Flame Blow-off: Flame Structure

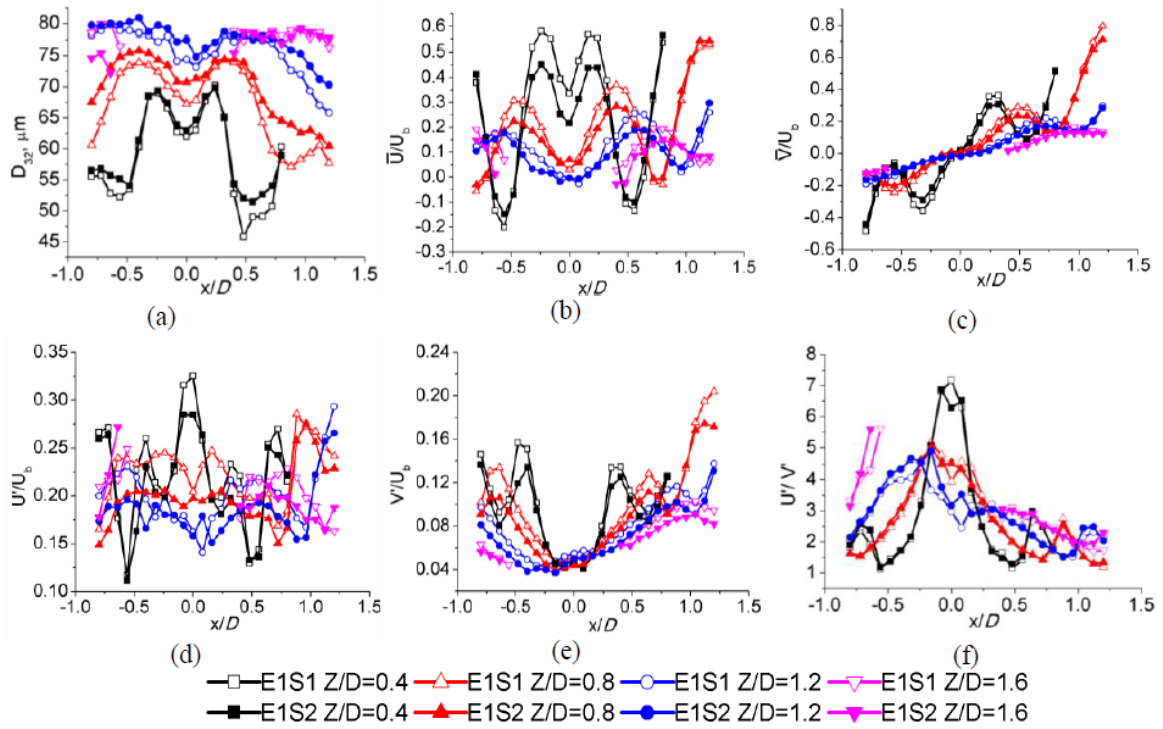


Figure 18. Distributions of (a) Sauter mean diameter, and normalised droplet mean (b) axial and (c) radial velocity, normalised rms fluctuations of (d) axial and (e) radial velocity, and (f) the ratio of the two velocity component fluctuations. Ethanol stable flames: E1S1 (open symbols) and E1S2 (closed symbols) at various downstream locations. E1S1 and E1S2 have the same fuel loading ($\dot{m}_f = 0.27\text{g/s}$) and air velocity of 17.1 m/s and 20.0 m/s respectively.

4. Spray Flame Blow-off: Flame Structure

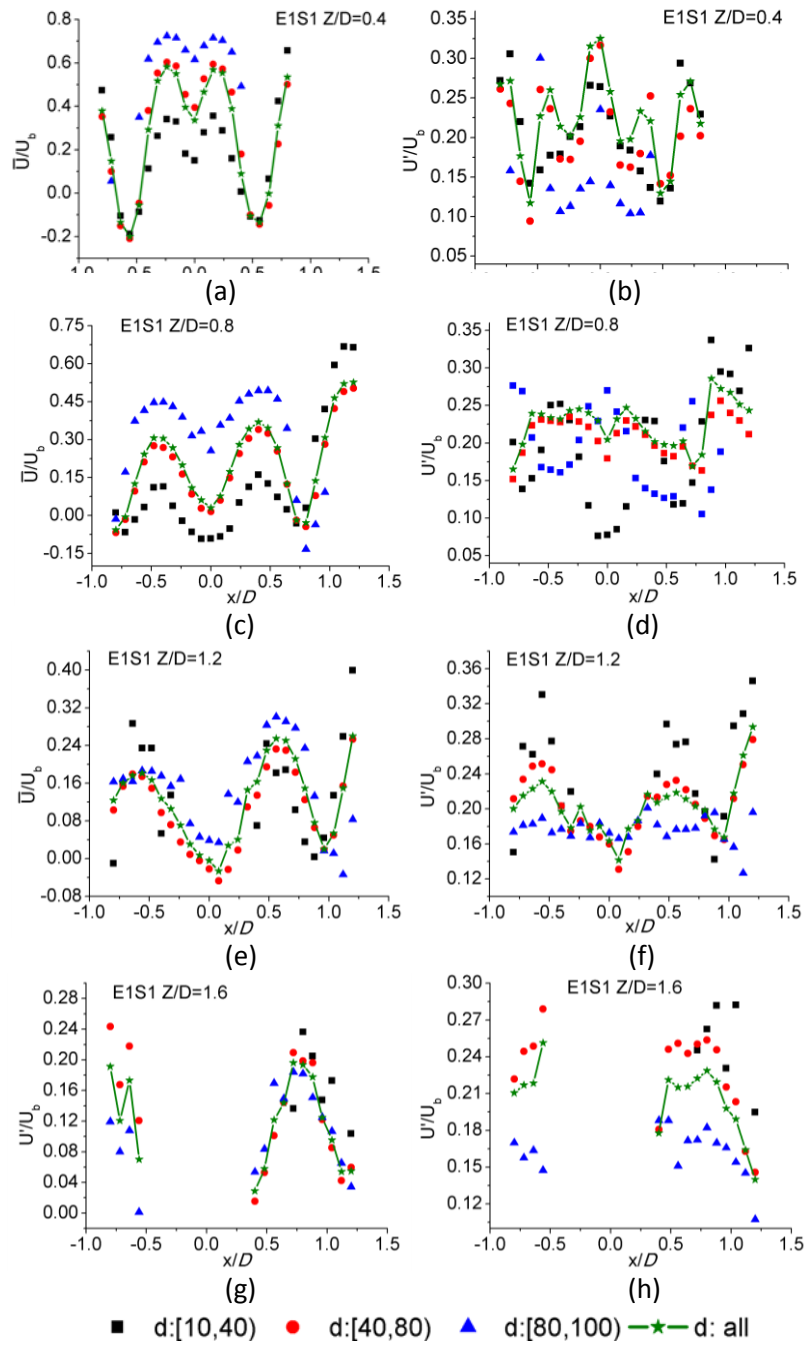


Figure 19. Mean (a, c, e, g) and rms (b, d, f, h) axial droplet velocity conditional on the droplet size ranges (square: 10-40 μm ; circle: 40-80 μm ; triangle: 80-100 μm) and the mean and rms axial velocity using all droplets (star) vs. radius, measured at various downstream locations (a,b: 10; c,d: 20; e,f: 30; g,h: 40, mm). Ethanol stable flame: E1S1 ($\dot{m}_f = 0.27\text{g/s}$, $U_b = 17.1\text{ m/s}$).

4. Spray Flame Blow-off: Flame Structure

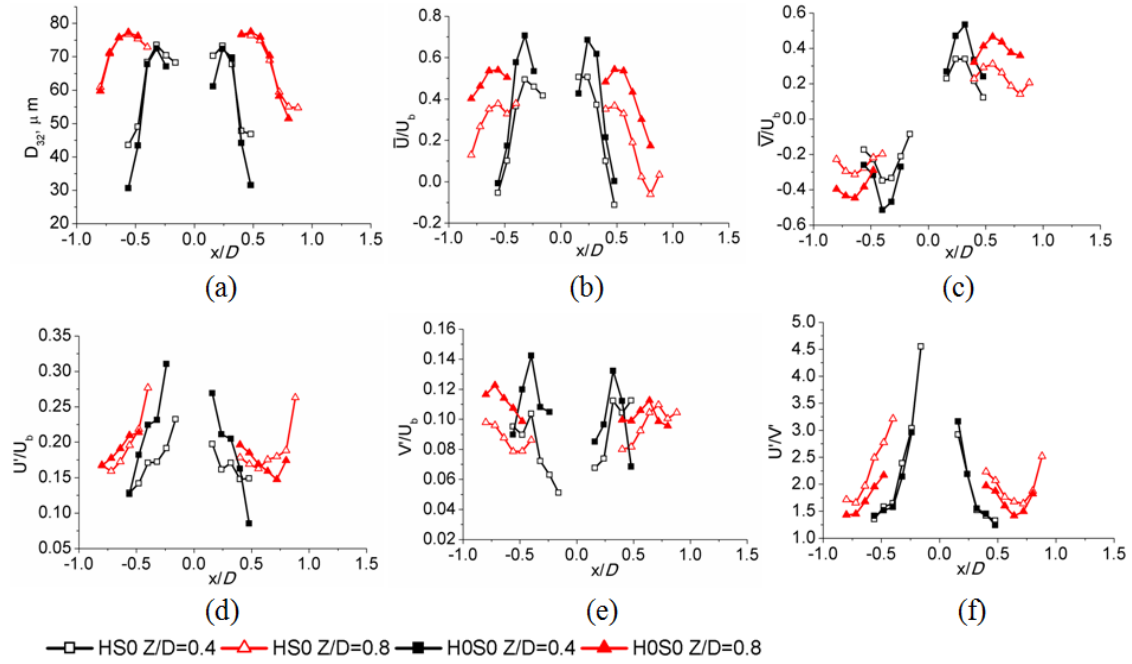


Figure 20. Distributions of (a) Sauter mean diameter, and normalised droplet mean (b) axial and (c) radial velocity, normalised rms fluctuations of (d) axial and (e) radial velocity, and (f) the ratio of the two velocity component fluctuations. Heptane stable flames: HS0 (open symbols) and H0S0 (closed symbols) at various downstream locations. HS0 and H0S0 have the same air velocity of 14.3 m/s ($Re_g=11222$) and different fuel loading of 0.15g/s and 0.20g/s (corresponding to We_l of 339 and 602) respectively.

4. Spray Flame Blow-off: Flame Structure

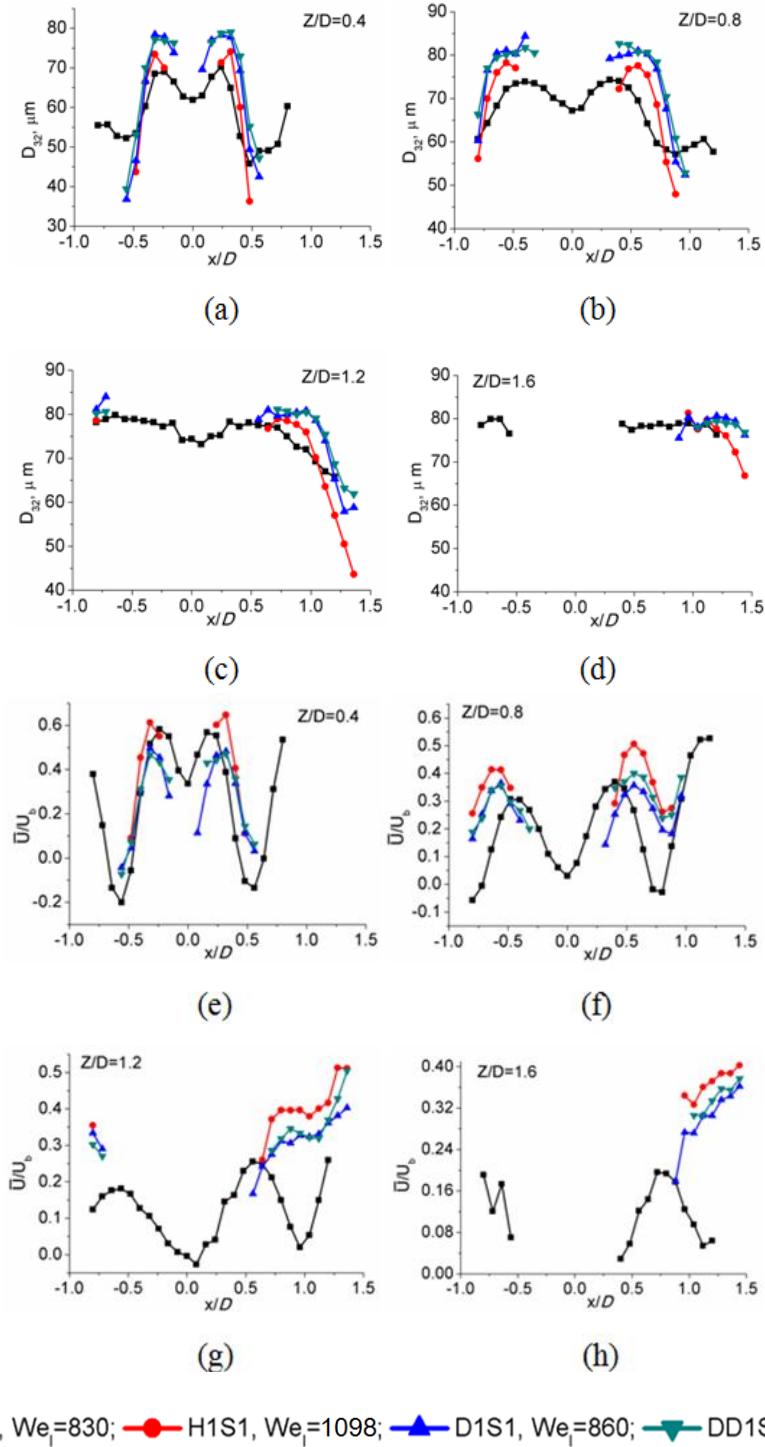


Figure 21. Comparison of the SMD (a-d) and normalised mean axial velocity (e-h) of the ethanol (E1S1, square), heptane (H1S1, circle), decane (D1S1, up triangle), and dodecane (DD1S1, down triangle) flames at (a,e) $z=10$ mm, (b,f) $z=20$ mm, (c,g) $z=30$ mm and (d,h) $z=40$ mm. The fuel and air flow are identical for all flames ($\dot{m}_f = 0.27\text{g/s}$, $U_b=17.1$ m/s). The liquid Weber number is in the range of 774 to 1098 as indicated above.

4. Spray Flame Blow-off: Flame Structure

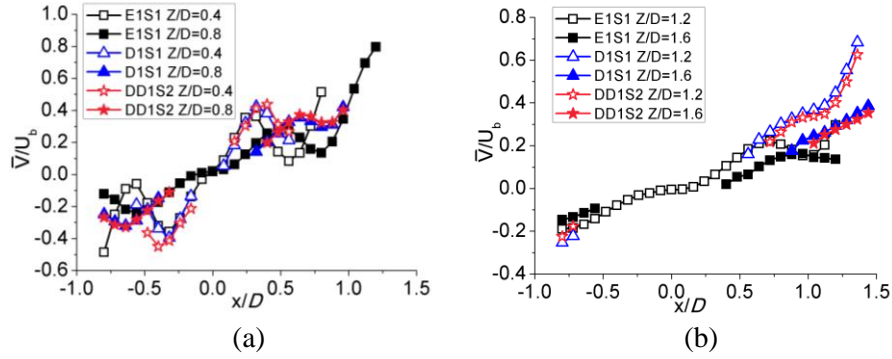


Figure 22. Comparison of the normalised mean radial velocity of the ethanol (E1S1, square), decane (D1S1, up triangle), and dodecane (DD1S1, star) flames at (a) $z=10$ mm (open) and 20 mm (closed), and (b) $z=30$ mm (open) and $z=40$ mm (closed). The fuel and air flow are identical for all flames ($\dot{m}_f = 0.27$ g/s, $U_b=17.1$ m/s).

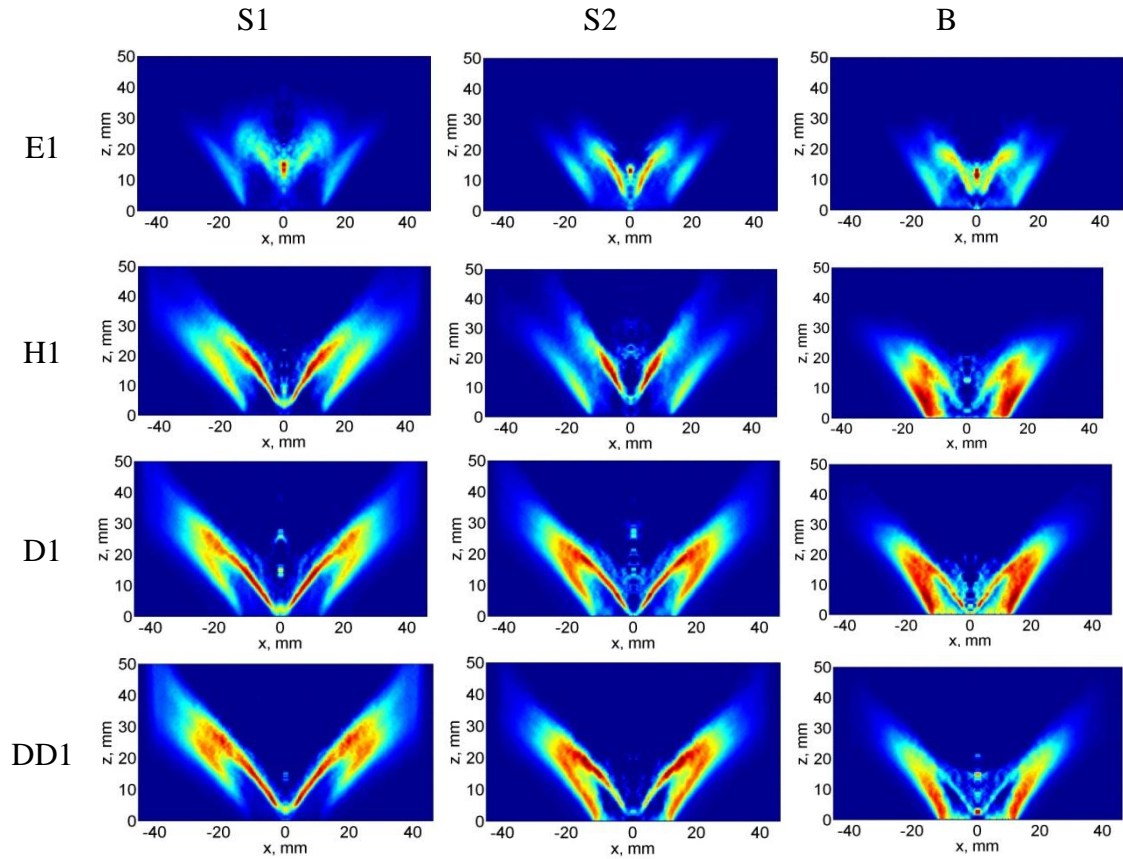


Figure 23. Inverse Abel transformed mean OH^* of stable flames at far from (column 1: S1) and close to blow-off (column 2: S2), and unstable flames at blow-off condition (column 3: B) from the four fuels: row 1: ethanol (E1), row 2: heptane (H1), row 3: decane (D1) and row 4: dodecane (DD1). The fuel flow rate of these flames is 0.27 g/s. The corresponding air flow rate is indicated in Table 1.

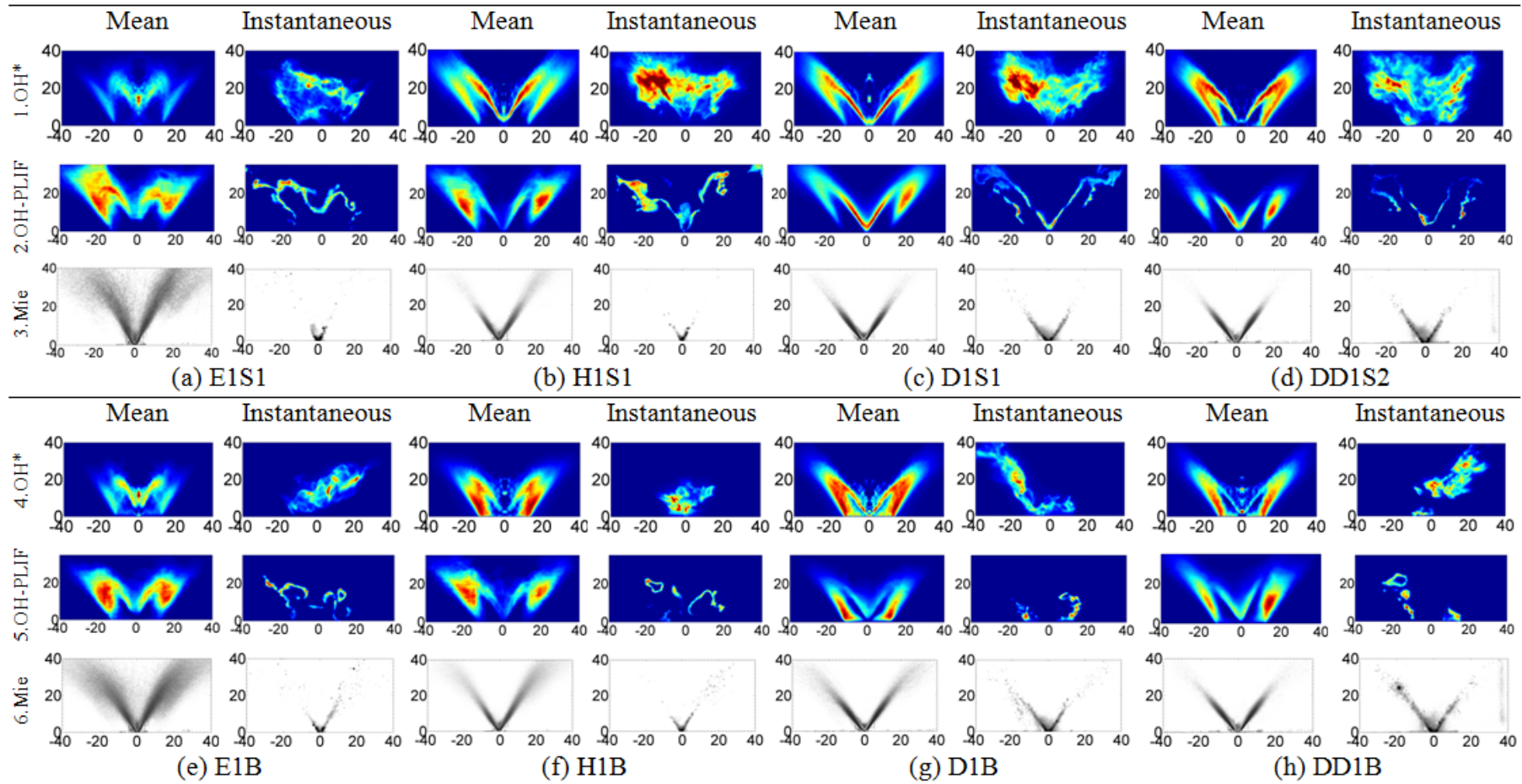


Figure 24. The mean and instantaneous images of OH* chemiluminescence (row 1, 4), OH-PLIF (row 2, 5), and Mie scattering (row 3, 6) from different stable flames (a-d) of ethanol (E1S1), heptane (H1S1), decane (D1S1) and dodecane (DD1S2), and unstable flames (e-h) of ethanol flame E1B, heptane flame H1B, decane flame D1B and dodecane flame DD1B at the blow-off condition, but using data before the blow-off event. The mean OH* image is shown after inverse Abel transform. All the flames above have the same fuel flow rate at 0.27 g/s, and the stable cases have the same air velocity of 17.1 m/s, while the unstable flame cases at blow-off conditions have bulk velocities as shown in Table 1. Same colormap per row.

4. Spray Flame Blow-off: Flame Structure

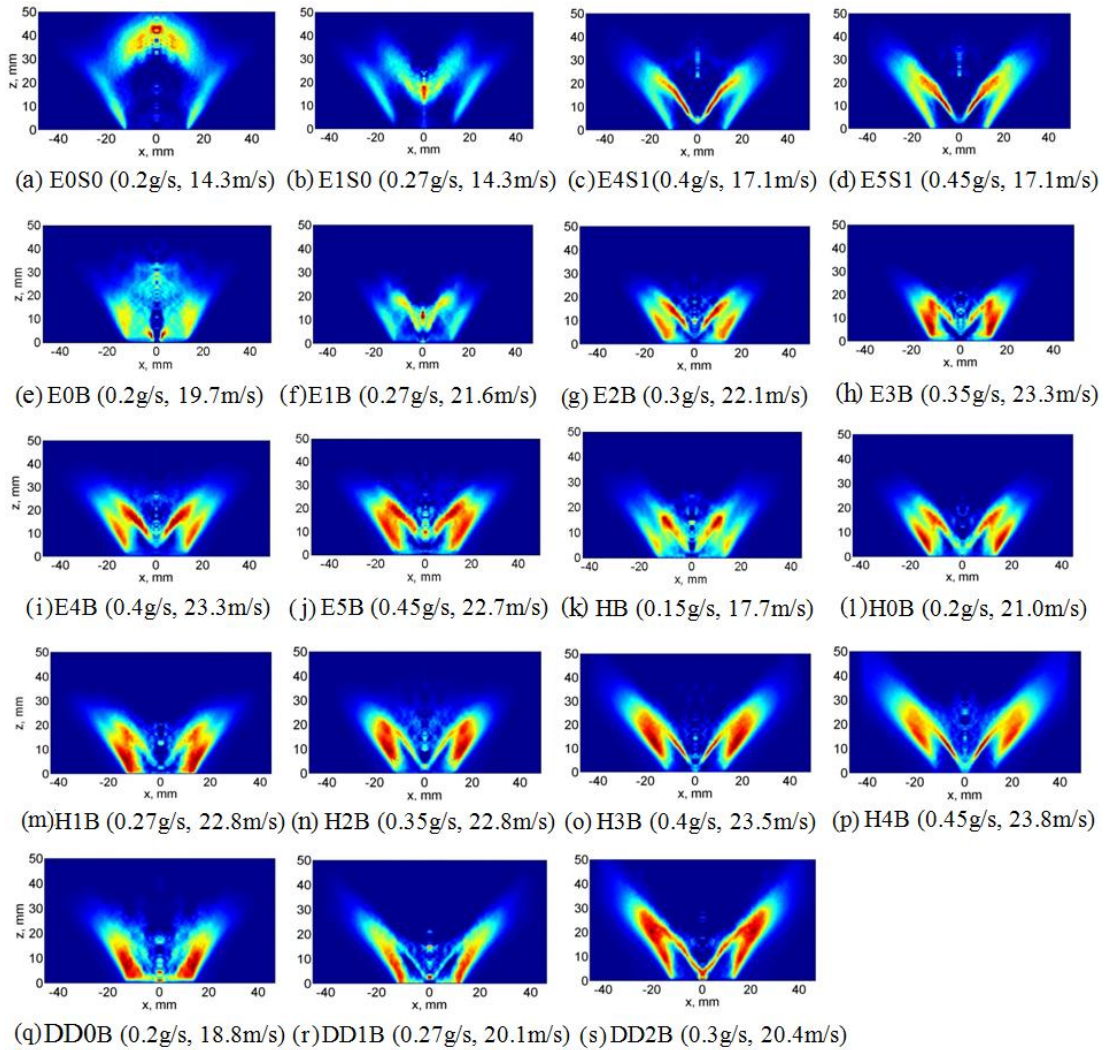


Figure 25. Inverse Abel transformed mean OH* chemiluminescence images for (a-d) stable flames of ethanol, and (e-s) flames at blow-off conditions (e-j. ethanol, k-p. heptane and q-s. dodecane). The corresponding fuel mass flow rate and air bulk velocities are shown next to the flame names.

4. Spray Flame Blow-off: Flame Structure

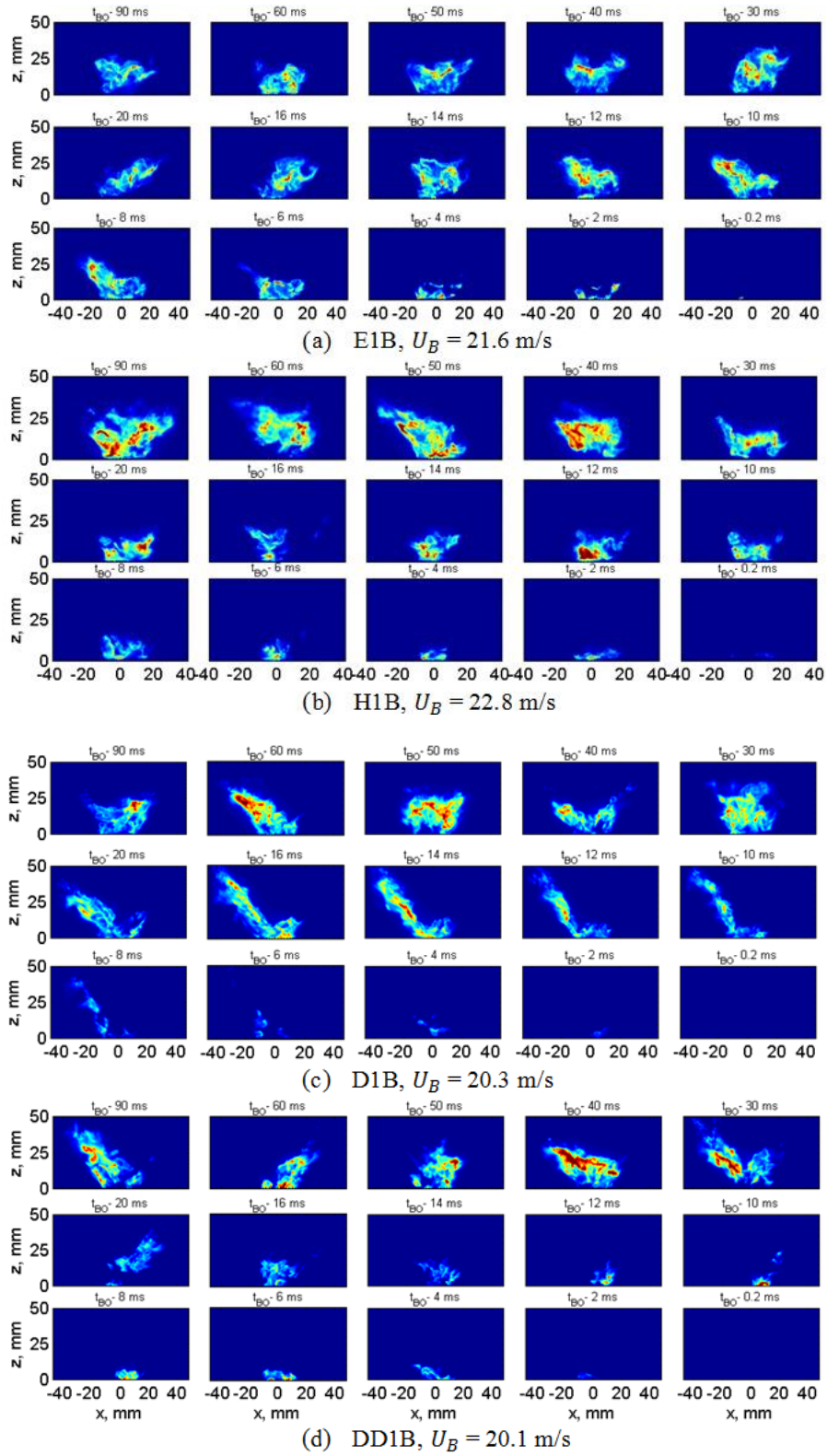


Figure 26: Instantaneous OH* images of swirl-stabilised spray flames of (a) ethanol (E1B), (b) heptane (H1B), (c) decane (D1B) and (d) dodecane (DD1B) at the blow-off transient event (same colormap for each flame). The fuel flow rates of the four flames are the same, at

4. Spray Flame Blow-off: Flame Structure

0.27 g/s. The relative time referenced to the time of complete disappearance of OH* is indicated on top of each image.

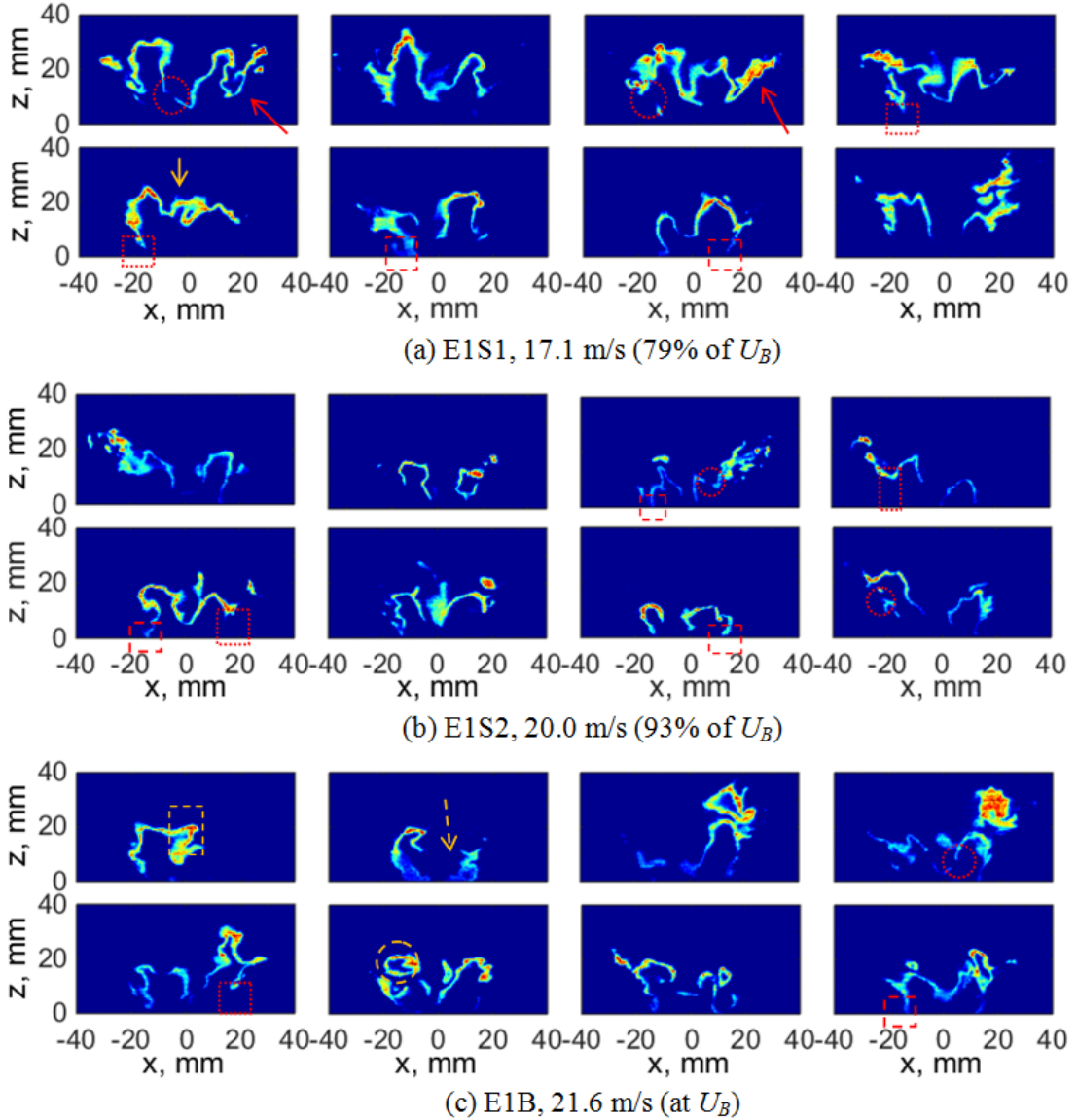


Figure 27. Instantaneous OH-PLIF images of (a,b) ethanol stable flames and (c) the ethanol unstable flame at the blow-off condition before the blow-off event. The fuel flow rate is 0.27 g/s. Images not in sequence (same colormap for each flame). Dot-circle: breaks in inner or outer branch, dot-square: lift-off at bluff-body edge, dash-square: attachment at bluff-body edge, red-arrow: divergence of outer OH branch, yellow-arrow: lift of inner OH branch, yellow-dash-arrow: absence of inner OH branch, yellow-dash-rectangular: movement of inner OH branch, and yellow-dash-circle: spread of flame kernel.

4. Spray Flame Blow-off: Flame Structure

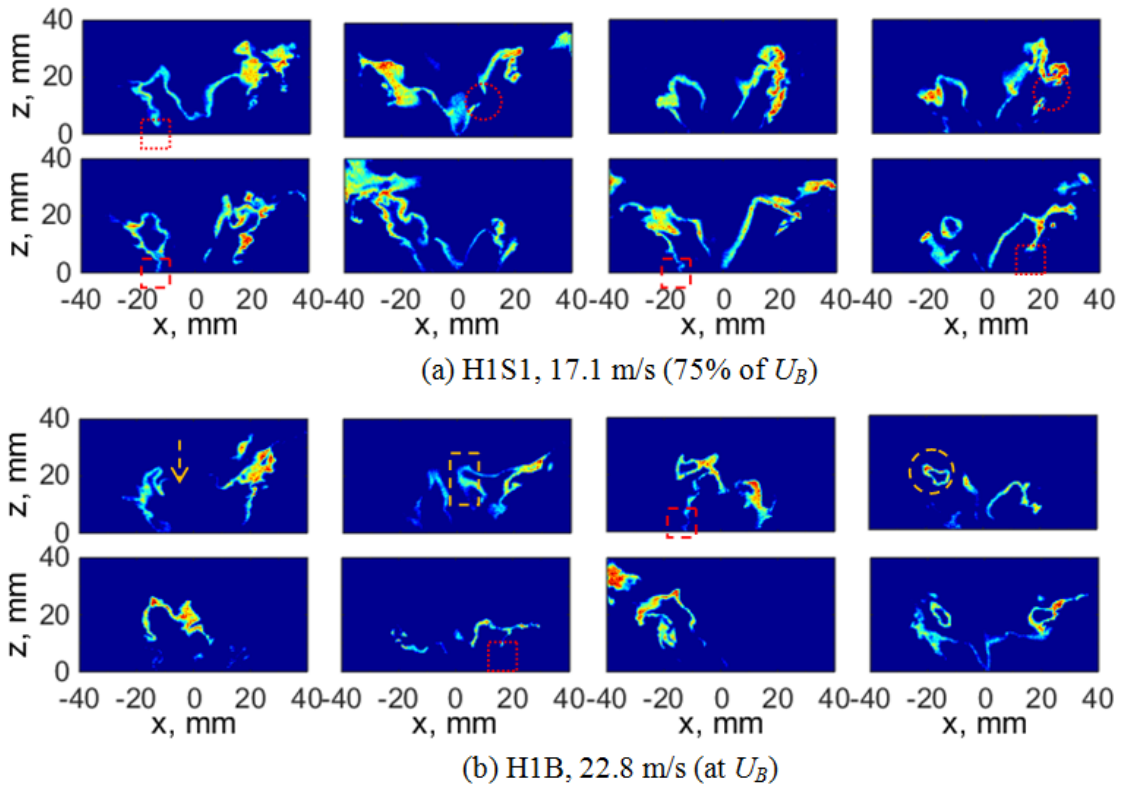


Figure 28. Instantaneous OH-PLIF images of (a) the stable heptane spray flame and (b) the unstable heptane spray flame at blow-off condition before the blow-off event. The fuel flow rate is 0.27 g/s. Images not in sequence (same colormap for each flame). Dot-circle: breaks in inner or outer branch, dot-square: lift-off at bluff-body edge, dash-square: attachment at bluff-body edge, yellow-dash-arrow: absence of inner OH branch, yellow-dash-rectangular: movement of inner OH branch, and yellow-dash-circle: spread of flame kernel.

4. Spray Flame Blow-off: Flame Structure

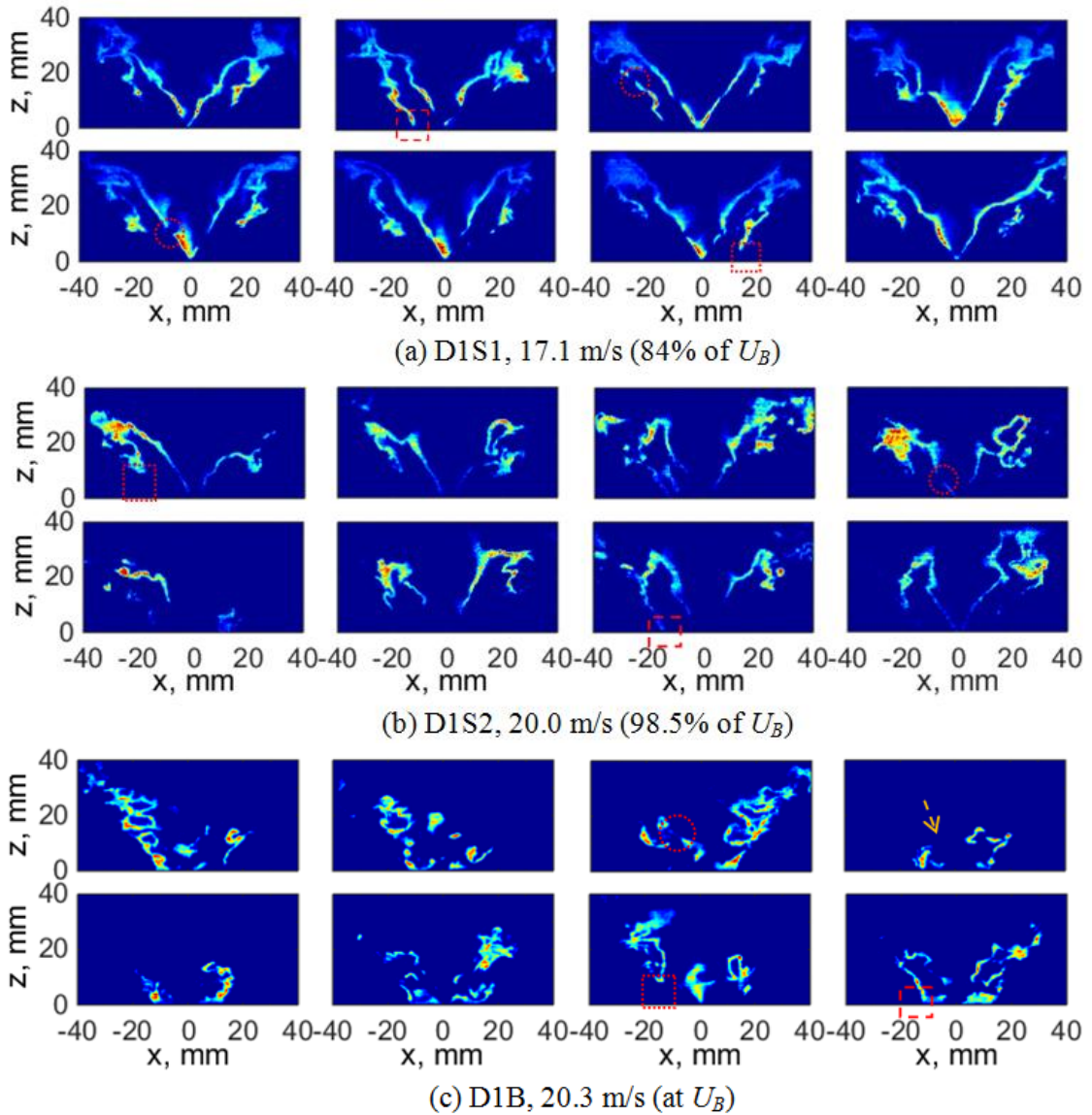


Figure 29. Instantaneous OH-PLIF images of (a,b) the stable decane spray flame and (c) the unstable decane spray flame at blow-off condition before the blow-off event. The fuel flow rate is 0.27 g/s. Images not in sequence (same colormap for each flame). Dot-circle: breaks in inner or outer branch, dot-square: lift-off at bluff-body edge, dash-square: attachment at bluff-body edge, and yellow-dash-arrow: absence of inner OH branch.

4. Spray Flame Blow-off: Flame Structure

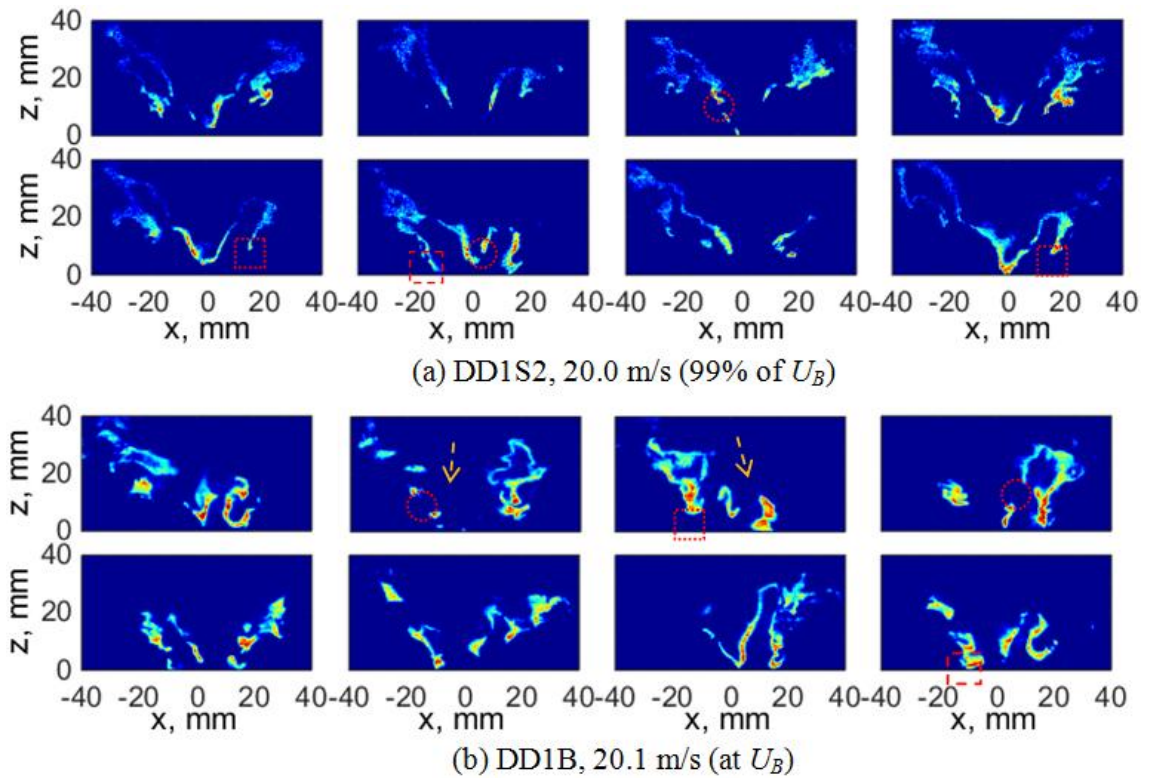
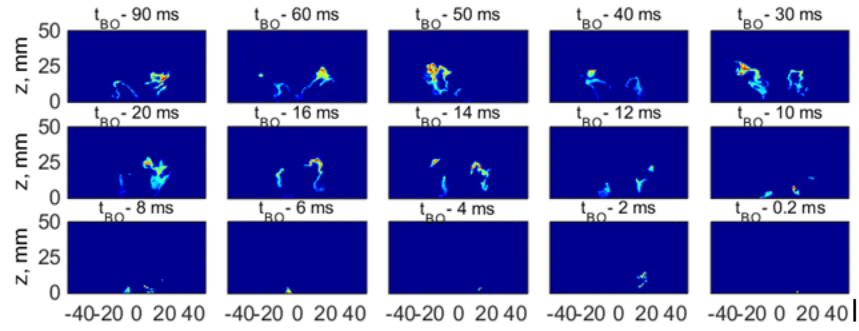
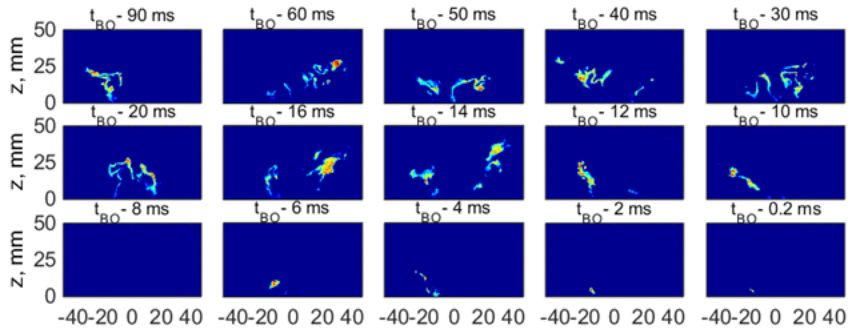


Figure 30. Instantaneous OH-PLIF images of (a) the stable dodecane spray flame and (b) the unstable dodecane spray flame at blow-off condition before the blow-off event. The fuel flow rate is 0.27 g/s. Images not in sequence (same colormap for each flame). Dot-circle: breaks in inner or outer branch, dot-square: lift-off at bluff-body edge, dash-square: attachment at bluff-body edge, and yellow-dash-arrow: absence of inner OH branch.

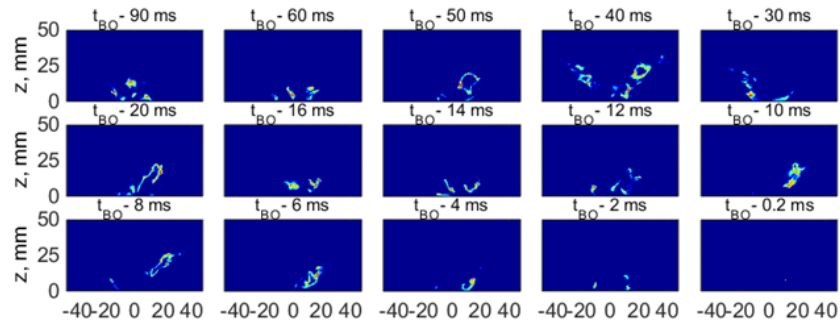
4. Spray Flame Blow-off: Flame Structure



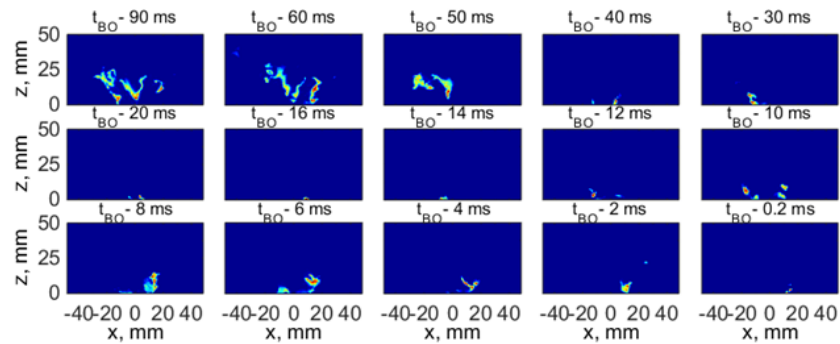
(a) E1B, $U_B = 21.6$ m/s



(b) H1B, $U_B = 22.8$ m/s



(c) D1B, $U_B = 20.3$ m/s



(d) DD1B, $U_B = 20.1$ m/s

Figure 31. Instantaneous OH-PLIF images from flames of ethanol (a), heptane (b), decane (c) and dodecane (d) during the blow-off event (same colormap for each flame). The fuel flow rate was 0.27 g/s and the velocity for each blow-off event is indicated. The relative time referenced to the time of complete disappearance of OH is indicated on top of each image.

4. Spray Flame Blow-off: Flame Structure

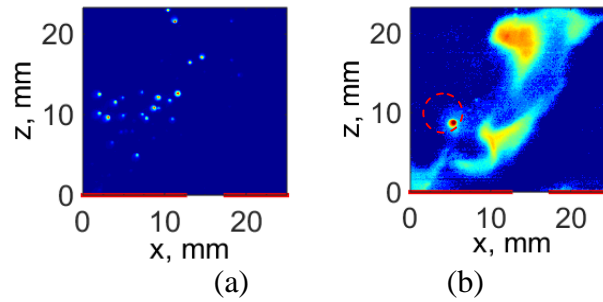


Figure 32. (a) Un-ignited spray, CH_2O image; (b) example CH_2O image of H1S1 flame. The colour map is logarithmic.

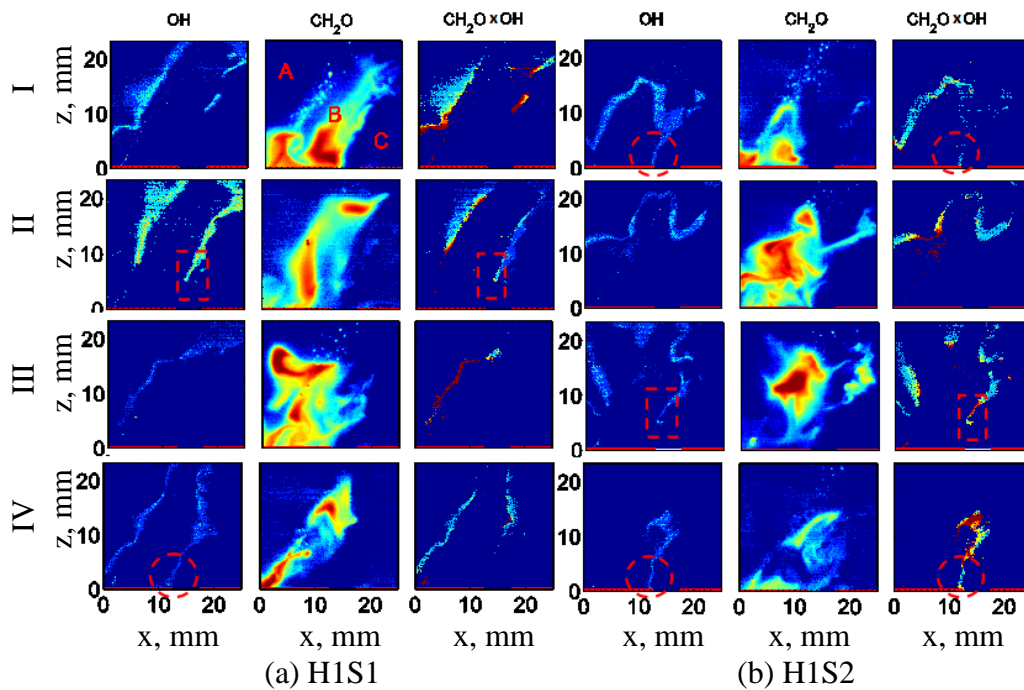


Figure 33. Instantaneous CH_2O , OH , and images for H1S1 and H1S2. I-IV are discussed in the text. The CH_2O image colour map is logarithmic.

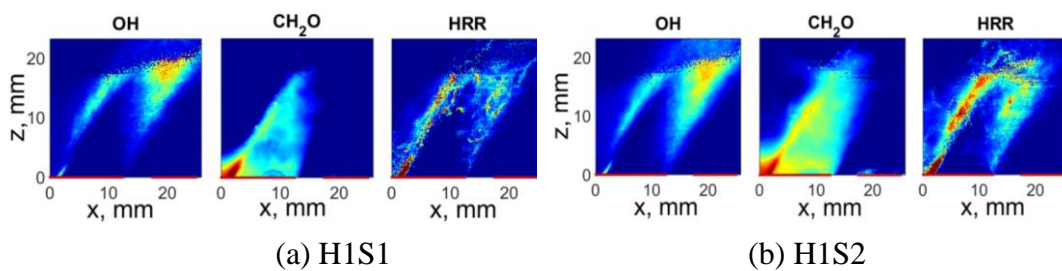


Figure 34. Mean OH , CH_2O , and $\text{CH}_2\text{O} \times \text{OH}$ for H1S1 and H1S2.

Chapter 5

Spray flame behaviour at the blow-off event

This chapter discusses the dynamic behaviour of swirling spray flames at the blow-off event in terms of the blow-off transient duration, the lift-off height statistics, the topology of the OH islands and the Proper Orthogonal Decomposition (POD) analysis¹. The blow-off correlation was firstly discussed for the four fuels. Secondly, a quantification of the duration of the blow-off event is attempted based on the evolution of the OH* images. The duration is evaluated at various fuel flow rates of the four fuels. Next, the lift-off height statistics, the topology of the OH islands, and the percentage of quenched stoichiometric mixture fraction iso-surface are determined as additional measures that can help with the validation of combustion models focusing on capturing extinction. Finally, POD is also used to extract the dominant structure and the corresponding motion in OH* and OH-PLIF images of stable flames and unstable flames at blow-off.

¹: the POD analysis is a collaborative work with Simone Lombardi, who was a PhD student in Department of Engineering, Università del Sannio, Italy. Lombardi has provided a thoughtful discussion on the algorithm and performance of the POD.

5.1 Results and Discussion

5.1.1 Blow-off correlation

Several well-known blow-off correlations (premixed: Radhakrishnan et al. [45]; Non-premixed: Broadwell [54]; Spray: Ateshkadi et al. [4]) could be applied to the current flames to collapse the blow-off data from various fuels. The correlation proposed by Radhakrishnan et al. [45], originally developed for the blow-off of turbulent bluff-body premixed flames, has also been used successfully for limited heptane data and for both premixed and non-premixed methane flames by Cavaliere et al. [6], and here its accuracy is explored further for the present experiments that involve more liquid fuels. This correlation is based on a conceptual picture of combustion in small-scale (Kolmogorov) turbulent structures. The blow-off was deemed to occur when the time ratio $1/Da_1$ predicted by Eq. 19 exceeds a critical value (R_τ):

$$\frac{1}{Da_1} = \frac{\tau_c}{\tau_e} = \left(\frac{U_B \nu}{L}\right)^{1/2} / S_L > R_\tau \quad \text{Eq. 19}$$

where ν is the kinematic viscosity, which is evaluated at the unburnt reactants conditions for premixed systems but at a temperature halfway between the reactants and the adiabatic flame temperature for sprays, as tested by Cavaliere et al. [6] following the suggestion by Mellor [135]. S_L is the laminar flame speed, evaluated at the premixed mixture equivalence ratio for premixed flames but at stoichiometry for non-premixed and spray flames; L is the length of the recirculation zone taken as proportional to the characteristic size of the flame holder. The values of $1/Da_1$ of the current experimental data calculated from Eq. 19 are plotted in Fig. 35. The correlation seems to work better for ethanol and heptane spray flames, with the ratio being almost constant with various fuel loadings; the mean critical value is around 0.9 of ethanol flames and 1.1 of heptane flames. The non-dimensional value ($1/Da_1$) is slightly increasing with fuel loading for decane and dodecane.

5.1.2 Blow-off transient and its duration

Figure 36 plots several instantaneous (coloured line) and average (black line) time series of the normalised integrated intensity of OH* signals at blow-off conditions for

5. Spray flame behaviour at the blow-off event

the four fuels. The integral OH* gradually decreases before the blow-off event, but is relatively constant for some time before the blow-off event begins. (It was during this period that data were collected for the flame conditions denoted as “blow-off” in Figs. 23-30). The characteristic duration of the blow-off event is estimated as the time needed for the integrated OH* to fall from 90% to 10% of the normalised value, and is around 10 to 30 ms for each fuel. The average transient time, τ_{ext} , estimated from five individual blow-off events, is further normalised by the characteristic time flow expressed by D/U_B , at various fuel flow rates (and therefore with different U_B ; Fig.16), and is plotted for different fuels in Fig. 36(right). The values are in the same range as previously reported for heptane spray flames with a different atomiser [6]. No apparent trend is shown within each dataset for each fuel, and no trend is apparent across fuels. The mean transient duration is around 11 characteristic flow times using all data together. This normalised blow-off event duration is lower than the one for premixed (~38) and non-premixed methane flames (~37) reported previously [6] at the same burner, attributed in [6] to a feedback mechanism concerning a spray in a progressively extinguishing flame: as the flame gets progressively smaller and therefore the IRZ cooler, evaporation is slower and so the burner is starved of fuel vapour, which accelerates the flame annihilation process. This makes the normalised extinction transient duration for the spray flame shorter than for gaseous fuelled-flames.

A similarly estimated extinction time based on the OH-PLIF images is smaller, reaching only a few (4.5 in average) flow characteristic times D/U_B . This duration is roughly half of the blow-off transient time obtained from the OH* images discussed in Fig. 36 and the difference can be understood by considering that OH* is a line-of-sight technique and so picks up emission from out-of-plane flame fragments that would not give rise to any OH-PLIF signal.

5.1.3 Lift-off height statistics

Figure 37 shows the probability density function of the lift-off height, calculated in OH-PLIF images as the axial distance of the first emergence of OH in the outer flame branch for the bluff body corner. In general, the lift-off height decreases as the air bulk velocity increases, and at the blow-off condition the probability of the occurrence

5. Spray flame behaviour at the blow-off event

of flame attachment (zero lift-off height) increases. For ethanol, the mean lift-off height is 6.2 mm for E1S1 (79% of U_B), 4.5 mm for E1S2 (93% of U_B) and 4.2 mm for E1B (at U_B). The same conclusion is obtained for the other fuels as well (Figs. 37b-d). The mean lift-off heights normalised by the bluff-body diameter for the four fuels are plotted in Fig. 38 and listed in Table 5. At the stable flame, the normalised average lift-off height is larger with a lower volatility fuel (for example, under the same air and fuel flow rates conditions, the value is 0.25 for the ethanol stable flame (E1S1) and is 0.41 for the dodecane stable flame (DD1S2)). At the blow-off conditions, no direct correlation is found between the lift-off height and fuel volatility or the overall equivalence ratio.

5.1.4 Local quenching analysis

For the heptane flames only, the degree of local extinction was quantitatively estimated by analysing the data from the simultaneous CH_2O -OH PLIF discussed in Ch. 4.2.7. It was suggested from the laminar flame simulations discussed in Ch. 3.2 that the boundary of the CH_2O region can mark approximately the stoichiometric (ξ_{st}) iso-line. The simultaneous presence of OH along the ξ_{st} iso-line is then deemed to correspond to a reaction sheet, while absence of OH is deemed to correspond to a local extinction. An example image of the merged OH and CH_2O signals is shown in Fig. 5 (Ch. 2) that demonstrates the method to obtain the quenched flame sheet length. Note that this processing method considers a lifted flame as extinguished all the way until the lift-off height discussed in Fig. 37. However, it also includes breaks in the OH sheet from all locations. The CH_2O -PLIF technique was not successful for the ethanol flame due to significant parent fuel interference and availability of the instruments did not allow measurement with the decane and dodecane fuels, which must be attempted in the future.

From each image, the percentage of length of the estimated ξ_{st} iso-line that does not have OH is denoted by b . A total number of 400 instantaneous images were processed for two stable heptane flames: (1) H1S1 (far from blow-off), and (2) H1S2 (close to blow-off). The PDF of b at the two conditions are shown in Fig. 39. The mean value of b for H1S1 was 0.21 and the standard deviation was 0.136, while flame

5. Spray flame behaviour at the blow-off event

H1S2 had a mean value of 0.34 and a larger standard deviation of 0.167. Therefore the degree of extinction increases as the air bulk velocity increases, consistent with expectations from non-premixed jet and swirl flames [10,13,21]. Although the above estimate is approximate due to the uncertainty by which the CH₂O signal can truly mark the stoichiometric iso-surface, it can provide a further useful metric for modelling.

5.1.5 OH morphology analysis

In an effort to produce some quantitative measure of the degree of local extinction from the single-scalar planar imaging, some further analysis of the OH-PLIF images is discussed. From each OH image, after binarisation, two parameters are extracted: (i) the area, A , of a connected OH region (“island”); and (ii) the perimeter, P , of the OH region, which then gives the circularity index F , where $F = 4\pi A/P^2$ (the circularity index as defined is unity for a circular object and is zero for a line object). An example OH image is shown in Fig. 40: four separate “islands” (objects) are found, for each of which we calculate the above.

The averaged value of the above morphology metrics of the OH-PLIF images from the stable and unstable flames of the four fuels are shown in Fig. 41. The mean object area decreases, while the circularity index increases at conditions approaching blow-off, suggesting that the OH images are more fragmented with increasing air bulk velocity towards blow-off. There is a slight trend of reducing circularity as the fuel volatility decreases, which is consistent with the qualitative observation that the decane and dodecane fuels tend to have OH sheets that are narrower and more aligned with the spray than the ethanol and heptane flames.

5.1.6 POD analysis

In this sub-section, the POD results (OH* POD and OH-PLIF POD) are discussed for the four fuels spray flames at stable condition and at blow-off. For flames at blow-off, only the images before the blow-off transient process are included in the POD analysis. The OH* POD results are discussed in Figs. 42-46: the first few modes (Fig. 42), the relative and cumulative POD modes energy spectra (Fig. 43 and Fig. 44, respectively), the instantaneous OH* images and their reconstruction based only on a

5. Spray flame behaviour at the blow-off event

small number of modes (Fig. 45), and the PSDs of the POD time coefficients (Fig. 46). The OH-PLIF POD results are presented in a similar way in Figs. 46-50. The following discussion focuses on: (i) the basic structure of the flame extracted from the POD; (ii) its temporal evolution; (iii) the difference between the stable flame and the flame at blow-off; and (iv) the similarity and difference between the various fuels.

5.1.6.1 OH* POD

The mean image (mode 0) and the first five proper orthogonal modes from the OH* are plotted in Figs. 42a-d for two flames of each fuel (ethanol, heptane, decane and dodecane): S (at stable condition, upper rows) and B (at blow-off, lower rows). The flow conditions are identical to the flames discussed in Fig. 24 and are listed in Table 1. For most of the eight flames (Figs. 42a-d), Mode 1 highlights a roughly antisymmetric pair of heat release fluctuations about the flame axis. The HR fluctuations pair is located downstream of the spray jet axis and moves towards upstream at the extinction (Figs. 42 b-d). The time evolution of reconstructed images by Mode 1 with its modal time coefficients suggests a transverse motion of the flame. The relative energy of Mode 1 increases at blow-off (Fig. 43, rows 2-4, right) except the one for ethanol flame E1B (Fig. 43, row 1, right), of which Mode 1 (Fig. 42a lower row) highlights a variance along the flame axis, possibly associated to axial oscillations, has less relative energy than the first mode of the stable flame E1S1.

Modes 2-5 have less energy compared with Mode 1 of the same flame, and reveal heat release fluctuations along the spray jet axis (i.e. flames H1S1 and H1B, mode 2; D1S1 and D1B1, mode 4, etc.), along the flame axis (i.e. flame E1S1 modes 2 and 5; E1B mode 1; H1S1, H1B and D1S1 mode 5, etc), the variance along the radial direction (i.e. flame H1S1 mode 2; H1B, D1B and DD1B mode 3, etc) (could be related with the transverse motion), and the combination of the previous spatial features (i.e. flame E1S1 mode 3; D1B mode 5; DD1B mode 4, etc).

The relative and cumulative energy spectra (Figs. 43-44) reveals in general an increase in the first few POD modes of OH* at the flames blow-off (Fig. 44 red) compared with the stable ones (Fig. 44 blue), except for the ones for ethanol flames (Fig. 44 dash lines). For example, the first 50 POD modes for the flame D1S1 and D1B have cumulative energy of 77.47% and 82.88% respectively, while the first 5

5. Spray flame behaviour at the blow-off event

modes contain about 41.45 % of the energy for D1S1 and about 50.36 % for D1B; this is probably related to the more pronounced mode 1 for the blow-off condition which contains 28.69% for D1B and 17.88% for D1S1. This suggests that at approaching blow-off, the fluctuation associated with the transverse motion is more dominant.

As for ethanol flames, the mode 1 of stable flame E1S1 reveals a transverse motion contains about 21.02% of the energy, which drops at extinction condition (E1B) to 13.79% and is substituted with an axial oscillation motion. The transverse motion at extinction condition is revealed in mode 2 containing about 12.39% energy. The departure of the dominant spatial features of the ethanol flame at blow-off compared with the other fuels flames could be related to the fuel atomisation effect. It is shown previously for the mean OH* and Mie images (in Ch. 4) that the spray angle is narrower for flame E1B and E1S1 compared with the other fuels flames. Additionally, the PDA results also reveal a different atomisation process for the two ethanol flames compared with the others, as in which the spray is not fully open-up and the droplets are also presented along the flame axis. Therefore, the axial variation structure could be more pronounced for flame E1B instead of a transverse motion.

Next, the snapshots obtained by reconstruction of the data with the mean image and mode 1 or the first five modes are compared with the raw data shown in Fig. 45 for two decane flames. The dominant structure of the asymmetric heat release fluctuations against the flame axis and its transverse motion cannot be seen as easily in the raw OH* images (Fig. 45, upper row) due to the underlying small-scale fluctuations, but are shown in the reconstructed movie (Fig. 45, middle row) with mean image (mode 0; constant in time) and the mode 1, which represents the principal left/right oscillation. The reconstructed movies for the blow-off condition (Fig. 45b, middle and lower rows), in particular, show that almost half of the flame may be completely quenched during this transverse motion. The reconstruction of the data with the first few (in this case, the first five) POD modes (Fig. 45, lower row) has allowed the filtering of the spatial features of small scale, so that it has been possible to visualise better the dominant shape. Looking at modes 1 to 3 for D1B (Fig. 42c lower row) together and the reconstructed movie suggests that at the blow-off condition, the flame seems to have a wedge-like shape that rotates at about 30 Hz. The

5. Spray flame behaviour at the blow-off event

clarity of this motion from the reconstructed POD snapshots, and the difference between the stable flame and the one at extinction, demonstrates the power of POD to extract the dominant features of the OH* movies.

Finally, the PSDs of the first 10 normalised OH* POD coefficients are plotted in Figs. 46 (a,c,e,g) (the PSDs were shifted along the y -axis for clarity) for the stable and blow-off flames of the four fuels. Many POD modes contain a broad peak between about 30 and 60 Hz and occasionally its harmonics. This result reveals the dynamics, in terms of frequency, of the flame. The PSDs for the various fuels are similar. The transverse mode (mode 1) does not show a strong peak in its PSD, although a clear motion is seen (e.g. decane flames: Fig. 45). The coefficients of the higher modes tend to have broad peaks, such as 24.4 Hz for modes 2 and 5 and the harmonic at 48.8 Hz for modes 3 and 4 of flame D1S1. For the flames at blow-off, where a significant part of the flame has been quenched (e.g. decane flame D1B Fig. 45b), the absence of a peak in the PSDs of the coefficients of Mode 1 suggests that there is no strong periodicity associated with the flame's motion. The axial modes (e.g. flame E1S1, H1B, D1B, DD1S2: Modes 2-3), however, have broad spectral peaks at 48.8 Hz. Interestingly, these spectral peaks depend little on the flow velocity. LES of swirling flames (see, for instance [160,161] and references therein) often show similar peaks in the POD coefficients attributed to precessing vortex cores (PVC) or other vortical motions; the Strouhal numbers of the present peaks though are too low compared to the $o(1)$ Strouhal number usually reported for PVC [206].

All PSDs include a portion with a $-5/3$ decay, typical of the energy spectrum of turbulence, and the OH* shows a sharper drop-off after about 1 kHz (Figs.46 a,c,e,g). The higher the mode number, the higher the contribution of the high frequency motions to the POD coefficients fluctuations. For the flames (heptane, decane and dodecane) at extinction, the coefficients of mode 1 do not have any significant content above 100 Hz, due to the pronounced slow transverse motion, while the flame far from extinction has higher frequency content.

5.1.6.2 OH-PLIF POD

The first few OH-PLIF POD modes of the four stable flames are shown in Figs. 47a-d (upper). Mode 1 overall shows that when one side lifts-off the corner of the bluff

5. Spray flame behaviour at the blow-off event

body, the other side tends to remain attached (e.g. flame D1S1: Fig. 47c). It may suggest the asymmetric lift-off. For some of the fuels, a mild peak at 24-60 Hz associated with this motion: flame E1S1, none; H1S1 and D1S1 at 34.18 Hz; DD1S2 at 58.59 Hz. For low volatility flames D1S1 and DD1S2, mode 2 (Figs. 47c-d, upper) suggests that when there is significant OH at the fuel injector (the apex of the inner conical flame), the rest of the flame shows less OH and *vice versa*. An alternative interpretation is that the flame tends to lift from the nozzle. A mild peak at around 48 Hz and 24 Hz associated with this motion, respectively. This spatial feature is not obvious in the first few modes of the high volatility fuels of ethanol and heptane (Figs. 47a-b). Mode 3 of the stable decane and dodecane stable flames shows the inner OH branch roughly aligned with the spray, appearing continuously, while the outer flame branch is absent. No peak is seen associated with this motion. A similar spatial feature is highlighted in modes 4-5 for stable heptane flame, but is not shown for ethanol flames. Mode 4 or mode 5 of the low volatility fuels shows the asymmetric motion associate with the lifted OH at fuel nozzle exit, and a mild peak at around 34-44 Hz is shown. This feature is also shown in mode 5 for heptane stable flame H1S1 and ethanol extinction flame E1B, but is less pronounced in the first few modes for the ethanol stable flame E1S1.

The four extinction flames remain more attached to the corners of the bluff-body, especially for flames of low volatility fuels (Figs. 47c-d, lower). Some similar features are highlighted in the first few modes as in the ones for the previous discussed stable flames: Mode 1 (Figs. 47a-d lower) shows an increase of OH on one side when the other side has a reduction in OH. A broad peak at around 24-44 Hz separately is associated with this structure. Higher modes show a behaviour characterised by asymmetric lift-off (one side remains attached while the other lifts-off) and flame breaks. Another feature with these modes of the extinction flames is the thicker appearance of the outer branch and the decay of the inner branch, which is different from the dominant modes shown in the stable counterparts.

Next, the POD energy spectrum for the PLIF images (Figs. 48-49) shows that the energy contained in mode 1 is less dominant compared with the one for OH*. Besides, a larger number of modes is needed to represent the same percentage of energy than

5. Spray flame behaviour at the blow-off event

for OH* (i.e., to reach 50% of the energy, around 25 modes is required in OH-PLIF, but in OH* only 5 modes is needed) and that the differences between the flames are smaller. Additionally, the PSD of the OH-PLIF POD coefficients (Figs. 46 b,d,f,h) shows broad peaks at the same frequency range than the OH*, but there is significantly more high-frequency content, with the $-5/3$ slope extending now to the Nyquist frequency of the present acquisition system (2.5 kHz). The spectra show no evidence of the sharper drop-off at 1 kHz observed in the OH*. This may be associated with the intrinsic averaging performed in the line-of-sight chemiluminescence imaging that would tend to smear the small scale motion.

Finally, the instantaneous OH-PLIF images and the reconstructed snapshots are compared in Fig. 50 for the two decane flames: D1S1 at stable condition and D1B at extinction. It shows that the lift-off is reproduced in reconstructed snapshots using the mean and modes 1 to 25 (Fig. 50a, row 4), but is not captured accurately in reconstructed snapshots using the mean and modes 1 only (Fig. 50a, row 2) or modes 1-5 (Fig. 50a, row 3). The snapshots reconstructed using more modes captures the PLIF images in more detail, such as the flame breaks in the inner and outer branch, the thin inner branch, the lifted OH away from the spray nozzle, and the curvature of the outer branch. For the D1B1 flame in particular, the fragmentation, lift-off and attachment to the bluff body seen in the original (Fig. 50b, row 1) is also seen in the reproduction using modes 1-25 (Fig. 50b, row 4). These spatial features are sometimes captured by using modes 1-5 (Fig. 50b, row 3) but with less accuracy. Thus, it was needed to include many modes to achieve a representative reconstruction due to the broader energy content distribution of the POD modes in OH-PLIF compared to the OH*. Exploring how many (or which) modes are needed to reproduce particular features of the OH-PLIF movie can help identify the underlying mechanisms.

The analysis suggests that the footprint of extinction in the present swirl flames, particularly of the low volatility fuels, as seen from line-of-sight OH* images, is the emergence of a wedge-shaped reaction zone, with about one half of the flame quenched, that slowly rotates. From the perspective of planar OH-LIF, global blow-off is manifested by asymmetric lift-off from the corners of the bluff-body, and with severe fragmentation of the inner and outer parts of the flame. For OH*, only mode 1

5. Spray flame behaviour at the blow-off event

is sufficient to recover the flame motion before blow-off, whereas OH-PLIF needs about 25 modes to be properly represented.

5.2 Conclusion

This chapter describes the blow-off correlation and the dynamics of spray flames blow-off, in terms of the transient duration of the blow-off event, lift-off height, quenching percentage of the stoichiometric mixture fraction iso-line, and the POD analysis. The blow-off correlation proposed by Radhakrishnan et al. [45], using the concept of small-scale coherent turbulent structures, is found collapse the blow-off data reasonably well from the present experiments with the various liquid fuels.

The average blow-off duration, τ_{ext} , calculated from the OH* evolution is a few tens of milliseconds for all fuels and a range of fuel loadings. It corresponds to an average value around 11 times the characteristic flow time scale (expressed by D/U_B), but with large scatter. This normalised transient duration is shorter than the one reported [6] for premixed at ~ 38 , and for non-premixed methane flames at ~ 37 with the same burner.

The average lift-off height for all the flames studied here is around $(0.1 - 0.4) D$, which decreases as the air bulk velocity increases, meanwhile the occurrence of the attachment (zero lift-off height) event increases. The mean lift-off height seems increase as fuel volatility decreases under the identical fuel and air flow rates conditions.

The quenching fraction of the stoichiometric mixture fraction (ξ_{st}) iso-line is studied via combined CH₂O and OH PLIF imaging technique of two stable heptane flames at far from and close to blow-off condition. The measurement is not applied for the other fuels due to the intense interference from the fuel fluorescence and the low signal to noise ratios. It is found that in heptane flames, the quenching percentage along the ξ_{st} iso-line increases at approaching blow-off condition: it is 0.21 ± 0.136 at far from blow-off (flame H1S1) and 0.34 ± 0.167 at close to blow-off (flame H1S2). The morphology of OH images at different departures from blow-off reveals that the integral OH area decreases as approaching blow-off; the OH is more fragmented at the blow-off condition.

5. Spray flame behaviour at the blow-off event

Finally, POD has been used for the analysis of 5 kHz OH* chemiluminescence and OH-PLIF images from the four fuels spray flames at stable condition and at blow-off condition. Similar dominant spatial features are revealed by the first few POD modes for the different fuels. The OH* POD modes overall indicate a strong transverse motion more prominent at the blow-off condition than at the condition far from blow-off for most of the fuels except ethanol, for which an axial oscillation motion is more pronounced at extinction. The OH-PLIF POD modes highlights an asymmetric lift-off at bluff-body, and flame breaks, fragmental, flame branch thickening at extinction. Additionally, both OH* and OH-PLIF first few POD modes shows the attachment to the bluff-body at blow-off conditions. The reconstructed snapshots from the first few POD modes enable visualise the basic flame fluctuation structure without underlying small-scale fluctuations. Reconstructed snapshots by the first five OH* POD modes reveal a wedge-like shape slowly rotating at extinction condition. However, it requires more modes in the reconstruction of OH-PLIF (25 modes in the current cases) than OH* to reveal accurately the lift-off, flame breaks, and the attachment features of the extinction flames.

The analysis in this chapter provides useful information for validation of combustion models focusing on local and global extinction.

5. Spray flame behaviour at the blow-off event

5.3 Tables for Chapter 5

Table 5. Average lift-off heights of stable and unstable spray flames. The fuel flow rate (\dot{m}_f) for each condition was 0.27 g/s.

Name	E1S1	E1S2	E1B	H1S1	H1B	D1S1	D1S2	D1B	DD1S2	DD1B
U_b [m/s]	17.1	20.0	21.6	17.1	22.8	17.1	20	20.3	17.1	20.1
U_b/U_B	79%	93%	1	75%	1	84%	98.5%	1	85%	1
$\phi_{overall}$	0.19	0.16	0.15	0.32	0.24	0.31	0.27	0.24	0.27	0.27
h_{lf}/D	0.25	0.18	0.17	0.25	0.23	0.38	0.19	0.08	0.41	0.22

5. Spray flame behaviour at the blow-off event

5.4 Figures for Chapter 5

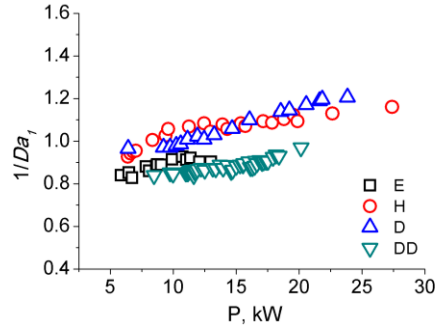


Figure 35. The blow-off limits correlation for the four fuels studied in this work (E-ethanol; H-heptane; D-decane and DD-dodecane), calculated with the method proposed by Radhakrishnan et al. [45].

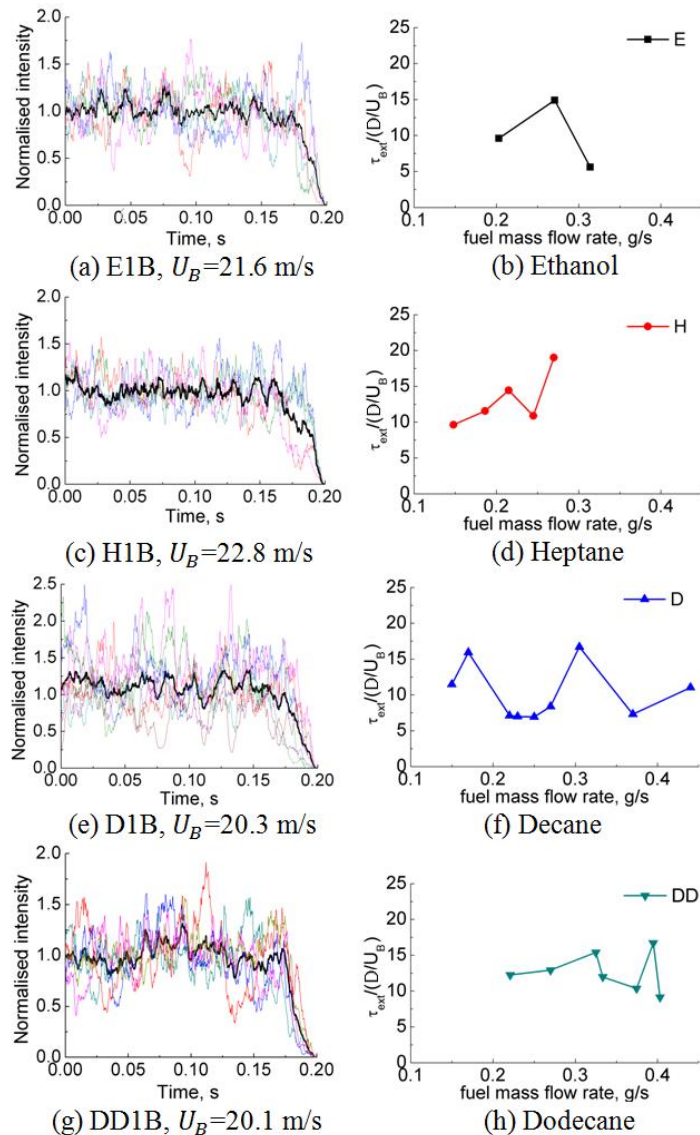


Figure 36. (Left) Integrated OH^* during the blow-off event (the color line stands for instantaneous time series, black line indicates the average value) and (right) the normalised transient duration at various fuel loadings of flames of (a,b) ethanol (flame E1B), (c,d) heptane (flame H1B), (e,f) decane (flame D1B) and (g,h) dodecane (flame DD1B). The fuel flow rate of (a),(c),(e), and (g) is 0.27g/s .

5. Spray flame behaviour at the blow-off event

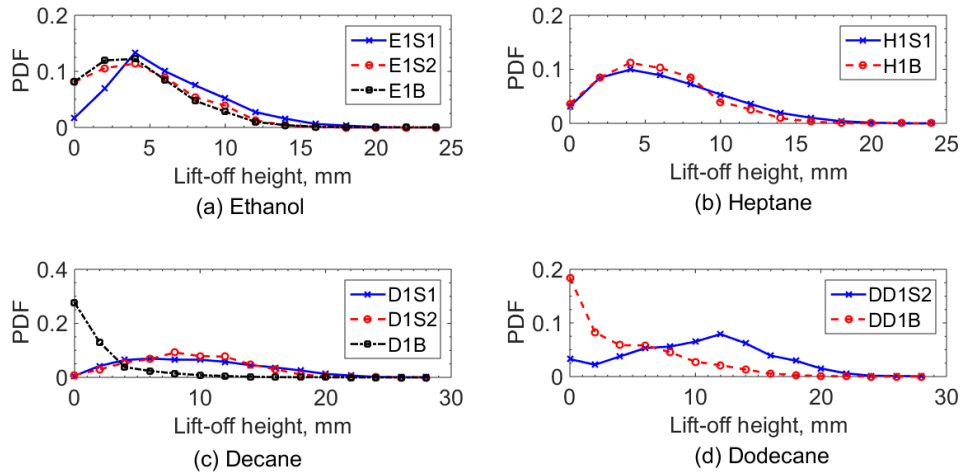


Figure 37. PDF of lift-off height of flames of (a) ethanol, (b) heptane, (c) decane, and (d) dodecane at different distances from the blow-off condition. The fuel flow rate for all the flames is 0.27 g/s. The flow parameters are listed in Table 1.

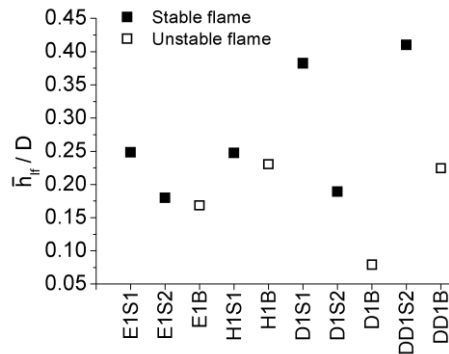


Figure 38. The average lift-off height normalised by the bluff body diameter for various flames. The fuel flow rate is 0.27 g/s and the air velocity for each flame is marked on Fig. 16.

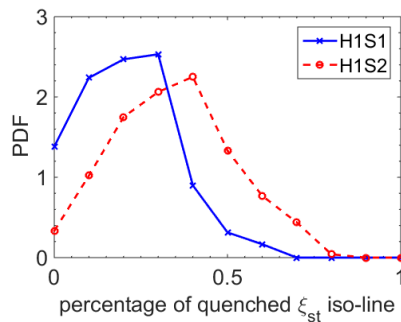


Figure 39. PDF of the percentage of quenched stoichiometric mixture fraction iso-line of heptane spray flames at far from (H1S1) and close to (H1S2) blow-off condition. The fuel flow rate for both flames is 0.27 g/s. The flow parameters are listed in Table 1.

5. Spray flame behaviour at the blow-off event

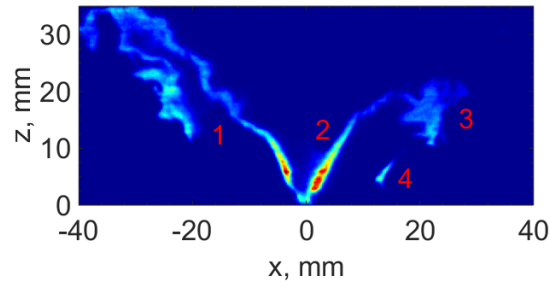


Figure 40. An example OH-PLIF image of stable decane flame (D1S1, fuel flow rate is 0.27g/s and air bulk velocity is 17.1m/s). The image includes four separated “islands”. The total area of the binarised OH signal normalised by D^2 (D is the bluff-body diameter) is 0.60. The circularity (F) of these subregions is 0.08, 0.25, 0.57, 0.32 for regions 1-4 respectively.

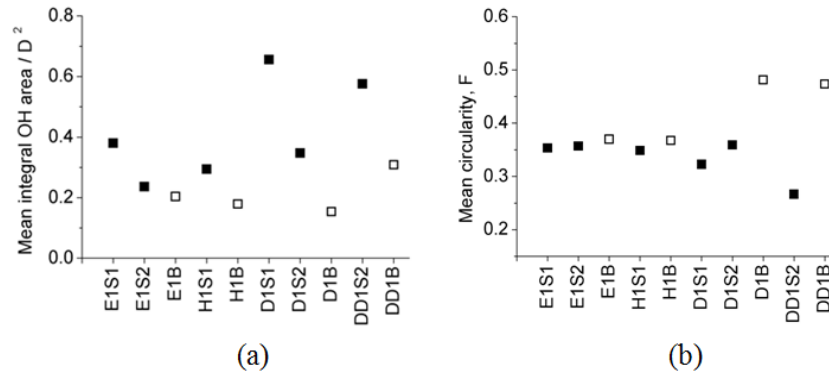
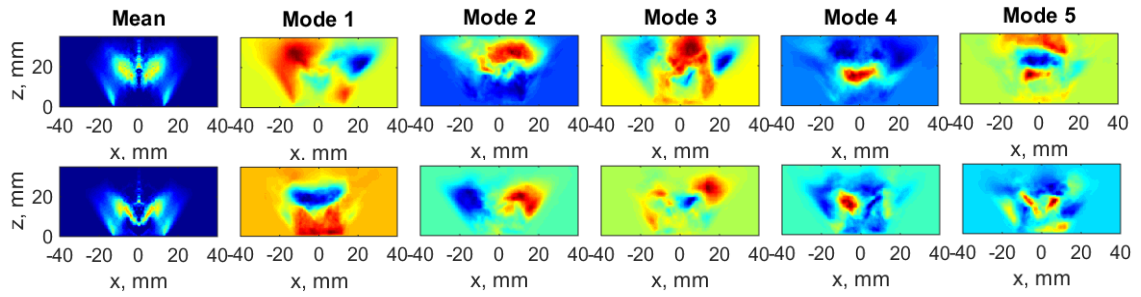
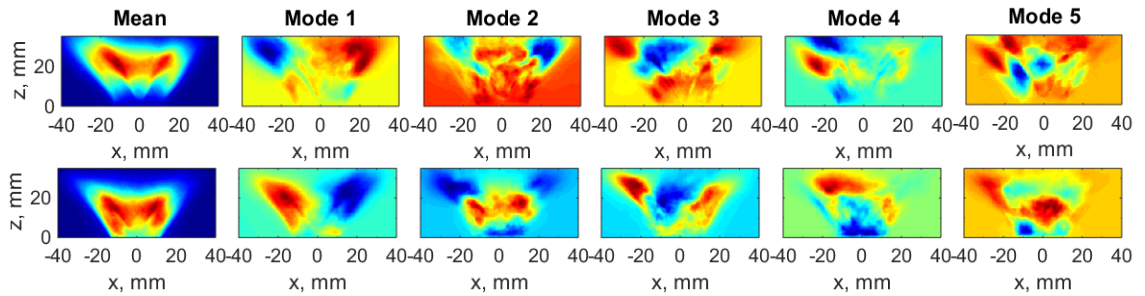


Figure 41. Morphology of the OH-PLIF images from the different flames: the average value of (a) normalised integral binary area, (b) the average circularity, F . Open symbols: unstable flames; Closed symbols: stable flames.

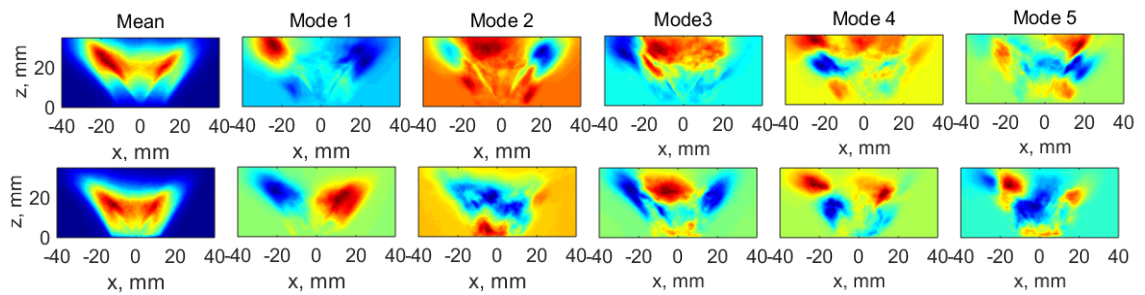
5. Spray flame behaviour at the blow-off event



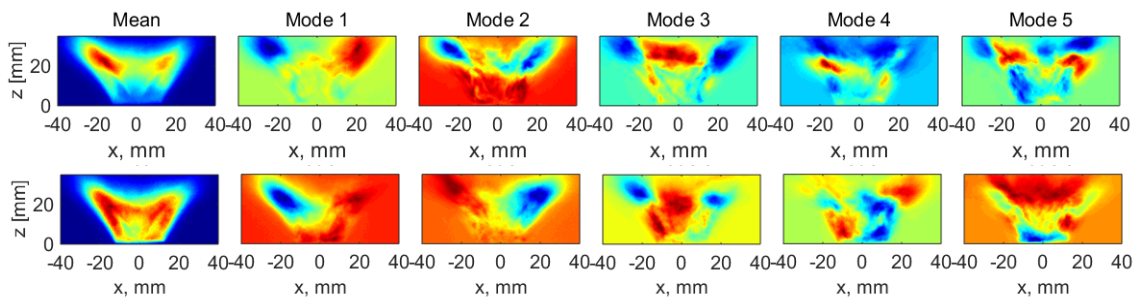
(a) E1S1 (upper) and E1B (lower)



(b) H1S1 (upper) and H1B (lower)



(c) D1S1 (upper) and D1B (lower)



(d) DD1S2 (upper) and DD1B (lower)

Figure 42. Mean image and the first 5 POD modes from OH^* of the four fuels flames at stable condition and blow-off, (a) flame E1S1 and E1B, (b) flame H1S1 and flame H1B, (c) flame D1S1 and flame D1B, and (d) flame DD1S2 and flame DD1B.

5. Spray flame behaviour at the blow-off event

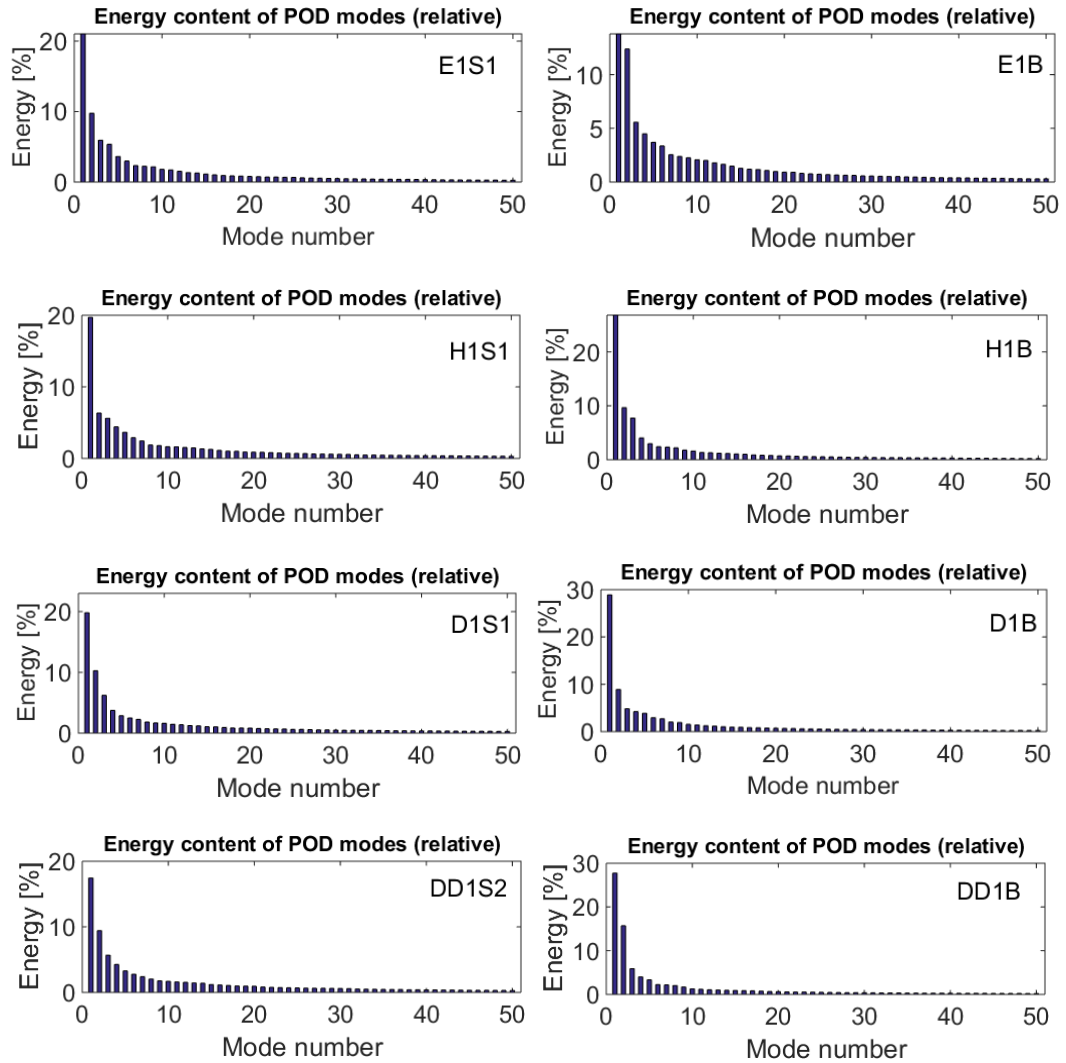


Figure 43. Relative energy of the OH* POD modes of the spray flames at stable condition (left) and blow-off (right). Rows 1 to 4 are flames of ethanol, heptane, decane and dodecane respectively.

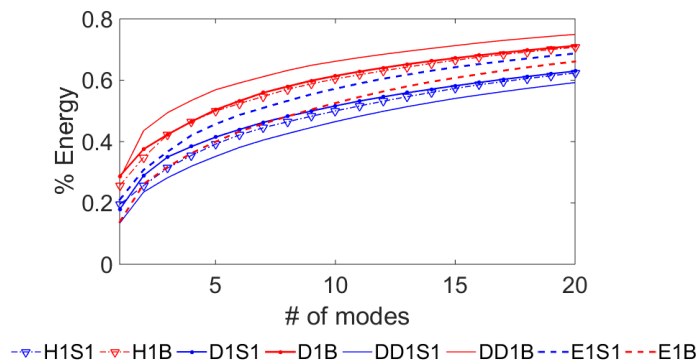


Figure 44. Cumulative energy of the POD modes of OH* chemiluminescence for flames of the four fuels at stable condition and blow-off.

5. Spray flame behaviour at the blow-off event

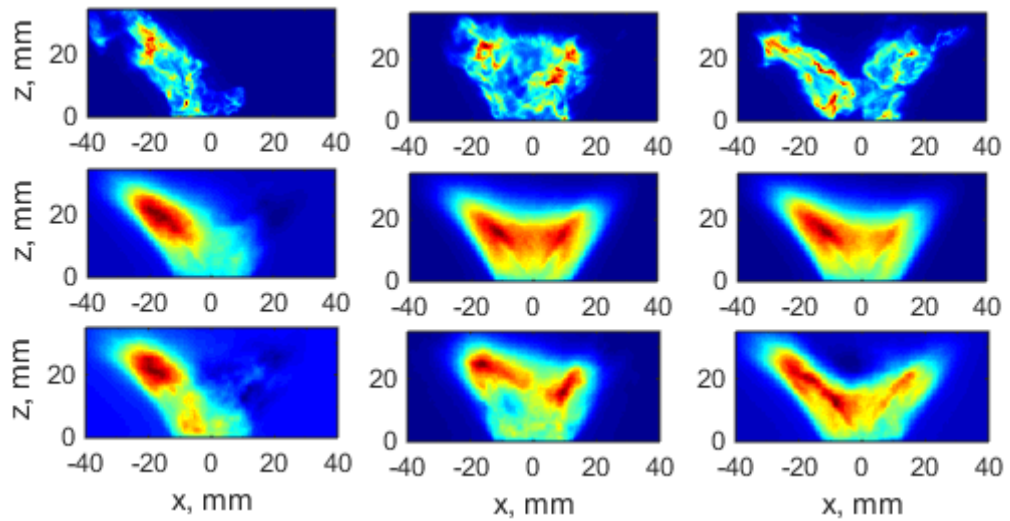
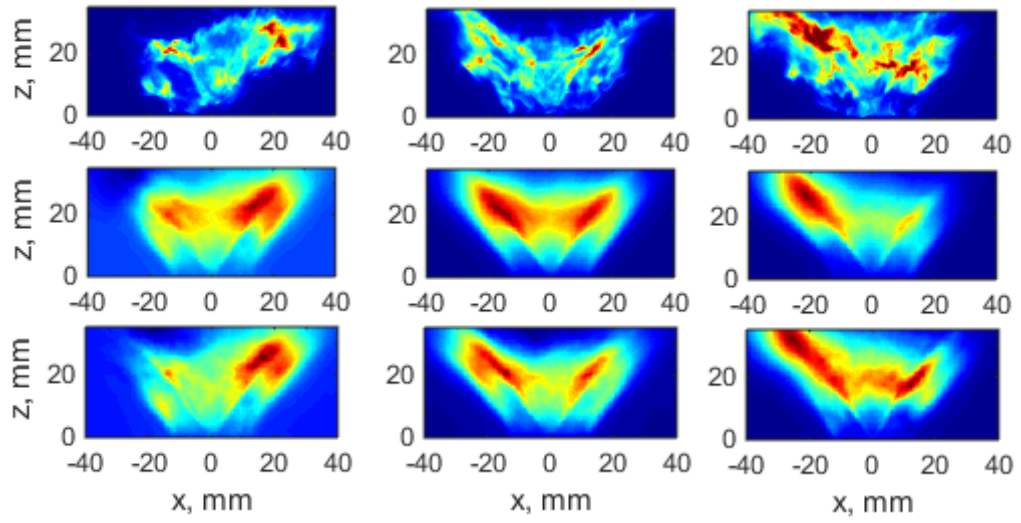


Figure 45. (a) flame D1S1 and (b) flame D1B: (Upper) Snapshots from raw OH* movie; Snapshots at the same times from reconstructed OH* movie using (middle) the mean and mode 1 only; and (lower) the mean and modes 1 to 5.

5. Spray flame behaviour at the blow-off event

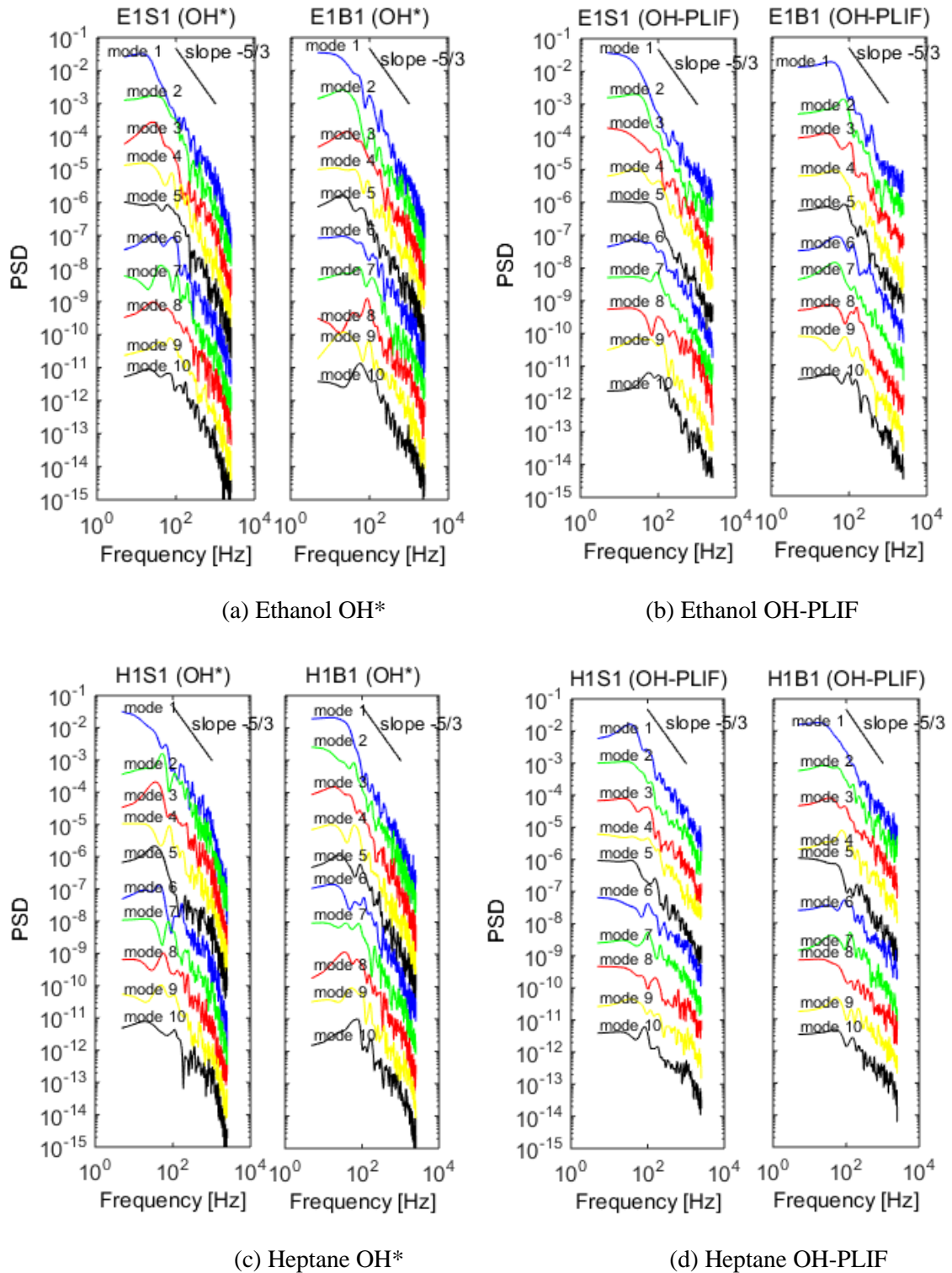
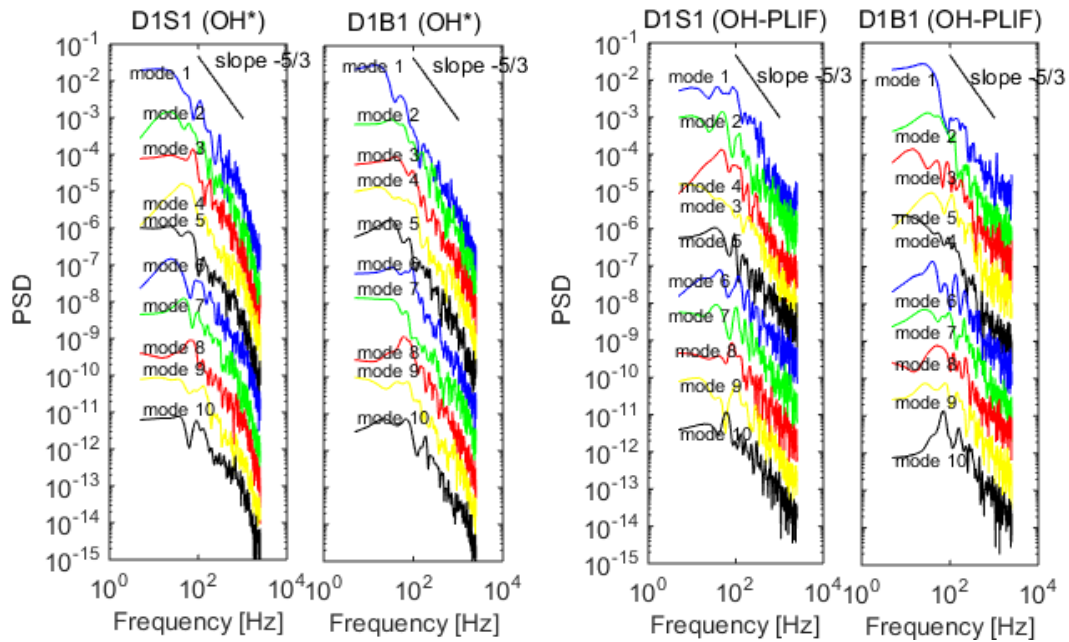


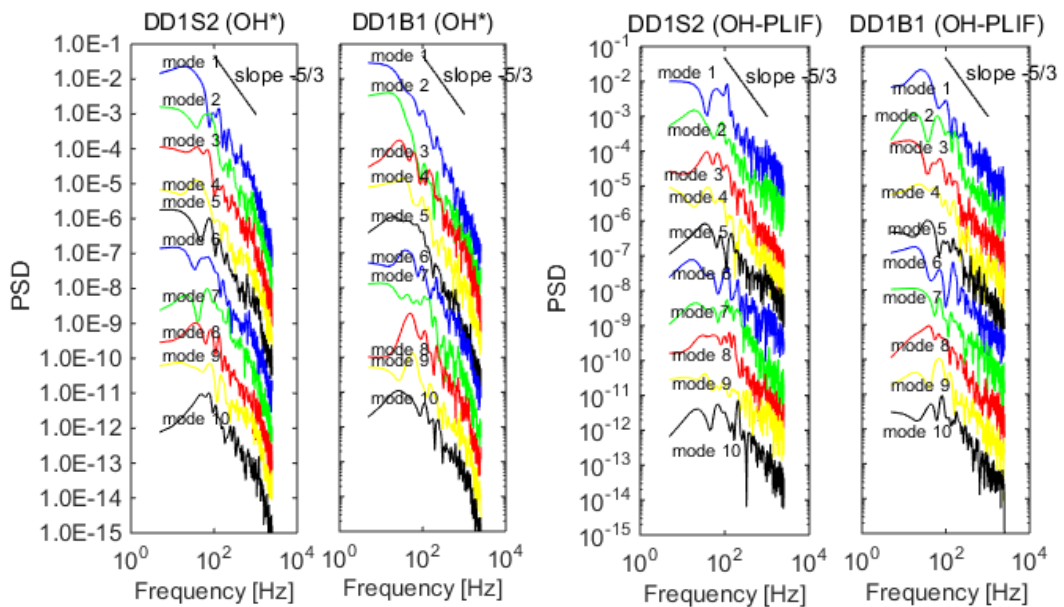
Figure 46. PSD of POD coefficients from modes 1 to 10 of OH* (a,c,e,g) and OH-PLIF (b,d,f,h) for the four fuels spray flames at stable condition (left) and at blow-off (right): (a-b) ethanol flames, (c-d) heptane flames, (e-f) decane flames, and (g-h) dodecane flames.

5. Spray flame behaviour at the blow-off event



(e) Decane_OH*

(f) Decane_OH-PLIF

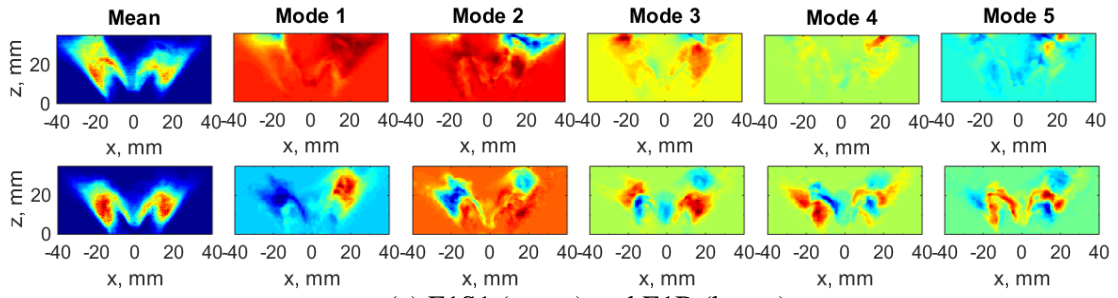


(g) Dodecane_OH*

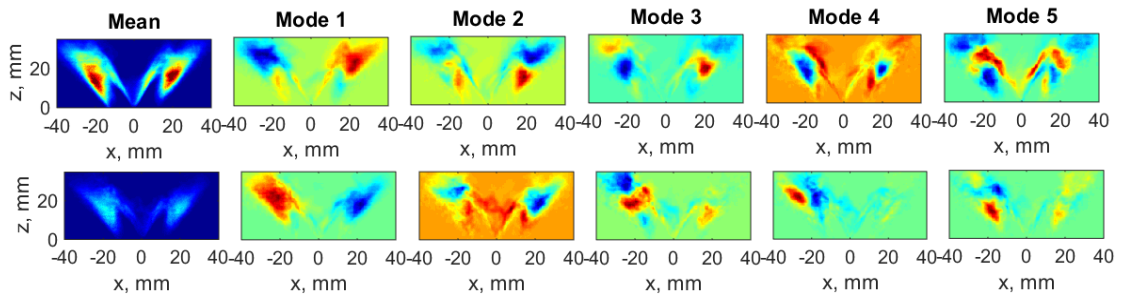
(h) Dodecane_OH-PLIF

(Continued) Figure 46. PSD of POD coefficients from modes 1 to 10 of OH* (a,c,e,g) and OH-PLIF (b,d,f,h) for the four fuels spray flames at stable condition (left) and at blow-off (right): (a-b) ethanol flames, (c-d) heptane flames, (e-f) decane flames, and (g-h) dodecane flames.

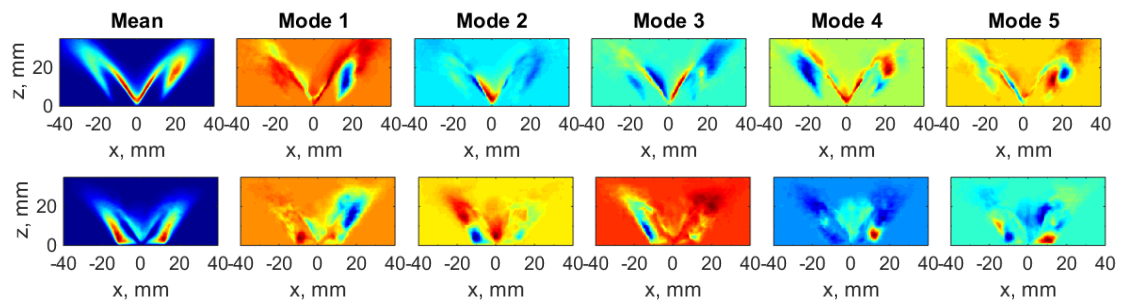
5. Spray flame behaviour at the blow-off event



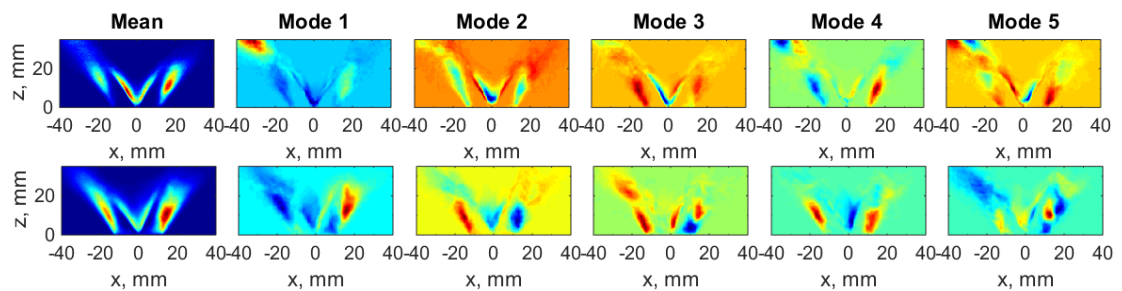
(a) E1S1 (upper) and E1B (lower)



(b) H1S1 (upper) and H1B (lower)



(c) D1S1 (upper) and D1B (lower)



(d) DD1S2 (upper) and DD1B (lower)

Figure 47. Mean OH-PLIF and modes 1 - 5 of spray flames at stable condition (upper row) and at blow-off (lower row), (a) flame E1S1 and flame E1B, (b) flame H1S1 and flame H1B, (c) flame D1S1 and flame D1B, and (d) flame DD1S2 and flame DD1B.

5. Spray flame behaviour at the blow-off event

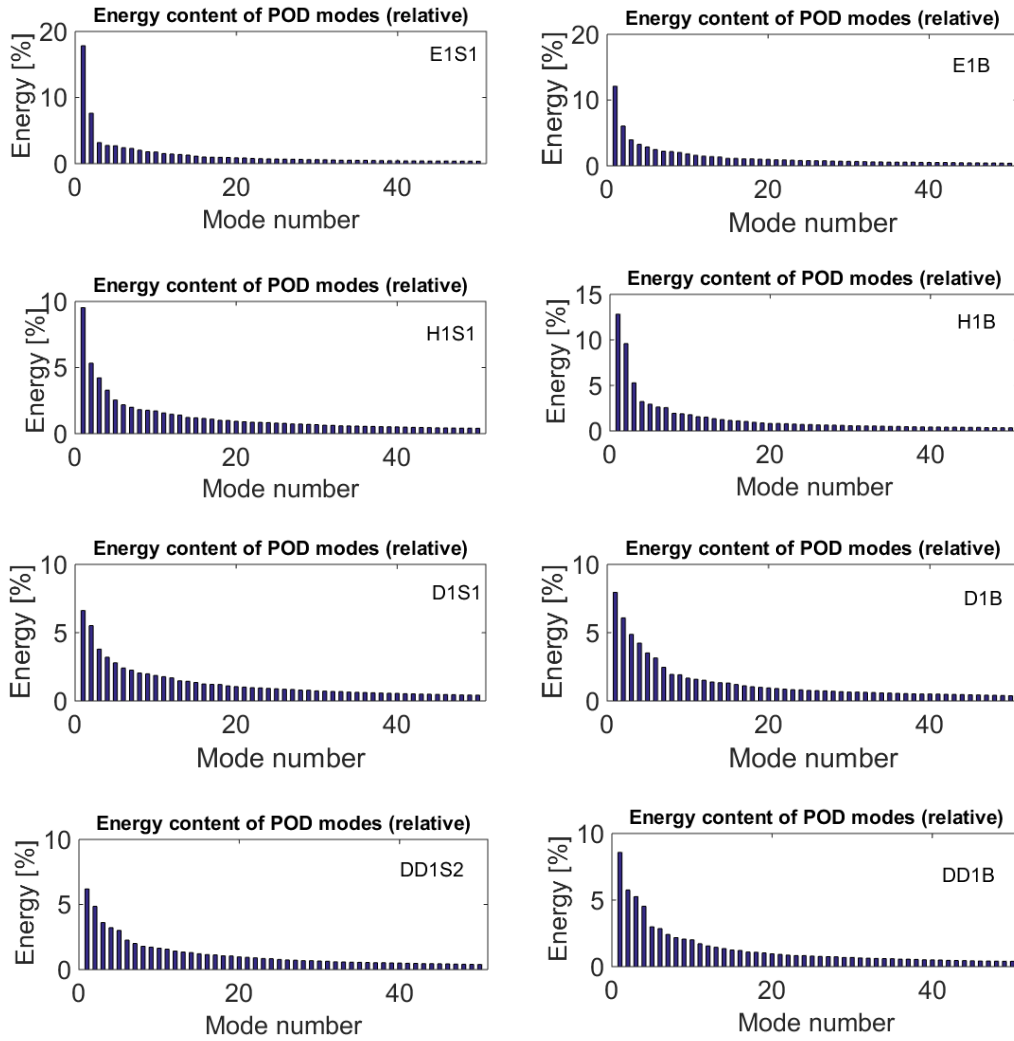


Figure 48. Relative energy of the OH-PLIF POD modes of the spray flames at stable condition (left) and blow-off (right). Rows 1 to 4 are flames of ethanol, heptane, decane and dodecane respectively.

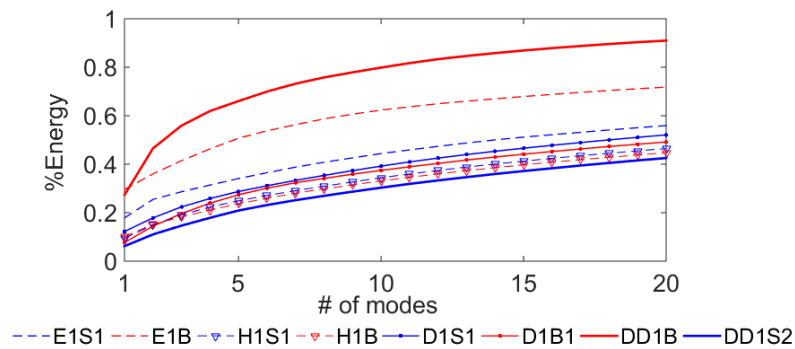
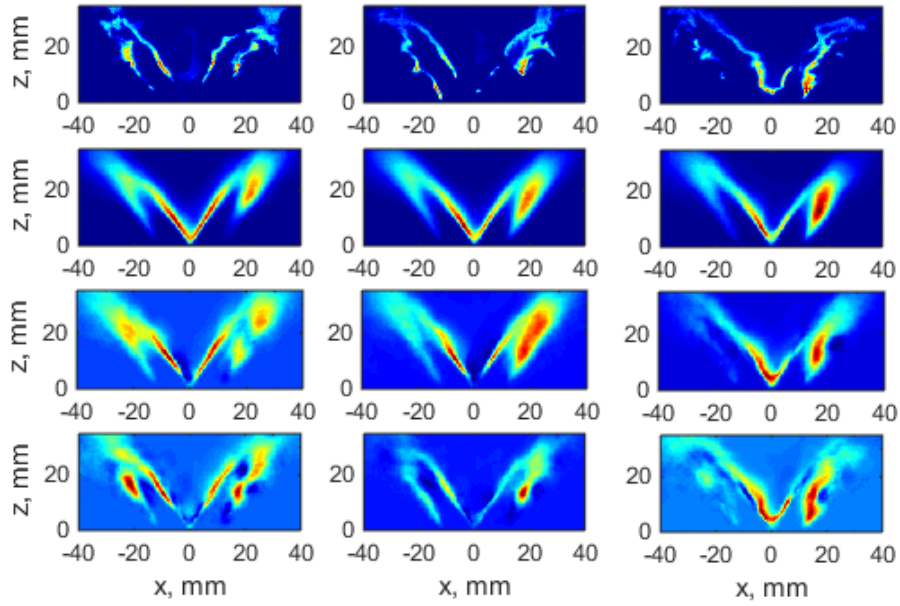
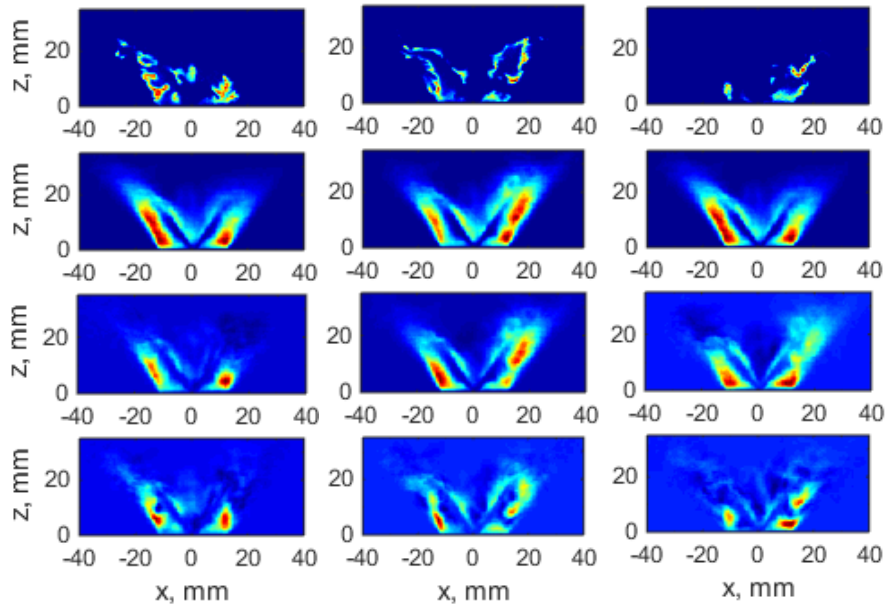


Figure 49. Cumulative energy of the POD modes of OH-PLIF for flames of the four fuels at stable condition and blow-off.

5. Spray flame behaviour at the blow-off event



(a) D1S1_OH-PLIF



(b) D1B_OH-PLIF

Figure 50. (a) flame D1S1 and (b) flame D1B: (row 1) Snapshots from raw OH-PLIF movie; Snapshots at the same times from reconstructed OH-PLIF movie using (row 2) the mean and mode 1 only; (row 3) the mean and modes 1 to 5; and (row 4) the mean and modes 1 to 25.

Chapter 6

Laser-induced breakdown spectroscopy measurements on turbulent flames

This chapter describes an attempt at local air fuel ratio measurements in turbulent gaseous flames and turbulent spray flames by laser-induced breakdown spectroscopy¹ (LIBS). LIBS has been applied in premixed laminar flames to correlate fuel/air ratios under limited lean equivalence ratio ranges. In the current work, a novel calibration scheme is first proposed for gaseous-fuelled flames, so that the LIBS technique could be applied to an extended range of equivalence ratios from lean to rich mixtures. With the proposed calibration method, LIBS was applied for turbulent premixed flame and turbulent jet flames. Next, two different issues are addressed for the performance of LIBS in liquid-fuelled flames: firstly, the development of calibration curves suitable for liquid-fuelled flames and, secondly, the spatial mapping of the distribution of the fuel in the spray flames studied in current work. The LIBS setup and data analysis were included in Ch. 2. Here we continue by the discussion of the calibration scheme and the corresponding results in the various configurations.

¹: the LIBS measurement is a collaborative work with Maria Kotzagianni, who was a PhD student in Department of Physics, University of Patras, Greece. Kotzagianni has provided a valuable contribution to the LIBS technique and a thoughtful discussion on the spectra collection and on the calibration scheme proposed in this work.

6.1 LIBS measurements in turbulent gaseous flames

6.1.1 Burner configurations and flow conditions

The LIBS was first studied in uniform-flowing methane/air mixtures, exiting from a 23 mm inner diameter (ID) tube (Fig. 51a), with mixture compositions spanning a wide range of equivalence ratios (ϕ) from 0 (pure air) to ∞ (pure fuel), for investigating the calibration methods. The flow rates of the mixture varied from 10-200 SLPM, which correspond to velocities of 0.4-8.0 m/s, and therefore Reynolds numbers of 586 to 11720. The mixtures were assumed fully mixed and uniformly distributed across the pipe. The plasma was induced in the centre of the immediate exit of the pipe (corresponding to the height to diameter (h/d) value of 0.4). The different compositions of the mixture were characterised via the mole fraction of methane, X_{CH_4} , which was set to the range between 0 - 1. From X_{CH_4} , the corresponding equivalence ratio (ϕ) was also obtained as a reference.

Following the calibration, LIBS was examined in a turbulent premixed flame of CH_4 , established from the same bluff-body swirl burner (excluding the spray nozzle and enclosure, Fig. 51b). The LIBS technique was evaluated for both cold reactant and hot product with identical ϕ . Note that the recirculating flame is exposed to the ambient air, so ϕ is expected to drop to zero at large distances from the flame brush; while the same ϕ value is expected from both the reactants and the products across the flame.

Finally, LIBS was applied in turbulent lifted reacting and non-reacting methane-air jets. The jet burner (Fig. 51c) consisted of two coaxial stainless steel tubes: the jet (composing of (70%vol CH_4 , 30%vol air) for the reacting case and (30%vol CH_4 , 70%vol air) for the non-reacting case) was supplied from the inner tube (5 mm ID, the length-to-diameter ratio 128); and an annular laminar airflow was supplied from the outer tube (200 mm ID) to surround and protect the jet mixture from disturbances from the environment [207]. The jet exit velocity was 17 m/s ($\text{Re} = 5577$ (reacting) and 5743 (non-reacting)) and the surrounding air velocity was 0.1 m/s ($\text{Re} = 1255$).

In all the cases, methane was supplied by a high purity bottle (99.99%); air was supplied from an air compressor and was pre-filtered for water, particulates, and oil

6. LIBS measurements on turbulent flames

content. Both air and methane flow rates were regulated and measured by rotameters (Roxspur LG/NG series, accuracy $\pm 1.25\%$ FS).

6.1.2 Uniform-flowing methane-air mixtures -- Calibration scheme

6.1.2.1 Spectra of CH₄-air mixtures of different compositions

The typical emission spectra of the LIBS plasma obtained in different CH₄-air composition mixtures (from the 23 mm ID burner) are presented in Fig. 52. When the plasma is induced in air ($X_{\text{CH}_4} = 0$), its emission spectrum is mostly dominated by atomic lines of oxygen and nitrogen. Some of the most intense ones are the N(I)-744.2 nm, N(I)-821.6 nm, N(I)-871.1 nm, O(I)-777.3 nm, and O(I)-844.6 nm. Additionally, some of them are triplets with the examples of the N(I)-744.2 nm and O(I)-777.3 nm, which consist of the N(I)-742.4, 744.2, 746.8 nm lines and the O(I)-777.2, 777.4 and 777.5 nm lines respectively [208]. All of these emission lines originate from the dissociation of the molecules of N₂ and O₂ from the dry air in the experiments, while no emission correlated to carbon containing molecules or carbon atoms are apparent.

When mixing the dry air with fuel, some additional emission lines are observed in the spectra. Apart from the emission correlated to the molecules of air, the well-known molecular bands of cyanogen (CN) are also clearly observed. The CN emission generally consists of the vibrational sequences $\Delta v = 1, 0, -1$ of the CN band system $B^2\Sigma^+ - X^2\Sigma^+$ observed around 359.0 nm, 388.3 nm and 421.6 nm, whose formation is mainly from the dissociation of carbon (e.g. CH₄, CO₂) and nitrogen (e.g. N₂) containing molecules in the plasma, which then combine leading to the formation of energetically excited molecules of CN [209,210]. In addition, the Balmer atomic lines H _{α} at 656.3nm and the H _{β} at 486.1nm of hydrogen are clearly shown in the emission spectra and their presence is also related to the dissociation of the molecules of methane.

When continuing increasing the mixture's fuel content to a richer condition, as in the case of $X_{\text{CH}_4} = 0.7$ shown in Fig. 52, new molecular bands are detected in the visible region of the spectrum in addition to the previous emission, and more specifically at 473.7, 516.5 and 563.5 nm assigned to the C₂ Swan system $d^3\Pi_g - a^3\Pi_u$ with $\Delta v = 1, 0, -1$. In the case of pure fuel ($X_{\text{CH}_4} = 1$), almost all of the aforementioned

6. LIBS measurements on turbulent flames

emission lines are absent excepting for the emission assigned to the C₂ Swan band originating from the molecules of methane. Finally, negligible background emission attributed to Bremsstrahlung process (i.e. high-energy electrons emit photons when they decelerate in collisions; this continuum radiation is usually seen at shorter delay times, i.e. at early plasma times, and is replaced by the element-specific atomic and molecular emission subsequently) is detected in any of the previous emission, due to the long time delay ($t_d = 8\mu\text{s}$) employed between the laser pulse and the beginning of collection, permitting a quantitative analysis based on the total intensities (the integral of the specific atomic or the molecular emission lines) or the ratio of the total intensities of the different species.

6.1.2.2 Integral intensities of species emission lines

To further evaluate the variations of these spectral features present in the different spectra from the various composition mixtures, the total intensities of the atomic and the molecular emission lines were calculated using the averaging method (Ch. 2.4.1.3). Specifically, two atomic (H α , O) and two molecular emission lines (CN, C₂) and some ratios (H α /O, C₂/CN) were examined to find the correlation between them and the mole fraction of methane in the mixture. The total intensity corresponds to the integrated area below the emission line defined around its central wavelength subtracting with the corresponding continuum underneath. Also, the matching emission spectra are the average of 100 scans and any noise from the laboratory light and the flame luminosity collected as a background spectrum has been removed prior to the acquisition of the spectra.

Figures 53-54 represent the total intensities of the H α -656.3 nm and O-777.3 nm atomic lines and of the CN-388.3 nm and C₂-516.5 nm molecular bands respectively as a function of the mole fraction of methane in the various mixtures for three different laser energies. The corresponding equivalence ratios are also marked in Figs. 53-54 as a reference. A different behaviour between the hydrogen and the oxygen atomic lines is seen in Fig. 53. Same trend of each specific emission is observed among the different laser energies used. Firstly, the O-777.3 nm emission decreases sharply with X_{CH_4} , after about $X_{\text{CH}_4} = 0.4$, the atomic emission is completely attenuated. This observation is related either to the reduction of the concentration of

6. LIBS measurements on turbulent flames

the oxygen molecules in the mixture, or to the defined acquisition time of the detector. In the latter case, a shorter detection time is recommended (Ferioli et al. [172]). This is because species concentrations can be rapidly changed by the fuel concentration (which has a strong impact on the measured lifetimes of the emission lines) and the quenching effects stemming from high cooling rate of the plasma.

The hydrogen lines H_{α} -656.3 nm (Fig. 53) for all the three laser energies, increase in the range of X_{CH_4} from 0 to 0.1 and reach a plateau and then decay until $X_{CH_4} = 0.7$. Beyond $X_{CH_4} = 0.7$, the emission of the H_{α} atomic line could not be distinguished from the background continuum emission. The trend of the data point of the H_{α} emission suggests that the self-absorption effect might have occurred during the experiments. Moreover, despite the abundance of hydrogen atoms originating from the methane in richer mixtures, the rapid decay of the hydrogen line for $X_{CH_4} > 0.2$ could alternatively imply some radical-removal chemical mechanism, since the fall of the hydrogen line, and the disappearance of the oxygen line approximately coincide with the initiation of the formation of the C_2 molecular band (Fig. 54, discussed later). Similarly observed, in an experimental research on hydrocarbon liquid-gas mixtures by Kido et al. [181], they report that a stronger quenching of H emission is expected in rich and high pressure environments.

The CN (388.3 nm) emission band increases almost linearly with X_{CH_4} in the range of 0 - 0.15 roughly for all excitation energies (Fig. 54). This feature has been reported in the past for both electrical spark induced and laser (ns and fs laser pulses) induced optical breakdown in methane-air mixtures [174,211]. For even higher values of X_{CH_4} , the CN emission levels off for $0.15 < X_{CH_4} < 0.3$ and eventually decreases to zero. The decrease of CN in the rich mixtures is due to the drop of the proportion of N_2 molecules as X_{CH_4} increases up to 1, when no more N_2 exists in the mixture.

Finally, negligible emission of the C_2 (516.5 nm) molecular band (Fig. 54) appears for low X_{CH_4} values mixtures where dominant CN band is observed until CN band begins to flatten out at around $X_{CH_4} = 0.2 - 0.3$, and then a sudden increase of C_2 band intensity is observed until around $X_{CH_4} = 0.5$, at which the intensity of C_2 reaches a maximum and begins to fall for higher values of X_{CH_4} . Eventually, the intensity of the C_2 band decreases to a small, but finite value at $X_{CH_4} = 1$. These behaviours of C_2 are

6. LIBS measurements on turbulent flames

basically the same for all the laser energies used. It suggests that the original formation of the C_2 molecules is more linked to the mole fraction of methane and the chemical reactions taking place in rich mixtures rather than the impact of the laser beam on the mixture and the plasma formation. It is expected that in general the richer the mixture, the higher the intensity of the C_2 band. However, the decrease is observed here for $X_{CH_4} > 0.5$, which has also been reported in the mixtures of air, CO_2 , N_2 and C_3H_8 studied by Sturm et al. [212]. They explained that the environment of the plasma formation might influence the results, since both the absorption and the plasma conditions may change from case to case and especially when only fuel is present. Also, Li et al. [213] reported that the presence of the combustion products like H_2O and CO_2 far from the spark could cause the decrease of the observed intensities of the intermediates of the flame such as the C_2 and the CN.

6.1.2.3 Intensity ratios of the species emission lines and the calibration scheme

Although the physical mechanisms leading to the reduction of some emissions with increasing methane content are not fully understood yet, a correlation of the H_α/O and C_2/CN versus the mole fraction of methane in the mixture is obtained. The ratios are essentially independent of various experimental parameters, such as the fluctuations of the laser energy, the stochastic events, like the plasma formation, and the collection system. This provides them reliable for direct correlation to the actual mole fraction of methane or the equivalence ratio of the local mixture. Figures 55-56 show the H_α/O and C_2/CN ratio as a function of the mole fraction of methane, in mixtures of various compositions, for three different laser energies: 155, 230 and 300 mJ. Each data point was obtained by the averaging method, and in the case of molecular emissions, their total intensities were determined by the total intensity of the corresponding head bands.

For the range of $0 \leq X_{CH_4} < 0.3$ ($0 \leq \phi < 4.0$), there is an almost linear dependence of the H_α/O ratio to X_{CH_4} for all values of the laser energy used (Fig. 55). Specifically, in the case of the lowest laser energy (squares), the linearity is valid until $X_{CH_4} = 0.3$, after which the slope drops gradually at higher values of X_{CH_4} . The linear dependence reaches to a higher value of X_{CH_4} as the laser energy increases: for $E = 230$ mJ, the same energy used during the experiments with the turbulent flames discussed later in

6. LIBS measurements on turbulent flames

sections 6.1.3 and 6.1.4, the H_{α}/O ratio is proportional to the mole fraction of methane up to $X_{CH_4} = 0.5$ ($\phi = 9.5$), and it reaches a maximum value of $X_{CH_4} = 0.6$ ($\phi = 14.3$) for the highest energy employed ($E = 300$ mJ, Fig. 55). Such progression is mostly caused by the O-777nm line, since the higher energy gives rise to more excited atoms of oxygen making the lifetime of the atomic line in general shifted to longer times [172]. This means that under the current detector's temporal configuration and for the higher energy, the O-777.3nm line can be detected in even richer mixtures. But although this linear dependence seems to be improved by the increase of the laser energy, the usage of this ratio *vs.* X_{CH_4} as a calibration curve could safely be used in the range $0 \leq X_{CH_4} < 0.3$. Moreover, the H_{α}/O ratio *vs.* X_{CH_4} is to be used in the lower range of X_{CH_4} until the value at which the sudden emerging of C_2 band appears (discussed later).

The C_2/CN ratio (Figure 56), on the other hand, is zero for $X_{CH_4} < 0.3$, in accordance to the comments of Fig. 54. As mentioned earlier, the C_2 molecular band occurs only at very rich fuel-air mixtures ($X_{CH_4} \geq 0.3$, i.e. $\phi \geq 4.0$, Fig. 54) explaining why the ratio is negligible until that value. However, after the formation of the C_2 band, the C_2/CN ratio is monotonically increasing to the mole fraction of methane up to $X_{CH_4} = 0.9$. In the case of even more methane in the mixture, the intensity of the CN molecular band becomes very weak levelling the intensity of the background emission (Fig. 54), suggesting that the ratio blows-up for such extreme values. The laser energy plays little role in the C_2/CN ratio for values of X_{CH_4} up to 0.9, while the differences observed in the values of the C_2/CN ratio for the different energies and for X_{CH_4} ranging between 0.9-1.0 are related to the almost complete absence of the CN band.

Based on the above discussions, one could suggest that the calibration curves from the two ratios *vs.* X_{CH_4} shown in the Figs. 55-56 together could be applied for the measurement of the methane content. The x-axis can alternatively be expressed in terms of the equivalence ratio, or in terms of the mass fraction of methane, which can be inferred as the mixture fraction in flames. Out of all the spectral features in the acquired emission spectrum, the C_2 molecular band is the clearest indicator of which of the two ratios should be used. Thus, in case of absence of the C_2 molecular band, the H_{α}/O ratio (Fig. 55) will be the right diagnostic tool for the determination of the

6. LIBS measurements on turbulent flames

X_{CH_4} , otherwise the indication of the C_2 band implies that the C_2/CN ratio (Fig. 56) should be used. In both, the influence of parameters such as the laser energy and the collection optics is eliminated assuring the validity of the technique. This measurement strategy is employed for turbulent premixed and non-premixed flames in Sections 6.1.3 and 6.1.4.

6.1.2.4 Shot-to-shot variation

Shot-to-shot variations of LIBS were investigated for the measurements in turbulent flames, where there may be large temporal and spatial fluctuations in equivalence ratio [214]. LIBS experiments were carried out in uniform premixed methane-air mixtures and the results (Figs. 57-58) were acquired based on the analysis of 100 single-shot independent measurements. The precision of the LIBS technique was examined.

Figures 57-58 show the single-shot spectra line intensity ratios H_α/O and C_2/CN for different mole fractions of methane. Each data point corresponds to a single shot in the uniform mixture of the indicated composition. For $X_{\text{CH}_4} < 0.1$, the shot-to-shot variation of the H_α/O ratio is small and about 15 % of the mean value. As the mole fraction of methane gets higher, the variation increases significantly. This behaviour overlaps with the region of X_{CH_4} where the H and O atomic lines intensities decay shown in Fig. 53. It indicates that a greater stochasticity of the plasma processes is associated with this reduction of the intensities of the emission lines, leading to a larger divergence from the average value. On the contrary, such an increase in the variation of the C_2/CN ratios vs. X_{CH_4} is not occurring, as can be seen in Fig. 58, with the root-mean-square (rms) of C_2/CN ratios roughly 20% of the mean value. This scatter can be correlated to a number of different parameters, such as the energy stability of the laser source, the plasma's temperature and electron density, or even the interaction with the mixture. Similar shot-to-shot measurements have been performed in a four-cylinder engine [178]. The relative standard deviation in their case was ranging between 2.7-3% of the mean value, which was much less than the one presented earlier, which varied from 15-20%. The higher rms value obtained in the current measurements could be related to the spectrometer and collection delay time used. Further work along these lines could be performed.

6. LIBS measurements on turbulent flames

The ratios H_α/O and C_2/CN were obtained from the instantaneous and the averaging methods respectively at different values of X_{CH_4} and are plotted in Figs. 59-60 for the range in which the calibration curve is intended to be used. Clearly, the two approaches are very close for lean (based on H_α/O) and for very rich compositions (based on C_2/CN). In the range $0.15 < X_{CH_4} < 0.30$, where the H_α/O atomic line can still be used with the average method (Fig. 55, the upper limit for this calibration branch depends on the laser energy), the correlation becomes non-linear and the precision of the single-shot measurement is not good for shot-to-shot measurements. Alternatively, the fact that there may be significant shot-to-shot variations of the chosen ratios for some mixture compositions may call in to question the use of the averaging method for the calibration and/or the measurement. The reason for this is, if the ratio of each peak is taken from the average spectrum acquired/accumulated by the spectrometer, this procedure is not necessarily identical to finding the ratio from each single acquisition and then averaging. This may not be a problem for laminar flames, where the equivalence ratio is not fluctuating in time, but it could be an issue for turbulent flames. The shot-to-shot variations should be explored further with high-quality gated spectrometers.

6.1.3 Turbulent premixed flames

Figure 61(left) shows the photograph of the turbulent premixed flame studied. The equivalence ratio in the premixed flame is expected to be constant across the reactants (region A) and the products (B), and it is expected to reduce to zero at the edges of the annular jet towards the ambient air and to decrease as we go downstream. Figure 62 reproduces these expectations. In particular, the central region of the flame, which is filled with combustion products, has the same equivalence ratio as the incoming mixture (empty symbols, at four downstream locations), which demonstrates that the technique measures the correct ϕ in hot products of a flame. In addition, the shot-to-shot method (pink-solid) seems to produce more consistent results than the averaging method (black-solid) at the flame front, across which ϕ is again uniform, as expected. These results demonstrate that the LIBS spectra, when acquired from plasmas with enough energy, reproduce the proper equivalence ratio in both the reactants and the products sides of turbulent premixed flame.

6.1.4 Turbulent reacting and non-reacting jets

A photograph of the lifted jet flame investigated is shown in Figure 61 (right), the horizontal lines indicating the downstream locations where the mixture fraction measurement was performed via LIBS technique. Note that the flame was lifted. This flame was achieved with 30% (by volume) air mixed with the fuel (methane, 70% vol), which is small enough premixing for the flame to be of a non-premixed character. In a second series of experiments, the amount of fuel at the jet was very small (30% by volume), which does not result in an established flame and the fuel behaves like a passive tracer. The presence of fuel can still be detected by the LIBS spectra hence providing a measurement of the mixture fraction in a non-reacting axisymmetric jet, for which significant information exists for comparison purposes.

Figures 63-64 show the mean mixture fraction, based on 100 instantaneous spectra at each point shown. Each of these spectra has been analysed with the method described earlier in Ch. 2.4.1.3. Each spectrum gave a single value of carbon mass fraction, which was further normalised by the value at the nozzle exit to give the mixture fraction. Therefore, the single spectrum acquired here at every point resulted in a single measurement of mixture fraction, from which the mean was calculated and presented in Figs. 63-64.

The claim that the measurement gives the mixture fraction relies on the assumption that the LIBS H_2/O or C_2/CN ratio is independent from whether the mixture is unreacted or fully burnt. This assumption is partly justified by the data with the premixed flame (Ch. 6.1.3), which gave the same equivalence ratio in the products and the reactants. Figure 63 presents the data measured in the turbulent jet flame (shown in Fig. 61, right). It is expected to observe a wide range of compositions and reaction progress at the same point, due to the intense inhomogeneity of the mixture and the flame base fluctuations. As an independent measurement of mixture fraction is not available, it is not easy to assess the quantitative accuracy of the data in Fig. 63. However, some interesting features are implied by further exploration of these data. First, when the mean mixture fraction (Fig. 63 left, solid) is normalised by the value at the centreline, a self-similar profile emerges (Fig. 63, right). Next, the rms divided by the centreline mean value (Fig. 65, right) gives values around 25%, decreasing to zero

6. LIBS measurements on turbulent flames

towards the air. This behaviour is fully consistent as expected from jet diffusion flames. In detail, for the data at 30 jet diameters, the mixture fraction profile measured (Fig. 63 left, red-solid) is not far from expectation from empirical correlations [90] (Fig. 63 left, red-empty). When the jet mixing correlation is applied to flames, the burnt gas density has been used, following Ref. [215].

The fuel mass fraction measurements have also been performed in a jet with low CH_4 concentration which does not lead to the establishment of a self-sustained flame. Obviously, the volume hit by the laser spark and a small region downstream do react temporarily due to the local initiation of chemical reactions, but the dominant streamwise flow takes these regions downstream, no flame propagates upstream, and the parts of the jet upstream of the LIBS volume are not affected and are therefore treated as inert. The results are shown in Fig. 64. It shows that the LIBS measurement agrees quantitatively with previous passive scalar mixing experiments [90] (Fig. 64 left) and the measurement reproduces the self-similar behaviour expected in such inert turbulent axisymmetric jet (Fig. 64 right).

The rms values of the instantaneous mixture fraction, normalised by the measured mean value at the centreline, are shown in Fig. 65 (left: non-reacting case; right: reacting case). This normalised ratio (rms/mean scalar at the centreline) of turbulent axisymmetric jets in the self-preservation region reaches an asymptotic value of about 20-25% [216], and the present measurements give that this ratio is constant with streamwise distance and about 27%. This may imply that the present LIBS system reproduces reasonably well the expected rms of mixture fraction on the axis of these turbulent jets. Away from the axis, the rms smoothly decreases to zero, as expected. However, that the reasonable measurement of the rms here is mostly attributed to the fact that in the present experiments, the absolute amount of fuel is low at the measurement locations, due to mixing with ambient air and due to the air premixing in the jet fluid, which means there are very few samples with large enough carbon content to give C_2 signal and hence rely on the C_2/CN part of the calibration scheme that has lower precision.

These results and the good agreement with the expected mixture fraction distribution in jets suggest that the present LIBS technique, with the novel calibration

6. LIBS measurements on turbulent flames

scheme proposed, can measure the mean mixture fraction in turbulent non-premixed systems with acceptable accuracy. It can also provide a good approximation to the rms of the mixture fraction, provided there are not too many fluid samples with very high carbon content in which case the mean is captured well but the rms is higher due to the worse precision associated with the generation of the CN and C₂ lines.

6.2 LIBS measurements in swirling spray flames

6.2.1 Burner configurations and flow conditions

In order to obtain the calibration curve of LIBS measurements in the spray system, the LIBS plasma was induced in a set of spatially uniform dispersion of C₇H₁₆ (liquid and gaseous phases) - air mixtures at various overall equivalence ratios ($\phi = 0$ to 10) in a spray burner (Fig. 51d, developed by Mukund Gupta at Cambridge University) [217]. The spray was produced by an air-assist atomiser in a plenum, followed by mixing with extra air and a contraction to produce a uniform flow of air carrying the droplets. Due to the finite residence time of the droplets between the injection zone until the plasma induced region, at the atmospheric conditions studied, some of the liquid fuel may have evaporated. Therefore, the LIBS measurements were performed in a region of known overall equivalence ratio with an unknown percentage of fuel that exists in the vapour phase. However, the laser spark energy is chosen high enough to ensure the ionisation of all the fuel content in the measured volume that is discussed later.

The same enclosed swirl spray burner shown in Fig. 1(left) with a different atomiser (Lechler, #212.054.17.AC, hollow-cone spray angle of 60°) was used to stabilise a heptane spray flame identical to the one studied in Ref. [6]; four pieces of UV grade optical quartz plates formed an enclosed area of 97 mm width square with 150 mm length. The fuel was pressurised by N₂ supplied from a nitrogen-compressed cylinder. The air flow was supplied by an air compressor and further dried and particle filtered. The air and fuel flow rates were metered using respectively an mass flow controller (Alicat, MFC 1000 SLPM, uncertainty of \pm (0.8% of reading + 0.2% of full scale (FS)); repeatability of \pm 0.2% of FS) and a Bronkhorst liquid flow controller (LIQUI-flow, L30, 0-2 g/s, 0.01 g precision). The fuel and air flow condition was 0.12 g/s and 500 SLPM respectively. The global equivalence ratio was $\phi = 0.167$

6. LIBS measurements on turbulent flames

(corresponding to the fuel air ratio (FAR) of 0.011). Note that a wide range of the local ϕ from zero (in the air stream) to very high values (close to the spray injection) is expected in the studied configuration; obtaining this distribution is the target of the present LIBS measurement.

Figure 66 shows photographs of the studied swirl spray flame. The different regions of the flame are indicated: A – corresponds to the annular air jet and the outer recirculation zone, B - denotes the flame brushes around the hollow cone spray, and C - indicates the inner recirculation zone where gases temperature should be high and with absent spray. The horizontal lines (Fig. 66 right) indicate the downstream locations where radial profiles of ϕ were measured.

6.2.2 Uniform dispersed C_7H_{16} -air mixture

Performing LIBS measurements in droplets including the formation of the plasma and the acquisition of the emissions are challenging because of the large influence of the droplets on the occurrence of breakdown. Uncertainty occurs in the induced plasma positions mostly due to the inconsistency of the amount of droplet at the Rayleigh length (the distance along the propagation direction of a beam from the waist to the place where the area of the cross section is doubled) and the small fluctuations of the laser energy [180,183,218]. This implies that the effective spatial resolution of the spark volume is lower than the instrument. This is illustrated from direct photographs of laser pulse induced sparks in a uniform C_7H_{16} -air dispersion at a high enough flow speed condition so that a flame is not ignited (Fig. 67). The volume of the plasma varies from the three cases shown is attributed to the various focusing conditions of the laser beam. From top to bottom, the focal length of the focusing lens is 150 mm, 75 mm and 50 mm respectively. It shows that the breakdown of the medium and the plasma formation are occurring at different positions due to the different values of the Rayleigh length (the focus point for each case is on the centreline of the burner exit). In the case of the focusing lens with $f = 50$ mm the sparks are formed at the focusing point, but for the other two lenses $f = 75$ mm and $f = 150$ mm the sparks are created in random locations spanning many millimetres before and at the focal plane along the laser pulse propagation. Bourgeois et al. [219] suggested that when the incident laser beam is absorbed by the droplets which are instantaneously vaporised, it leads to a

6. LIBS measurements on turbulent flames

vapour explosion. This explosion generates high density spherical waves which may reduce the propagation of the laser beam. The front of these waves heats up by absorbing energy from the incident laser beam and the plasma occur some tens of ns later. As a result, the origin of each micro-plasma is caused by the presence of several individual droplets at different positions within the focal volume. Therefore a shorter focal length lens is preferred to acquire a uniform and compact plasma formation. The 50 mm lens seems appropriate. However, the $f = 75$ mm focusing lens was used in the measurements in the studied swirl flame due to the limitation from the enclosure's dimension. In the measurement, the average-method was used. Each spectrum shown (Figs. 68a-b) corresponds to an average of 200 single-shot measurements which improves dramatically the signal to noise (S/N) ratio of the spectrum. The total intensities of the spectral lines ratios were obtained and plotted as a function of overall equivalence ratios as calibration curves for the measurements in the swirl flames. Since the droplet-containing region has small dimensions in the swirling flame (see Mie scattering image, Fig. 71, discussed later), the issues of broadened spatial resolution of the LIBS measurement and the natural fluctuations of the S/N ratio are not big, although a more systematic study is needed.

Figure 68a plots some typical LIBS spectra acquired from the uniform-spray burner for the calibration scheme. Different emission lines features were exhibited when the plasma was formed in C_7H_{16} -air dispersion of various overall equivalence ratios. Similar to the lines observed previously of the plasma emission induced in gaseous mixtures of CH_4 -air, one of the most intense spectral features shown in these spectra is the molecular band of cyanogens (CN), $B^2\Sigma^+ - X^2\Sigma^+$ with $\Delta v = 0$ at 388.3 nm, together with the one with $\Delta v = 1$ at 359.0 nm and $\Delta v = -1$ at 421.6 nm. The appearance of this molecule is attributed to the initial dissociation of the present molecules of heptane (C_7H_{17}) and nitrogen (N_2) and the subsequent combination for the formation of the excited molecules of CN. In the case of pure air ($\phi = 0$, Fig. 68a), the absence of one of these two constituents at the plasma formation position results in the absence of the CN band from the acquired spectra.

Apart from CN molecular bands, some other atomic lines and molecular bands are also recognised (Fig. 68a). When the spectra is obtained from lean mixtures, the

6. LIBS measurements on turbulent flames

atomic lines of hydrogen (at 656.3 nm and at 486.1 nm), oxygen (at 777.3 nm and at 844.7 nm), and nitrogen (at 744.2 nm, at 821.6 nm and at 871.2 nm) are clearly depicted, attributed to the vapourisation and the dissociation of heptane droplets and the atomisation of N_2 and O_2 from the air. However, when the spectra is created from fuel-rich mixtures, the dominating spectral feature of the C_2 Swan band is observed at 516.5 nm with $\Delta v = 0$, 468.0 nm with $\Delta v = -1$ and 563.0 nm with $\Delta v = 1$. All the above observed spectra features are very similar with the ones seen from the gaseous mixtures discussed earlier in section 6.1.2.1.

6.2.3 Measurements in turbulent spray flames

The typical LIBS spectra obtained from the different regions of the spray flame (Fig. 66a) are shown in Fig. 68b. The spectra are overall similar to those obtained previously in the uniform dispersions of C_7H_{16} - air. The fuel-rich region (Fig. 66a (B), top row spectra) indicates strong emission of CN and C_2 , where emission of O is almost absent. However, in the fuel-lean region (A, C), CN and C_2 are either of reduced or negligible intensity, meanwhile, increased emission from O and H_α are seen. The absence of C_2 and O in the leaner and richer conditions respectively, suggests that the C_2 molecular band and the oxygen line exhibit a more complicated behaviour where their appearance in the spectra is not only dependent on the presence or not of the corresponding molecules, i.e. C_7H_{16} and O_2 , but also on their concentration in the mixture.

Similar to the study in the CH_4 -air mixtures, the LIBS calibration curves were first studied to investigate the dependence between the intensity of these spectral lines to the amount of the fuel in the mixture. A systematic investigation was carried out in uniform air- C_7H_{16} dispersions of equivalence ratio $\phi = 0-10$. The derived calibration curves by the average method of H_α/O ratio vs. ϕ (0-0.7) and of C_2/CN ratio vs. ϕ (0-10) are plotted in Figs. 69-70. First, the average H_α/O ratio presents a linear correlation with ϕ in the lean conditions (Fig. 69a). On the single-shot bases, an example of a scatter plot of 200 individual H_α and O peaks (taken at $\phi = 0.62$) is plotted in Fig. 69b, which in general shows a linear correlation between single-shot H_α and O emission intensities with ϕ . The causes of the shot to shot deviation of the emission intensities are: (1) the fluctuations of laser energy, (2) the probabilistic

6. LIBS measurements on turbulent flames

nature of the spark formation process, and (3) the natural stochasticity of total amount of fuel in the sparked volume (due to the non-homogeneity of the fuel vapour contained in the inter-droplet region, and due to the random spatial distribution of the droplets). The average method was thus used in the spray flame to eliminate the error caused by shot to shot variance of plasma collection volume. Second, the derived calibration curve of C_2/CN ratio vs. ϕ (0-10) based on the average method is plotted in Fig. 70. Same trend is observed as presented in the calibration curve in uniform CH_4 -air mixtures (Fig. 56). The ratio is around zero at fuel lean conditions and increases sharply after $\phi = 4$. Next, due to the limitation of the current uniform-spray burner in performing a higher equivalence ratio mixture ($\phi > 10$), the calibration curve in the rich mixture part ($C_2/CN \geq 0.4$, $\phi \geq 6$) is extended by polynomial extrapolation of the C_2/CN ratio vs. ϕ curve, while, for the calibration of a leaner mixture with a lower C_2/CN ratio value ($C_2/CN < 0.4$, $\phi < 6$), a linear extrapolation of H/O ratio vs. ϕ is used instead. For future measurements, a wider range of ϕ in uniform dispersions should be studied. Extrapolating the calibration curve is needed only for the small regions in the swirling flame where the spray is dense, i.e. only for a few mm from the injection point in the axial and radial directions.

Following the calibration, LIBS measurements were performed in the spray flame to obtain the profiles of equivalence ratios. A time-averaged Mie scattering image, superimposed an mean OH-PLIF image reported previously [6] of the same spray flame studied is shown in Fig. 71 as a supplement to visualises the locations where spray droplets exist, and hence outline the potentially high concentration of C_7H_{16} (liquid and vapour) regions. Also indicated by the OH-PLIF image is the reaction zone, where according to the laminar counterflow flame calculations (Ch. 3.2.2, Fig. 12), OH is only present in a narrow region near the stoichiometric location in mixture fraction space, peaking close to the stoichiometric line and towards the lean side, and consumed quickly in the lean and rich region. Thus, the absence of OH signal above the bluff body (radius in the range [-12.5, 12.5] mm) indicates fuel rich mixtures (high ϕ values), and the absence of OH signal from the outer annual air jet suggests lean mixtures. The horizontal lines in Fig. 71 indicate the locations where LIBS is performed.

6. LIBS measurements on turbulent flames

The radial distributions of the four aforementioned species emissions and their ratios in the spray flame at four different heights (indicating in Fig. 66b) are plotted in Fig. 72. At lower heights (h1, h2), maximum intensity of O line is shown at the annular air jet and (for h2) at the inner recirculation zone centre, but is absent in the fuel jet region; H_α emission is seen both in fuel and combustion products; C_2 , CN peak at the hollow cone spray. Very close to the nozzle (h1), a huge amount of C_2 is apparent, consistent with the intense Mie scattering signal there. At the lowest height (h1, 5mm), the H_α/O ratio peaks at the hollow-cone spray and the value decreases towards the centre line, at the meantime, the C_2/CN ratio rises sharply towards the centre line, indicating fuel-rich in the centre line region. This agrees with the mean Mie image (Fig. 71) which suggests a high signal at this location. The low value of the H_α/O ratio shown in this region also agrees with the observation earlier in LIBS measurement of uniform CH_4 -air mixtures (Ch. 6.1.2, Fig. 55) that in fuel-rich conditions, no correlation of H_α/O ratio vs. ϕ is apparent and the ratio decreases. At higher heights above the flame (h3, h4), evident is an almost uniform distributed intensity profile of all these species and their ratios along the radial direction, which consistent with the fact that the intense mixing caused by the swirl homogenises the mixture.

Finally, the local equivalence ratio profiles were derived from the above species profiles by the calibration scheme of H_α/O ratio vs. ϕ (measured in the range 0-0.7) linearly extended in ϕ for the range $0.7 < \phi < 6$, and the C_2/CN ratio vs. ϕ (measured in the range 0-10) extrapolated using a polynomial fit for $\phi > 10$. The result is plotted in Fig.73. The overall trend is quite reasonable. ϕ peaks at the spray jet (h1-h2) and becomes homogeneous further downstream (h3-h4) due to the mixing. The value is almost zero in the annular air jet. Passed the annular air jet in the radial direction, a higher ϕ is obtained than the value at the annular air locations, suggesting the location of the outer recirculation zone. At the farthest location (h4), where ϕ is uniform in the radial coordinate, the measured ϕ by LIBS is close to the mean equivalence ratio estimated from the sampling probe measurements by Cavaliere [220], implying the measurement of the equivalence ratio there is quantitatively reasonable.

6.3 Conclusions

Laser-Induced Breakdown Spectroscopy in uniform flowing methane-air mixtures of compositions ranging from only air to only fuel was investigated in order to explore calibration schemes for further measurements in turbulent premixed and turbulent non-premixed flames. The differences among the various spectra are discussed and the intensity ratios $H_{\alpha}(656.3\text{nm})/O(777.3\text{nm})$ and $C_2(516.5\text{nm})/CN(388.3\text{nm})$ were found to depend monotonically and almost linearly to the mole fraction of methane in the ranges 0-0.3 and of 0.3-1.0 respectively, therefore providing a scheme for measurement in non-premixed systems spanning a wide range of equivalence ratios. It is found that, with proper attention to the calibration and to the laser energy, the local equivalence ratio in flames can be measured from both unreacted and reacted mixtures, in both premixed and non-premixed flames. The last part of this chapter presents LIBS for liquid droplet heptane-air dispersions spanning a wide range of overall fuel-air equivalence ratios and for turbulent swirling spray flames. The differences among the various emission spectra are discussed. The intensity ratio $H_{\alpha}(656.3\text{nm})/O(777.3\text{nm})$ was found to depend monotonically and almost linearly to the mass fraction of C_7H_{16} in the range 0-0.044 (equivalence ratio $\phi = 0$ to 0.7), and a correlation could be developed from the $C_2(516.5\text{ nm})/CN(388.3\text{ nm})$ ratio vs. ϕ in the range $\phi = 0$ to 10. Using this calibration scheme, the local equivalence ratio in a turbulent spray flame has been measured and the results are consistent with our expectations and inferences from previous data.

6.4 Figures for Chapter 6

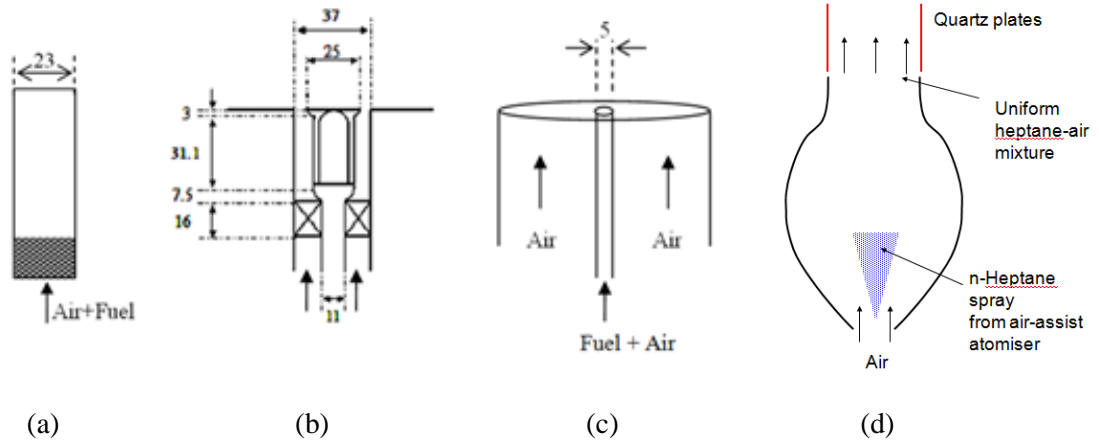


Figure 51. Schematic of the experimental arrangements used for calibration (a), turbulent premixed flames (b), turbulent jet non-premixed flames (c), and schematics of the uniform dispersion apparatus [217] (d).

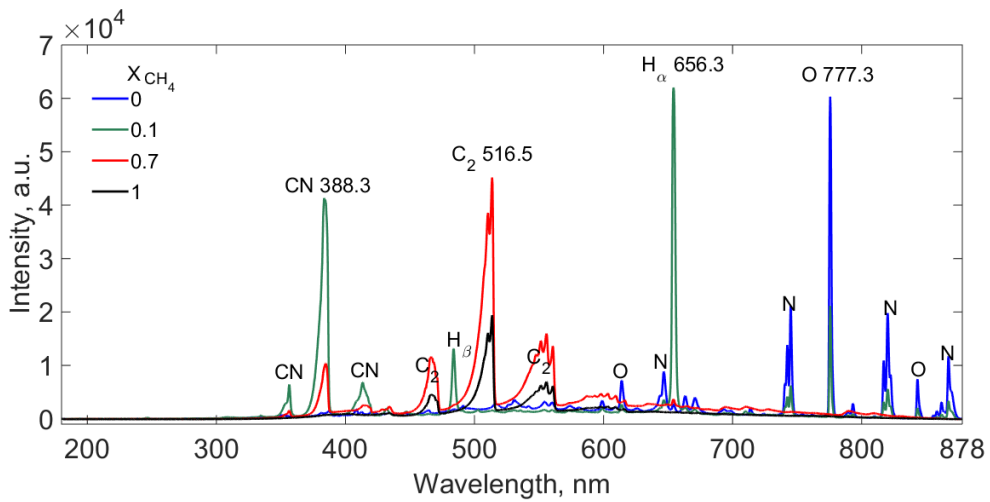


Figure 52. Emission spectra of laser induced plasma in methane-air mixtures with $X_{CH_4} = 0, 0.1, 0.7, \text{ and } 1$.

6. LIBS measurements on turbulent flames

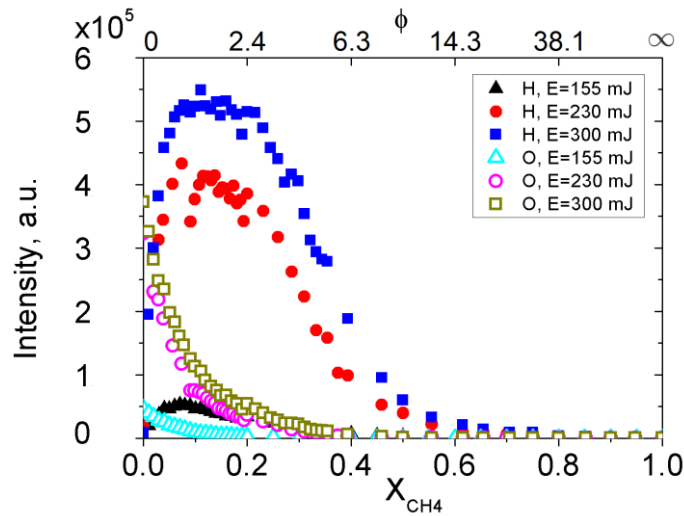


Figure 53. Total intensity of H α (656.3 nm) and O (777.3 nm) atomic lines calculated by the averaging method as a function of the mole fraction of methane, or the equivalence ratio (ϕ), calculated from the emission spectra of the plasma resulting from three different laser energies and induced in the centre of the 23 mm ID burner.

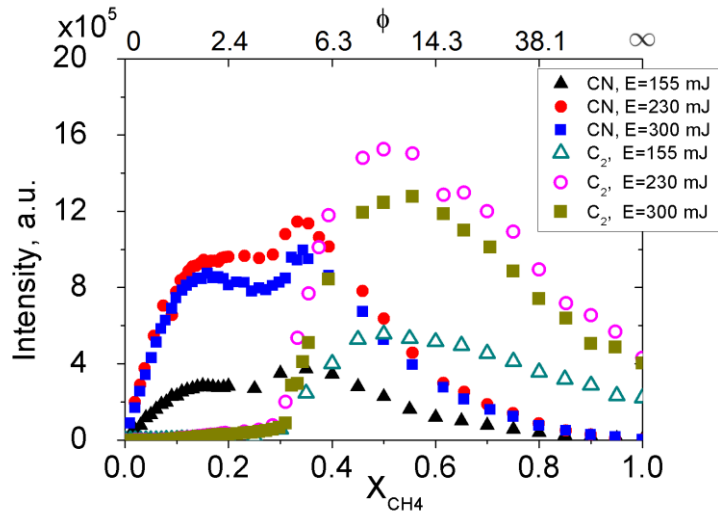


Figure 54. Total intensity of CN (388 nm) and C $_2$ (516.5 nm) molecular bands calculated by the averaging method as a function of the mole fraction of methane, or the equivalence ratio (ϕ), calculated from the emission spectra of the plasma resulting from three different laser energies and induced in the centre of the calibration burner.

6. LIBS measurements on turbulent flames

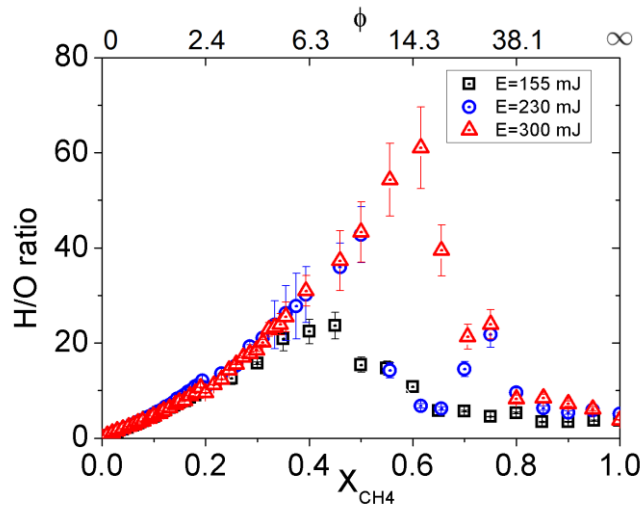


Figure 55. Calibration curve for the ratio $H_{\alpha}(656.3 \text{ nm}) / O(777.3 \text{ nm})$ as a function of X_{CH_4} calculated by the averaging method, measured from emission spectra of plasma resulting from three different laser energies.

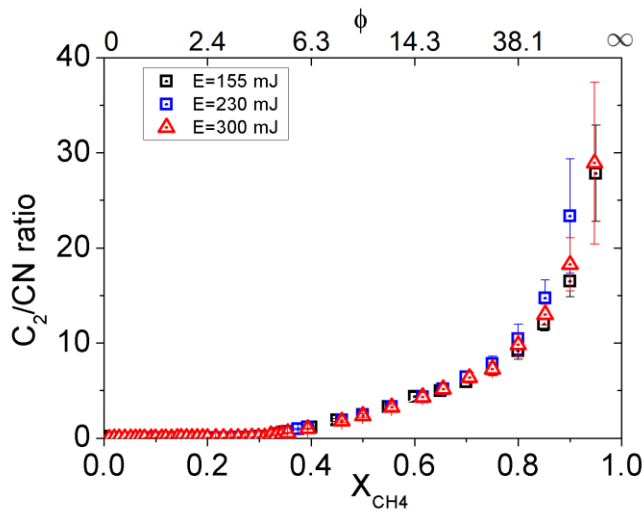


Figure 56. Calibration curve for the ratio $C_2(516.5 \text{ nm}) / CN(388.3 \text{ nm})$ as a function of X_{CH_4} calculated by the averaging method, measured from emission spectra of plasma resulting from three different laser energies.

6. LIBS measurements on turbulent flames

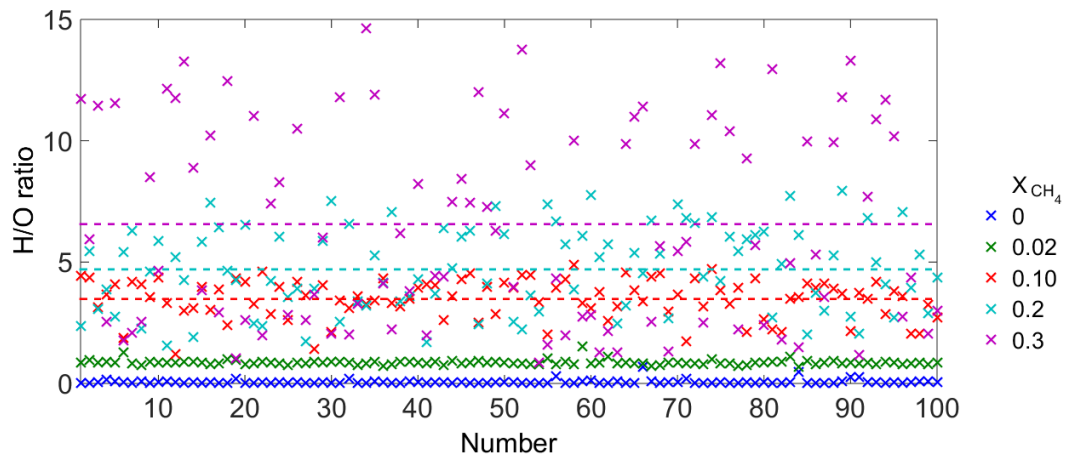


Figure 57. Ratio H_{α} (656.3) / O (777.3) obtained in air and in different mixtures of methane and air obtained from the 100 single-shot spectra. The dashed lines represent the average values of the ratios in the cases of $X_{CH_4} = 0.10, 0.20,$ and 0.30 .

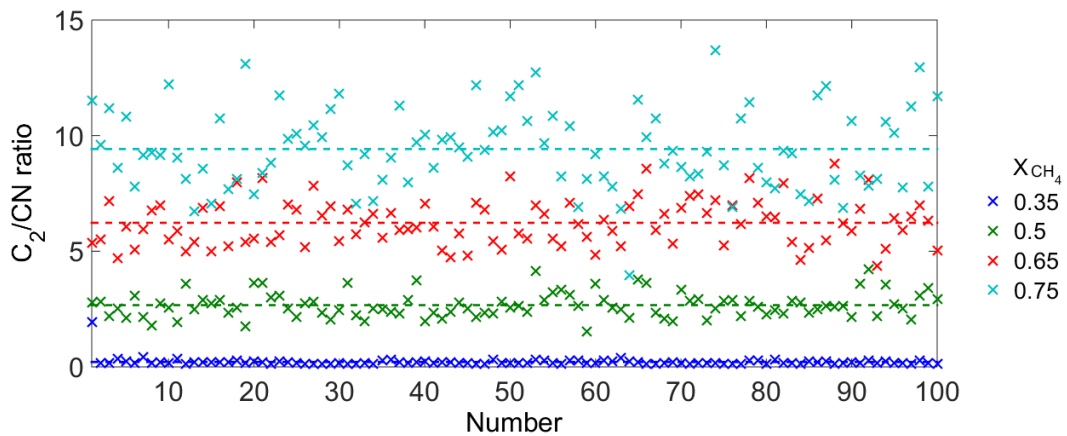


Figure 58. Ratio C_2 (516.5) / CN (388.3) obtained in different mixtures of methane and air obtained from the 100 single-shot spectra. The dashed lines represent the average values of the ratios in the cases of $X_{CH_4} = 0.10, 0.20,$ and 0.30 .

6. LIBS measurements on turbulent flames

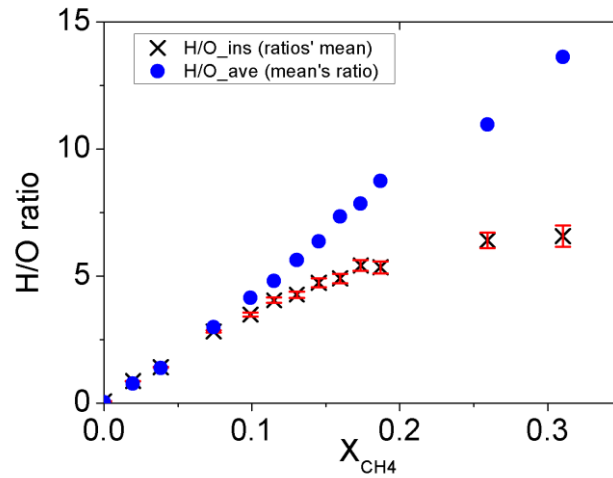


Figure 59. Calibration curve for the H_{α} (656.3) / O (777.3) ratio obtained by the averaging method and the instantaneous method respectively. Each data point of the instantaneous method corresponds to the average of 100 single-shot measurements taken under the same experimental conditions.

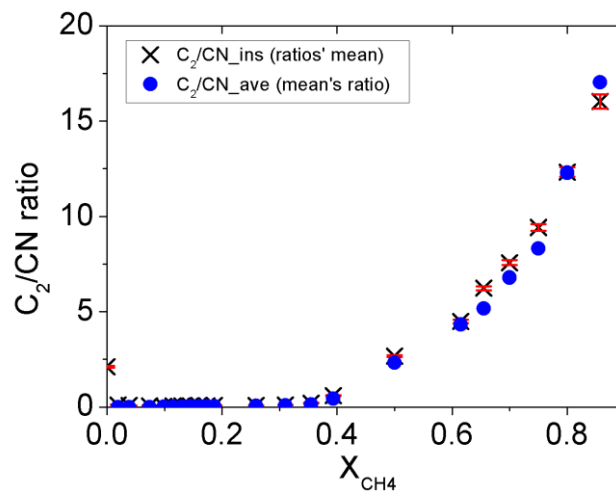


Figure 60. Calibration curve for the C_2 (516.5) / CN (388.3) ratio obtained by the averaging method and the instantaneous method respectively. Each data point of the instantaneous method corresponds to the average of 100 single-shot measurements taken under the same experimental conditions.

6. LIBS measurements on turbulent flames

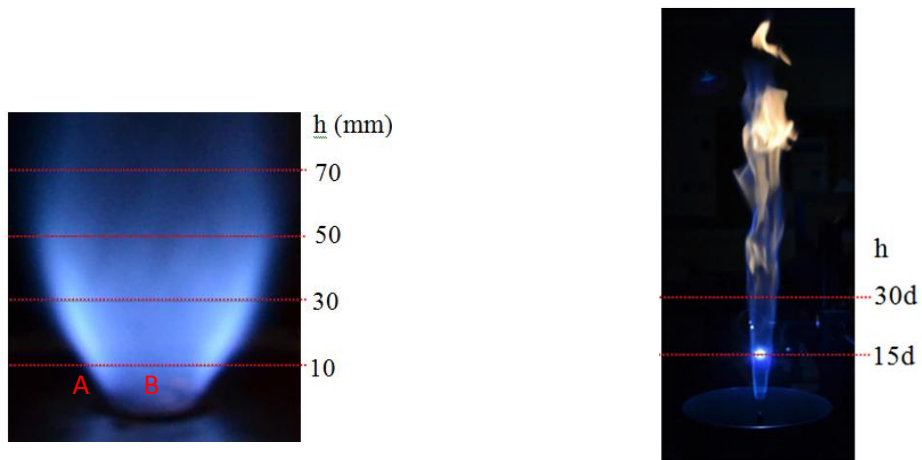


Figure 61. Left: Photograph of the swirling premixed flame. Equivalence ratio: 0.81, velocity at annulus 10.2 m/s. Right: Photograph of the lifted methane air flame with a spark visible. Jet velocity 17 m/s, jet fluid composition 70% CH₄, 30% air by volume. The horizontal lines on each photo reflect the locations where radial profiles of equivalence ratio were taken. Not to scale.

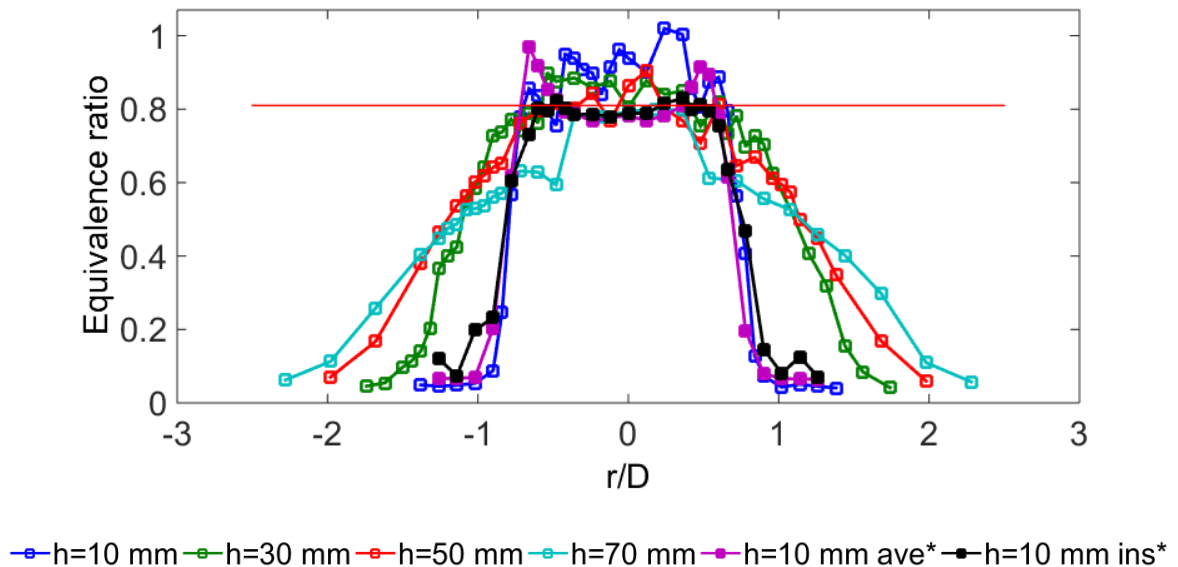


Figure 62. Radial distributions of mean equivalence ratio in the premixed recirculating flame at different heights from the bluff body as a function of radius. The filled squares correspond to measurements at $h=10\text{mm}$ from the burner employing both suggested analytical methods, namely averaging and instantaneous. The inlet equivalence ratio of 0.81 is shown by the horizontal line.

6. LIBS measurements on turbulent flames

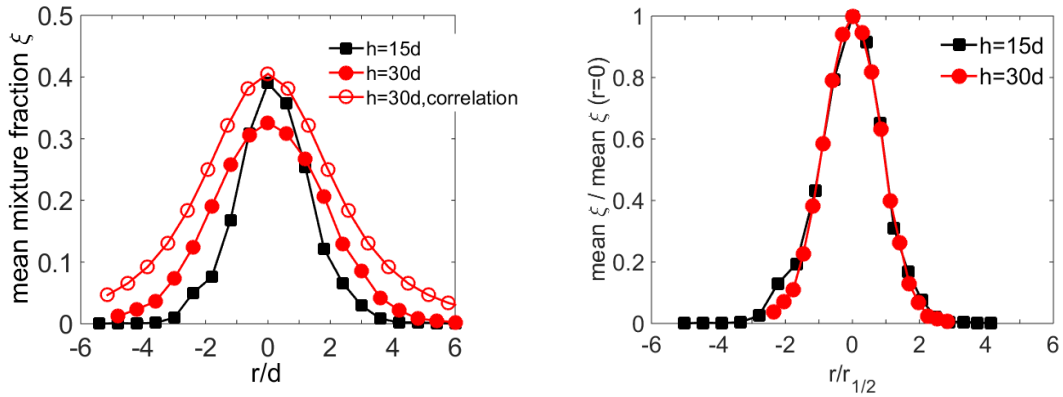


Figure 63. Left: Radial distribution of mean mixture fraction in the turbulent jet flame at two different axial stations as a function of the radial position r/d . Included is the empirical fit from Lawn [90]. Right: the same data, but normalized by the centreline value plotted versus radial distance normalised by the radius at FWHM mixture fraction.

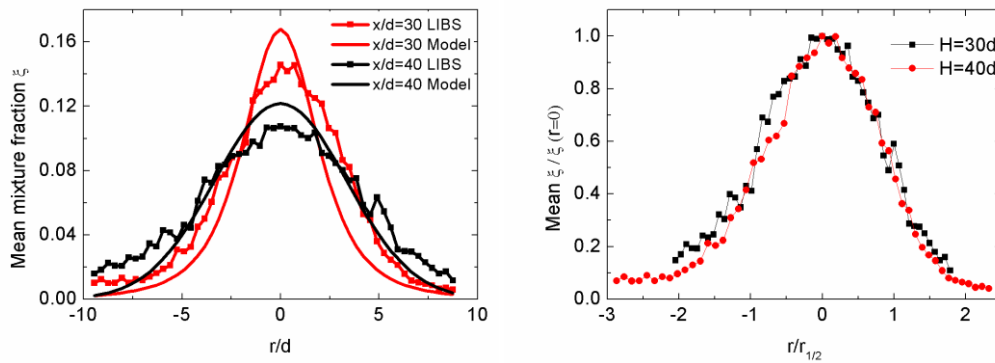


Figure 64. Inert flow. Left: Radial distribution of mean mixture fraction in the non-reacting jet at two different axial stations as a function of the radial position r/d . Included is the empirical fit from Lawn [90]. Right: the same data, but normalized by the centreline value plotted versus radial distance normalised by the radius at FWHM mixture fraction.

6. LIBS measurements on turbulent flames

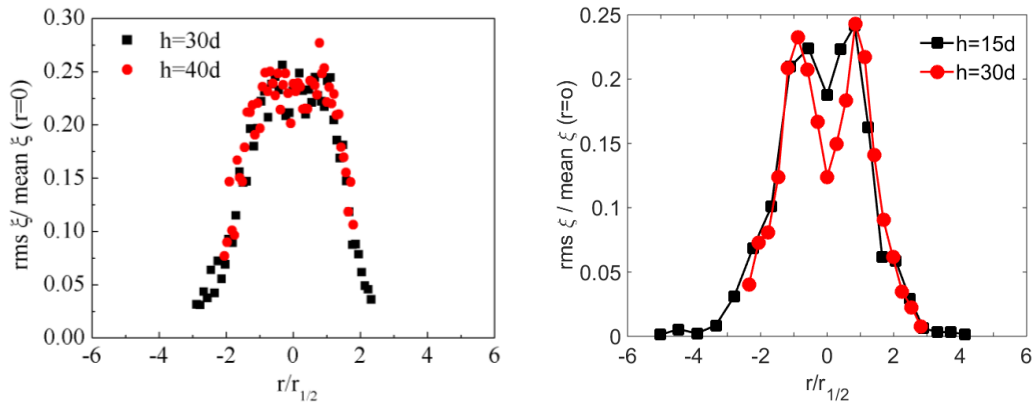


Figure 65. Radial distribution of normalised r.m.s. by the centreline value the mean mixture fraction at two different axial stations in the non-reacting jet (left), and in the lifted jet flame (right).

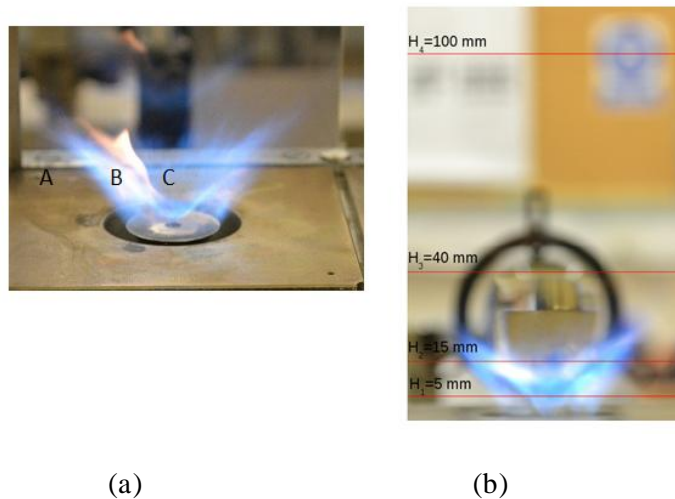


Figure 66. (a) Photograph of the swirl heptane spray flame. Region A marks the air annular flame and the outer recirculation zone; region B marks the flame brush around the hollow-cone spray; region C indicates the inner recirculation zone. (b) Photograph of the spray flame showing the measurement stations (horizontal lines) where radial profiles of equivalence ratio were taken. Not to scale.

6. LIBS measurements on turbulent flames

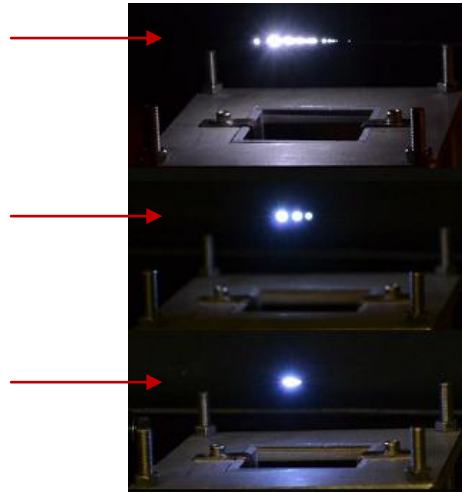


Figure 67. Photographs of a typical spark generated in C₇H₁₆-air dispersion in the uniform-dispersion spray burner by three different focusing lenses: top $f = 150$ mm, centre $f = 75$ mm, and bottom $f = 50$ mm . (Red arrows point at the focusing direction of the laser beam.)

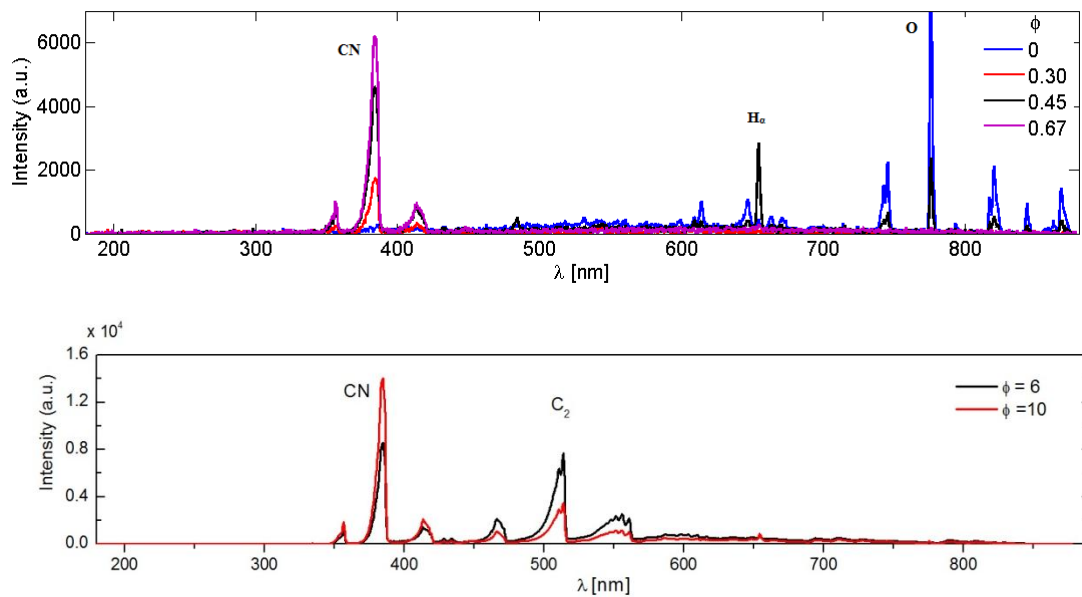


Figure 68a. Emission spectra from plasma created in uniform heptane-air dispersions for various equivalence ratios from lean (top) to rich (bottom).

6. LIBS measurements on turbulent flames

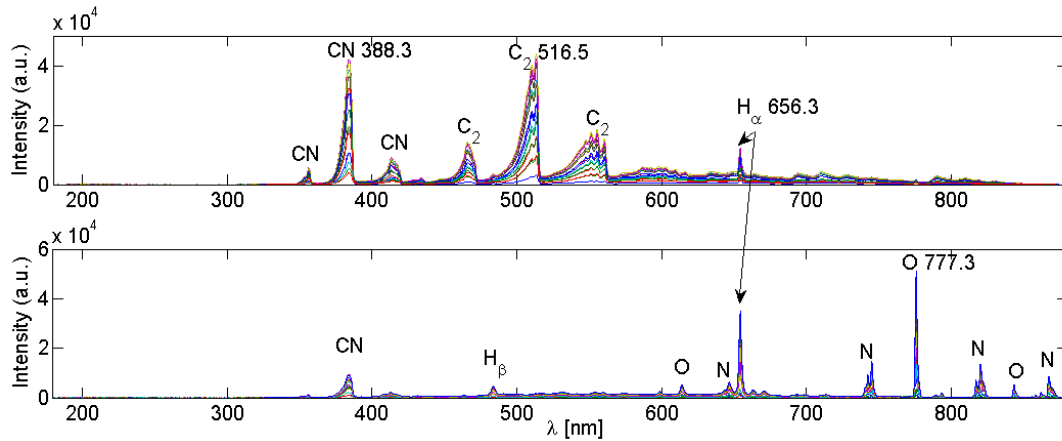


Figure 68b. Top: Laser induced plasma emission spectra obtained from the swirl heptane spray flame corresponding to various locations in region B (upper) and regions A and C (lower).

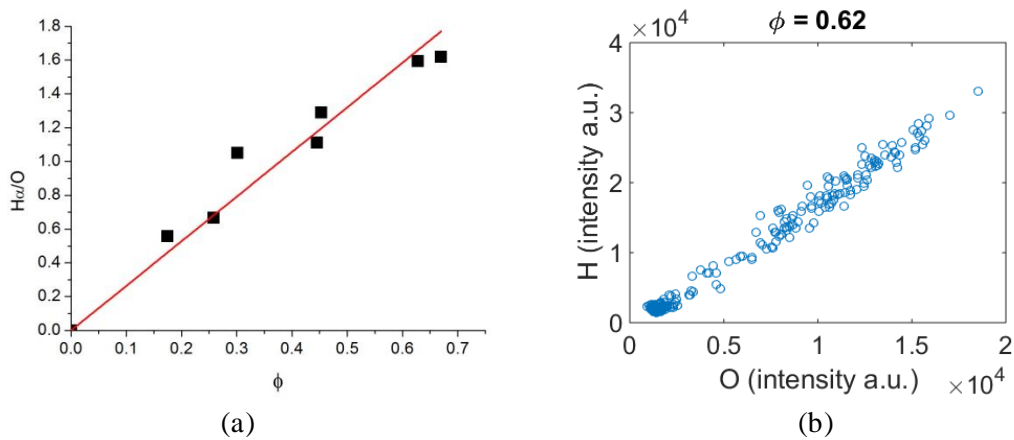


Figure 69: (a) Dependence of the ratio H_{α} (656.3 nm) / O (777.3 nm) vs. ϕ in uniform C_7H_{16} -air dispersion. (b) Total intensity of the H_{α} and O atomic emission lines obtained from 200 instantaneous spectra measurements in uniform C_7H_{16} -air dispersions ($\phi = 0.62$).

6. LIBS measurements on turbulent flames

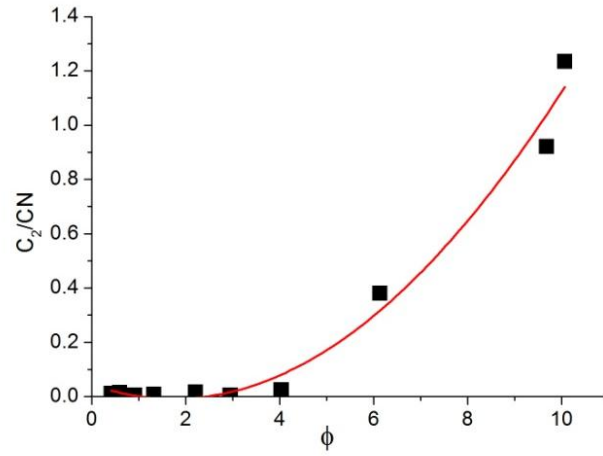


Figure 70. Dependence of the ratio C_2 (516.5 nm) / CN (388.3 nm) vs. ϕ in uniform C_7H_{16} -air dispersion. The ratio is calculated by the averaging method.

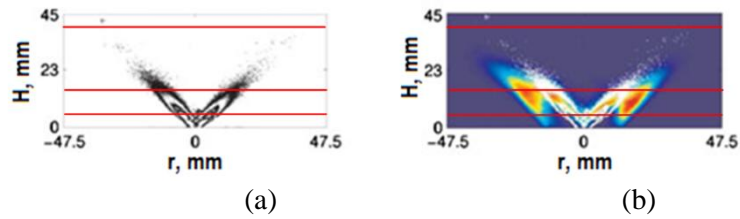


Figure 71. Time-averaged images of (a) spray Mie scattering and (b) OH-PLIF images superimposed on the Mie scattering images of the swirl spray flame. From Cavaliere et al. [6].

6. LIBS measurements on turbulent flames

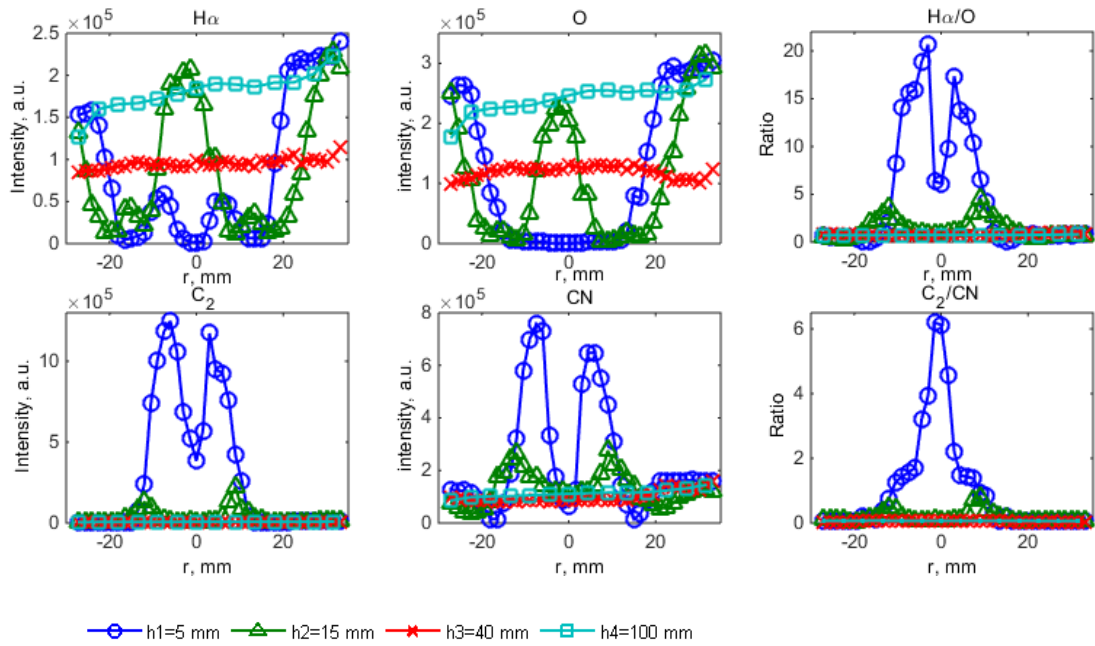


Figure 72. Radial distribution of the species emission ($H\alpha$ (656.3 nm), O(777.3 nm), C_2 (516.5nm) and CN(388.3nm)) obtained at the indicated axial station in the swirl spray flame by the averaging method. Each data point corresponds to the average of 200 single-shot measurements.

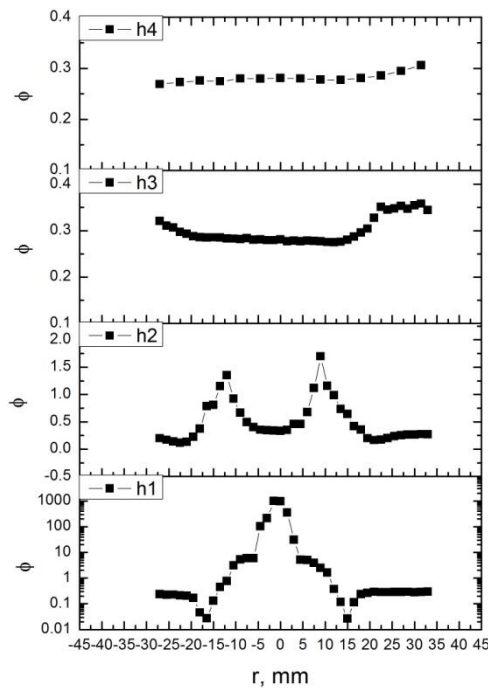


Figure 73. Radial distribution of mean equivalence ratio in the swirl spray flame at different heights from the bluff body as a function of radius. $h_1=5$ mm, $h_2=15$ mm, $h_3=40$ mm, $h_4=100$ mm.

Chapter 7

Conclusions and suggestions for further research

7.1 Conclusions from this work

This work describes an experimental investigation on the flame structure and the dynamic behaviour of recirculating spray flames of ethanol, heptane, decane and dodecane, at far from and close to blow-off conditions, and at the blow-off event. The main tasks for this work were to evaluate characteristics of swirling spray flames at the stable condition and at the extinction condition, and to examine fuel volatility effect on the blow-off behaviour. Laminar flame calculations of premixed and non-premixed configurations of these fuels were carried out and provided information on the flame structure in terms of species molar fraction, temperature, and heat release rate at various equivalence ratios or various strain rates conditions. The correlation between HRR and the product $X_{\text{CH}_2\text{O}} \times X_{\text{OH}}$ was also evaluated in these simulations. These provide a reference for the following joint PLIF (CH_2O -PLIF and OH-PLIF, at

7. Conclusions and suggestions for further research

10Hz) measurement on the heat release and the flame structure of spray flames. For visualising the flame structure and the dynamics of the stable and unstable flames during the blow-off event, several fast (5 kHz) laser diagnostic methods were applied, namely OH* chemiluminescence, OH-PLIF and Mie scattering imaging. Those qualitative measurements visualised the variations of the heat release region, the main reaction zone, and the spray pathway at the different departures from the blow-off. Additionally, quantitative measurements of the blow-off duration and the lift-off height were also obtained via these fast imaging techniques. The droplets size and velocity distributions were resolved via LDA/PDA measurements and compared between the various fuels and flow conditions. These data are also useful for validation of CFD for spray flames at close to blow-off condition. Lastly, POD analysis were applied on the OH* and OH-PLIF images, to further extract the basic structures and their motions in the spray flames. A quantitative measurement of quenching percentage along the stoichiometric iso-line was also described, which provides an additional measure to the local extinction and a validation for the modelling. LIBS method has been investigated in the turbulent flames of premixed, non-premixed and spray flames. Its capability on the measurement of the local fuel air ratio in these flames was investigated. The following sections summarise the key conclusions from this work presented in the previous chapters. This chapter closes with some recommendations for the future research.

7.1.1 Laminar flame calculations

Two configurations were used: freely propagating premixed flames and counterflow non-premixed flames. The laminar flame structure were obtained using detailed mechanisms and transport properties for the gaseous-fuelled flames of ethanol, heptane, decane, dodecane and “Aachen” fuel surrogate. For the premixed flames, it shows a broad distribution of OH extending to the post flame region, and narrow profiles of CH₂O and HRR. CH₂O centred at the mid-temperature region. HRR overall coincides with the overlap region of OH and CH₂O, and the HRR peaks close to the peak of the latter at all the conditions. A correlation between the HRR and the product of $X_{\text{CH}_2\text{O}} \times X_{\text{OH}}$ is seen in all the single-component fuels for a range of ϕ . However, the HRR is not quantitatively represented by the product of $X_{\text{CH}_2\text{O}} \times X_{\text{OH}}$, especially

7. Conclusions and suggestions for further research

for “Aachen” fuel surrogate at lean conditions. At rich conditions and for the other fuels, the normalised two variables are close. The percentage of normalised HRR area covered by the normalised area of the product $X_{\text{CH}_2\text{O}} \times X_{\text{OH}}$ lies in between 0.7 ~ 1.05 for all the fuels and flow conditions studied, and a higher percentage is seen at rich conditions. When compared the relative profiles from the different fuels, it shows that, at the stoichiometric condition, T has a slower slope in heptane flame than the others; the peak of $X_{\text{CH}_2\text{O}}$ maximises in decane flame, followed by “Aachen” fuel surrogate, ethanol, dodecane flame, and minimises in heptane flame; and the HRR increases with the fuel carbon number for the single-component hydrocarbon fuels. Note that these profiles may be related to the specific mechanism applied. The laminar flame speed at various equivalence ratios for the different fuels was also obtained and indicates a peak value at around $\phi = 1.1$. A minor rise in the peak of adiabatic flame temperature is seen with a higher carbon number fuel. The trends of S_L and T_{ad} are in agreement with the literature. The correlation between HRR and the product $X_{\text{CH}_2\text{O}} \times X_{\text{OH}}$ in these premixed flames supports the qualitative measurements of HRR via simultaneous acquisitions of CH_2O and OH for the laminar premixed flames of the four single-component fuels studied.

For the counterflow non-premixed flames, detailed flame structure was resolved in the mixture fraction space for ethanol, heptane and decane at a range of strain rates. Evidently, formaldehyde lies in the fuel-rich region and is destructed sharply close to the stoichiometric line at both low and high strain rates for all the fuels. OH lies in a narrow region with minor variations at the different strain rates. OH peaks close to the stoichiometric line for all the conditions. The spatial location of HRR is overall marked well by the overlap region of CH_2O and OH . The peak of HRR aligns close to the peak of the product CH_2O and OH , although HRR is not quantitatively represented by the latter. At lean side of the stoichiometric line, the latter only represents 50% of the total HRR at low strain rates. At high strain rates the two variables are close. When compared the flame structure of the various fuels at both low and high strain rate conditions, it shows a higher peak and a wider width of the OH for ethanol flames, and a higher peak of CH_2O in the reaction zone for decane flames. The percentage of normalised HR area covered by the normalised area of product of CH_2O

7. Conclusions and suggestions for further research

and OH lies in around 0.65 ~ 0.85 for a range of strain rates, and the value increases with the strain rates for all the fuels. The correlation between HRR and the product $X_{\text{CH}_2\text{O}} \times X_{\text{OH}}$ is better at high strain rate conditions for heptane and decane flames; however, the normalised HRR is less represented by the normalised product of CH₂O and OH at low strain rates of these fuels and at the lean side of the stoichiometric line for both low and high strain rates of ethanol flames. Lastly, the extinction strain rate was obtained for the various fuels and its value increases with a higher carbon numbers fuel, for which a higher temperature is also obtained in the reaction zone. The counterflow non-premixed flames simulations validate the use of joint CH₂O-OH measurements to locate the main heat release zone of non-premixed flames of ethanol, heptane, decane at conditions close to blow-off. It also suggests that the boundary of CH₂O aligns close to the stoichiometric line at all the conditions for all the fuels studied, thus supports the use of the boundary of CH₂O as an approximation of the stoichiometric iso-line in non-premixed flames of these fuels.

7.1.2 Spray flame structure

Spray flames of ethanol, heptane, decane and dodecane at far from and close to blow-off and at the blow-off transient process were investigated via 5 kHz OH* chemiluminescence, OH-PLIF and Mie imaging. The droplets size and velocity distributions were resolved by LDA/PDA. The results visualise two main reaction zone and heat release region: one aligns in between the hollow-cone spray jet and inner recirculation zone; the other lies in between the spray jet and the outer annular air. The mean HR zone is in general thin and becomes thicker at unstable (blow-off) conditions. The flame location is affected by the fuel type: the low volatility fuels show a longer penetrating length of droplets and a larger mean droplet size with a smaller dispersion of the spray. The OH* and OH-PLIF images indicate a longer, straighter, and more anchored flame sheet for the low volatility fuels. The flame location is also affected by the spray location which is in turn affected by the spray atomisation process. The stable flames show intermittent lift-off at the bluff-body edges. Local breaks of OH images are seen in both inner branch in between the recirculation gas and the spray, and in the outer shear layer. The frequency of the

7. Conclusions and suggestions for further research

occurrence of local breaks increases at close to blow-off conditions.

At the blow-off condition, intense quenching of the inner reaction zone is evident. The intense local extinction eventually leads to the global blow-off of the spray flames. Evidently, a shorter flame is obtained at the blow-off condition and appears more attached to the bluff-body surface. During the blow-off transient process, the HR region is gradually reduced in size and the last flame fragment is usually seen around the spray injection point. Besides, a distinctive asymmetric pattern of the HR image, consisting with half the flame surviving in a wedge-like shape and slowly moving around the burner, is shown for the low-volatility fuels (decane and dodecane), but this feature is not obvious in ethanol or heptane, suggesting the importance of fuel evaporation on the HR region close to blow-off. The observation of single wedge-like HR region is supported by the instantaneous Mie images of the unstable flames, where a non-axisymmetric profile of the spray is observed.

Next, the flame structure and the HR were studied via simultaneous measurements (at 10 Hz) of CH₂O and OH PLIF for two heptane flames at far from and close to blow-off condition. The noise from Mie scattering of the droplets was eliminated in the acquisition. The CH₂O-PLIF marks the fuel-rich region and lies in a broad region on both sides of the hollow-cone spray and is bounded by the OH. The instantaneous OH images show the similar features as observed in fast (5 kHz) OH-PLIF. The overlap region of OH and CH₂O in general coincides with OH images for both instantaneous and average images, suggesting the high-speed OH-PLIF measurements could be a reliable marker of HR regions in the spray flames. The average CH₂O × OH heat release rate images at both conditions are agreed well with line-of-sight Abel-transformed OH* chemiluminescence measurements. Quite similar flame shape and locations are revealed from both measurements.

Finally, an attempt of measurements of the local equivalence ratio in spray flames was investigated via the LIBS technique. First, LIBS was evaluated in gaseous-fuelled flames of methane: an extended calibration scheme covering a wide range ϕ was first developed in the uniform air-methane mixture consisting from pure air to pure fuel. The calibration method uses H _{α} /O and C₂/CN ratios for lean and rich conditions separately, and uses an arbitrary threshold of the C₂ signal as an indicator of which

7. Conclusions and suggestions for further research

calibration curve to be used. The shot-to-shot variance of the two ratios was also found to be 15-20% uniform mixtures having the indicated composition. As the mole fraction of methane gets higher, these variations of H_α/O increase significantly. This limits the use of the single shot spectrum in turbulent non-premixed systems. Thus the average method was used in the following turbulent premixed flame, turbulent non-premixed jets and the turbulent spray flame. For turbulent premixed flame, LIBS gives the same result in both reactant and hot product, suggesting LIBS measurements is not affected by the local temperature. For both turbulent reacting and non-reacting jet, LIBS provided a reasonable measurement of mixture fraction profiles. For spray flames, LIBS was calibrated in a uniform spray-air stream. The intensity ratios H_α/O and C_2/CN were used as the calibration scheme. The local equivalence ratio has been measured in a turbulent spray flame and the results are consistent with our expectations from previous data.

7.1.3 Spray flames dynamic behaviour

The blow-off limits were obtained for the four fuels at a range of fuel flow rates. The blow-off correlation was examined by the criteria proposed by Radhakrishnan et al. [45], using the concept of small-scale coherent turbulent structures, and collapsed the blow-off data well for all these fuels. The dynamic behaviour of the spray flames was evaluated in terms of blow-off transient duration, the lift-off height, the quenching percentage of ξ_{st} iso-line, and POD analysis. The average blow-off duration calculated from OH* evolution is found to be a few tens of milliseconds for all the fuels and a range of fuel flow rates, corresponding to an order of magnitude higher of the characteristic flow time (expressed by D/U_B). The average lift-off height, at around $(0.1 - 0.4) D$, decreases as air bulk velocity increases, and as fuel volatility increases. The occurrence of the flame attachment (zero lift-off height) event increases as air bulk velocity increases. An increase in the length of local quenching along ξ_{st} iso-line is found in heptane flames at close to blow-off condition: it is 0.21 ± 0.136 at far from blow-off (flame H1S1) and 0.34 ± 0.167 at close to blow-off (flame H1S2). The morphology of OH images reveals a fragmented and decreased the integral OH area at the blow-off condition. The POD analysis was attempted in swirling spray

7. Conclusions and suggestions for further research

flames of the four fuels and at different departure to blow-off. The first few POD modes show several similar spatial features for the different fuels. A strong transverse motion is more prominent at the blow-off condition than at far from blow-off condition for most of the fuels except ethanol, for which an axial oscillation motion is more pronounced at extinction. The OH* POD first few modes also feature fluctuations along the spray jet, along the flame axis, and along the radius. The OH-PLIF POD modes highlights flame breaks, fragment, an asymmetric lift-off at bluff-body, and flame branch thickening at extinction. The flame attachment at blow-off is also highlighted by both OH* and OH-PLIF first few POD modes. The reconstructed snapshots with the first few POD modes enable visualisation of the basic flame fluctuation structure without underlying small-scale fluctuations. For OH*, they reveal a wedge-like shape slowly rotating at extinction condition; and for OH-PLIF they show the lift-off, flame breaks, and the attachment of the extinction flames. The aforementioned measurements and analysis provide useful information for validation of combustion models focusing on local and global extinction.

7.2 Suggestions for further research

The detailed flame structure has been studied for counterflow non-premixed gaseous-fuelled flames for the various hydrocarbon fuels. The simulations with droplets could be investigated for study the fuel volatility effect on the extinction strain rate and the detailed flame structure at close to extinction. The droplets size and velocity distributions effect on the flame structure could also be evaluated.

It was shown that CH₂O images mark the fuel rich region, low-temperature reaction zones, and the stoichiometric iso-line. The high-speed imaging of CH₂O-PLIF at blow-off transient process could provide useful information on the flame structure and the blow-off mechanism. Local extinctions and lift-offs were observed and the quenching percentage of the stoichiometric iso-line was measured at far from and close to blow-off conditions in the current study. The fast OH-PLIF as well as the CH₂O-PLIF could be applied with simultaneous flow velocity measurement in the current spray flames to further subtract local extinction hole characteristics and to further study the stability mechanism of the lift-off.

7. Conclusions and suggestions for further research

For the improvement of the LIBS measurements in turbulent spray flames, LIBS calibration scheme could be further developed for rich mixtures of fuel droplets and air; and the shot to shot variance of LIBS should be investigated further by high-quality gated spectrometers. LIBS technique and the correlation between the ratio of $H\alpha/O$ or C_2/CN and equivalence ratio could also be investigated for other fuel's flames (e.g. ethanol flame etc.).

Finally, the blow-off behaviour and blow-off event could be investigated with the preheat air and pre-vaporised fuel system for the different single component fuels with the same burner. This helps understand the heterogeneous effect on the flame heat release, the flame structure, and blow-off limits.

Appendix

LDA/PDA measurements results on spray profiles of bluff-body swirl spray flames

A.1 Flow conditions

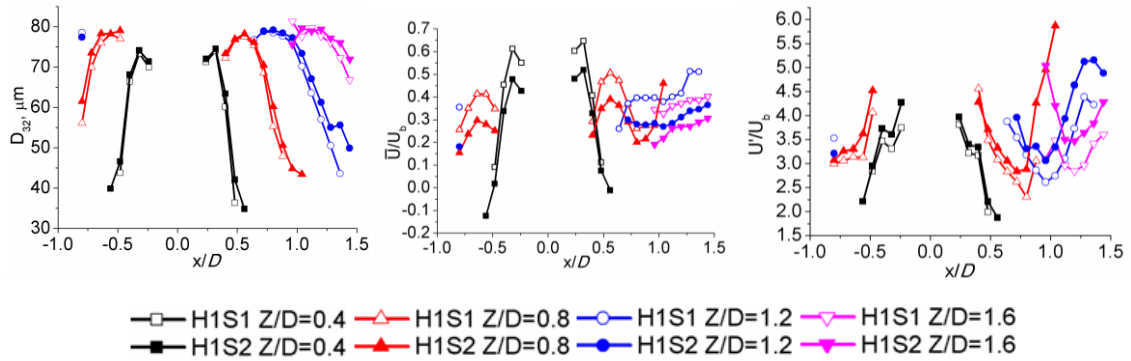
In this section, the PDA data from heptane, decane and dodecane flames were shown as supplemental plots of Ch. 4. Main features were discussed in section 4.2.3. Table A summarises the flow conditions.

Table A. Test cases evaluated by PDA for various departures from blow-off of the spray flames of heptane, decane and dodecane.

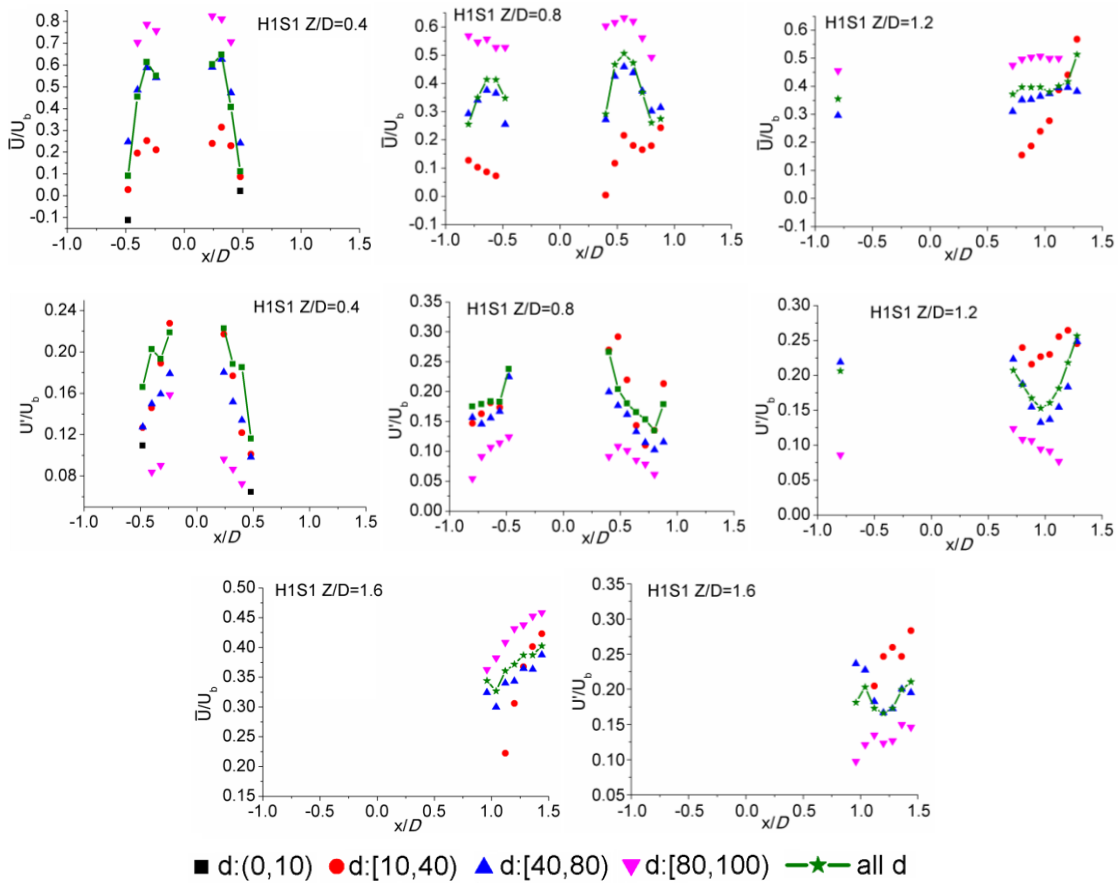
Name	HS0	H0S0	H0S1	H0S2	H1S1	H1S2	D1S1	D1S2	DD1S1	DD1S2
$U_b, \text{air}, \text{m/s}$	14.26	14.26	17.11	18.54	17.11	19.97	17.11	19.97	14.26	17.11
$U_l, \text{m/s}$	7.14	9.53	9.53	9.53	12.64	12.64	11.93	11.93	11.41	11.41
$\rho_l, \text{kg/m}^3$	668.3						720.7		753.2	
$\sigma, \text{N/m}$	2.01×10^{-2}						2.38×10^{-2}		2.54×10^{-2}	
$\nu_l, \text{m}^2/\text{s}$	0.61×10^{-6}						1.29×10^{-6}		1.98×10^{-6}	
Re_l	2329	3105			4192		1849		1153	
Re_g	11222		13466	14589	13466	15711	13466	15711	11222	13466
$D_{32(z/D=0.4)}$	73.5	72.5	71.7	72.7	74.1	74.5	78.4	78.7	77.3	79
Re_d	41.8	54.6	61.6	58.0	62.1	60.3	52.5	53.1	52.1	50.6
We_l	339	602			1098		860		774	
We_g	0.60	1.07			1.95		1.42		1.22	
Ta	26570	14946			8201		2800		1406	
Oh	0.008						0.016		0.024	

A.2 Results

A.2.1 Heptane flames (H1S1 vs. H1S2)



(a)



(b)

Figure A.1. (a) Distributions of Sauter mean diameter (left), normalised droplet mean axial velocity (middle), and normalised rms fluctuations of axial velocity (right); (b) mean and rms axial droplet velocity conditional on the droplet size ranges (square: 0-10 μm ; circle: 10-

40 μm ; up-triangle: 40-80 μm ; down-triangle: 80-100 μm) and the mean and rms axial velocity using all droplets (star) vs. radius, measured at various downstream locations (10, 20, 30 and 40 mm). Heptane stable flames: H1S1 ($\dot{m}_f = 0.27\text{g/s}$, $U_b = 17.1\text{ m/s}$) and H1S2 ($\dot{m}_f = 0.27\text{g/s}$, $U_b = 20.0\text{ m/s}$).

A.2.2 Heptane flames (H0S1 vs. H0S2)

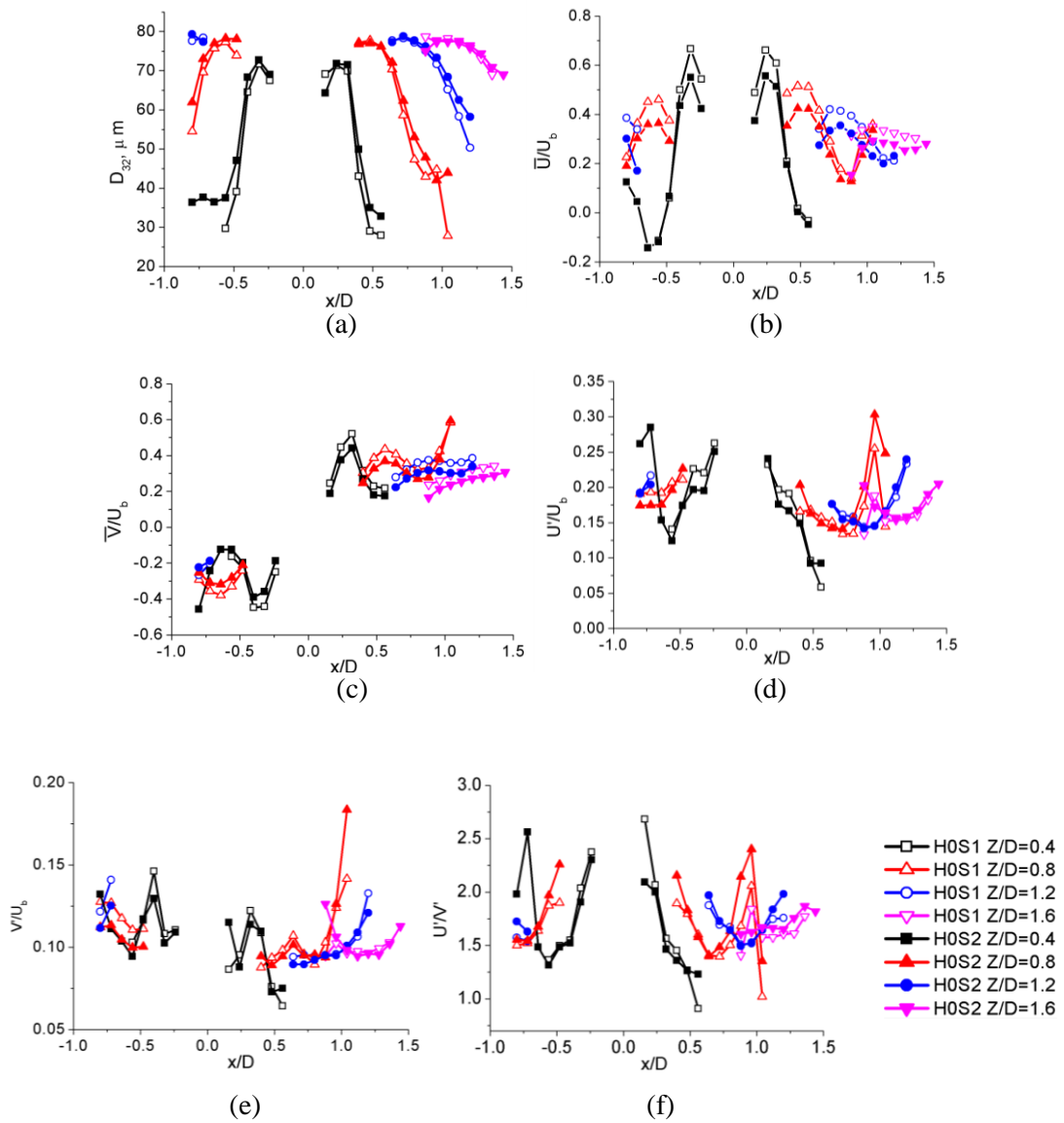


Figure A.2. Distributions of (a) Sauter mean diameter, normalised droplet mean (b) axial and (c) radial velocity, normalised rms fluctuations of (d) axial and (e) radial velocity, and (f) the ratio of the two velocity component fluctuations. Heptane stable flames: H0S1 ($\dot{m}_f = 0.20\text{g/s}$, $U_b = 17.1\text{ m/s}$) and H0S2 ($\dot{m}_f = 0.20\text{g/s}$, $U_b = 20.0\text{ m/s}$).

A.2.3 Decane flames (D1S1 vs. D1S2)

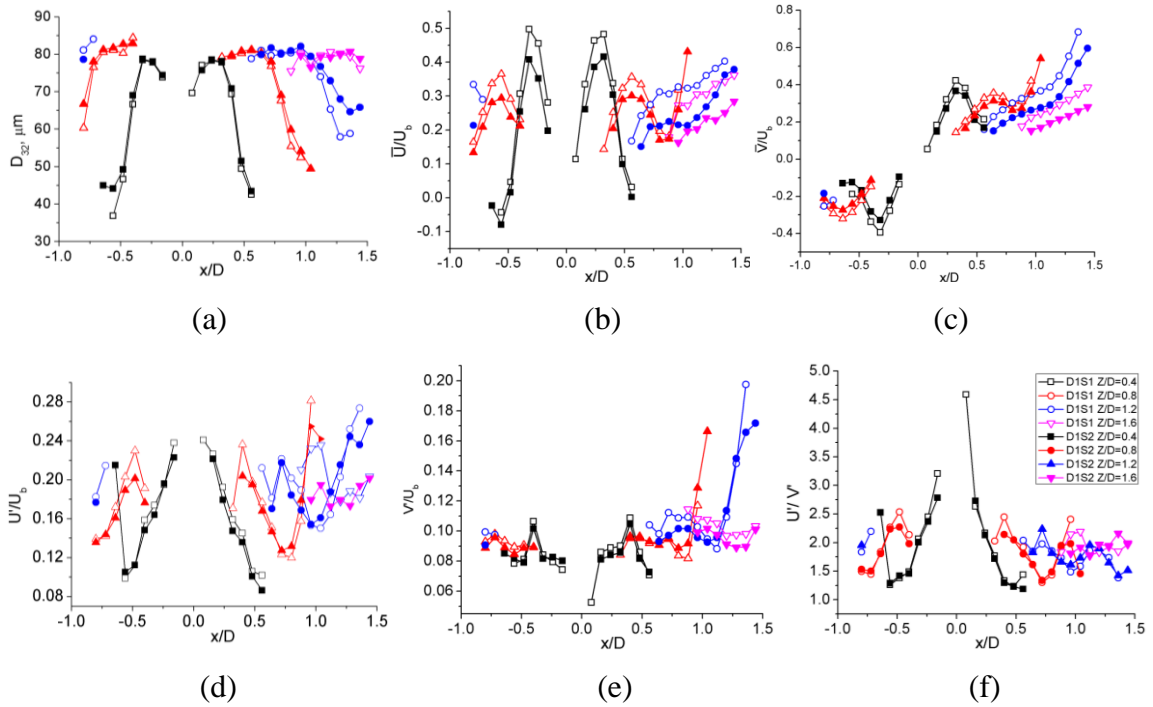


Figure A.3. Distributions of (a) Sauter mean diameter, normalised droplet mean (b) axial and (c) radial velocity, normalised rms fluctuations of (d) axial and (e) radial velocity, and (f) the ratio of the two velocity component fluctuations. Decane stable flames: D1S1 ($\dot{m}_f = 0.27\text{g/s}$, $U_b=17.1\text{ m/s}$) and D1S2 ($\dot{m}_f = 0.27\text{/s}$, $U_b=20.0\text{ m/s}$).

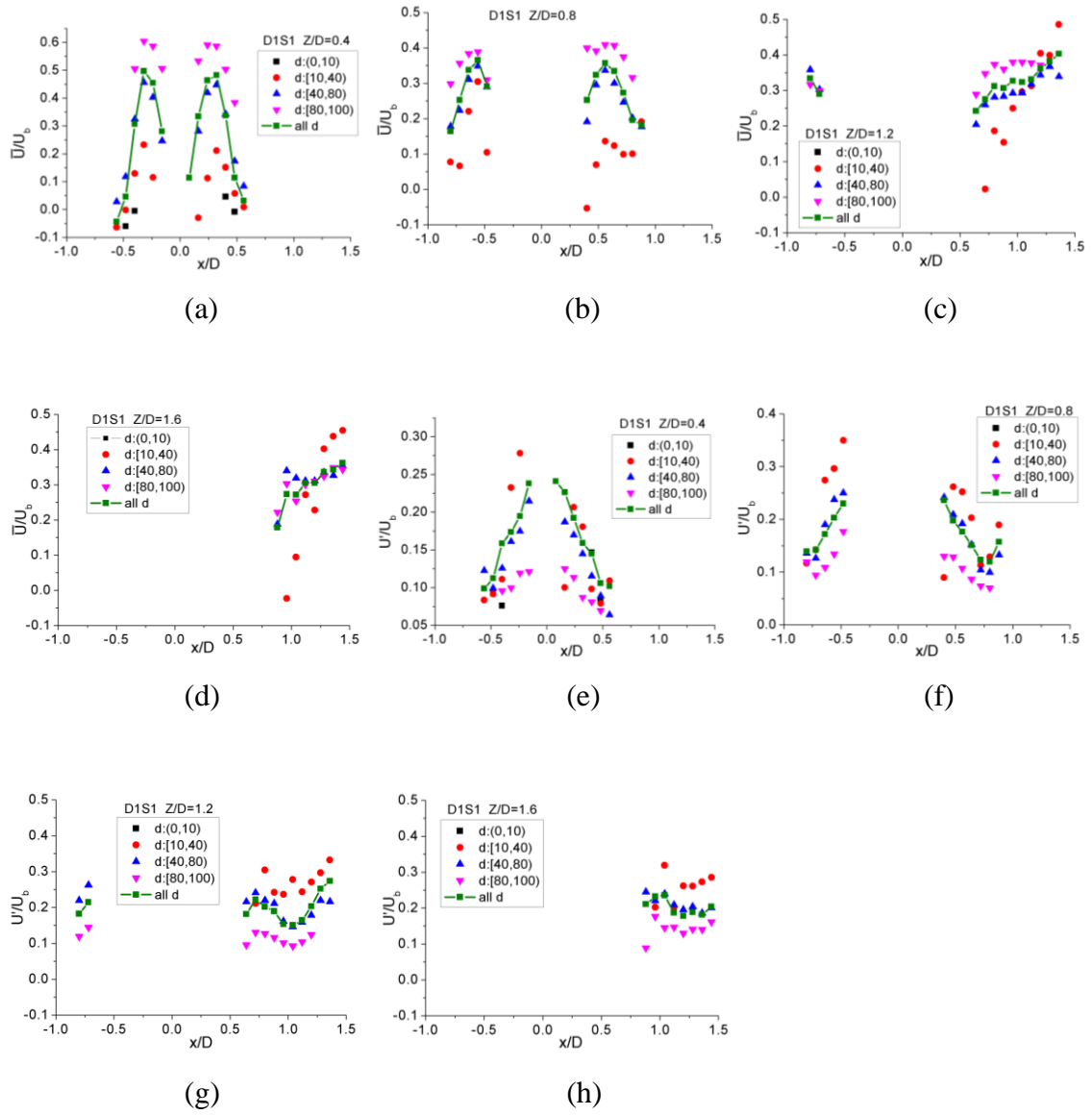


Figure A.4. Mean (a-d) and rms (e-h) axial droplet velocity conditional on the droplet size ranges (square: 0-10 μm ; circle: 10-40 μm ; up-triangle: 40-80 μm ; down-triangle: 80-100 μm) and the mean and rms axial velocity using all droplets (star) vs. radius, measured at various downstream locations (10, 20, 30 and 40 mm). Decane stable flames: D1S1 ($\dot{m}_f = 0.27\text{g/s}$, $U_b = 17.1\text{ m/s}$) and D1S2 ($\dot{m}_f = 0.27\text{g/s}$, $U_b = 20.0\text{ m/s}$).

A.2.4 Dodecane flames (DD1S1 vs. DD1S2)

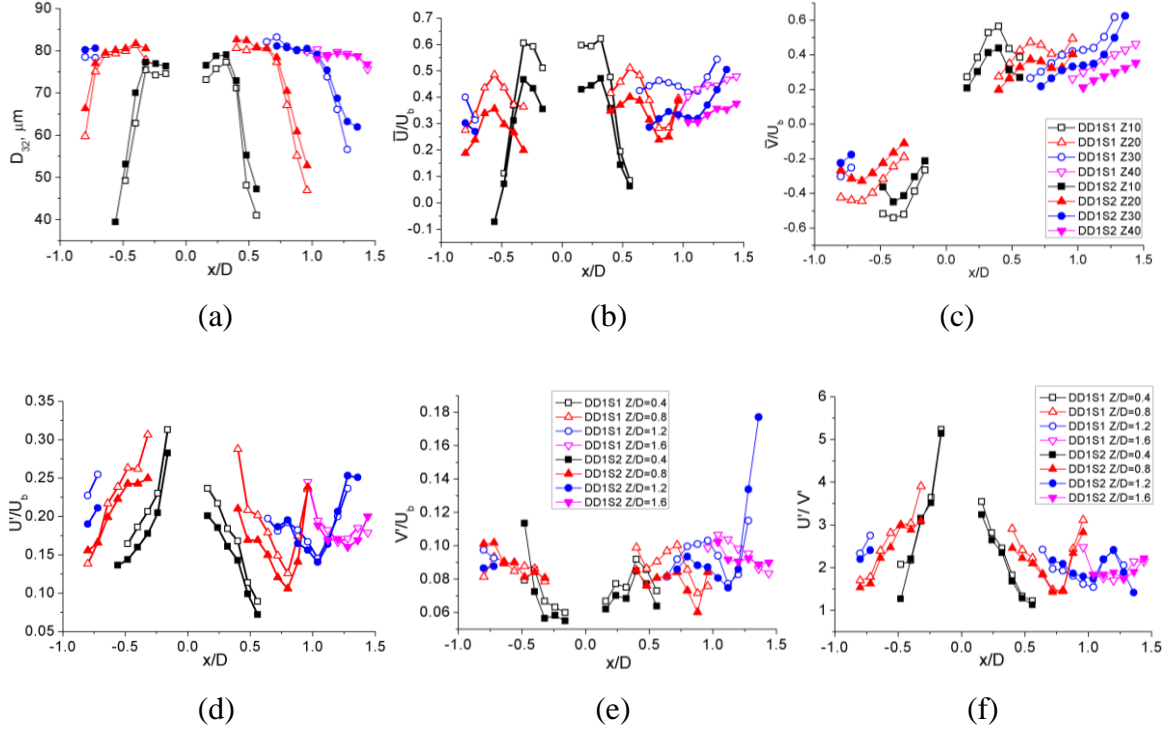


Figure A.5. Distributions of (a) Sauter mean diameter, normalised droplet mean (b) axial and (c) radial velocity, normalised rms fluctuations of (d) axial and (e) radial velocity, and (f) the ratio of the two velocity component fluctuations. Dodecane stable flames: DD1S1 ($\dot{m}_f = 0.27\text{g/s}$, $U_b = 14.3\text{ m/s}$) and DD1S2 ($\dot{m}_f = 0.27\text{g/s}$, $U_b = 17.1\text{ m/s}$).

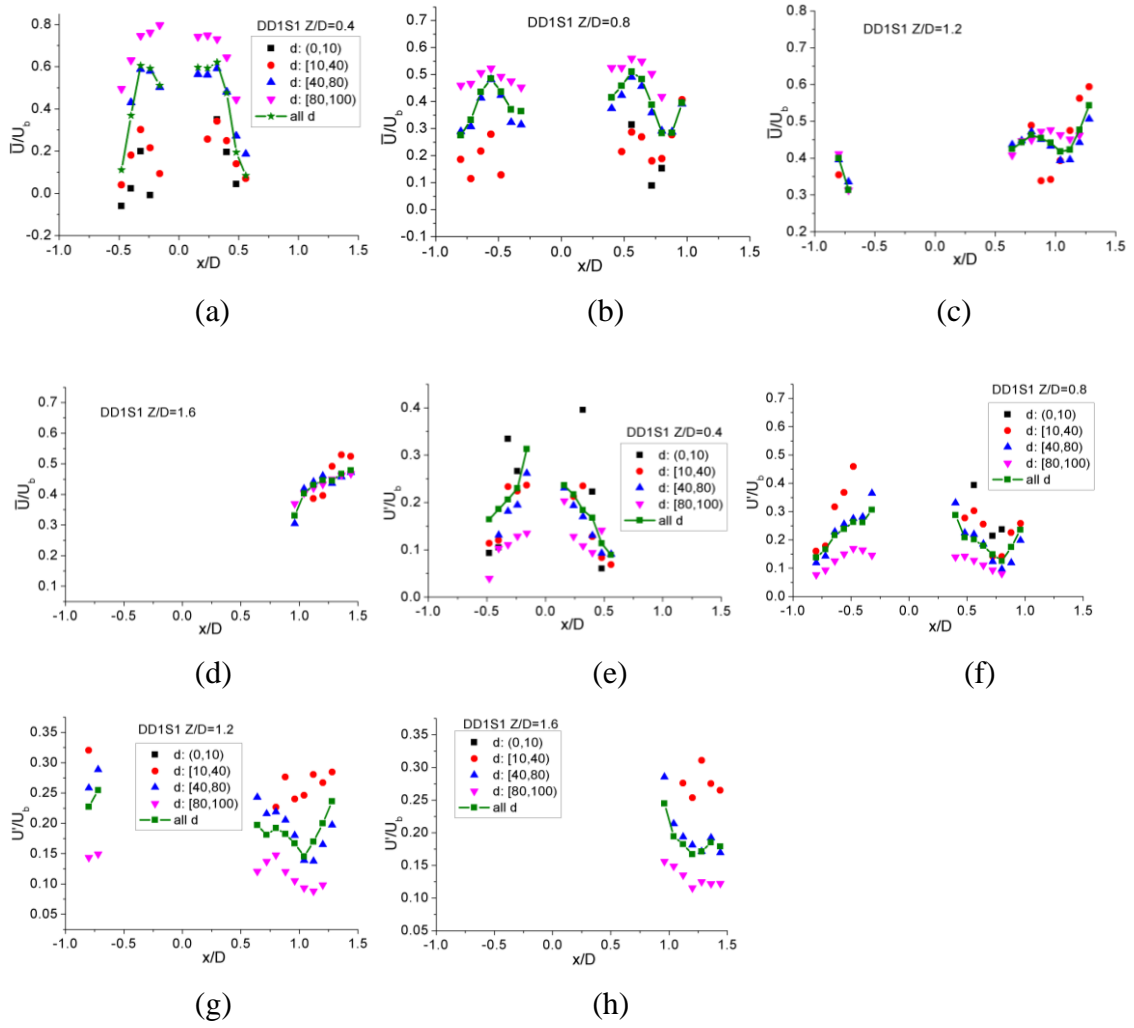


Figure A.6. Mean (a-d) and rms (e-h) axial droplet velocity conditional on the droplet size ranges (square: 0-10 μm ; circle: 10-40 μm ; up-triangle: 40-80 μm ; down-triangle: 80-100 μm) and the mean and rms axial velocity using all droplets (star) vs. radius, measured at various downstream locations (10, 20, 30 and 40 mm). Dodecane stable flames: DD1S1 ($\dot{m}_f = 0.27\text{g/s}$, $U_b = 14.3\text{ m/s}$) and DD1S2 ($\dot{m}_f = 0.27\text{g/s}$, $U_b = 17.1\text{ m/s}$).

References

- [1] Lefebvre AH. Gas turbine combustion: alternative fuels and emissions. CRC Press; 2010.
- [2] Ballal DR, Lefebvre AH. Weak extinction limits of turbulent heterogeneous fuel/air mixtures. *J Eng Gas Turbines Power* 1980; 102: 416–21.
- [3] Plee SL, Mellor AM. Characteristic time correlation for lean blowoff of bluff-body-stabilized flames. *Combust Flame* 1979; 35: 61–80.
- [4] Ateshkadi A, McDonell VG, Samuelsen GS. Lean blowout model for a spray-fired swirl-stabilized combustor. *Proc Combust Inst* 2000; 28: 1281–8.
- [5] Marinov S, Kern M, Zarzalis N, Habisreuther P, Peschiulli A, Turrini F, Sara ON. Similarity issues of kerosene and methane confined flames stabilized by swirl in regard to the weak extinction limit. *Flow Turbul Combust* 2012; 89: 73–95.
- [6] Cavaliere DE, Kariuki J, Mastorakos E. A comparison of the blow-off behaviour of swirl-stabilized premixed, non-premixed and spray flames. *Flow Turbul Combust* 2013; 91: 347–72.
- [7] Hardalupas Y, Taylor AMKP, Whitelaw JH. Mass flux, mass fraction and concentration of liquid fuel in a swirl-stabilized flame. *Int J Multiph Flow* 1994; 20: 233–59.
- [8] Hardalupas Y, Liu CH, Whitelaw JH. Experiments with disk stabilized kerosene-fuelled flames. *Combust Sci Technol* 1994; 97: 157–91.
- [9] Masri AR, Dibble RW, Barlow RS. The structure of turbulent nonpremixed flames revealed by Raman-Rayleigh-LIF measurements. *Prog Energy Combust Sci* 1996; 22: 307–62.
- [10] Masri AR, Kalt PAM, Barlow RS. The compositional structure of swirl-stabilised turbulent nonpremixed flames. *Combust Flame* 2004; 137: 1–37.
- [11] Masri AR, Kalt PAM, Al-Abdeli YM, Barlow RS. Turbulence–chemistry interactions in non-premixed swirling flames. *Combust Theory Model* 2007; 11: 653–73.
- [12] Dally BB, Masri AR, Barlow RS, Fiechtner GJ. Instantaneous and mean compositional structure of bluff-body stabilized nonpremixed flames. *Combust Flame*

1998; 114: 119–48.

[13] Juddoo M, Masri AR. High-speed OH-PLIF imaging of extinction and re-ignition in non-premixed flames with various levels of oxygenation. *Combust Flame* 2011; 158: 902–14.

[14] Meares S, Prasad VN, Juddoo M, Luo KH, Masri AR. Simultaneous planar and volume cross-LIF imaging to identify out-of-plane motion. *Proc Combust Inst* 2015; 35: 3813-20.

[15] Steinberg AM, Boxx I, Arndt CM, Frank JH, Meier W. Experimental study of flame-hole reignition mechanisms in a turbulent non-premixed jet flame using sustained multi-kHz PIV and crossed-plane OH PLIF. *Proc Combust Inst* 2011; 33: 1663–72.

[16] Meier W, Duan XR, Weigand P. Investigations of swirl flames in a gas turbine model combustor. *Combust Flame* 2006; 144: 225–36.

[17] Meier W, Boxx I, Stohr M, Carter CD. Laser-based investigations in gas turbine model combustors. *Exp Fluids* 2010; 49: 865-82.

[18] Sutton JA, Driscoll JF. Imaging of local flame extinction due to the interaction of scalar dissipation layers and the stoichiometric contour in turbulent non-premixed flames. *Proc Combust Inst* 2007; 31: 1487–95.

[19] Hult J, Meier U, Meier W, Harvey A, Kaminski CF. Experimental analysis of local flame extinction in a turbulent jet diffusion flame by high repetition 2-D laser techniques and multi-scalar measurements. *Proc Combust Inst* 2005; 30: 701–9.

[20] Böhm B, Heeger C, Boxx I, Meier W, Dreizler A. Time-resolved conditional flow field statistics in extinguishing turbulent opposed jet flames using simultaneous high speed PIV/OH-PLIF. *Proc Combust Inst* 2009; 32: 1647–54.

[21] Kaiser SA, Frank JH. Spatial scales of extinction and dissipation in the near field of non-premixed turbulent jet flames. *Proc Combust Inst* 2009; 32: 1639–46.

[22] Karpetsis AN, Barlow RS. Measurements of scalar dissipation in a turbulent piloted methane/air jet flame. *Proc Combust Inst* 2002; 29: 1929–36.

[23] Karpetsis AN, Barlow RS. Measurements of flame orientation and scalar dissipation in turbulent partially premixed methane flames. *Proc Combust Inst* 2005; 30: 665–72.

[24] Barlow RS, Karpetsis AN. Measurements of scalar variance, scalar dissipation, and length scales in turbulent piloted methane/air jet flames. *Flow Turbul Combust* 2004; 72:

427–48.

- [25] Barlow RS, Frank JH, Karpetis AN, Chen J-Y. Piloted methane/air jet flames: Transport effects and aspects of scalar structure. *Combust Flame* 2005; 143: 433–49.
- [26] Mauss F, Keller D, Peters N. A Lagrangian simulation of flamelet extinction and re-ignition in turbulent jet diffusion flames. *23rd Sym (Int) Combust* 1991; 23: 693–8.
- [27] Peters N. Local quenching due to flame stretch and non-premixed turbulent combustion. *Combust Sci Technol* 1983; 30: 1–17.
- [28] Peters N. Laminar flamelet concepts in turbulent combustion. *21st Sym (Int) Combust* 1988; 21: 1231–50.
- [29] Mastorakos E, Taylor AMKP, Whitelaw JH. Scalar dissipation rate at the extinction of turbulent counterflow nonpremixed flames. *Combust Flame* 1992; 91: 55–64.
- [30] Ihme M, Pitsch H. Prediction of extinction and reignition in nonpremixed turbulent flames using a flamelet/progress variable model. *Combust Flame* 2008; 155: 90–107.
- [31] Pitsch H, Cha C, Fedotov S. Flamelet modelling of non-premixed turbulent combustion with local extinction and re-ignition. *Combust Theory Model* 2003; 7: 317–32.
- [32] Cha CM, Kosály G, Pitsch H. Modeling extinction and reignition in turbulent nonpremixed combustion using a doubly-conditional moment closure approach. *Phys Fluids* 2001; 13: 3824.
- [33] Swaminathan N, Bilger RW. Study of the conditional covariance and variance equations for second order conditional moment closure. *Phys Fluids* 1999; 11: 2679–95.
- [34] Echekki T, Kerstein AR, Dreeben TD, Chen J-Y. “One-dimensional turbulence” simulation of turbulent jet diffusion flames: model formulation and illustrative applications. *Combust Flame* 2001; 125: 1083–105.
- [35] Xu J, Pope SB. PDF calculations of turbulent nonpremixed flames with local extinction. *Combust Flame* 2000; 123: 281–307.
- [36] Lindstedt RP, Louloudi SA, Váos EM. Joint scalar probability density function modeling of pollutant formation in piloted turbulent jet diffusion flames with comprehensive chemistry. *Proc Combust Inst* 2000; 28: 149–56.

References

- [37] Hewson JC, Kerstein AR, Local extinction and reignition in nonpremixed turbulent CO/H₂/N₂ jet flames. *Combust Sci Technol* 2002;174:35-66.
- [38] Prasad VN, Juddoo M, Masri AR, Jones WP, Luo KH. Investigation of extinction and re-ignition in piloted turbulent non-premixed methane–air flames using LES and high-speed OH-LIF. *Combust Theory Model* 2013; 17: 483–503.
- [39] Bijjula K, Kyritsis DC. Experimental evaluation of flame observables for simplified scalar dissipation rate measurements in laminar diffusion flamelets. *Proc Combust Inst* 2005; 30: 493–500.
- [40] Gordon R, Masri A, Mastorakos E. Heat release rate as represented by [OH] × [CH₂O] and its role in autoignition. *Combust Theory Model* 2009; 13: 645–70.
- [41] Ayoola BO, Balachandran R, Frank JH, Mastorakos E, Kaminski CF. Spatially resolved heat release rate measurements in turbulent premixed flames. *Combust Flame* 2006; 144: 1–16.
- [42] Harrington JE, Smyth KC. Laser-induced fluorescence measurements of formaldehyde in a methane/air diffusion flame. *Chem Phys Lett* 1993; 202: 196–202.
- [43] Zukoski EE, Marble FE. Experiments concerning the mechanism of flame blowoff from bluff bodies, Guggenheim Jet Propulsion Centre, Report, 1983; 82: 205-10.
- [44] Yamaguchi S, Ohiwa N, Hasegawa T. Structure and blow-off mechanism of rod-stabilized premixed flame. *Combust Flame* 1985; 62: 31–41.
- [45] Radhakrishnan K, Heywood JB, Tabaczynski RJ. Premixed turbulent flame blowoff velocity correlation based on coherent structures in turbulent flows. *Combust Flame* 1981; 42: 19–33.
- [46] Nair S, Lieuwen T. Acoustic detection of blowout in premixed flames. *J Propul Power* 2005; 21: 32–9.
- [47] Chaudhuri S, Cetegen BM. Blowoff characteristics of bluff-body stabilized conical premixed flames with upstream spatial mixture gradients and velocity oscillations. *Combust Flame* 2008; 153: 616–33.
- [48] Chaudhuri S, Kostka S, Renfro MW, Cetegen BM. Blowoff dynamics of bluff body stabilized turbulent premixed flames. *Combust Flame* 2010; 157: 790–802.
- [49] Dawson JR, Gordon RL, Kariuki J, Mastorakos E, Masri AR, Juddoo M. Visualization of blow-off events in bluff-body stabilized turbulent premixed flames. *Proc Combust Inst* 2011; 33: 1559–66.

References

- [50] Shanbhogue SJ, Husain S, Lieuwen T. Lean blowoff of bluff body stabilized flames: Scaling and dynamics. *Prog Energy Combust Sci* 2009; 35: 98–120.
- [51] Kariuki J, Dawson JR, Mastorakos E. Measurements in turbulent premixed bluff body flames close to blow-off. *Combust Flame* 2012; 159: 2589–607.
- [52] Kariuki J, Dowlut A, Yuan R, Balachandran R, Mastorakos E. Heat release imaging in turbulent premixed methane–air flames close to blow-off. *Proc Combust Inst* 2015; 35: 1443–50.
- [53] Kalghatgi GT. Blow-out stability of gaseous jet diffusion flames. Part I: in still air. *Combust Sci Technol* 1981; 26: 233–9.
- [54] Broadwell JE, Dahm WJA, Mungal MG. Blowout of turbulent diffusion flames. *20th Sym (Int) Combust* 1985; 20: 303–10.
- [55] Dahm WJA, Mayman AG. Blowout limits of turbulent jet diffusion flames for arbitrary source conditions. *AIAA J* 1990; 28: 1157–62.
- [56] Stamps D, Tieszen S. Blowout of turbulent jet diffusion flames. *Fuel* 2014; 118: 113–22.
- [57] Continillo G, Sirignano WA. Counterflow spray combustion modeling. *Combust Flame* 1990; 81: 325–40.
- [58] Gutheil E, Sirignano WA. Counterflow spray combustion modeling with detailed transport and detailed chemistry. *Combust Flame* 1998; 113: 92–105.
- [59] Gutheil E. Structure and extinction of laminar ethanol-air spray flames. *Combust Theory Model* 2001; 5: 131–45.
- [60] Dvorjetski A, Greenberg JB. Steady-state and extinction analyses of counterflow spray diffusion flames with arbitrary finite evaporation rate. *Combust Sci Technol* 2002; 174: 187–208.
- [61] Mikami M, Miyamoto S, Kojima N. Counterflow diffusion flame with polydisperse sprays. *Proc Combust Inst* 2002; 29: 593–9.
- [62] Tyliczszak A, Cavaliere DE, Mastorakos E. LES/CMC of blow-off in a liquid fueled swirl burner. *Flow Turbul Combust* 2014; 92: 237–67.
- [63] Syred N, Beér JM. Combustion in swirling flows: a review. *Combust Flame* 1974; 23: 143–201.

References

- [64] Beér JM, Chigier NA. Combustion aerodynamics. Halsted Press Division, Wiley; 1972.
- [65] Gupta AK, Lilley DG, Syred N. Swirl flows. Abacus Press; 1984.
- [66] Lilley DG. Swirl flows in combustion: a review. *AIAA J* 1977; 15: 1063–78.
- [67] Vanoverberghe K, Van den Bulck E, Tummers M. Flow structure of lifted swirling jet flames. *Flow Turbul Combust* 2004; 73: 25–47.
- [68] Olivani A, Solero G, Cozzi F, Coghe A. Near field flow structure of isothermal swirling flows and reacting non-premixed swirling flames. *Exp Therm Fluid Sci* 2007; 31: 427–36.
- [69] Weigand P, Meier W, Duan XR, Stricker W, Aigner M. Investigations of swirl flames in a gas turbine model combustor. *Combust Flame* 2006; 144: 205–24.
- [70] Tummers M, Hubner A, Vanveen E, Hanjalic K, Vandermeer T. Hysteresis and transition in swirling nonpremixed flames. *Combust Flame* 2009; 156: 447–59.
- [71] Tangirala V, Driscoll JF. Temperatures within non-premixed flames: effects of rapid mixing due to swirl. *Combust Sci Technol* 1988; 60: 143-162.
- [72] Al-Abdeli YM, Masri AR. Stability characteristics and flowfields of turbulent non-premixed swirling flames. *Combust Theor Model*, 2003; 7: 731-766.
- [73] Mastorakos E. Ignition of turbulent non-premixed flames. *Prog Energy Combust Sci* 2009; 35: 57–97.
- [74] Liñán A. The asymptotic structure of counterflow diffusion flames for large activation energies. *Acta Astronaut* 1974; 1: 1007–39.
- [75] Williams FA. Combustion theory: the fundamental theory of chemically reacting flow systems. Perseus Books Group; 1985.
- [76] Mastorakos E. Ignition of turbulent non-premixed flames. *Prog Energy Combust Sci* 2009; 35: 57–97.
- [77] Buckmaster J. Edge-flames. *Prog Energy Combust Sci* 2002; 28: 435–75.
- [78] Pantano C, Pullin DI. On the dynamics of the collapse of a diffusion-flame hole. *J Fluid Mech* 2003; 480: 311–32.
- [79] Chakraborty N, Mastorakos E. Numerical investigation of edge flame propagation

References

- characteristics in turbulent mixing layers. *Phys Fluids* 2006; 18: 105103.
- [80] Sripakagorn P, Mitarai S, Kosály G, Pitsch H. Extinction and reignition in a diffusion flame: a direct numerical simulation study. *J Fluid Mech* 2004; 518: 231–59.
- [81] Pantano C. Direct simulation of non-premixed flame extinction in a methane air jet with reduced chemistry. *J Fluid Mech* 2004; 514: 231-70.
- [82] Barlow RS, Karpets AN. Scalar length scales and spatial averaging effects in turbulent piloted methane/air jet flames. *Proc Combust Inst* 2005; 30: 673–80.
- [83] Watson K, Lyons K, Donbar J, Carter C. Simultaneous Rayleigh imaging and CH-PLIF measurements in a lifted jet diffusion flame. *Combust Flame* 2000; 123: 252–65.
- [84] Lyons KM. Toward an understanding of the stabilization mechanisms of lifted turbulent jet flames: experiments. *Prog Energy Combust Sci* 2007; 33: 211–31.
- [85] Glassman I, Yetter RA. *Combustion*. Fourth ed. Elsevier Inc. 2008.
- [86] Peters N, Williams FA. Liftoff characteristics of turbulent jet diffusion flames. *AIAA J* 1983; 21: 423–9.
- [87] Chen Y, Chang C, Pan K-L, Yang J-T. Flame lift-off and stabilization mechanisms of nonpremixed jet flames on a bluff-body burner. *Combust Flame* 1998; 115: 51–65.
- [88] Pitts WM. Assessment of theories for the behavior and blowout of lifted turbulent jet diffusion flames. *22nd Sym (Int) Combust* 1989; 22: 809–16.
- [89] Kevin M Lyons. Toward an understanding of the stabilization mechanisms of lifted turbulent jet flames. *Prog Energy Combust Sci* 2007; 33: 211–31.
- [90] Lawn CJ. Lifted flames on fuel jets in co-flowing air. *Prog Energy Combust Sci* 2009; 35: 1–30.
- [91] Nishimura T, Kunitsugu K, Morio K. The hysteresis phenomenon in flame lift-off on a bluff-body burner under airflow dominant conditions. *Combust Flame* 2012; 159: 1499–502.
- [92] Williams A. *Combustion of liquid fuel sprays*. Butterworths (Canada) Limited; 1990.
- [93] Sirignano WA. Fuel droplet vaporization and spray combustion theory. *Prog Energy Combust Sci* 1983; 9: 291–322.

References

- [94] Ashgriz N. Handbook of atomization and sprays: theory and applications. Springer Science & Business Media; 2011.
- [95] Law CK. Combustion physics. Cambridge University Press; 2006.
- [96] Turns SR. An introduction to combustion: concepts and applications. McGraw-Hill; 1996.
- [97] Greenberg JB, Alibagli D, Tambour Y. An opposed jet quasi-monodisperse spray diffusion flame. *Combust Sci Technol* 1986; 50: 255–70.
- [98] Schlotz D, Gutheil E. Modeling of laminar mono- and bidisperse liquid oxygen/hydrogen spray flames in the counterflow configuration. *Combust Sci Technol* 2000; 158: 195–210.
- [99] Dakhliya RB, Giovangigli V. Multiradii modeling of counterflow spray diffusion flames. *Proc Combust Inst* 2000; 28: 1039–45.
- [100] Dvorjetski A, Greenberg JB. Analysis of steady state polydisperse counterflow spray diffusion flames in the large Stokes number limit. *Proc Combust Inst* 2009; 32: 2205–14.
- [101] Massot M, Kumar M, Smooke MD, Gomez A. Spray counterflow diffusion flames of heptane: Experiments and computations with detailed kinetics and transport. 27th Sym (Int) Combust 1998; 27: 1975–83.
- [102] Dvorjetski A, Greenberg JB. Small Stokes number analysis of counterflow spray diffusion flames. 43rd AIAA Aerosp Sci Meet Exhib 2005; 1427.
- [103] Greenberg JB, Sarig N. An analysis of multiple flames in counterflow spray combustion. *Combust Flame*, 1996; 104: 431-459.
- [104] Dakhliya RB, Giovangigli V, Rosner DE. Soret effects in laminar counterflow spray diffusion flames. *Combust Theory Model* 2002; 6: 1–17.
- [105] Ihme M. Pollutant formation and noise emission in turbulent non-premixed flames PhD thesis, Stanford University, 2007.
- [106] Neophytou A, Mastorakos E. Simulations of laminar flame propagation in droplet mists. *Combust Flame* 2009; 156: 1627–40.
- [107] Greenberg JB, Kalma A. A study of stretch in premixed spray flames. *Combust Flame* 2000; 123: 421–9.

References

- [108] Silverman I, Greenberg JB, Tambour Y. Stoichiometry and polydisperse effects in premixed spray flames. *Combust Flame* 1993; 93: 97–118.
- [109] Polymeropoulos CE. Flame propagation in a one-dimensional liquid fuel spray. *Combust Sci Technol* 2007; 9: 197–207.
- [110] Hou S-S. Analysis of a stagnation-point premixed flame influenced by inert spray, heat loss, and non-unity Lewis number. *Appl Math Model* 2013; 37: 1333–46.
- [111] Ballal DR, Lefebvre AH. Flame propagation in heterogeneous mixtures of fuel droplets, fuel vapor and air. *18th Sym (Int) Combust* 1981; 18: 321–8.
- [112] Myers GD, Lefebvre AH. Flame propagation in heterogeneous mixtures of fuel drops and air. *Combust Flame* 1986; 66: 193–210.
- [113] Abramzon B, Sirignano WA. Droplet vaporization model for spray combustion calculations. *Int J Heat Mass Transf* 1989; 32: 1605–18.
- [114] Chen G, Gomez A. Counterflow diffusion flames of quasi-monodisperse electrostatic sprays. *24th Sym (Int) Combust* 1992; 24: 1531–9.
- [115] Li SC, Libby PA, Williams FA. Experimental and theoretical studies of counterflow spray diffusion flames. *24th Sym (Int) Combust* 1992; 24: 1503–12.
- [116] Li S. Spray stagnation flames. *Prog Energy Combust Sci* 1997; 23: 303–47.
- [117] Li SC, Williams FA. Counterflow heptane flame structure. *Proc Combust Inst* 2000; 28: 1031–8.
- [118] Santoro VS, Kyritsis DC, Gomez A. An experimental study of vortex-flame interaction in counterflow spray diffusion flames. *Proc Combust Inst* 2000; 28: 1023–30.
- [119] Santoro VS, Gomez A. Extinction and reignition in counterflow spray diffusion flames interacting with laminar vortices. *Proc Combust Inst* 2002; 29: 585–92.
- [120] Mikami M, Mizuta Y, Tsuchida Y, Kojima N. Flame structure and stabilization of lean-premixed sprays in a counterflow with low-volatility fuel. *Proc Combust Inst* 2009; 32: 2223–30.
- [121] Sasongko MN, Mikami M, Dvorjetski A. Extinction condition of counterflow diffusion flame with polydisperse water sprays. *Proc Combust Inst* 2011; 33: 2555–62.
- [122] Gao LP, D'Angelo Y, Silverman I, Gome A, Smooke MD. Quantitative comparison of detailed numerical computations and experiments in counterflow spray

diffusion flames. 26th Sym (Int) Combust 1996; 26: 1739–46.

[123] Darabiha N, Lacas F, Rolon JC, Candel S. Laminar counterflow spray diffusion flames: A comparison between experimental results and complex chemistry calculations. *Combust Flame* 1993; 95: 261–75.

[124] Watanabe H, Kurose R, Hwang S, Akamatsu F. Characteristics of flamelets in spray flames formed in a laminar counterflow. *Combust Flame* 2007; 148: 234–48.

[125] Masri AR, Gounder JD. Turbulent spray flames of acetone and ethanol approaching extinction. *Combust Sci Technol* 2010; 182: 702–15.

[126] O’Loughlin W, Masri AR. The structure of the auto-ignition region of turbulent dilute methanol sprays issuing in a vitiated co-flow. *Flow Turbul Combust* 2012; 89: 13–35.

[127] Masri AR, Gounder JD, O’Loughlin W, DeFina L. On the boundary conditions and spatial structure of turbulent jet flames of dilute sprays. 7th Mediterr Combust Symp Sardinia, Italy 2011.

[128] Kourmatzis A, Pham PX, Masri AR. Characterization of atomization and combustion in moderately dense turbulent spray flames. *Combust Flame* 2015; 162: 978–96.

[129] Zeldovich YB, Barenblatt GI, Librovich VB, Makhviladze GM. The mathematical theory of combustion and explosions. New York 1985.

[130] Nunome Y, Kato S, Maruta K, Kobayashi H, Niioka T. Flame propagation of n-decane spray in microgravity. *Proc Combust Inst* 2002; 29: 2621–6.

[131] Niioka T. Flame propagation in sprays and particle clouds of less volatile fuels. *Combust Sci Technol* 2005; 177: 1167–82.

[132] Longwell JP, Frost EE, Weiss MA. Flame stability in bluff body recirculation zones. *Ind Eng Chem* 1953; 45: 1629–33.

[133] Tabaczynski RJ, Ferguson CR, Radhakrishnan K. A turbulent entrainment model for spark-ignition engine combustion. SAE Technical Paper 1977; 770647.

[134] Kariuki J, Cavaliere DE, Letty C, Mastorakos E. A comparison of the blow-off behaviour of swirl-stabilized premixed and spray flames. 50th AIAA Aerosp Sci Meet Exp 2012; 505.

[135] Mellor AM. Semi-empirical correlations for gas turbine emissions, ignition, and

flame stabilization. *Prog Energy Combust Sci* 1980; 6: 347–58.

[136] Tsuji H. *Science of Machines* 1977: 1123.

[137] Kariuki J, Worth N, Dawson J, Mastorakos E. Visualisation of blow-off events of two interacting turbulent premixed flames. *51st AIAA Aerosp Sci Meet* 2013; 692.

[138] Bradley D, Gaskell PH, Gu XJ, Sedaghat A. Premixed flamelet modelling: factors influencing the turbulent heat release rate source term and the turbulent burning velocity. *Combust Flame* 2005; 143: 227–45.

[139] Peters N. Laminar diffusion flamelet models in non-premixed turbulent combustion. *Prog Energy Combust Sci* 1984; 10: 319–39.

[140] Dooley S, Won SH, Heyne J, Farouk TI, Ju Y, Dryer FL, et al. The experimental evaluation of a methodology for surrogate fuel formulation to emulate gas phase combustion kinetic phenomena. *Combust Flame* 2012; 159: 1444–66.

[141] Feikema D, Chen R, Driscoll J. Blowout of nonpremixed flames: maximum coaxial air velocities achievable, with and without swirl. *Combust Flame* 1991; 86: 347–58.

[142] Moore NJ, McCraw JL, Lyons KM. Observations on jet-flame blowout. *Int J React Syst* 2008; 2008: 1–7.

[143] Böhm B, Geyer D, Dreizler A, Venkatesan KK, Laurendeau NM, Renfro MW. Simultaneous PIV/PTV/OH PLIF imaging: conditional flow field statistics in partially premixed turbulent opposed jet flames. *Proc Combust Inst* 2007; 31: 709–17.

[144] Burkert A, Paa W, Reimert M, Klinkov K, Eigenbrod C. Formaldehyde LIF detection with background subtraction around single igniting GTL diesel droplets. *Fuel* 2013; 111: 384–92.

[145] Haessler H, Bockhorn H, Pfeifer C, Kuhn D. Formaldehyde-LIF of dimethyl ether during auto-ignition at elevated pressures. *Flow Turbul Combust* 2011; 89: 249–59.

[146] Donkerbroek a. J, van Vliet a. P, Somers LMT, Frijters PJM, Klein-Douwel RJH, Dam NJ, et al. Time- and space-resolved quantitative LIF measurements of formaldehyde in a heavy-duty diesel engine. *Combust Flame* 2010; 157: 155–66.

[147] Schrewe MR, Gandhi JB. Near-wall formaldehyde planar laser-induced fluorescence measurements during HCCI combustion. *Proc Combust Inst* 2007; 31: 2871–8.

References

- [148] Najm HN, Paul PH, Mueller CJ, Wyckoff PS. On the adequacy of certain experimental observables as measurements of flame burning rate. *Combust Flame* 1998; 113: 312–32.
- [149] Medwell PR, Dally BB. Effect of fuel composition on jet flames in a heated and diluted oxidant stream. *Combust Flame* 2012; 159: 3138–45.
- [150] Holmes P, Lumley JL, Berkooz G, Rowley CW. *Turbulence, coherent structures, dynamical systems and symmetry*. 2nd ed. Cambridge University Press; 2012.
- [151] Fogleman M, Lumley J, Rempfer D, Haworth D. Application of the proper orthogonal decomposition to datasets of internal combustion engine flows. *J Turbul* 2004; 5: 1-18.
- [152] Bizon K, Continillo G, Leistner KC, Mancaruso E, Vaglieco BM. POD-based analysis of cycle-to-cycle variations in an optically accessible diesel engine. *Proc Combust Inst* 2009; 32: 2809–16.
- [153] Bizon K, Continillo G, Mancaruso E, Merola SS, Vaglieco BM. POD-based analysis of combustion images in optically accessible engines. *Combust Flame* 2010; 157: 632–40.
- [154] Davis DW, Therkelsen PL, Littlejohn D, Cheng RK. Effects of hydrogen on the thermo-acoustics coupling mechanisms of low-swirl injector flames in a model gas turbine combustor. *Proc Combust Inst* 2013; 34: 3135–43.
- [155] Stöhr M, Boxx I, Carter CD, Meier W. Experimental study of vortex-flame interaction in a gas turbine model combustor. *Combust Flame* 2012; 159: 2636–49.
- [156] Kopp-Vaughan KM, Jensen TR, Cetegen BM, Renfro MW. Analysis of blowoff dynamics from flames with stratified fueling. *Proc Combust Inst* 2013; 34: 1491–8.
- [157] Kostka S, Lynch AC, Huelskamp BC, Kiel B V., Gord JR, Roy S. Characterization of flame-shedding behavior behind a bluff-body using proper orthogonal decomposition. *Combust Flame* 2012; 159: 2872–82.
- [158] Danby SJ, Echehki T. Proper orthogonal decomposition analysis of autoignition simulation data of nonhomogeneous hydrogen–air mixtures. *Combust Flame* 2006; 144: 126–38.
- [159] Frouzakis CE, Kevrekidis YG, Lee J, Boulouchos K, Alonso AA. Proper orthogonal decomposition of direct numerical simulation data: Data reduction and observer construction. *Proc Combust Inst* 2000; 28: 75–81.

References

- [160] Duwig C, Fureby C. Large eddy simulation of unsteady lean stratified premixed combustion. *Combust Flame* 2007; 151: 85–103.
- [161] Ayache S, Mastorakos E. Investigation of the “TECFLAM” non-premixed flame using large eddy simulation and proper orthogonal decomposition. *Flow Turbul Combust* 2012; 90: 219–41.
- [162] Phuoc TX, White FP. Laser-induced spark for measurements of the fuel-to-air ratio of a combustible mixture. *Fuel* 2002; 81: 1761–5.
- [163] Cremers DA, Radziemski LJ. *Handbook of laser-induced breakdown spectroscopy*. 2nd ed. Oxford, UK: John Wiley & Sons Ltd; 2013.
- [164] Noll R. *Laser-induced breakdown spectroscopy - fundamentals and applications*. 1st ed. Springer; 2012.
- [165] Thorne AP. *Spectrophysics*. Chapman and Hall; 1974.
- [166] Miziolek AW, Palleschi V, Schechter I. *Laser-Induced Breakdown Spectroscopy (LIBS) - fundamentals and applications*. 1st ed. Cambridge University Press; 2006.
- [167] Yueh FY, Singh JP. LIBS application to off-gas measurement. In Singh J, Thakur S. *Laser-induced breakdown spectroscopy*. 1st ed. Elsevier, 2007; 199–221.
- [168] Bak MS, Im S, Mungal MG, Cappelli MA. Studies on the stability limit extension of premixed and jet diffusion flames of methane, ethane, and propane using nanosecond repetitive pulsed discharge plasmas. *Combust Flame* 2013; 160: 2396–403.
- [169] Beduneau J. Measurements of minimum ignition energy in premixed laminar methane/air flow by using laser induced spark. *Combust Flame* 2003; 132: 653–65.
- [170] Do H, Carter C. Hydrocarbon fuel concentration measurement in reacting flows using short-gated emission spectra of laser induced plasma. *Combust Flame* 2013; 160: 601–9.
- [171] Eseller KE, Yueh FY, Singh JP. Laser-induced breakdown spectroscopy measurement in methane and biodiesel flames using an ungated detector. *Appl Opt* 2008; 47: 144–8.
- [172] Ferioli F, Buckley S. Measurements of hydrocarbons using laser-induced breakdown spectroscopy. *Combust Flame* 2006; 144: 435–47.
- [173] Hsu L-J, Alwahabi ZT, Nathan GJ, Li Y, Li ZS, Aldén M. Sodium and potassium released from burning particles of brown coal and pine wood in a laminar premixed

References

methane flame using quantitative laser-induced breakdown spectroscopy. *Appl Spectrosc* 2011; 65: 684–91.

[174] Kotzagianni M, Couris S. Femtosecond laser induced breakdown spectroscopy of air–methane mixtures. *Chem Phys Lett* 2013; 561-562: 36–41.

[175] Lee SH, Hahn HT, Yoh JJ. Towards a two-dimensional laser induced breakdown spectroscopy mapping of liquefied petroleum gas and electrolytic oxy-hydrogen flames. *Spectrochim Acta Part B* 2013; 88: 63–8.

[176] Yu X, Peng J, Yang P, Sun R, Yi Y, Zhao Y, Chen D, Yu J. Enhancement of a laminar premixed methane/oxygen/nitrogen flame speed using femtosecond-laser-induced plasma. *Appl Phys Lett* 2010; 97: 011503.

[177] Zimmer L, Okai K, Kurosawa Y. Combined laser induced ignition and plasma spectroscopy: Fundamentals and application to a hydrogen–air combustor. *Spectrochim Acta Part B* 2007; 62: 1484–95.

[178] Ferioli F, Puzinauskas PV, Buckley SG. Laser-induced breakdown spectroscopy for on-line engine equivalence ratio measurements. *Appl Spectrosc* 2003; 57: 1183–9.

[179] Joshi S, Olsen DB, Dumitrescu C, Puzinauskas PV, Yalin AP. Laser-induced breakdown spectroscopy for in-cylinder equivalence ratio measurements in laser-ignited natural gas engines. *Appl Spectrosc* 2009; 63: 549–54.

[180] Huang J-S, Ke C-B, Huang L-S, Lin K-C. The correlation between ion production and emission intensity in the laser-induced breakdown spectroscopy of liquid droplets. *Spectrochim Acta Part B* 2002; 57: 35–48.

[181] Kido A, Hoshi K, Kusaka H, Ogawa H, Miyamoto N. Instantaneous measurement of local concentration and vapor fraction in liquid-gas mixtures by laser-induced breakdown spectroscopy. *JSME Int J Series B* 2006; 49: 520–5.

[182] Zhang S, Yu X, Li F, Kang G, Chen L, Zhang X. Laser induced breakdown spectroscopy for local equivalence ratio measurement of kerosene/air mixture at elevated pressure. *Opt Lasers Eng* 2012; 50: 877–82.

[183] Huang J-S, Ke C-B, Lin K-C. Matrix effect on emission/current correlated analysis in laser-induced breakdown spectroscopy of liquid droplets. *Spectrochim Acta Part B* 2004; 59: 321–6.

[184] Letty C, Mastorakos E, Masri AR, Juddoo M, O’Loughlin W. Structure of igniting ethanol and n-heptane spray flames with and without swirl. *Exp Therm Fluid Sci* 2012;

43: 47–54.

[185] Dowlut AIGH, Hussain T, Balachandran R. Experimental investigation of dynamic response of acoustically forced turbulent premixed CH₄/CO₂/air flames. 19th Int C Sound Vib, 2012; 1: 498-505.

[186] Santoro RJ. Detailed studies of soot formation in laminar diffusion flames for application to modeling studies. Air Force Office Sci R, Final report, 1994.

[187] Petarca L, Marconi F. Fluorescence spectra and polycyclic aromatic species in a N-heptane diffusion flame. Combust Flame 1989; 78: 308–25.

[188] Sirovich L. Turbulence and the dynamics of coherent structures. I - Coherent structures. II - Symmetries and transformations. III - Dynamics and scaling. Q Appl Math 1987; 45: 561–71.

[189] Rotexo-Softpredict-Cosilab, GmbH and Co. KG Bad Zwischenahn (Germany), Cosilab Collection, Version 3.0, 2009.

[190] Ranzi E, Frassoldati A, Grana R, Cuoci A, Faravelli T, Kelley AP, Law CK. Hierarchical and comparative kinetic modeling of laminar flame speeds of hydrocarbon and oxygenated fuels. Prog Energy Combust Sci 2012; 38: 468–501.

[191] Held TJ, Marchese AJ, Dryer FL. A semi-empirical reaction mechanism for n-heptane oxidation and pyrolysis. Combust Sci Technol 1997; 123: 107–46.

[192] Honnet S, Seshadri K, Niemann U, Peters N. A surrogate fuel for kerosene. Proc Combust Inst 2009; 32: 485–92.

[193] Najm HN, Knio OM, Paul PH, Wycko PS. A study of flame observables in premixed methane-air flames. Combust Sci Technol 1998; 104: 1–6.

[194] Marinov NM. A detailed chemical kinetic model for high temperature ethanol oxidation. Int J Chem Kinet 1999; 31: 183–220.

[195] Lin SP, Reitz RD. Drop and spray formation from a liquid jet. Ann Rev Fluid Mech 1998; 30: 85–105.

[196] Tai J, Gan HY, Liang YN, Lok BK. Control of droplet formation in inkjet printing using Ohnesorge number category: materials and processes. IEEE; 2008; 761–6.

[197] Ohnesorge W. Formation of drops by nozzles and the breakup of liquid jets. J Appl Math Mech 1936; 16: 355–8.

References

- [198] Reitz RD. Atomization and other breakup regimes of a liquid jet. PhD Thesis Princeton Univ 1978.
- [199] Lefebvre AH. Atomization and sprays. CRC Press; 1988.
- [200] Beale J, Reitz R. Modeling spray atomization with the Kelvin-Helmholtz/Rayleigh-Taylor hybrid model. *Atomization Spray* 1999; 9: 623–50.
- [201] Reitz RD. Modeling atomization processes in high-pressure vaporizing sprays. *Atomization Spray Technol* 1987; 3: 309–37.
- [202] Im K-S, Lin K-C, Lai M-C, Chon MS. Breakup modeling of a liquid jet in cross flow. *Int J Automot Technol* 2011; 12: 489–96.
- [203] Mastorakos E, McGuirk JJ, Taylor AMKP. The origin of turbulence acquired by heavy particles in a round, turbulent jet. *Part Part Syst Char* 1990; 7: 203–8.
- [204] Hardalupas Y, Taylor AMKP, Whitelaw JH. Velocity and size characteristics of liquid-fuelled flames stabilized by a swirl burner. *Proc R Soc Lond A* 1990; 428: 129–55.
- [205] Dumouchel C. On the experimental investigation on primary atomization of liquid streams. *Exp Fluids* 2008; 45: 371–422.
- [206] Syred N. A review of oscillation mechanisms and the role of the precessing vortex core (PVC) in swirl combustion systems. *Prog Energy Combust Sci* 2006; 32: 93–161.
- [207] Ahmed S, Mastorakos E. Spark ignition of lifted turbulent jet flames. *Combust Flame* 2006; 146: 215–31.
- [208] Zimmer L, Okai K, Kurosawa Y. Combined laser induced ignition and plasma spectroscopy: fundamentals and application to a hydrogen–air combustor. *Spectrochim Acta Part B* 2007; 62: 1484–95.
- [209] Fuge GM, Ashfold MNR, Henley SJ. Studies of the plume emission during the femtosecond and nanosecond ablation of graphite in nitrogen. *J Appl Phys* 2006; 99: 014309.
- [210] Park HS, Nam SH, Park SM. Time-resolved optical emission studies on the laser ablation of a graphite target: The effects of ambient gases. *J Appl Phys* 2005; 97: 113103.
- [211] Letty C, Pastore A, Mastorakos E, Balachandran R, Couris S. Comparison of electrical and laser spark emission spectroscopy for fuel concentration measurements. *Exp Therm Fluid Sci* 2010; 34: 338–45.

References

- [212] Sturm V, Noll R. Laser-induced breakdown spectroscopy of gas mixtures of air, CO₂, N₂, and C₃H₈ for simultaneous C, H, O, and N measurement. *Appl Opt* 2003; 42: 6221–5.
- [213] Li H-L, Xu H-L, Yang B-S, Chen Q-D, Zhang T, Sun H-B. Sensing combustion intermediates by femtosecond filament excitation. *Opt Lett* 2013; 38: 1250–2.
- [214] Michel APM. Review: Applications of single-shot laser-induced breakdown spectroscopy. *Spectrochim Acta Part B* 2010; 65: 185–91.
- [215] Bilger RW. A mixture fraction framework for the theory and modeling of droplets and sprays. *Combust Flame* 2011; 158: 191–202.
- [216] Richards CD, Pitts WM. Global density effects on the self-preservation behaviour of turbulent free jets. *J Fluid Mech* 1993; 254: 417–35.
- [217] Gupta M. Spray flame project. MEng thesis. University of Cambridge 2013.
- [218] Janzen C, Fleige R, Noll R, Schwenke H, Lahmann W, Knoth J, et al. Analysis of small droplets with a new detector for liquid chromatography based on laser-induced breakdown spectroscopy. *Spectrochim Acta Part B* 2005; 60: 993–1001.
- [219] Bourgeois P, Althaus M, Hugenschmidt M. Influence of aerosols on gas-breakdowns induced by high-power-pulsed infrared laser radiation. *Proc SPIE XI Int Sym Gas Flow Chem Lasers & High-Power Laser Conf* 1997; 3092: 610-614.
- [220] Cavaliere DE. Blow-off in gas turbine combustors. PhD thesis, University of Cambridge, 2013.
- [221] Product overview / technical data: Series 212 Axial hollow cone nozzles. Lechler Inc., http://www.lechlerusa.com/index-en_US.
- [222] COSILAB Manual. Sec. 1D premixed flames and counterflow flames. Version 3, Page 13-14.